


University of Salerno

Department of Industrial Engineering

Ph. D. Thesis in

MECHANICAL ENGINEERING

XIV CYCLE (2013–2015)

Unsteady and three-dimensional fluid dynamic instabilities

Vincenzo Citro

Supervisor
Ch.mo Prof.
Paolo Luchini

Coordinator
Ch.mo Prof.
Vincenzo Sergi

Alla mia famiglia!

Acknowledgments

Prima di tutto desidero ringraziare il Prof. Paolo Luchini e il Prof. Flavio Giannetti che hanno influenzato profondamente il mio modo di pensare e di vedere le cose. Il Prof. Luchini mi ha insegnato veramente tanto ed il suo modo di inquadrare i problemi resta e resterá sempre per me fonte d'ispirazione. Lo ringrazio molto per la pazienza che mi ha dedicato e per tutti i commenti e le innumerevoli riletture dei miei lavori. Durante i congressi ho imparato ad ascoltare i suoi commenti che mi hanno sempre insegnato qualcosa. Ho imparato a chiedermi il perché delle cose e ad essere 'critico'. Lo ringrazio molto anche per avermi concesso il tempo e la libertá necessari in un momento delicato che purtroppo ho dovuto affrontare.

Flavio é stato per me un riferimento sempre chiaro e costante. Condividendo con lui lo studio negli ultimi anni ho imparato moltissimo! Spesso ha speso tempo ed energie per insegnarmi qualcosa. Posso solo essere veramente grato per tutte le sere in cui abbiamo lasciato lo studio alle 22:00 o tutte le volte in cui abbiamo finito un lavoro nel fine settimana. Umanamente ha reso quest'esperienza un'oppurtunitá.

Ringrazio molto Francesco Villecco e Nicola Cappetti per l'infinitá di consigli preziosi che mi hanno elargito e per la serenitá durante le infinite pause pranzo.

In questo percorso ho avuto il piacere e l'onore di lavorare anche con il Prof. Franco Auteri. E' stato un riferimento al di fuori di UniSa e lo ringrazio molto per i commenti sui miei lavori e non solo. Nel mio periodo 'milanese' ho avuto il piacere di conoscere anche Marco Carini. Ringrazio Luca Brandt che mi ha ospitato al KTH e che ha contribuito alla stesura dei miei lavori. In Svezia ho avuto la possibilitá e l'onore di conoscere anche Outi ed Iman. Ringrazio David Fabre e Joel Tchoufag che hanno reso la mia permanenza all'IMFT gradevole e stimolante. Le infinite mail scambiate con David hanno sicuramente giovato alla mia preparazione. Non posso non essere grato a Lorenzo e a Simone per la pazienza e l'amicizia.

Un ringraziamento sentito é rivolto a tutti i miei coautori che hanno reso

possibile l'esistenza di questa tesi. Senza il loro supporto non avrei potuto pensare di potermi occupare di argomenti cosí interessanti. Un grazie a Damiano, Mariarosaria, Rosaria, Mario, Serena, Raffaele, Donato, Raffaele, Marco, Emilia, Antonello, Francesca e chiunque abbia condiviso con me questo lungo viaggio.

Last but not least, ringrazio Mary per tutte le volte in cui mi é stata accanto nelle sere in cui avevo un grafico o una frase da aggiustare. Grazie per la pazienza, la forza e la serenitá. I miei genitori hanno reso possibile tutto ció. Grazie per avermi supportato e sopportato!

Abstract

Unsteady and three-dimensional fluid dynamic instabilities

Vincenzo Citro
DIIN, University of Salerno,
Via Giovanni Paolo II, 84084 Fisciano (SA), Italy

This thesis concerns with hydrodynamic stability of fluid flows. Direct numerical simulation (DNS) is used to investigate the non-linear dynamics of the flow and to obtain the basic states. We develop a new procedure (named `BoostConv`) able to stabilize the dynamical system without negatively impacting on the computational time of the original numerical procedure. The stability and transition of several flow configurations, such as the flow over an open cavity, the flow past a sphere or a hemispherical roughness element are investigated. In particular, a modal stability analysis is used to study the occurrence of possible bifurcations. Both direct and adjoint eigenmodes are considered and the region of the flow responsible for causing the global instability is identified by the structural sensitivity map. Moreover, we generalize the latter concept by including second-order terms. We apply the proposed approach to a confined wake and show how it is possible to take into account the spanwise wavy base-flow modifications to control the instability. Inspired by the sensitivity field obtained to localize the 'wavemaker' in complex flows, we introduce the Error Sensitivity to Refinement (ESR) suitable for an optimal grid refinement that minimizes the global solution error. The new criterion is derived from the properties of the adjoint operator and provides a map of the sensitivity of the global error (or its estimate) to a local mesh adaptation. Finally, we investigate the stability of unsteady boundary layers using the complex-ray theory. This theory allows us to describe the propagation of small disturbances by a high-frequency (optical) approximation similar to the one adopted for wave propagation in nonuniform media.

Preface

This thesis in fluid mechanics consists of two parts. The objective of the first part is to provide an overview of the different approaches used to study the hydrodynamic stability of fluid flows. We briefly introduce the theoretical framework, the numerical methods and set the proposed results into the inherent literature context. The second part consists of ten papers. The contents of each manuscript has not been altered compared to the published or submitted version. The following articles are included:

1. Iman Lashgari, Outi Tammisola, Vincenzo Citro, Matthew P. Juniper & Luca Brandt.
   The planar X-junction flow: stability analysis and control,
   Journal of Fluid Mechanics, Vol.753, pp. 1-28 (2014), doi:10.1017/jfm.2014.364

2. Outi Tammisola, Flavio Giannetti, Vincenzo Citro & Matthew P. Juniper.
   Second-order perturbation of global modes and implications for spanwise wavy actuation,
   Journal of Fluid Mechanics, Vol.755, pp. 314-335 (2014), doi:10.1017/jfm.2014.415

3. Vincenzo Citro, Flavio Giannetti, Luca Brandt & Paolo Luchini.
   Linear three-dimensional global and asymptotic stability analysis of incompressible open cavity flow,
   Journal of Fluid Mechanics, Vol.768, pp. 113-140 (2015), doi:10.1017/jfm.2015.72

4. Vincenzo Citro & Paolo Luchini.
   Multiple-scale approximation of instabilities in unsteady boundary layers,
   European Journal of Mechanics-B/Fluids, Vol.50, pp. 1-8 (2015), doi:10.1016/j.euromechflu.2014.10.004

5. Vincenzo Citro, Flavio Giannetti, Paolo Luchini & Franco Auteri.
   Global stability and sensitivity analysis of boundary-layer flows past a hemispherical roughness element,
   Physics of Fluids, Vol.27, pp. 084110 (2015), doi:10.1063/1.4928533

6. Vincenzo Citro, Flavio Giannetti & Jan O. Pralits.
   Three-dimensional stability, receptivity and sensitivity of non-Newtonian flows inside open cavities,
   Fluid Dynamics Research, Vol.47, pp. 015503 (2015), doi:10.1088/0169-5983/47/1/015503

7. Vincenzo Citro, Joel Tchoufag, David Fabre, Flavio Giannetti & Paolo Luchini.
   Linear stability and weakly nonlinear analysis of the flow past rotating spheres,
   Submitted to Journal of Fluid Mechanics

8. V. Citro, P. Luchini, F. Giannetti & F. Auteri
   Efficient stabilization and acceleration of numerical simulation of fluid flows by residual recombination,
   Submitted to Journal of Computational Physics

9. P. Luchini, F. Giannetti, V. Citro
   Error sensitivity to refinement: a criterion for optimal grid adaptation,
   Submitted to Theoretical and Computational Fluid mechanics

10. D. Fabre, J. Tchoufag, V. Citro, F.Giannetti & P.Luchini
    Weakly nonlinear analysis of freely moving sphere,
    Submitted to Theoretical and Computational Fluid mechanics

Proceedings and Conferences

The following papers, though related, have not been included into this thesis.

2013 P. Luchini, F. Giannetti & V. Citro
Short-wave analysis of instabilities in open and closed cavities,
In Euromech Colloquium 547 - Trends in Open Shear Flow Instability Paris 1-3 Luglio 2013, Paris - LadHyX, École polytechnique Pag.31.

2013 V. Citro & P. Luchini
Unsteady boundary-layer transition prediction,
In Proceedings of AIMETA 2013, Torino, Italy, 17-20 September 2013.

2013 F. Giannetti, V. Citro, L. Brandt & P. Luchini
Three-dimensional instability in open cavity flows,
In Proceedings of AIMETA 2013, Torino, Italy, 17-20 September 2013.

2013 P. Luchini, F. Giannetti & V. Citro
Short-wave analysis of 3D and 2D instabilities in a driven cavity,
Bulletin of the American Physical Society, Vol. 58, Pag.18. November 24-26, 2013; Pittsburgh, Pennsylvania - USA. (ISSN:0003-0503).

2013 O. Tammisola, F. Giannetti, V. Citro & M. Juniper
Second-order sensitivity of eigenvalues: large or spanwise wavy perturbations,
Bulletin of the American Physical Society, Vol. 58, Pag.18. November 24-26, 2013; Pittsburgh, Pennsylvania - USA. (ISSN:0003-0503).

2013 L. Brandt, V. Citro, F. Giannetti & I. Lashgari
Instability mechanisms in the viscoelastic flow past bluff bodies,
85th Annual Meeting - The Society of Rheology, Montral, Canada, 13-17 October 2013.

2014 P. Luchini, F. Giannetti & V. Citro
Error Sensitivity to Refinement: a criterion for optimal grid adaptation,
GIMC-GMA 2014, Cassino 11-13 June.

2014 D. Fabre, P. Bonnefis, F. Charru, S. Russo, V. Citro, F. Giannetti & P. Luchini.
Application of global stability approaches to whistling jets and wind instruments,
International Symposium on Musical Acoustics (ISMA'14), Le Mans, 6-12 Juiy.

2014 V. Citro, F. Giannetti, P. Luchini & F. Auteri
Boundary-layer flows past an hemispherical roughness element: DNS, Global stability and sensitivity analysis,
IUTAM Laminar Turbulent Transition (ABCM), Rio de Janeiro, 8 - 12 September.

2015 F. Giannetti, P. Luchini, V. Citro & F. Auteri
`BoostConv`*: finding unstable solutions of the equations of fluid motion*,
In Proceedings of AIMETA 2015, Genova, Italy, 14-17 September 2015. (ISBN: 978-88-97752-55-4)

2015 V. Citro, J. Tchoufag, F. Giannetti, D. Fabre, P. Luchini
Linear stability & weakly nonlinear analysis of rotating sphere,
In Proceedings of AIMETA 2015, Genova, Italy, 14-17 September 2015. (ISBN: 978-88-97752-55-4)

2015 F. Giannetti, V. Citro, P. Luchini, J. Tchoufag & D. Fabre
Global stability of the flow around a rotating sphere flows,
Global Flow Instability and Control Symposium VI, Crete, Greece, 28 Sept.-2 Oct. 2015.

Contents

I Theoretical framework, numerical methods & results 13

1 Introduction 15

2 Theoretical framework 17
2.1 Governing equations 17
2.2 Linear stability theory 17
2.3 Local analysis 18
2.4 Ray Theory 19
2.5 Two-dimensional and three-dimensional global stability analysis 22
2.6 Zero-dimensional asymptotic analysis 23

3 Adjoint problem and Structural sensitivity 27
3.1 Adjoint equations 27
3.2 Classical sensitivity analysis 28
3.2.1 Structural sensitivity 28
3.2.2 Sensitivity to base flow modifications 29
3.3 Second-order sensitivity 30
3.4 Inviscid Sensitivity analysis 31
3.5 Error Sensitivity to Refinement (ESR): an indicator for optimal grid adaptation 32

4 Stabilization of the solution of the Navier-Stokes equations 37
4.1 Iterative solution of a linear system 38
4.2 The Recursive Projection Method (RPM) 38
4.3 SFD 39
4.4 `BoostConv` 40

5 Numerical methods 45
5.1 *Freefem++* 45

5.1.1 Base flow 45
5.1.2 Direct and Adjoint eigenvalue solver 46
5.2 *Nek*5000 47
5.3 Finite-Difference Multigrid 48

6 Conclusions **51**

Bibliography **53**

II Papers **57**

Part I

Theoretical framework, numerical methods & results

Chapter 1

Introduction

The concept of stability bears on the reaction of a system to a small perturbation of its state. If the generic disturbance grows in time, the system is unstable. The stability of an airplane, a motorboat or a surgical robot, for example, could be crucial for the human life. Thus, it is very important, from a practical viewpoint, to be able to analyse the stability of a system. Quoting from L. D. Landau & E. M. Lifshitz [1] *"Yet not every solution of the equations of motion, even if it is exact, can actually occur in Nature. The flows that occur in Nature must not only obey the equations of fluid dynamics, but also be stable."*. Even if these statements are only qualitative and need to be translated in a more rigorous mathematical theory, they suggest the importance of this field.

The concept of stability can be simply formulated for a system of Ordinary Differential Equations (ODE). Such system can be at equilibrium, where the state does not depend on time, or can present a periodic state, with all components returning to the same values, after every period. However, before considering the stability of a system, the first fundamental question is about the *existence* of such states. Once this issue has been addressed, the stability features can be studied. Two scientists significantly contributed to this field: A. M. Lyapunov [2] and the French physicist H. Poincaré [3]. In particular, Lyapunov discussed the local stability properties of ODEs near their fixed points. The latter, instead, focused his attention on the occurrence of the chaotic motion in the whole state space.

Helmholtz[4], Kelvin[5] and Rayleigh[6] started the study of the stability of a fluid system neglecting the effect of the viscosity. Few years later, Reynolds[7] performed the famous experiment of the pipe flow in which he illustrated the conditions that lead to laminar, transitional and fully turbulent flow. Orr[8] and Sommerfeld[9], subsequently, considered a small distur-

bance superposed on a steady parallel flow. The Orr-Sommerfeld equations have been widely adopted to study the stability of parallel and quasi-parallel flow (the latter by using WKBJ theory).

In the last decades, the theory of flow instability received great attention (see *e.g.* Schmid & Henningson[10], Charru [11]). A crucial point, that drove the development in this field, was the availability of larger and larger computing resources. Theofilis[12], recently, reviewed the linear global instability analysis of flows in complex two-dimensional and three-dimensional geometries. Global analysis allows us to avoid the limitation of local theory but it is very expensive from the computational viewpoint, in particular in the computation of the eigenvalues and eigenvectors. Therefore such problems require advanced numerical techniques that are often developed for this specific purpose. This thesis is aimed at studying the stability of such complex flows, with a balanced attention to theoretical aspects, numerical tools and the physical mechanism of hydrodynamic instabilities.

Chapter 2

Theoretical framework

2.1 Governing equations

The dynamics of fluids is described by a system of partial differential equations (PDEs) proposed by C.-L. Navier and G. G. Stokes. The fluid is assumed to be a continuous medium and, therefore, all the variables are considered to be continuous functions of the spatial coordinates $(x, y, z) \in \mathbb{R}^3$ and time $t \in \mathbb{R}$. Furthermore, we assume that there is a linear relationship between the viscous stress and the strain rate, *i.e.* that the fluid is Newtonian. In case of vanishing volume forces, the Navier-Stokes system can be written in the following dimensionless form as:

$$\boldsymbol{\nabla} \cdot \boldsymbol{u} = 0, \tag{2.1a}$$

$$\frac{\partial \boldsymbol{u}}{\partial t} + (\boldsymbol{u} \cdot \boldsymbol{\nabla})\boldsymbol{u} = -\boldsymbol{\nabla} P + \frac{1}{Re}\nabla^2 \boldsymbol{u}, \tag{2.1b}$$

where $\boldsymbol{u}$ is the velocity vector with components (u, v, w) and P is the reduced pressure field. The characteristic length scale is denoted as L_{ref} and a reference velocity as U_{ref}. For example, L_{ref} can be the depth D of a cavity as in **paper 3**, the height k of a roughness element as in **paper 5** or the diameter of a sphere studied as in **paper 7** and in **paper 10**; the reference velocity can be the channel centerline velocity U_{CL} as in **paper 1** or the freestream velocity U_∞ (**paper 3,4,6,7,10**). The Reynolds number is defined as $Re = U_{ref} L_{ref}/\nu$ with ν the fluid kinematic viscosity.

2.2 Linear stability theory

For the purpose of a linear stability analysis, the total velocity $\mathbf{u}(x, y, z, t)$ and pressure $P(x, y, z, t)$ fields are written as the sum of base flow, $\boldsymbol{Q_b}(x, y, z)$

$= (u_b, v_b, w_b, P_b)$, and a small disturbance denoted by $\boldsymbol{q'}(x, y, z, t) = (u', v', w', P')$. Introducing this decomposition into the Navier-Stokes system (2.1) and neglecting second-order terms, we obtain two systems describing the spatial structure of the *base flow* and the behaviour of generally *unsteady perturbations*. In particular, the base flow is governed by the steady version of (2.1), whereas the perturbation field is described by the linearized unsteady Navier-Stokes equations (LNSE)

$$\frac{\partial \boldsymbol{u'}}{\partial t} + \mathcal{L}\{\boldsymbol{u}_b, Re\}\boldsymbol{u'} = -\boldsymbol{\nabla} P', \tag{2.2}$$

$$\nabla \cdot \boldsymbol{u'} = 0, \tag{2.3}$$

with the linearized Navier-Stokes operator $\mathcal{L}$:

$$\mathcal{L}\{\boldsymbol{u}_b, Re\}\boldsymbol{u'} = \boldsymbol{u}_b \cdot \boldsymbol{\nabla}\boldsymbol{u'} + \boldsymbol{u'} \cdot \boldsymbol{\nabla}\boldsymbol{u}_b - \frac{1}{Re}\boldsymbol{\nabla}^2\boldsymbol{u'}. \tag{2.4}$$

In order to solve the differential problem (2.2-2.3) we need to impose the appropriate conditions at the boundaries of the domain under investigation.

2.3 Local analysis

Initially, the linear stability theory focused on fluid flows that are homogeneous in two spatial directions, e.g. plane Poiseuille flow [13]. This implies that the streamwise and the spanwise base-flow gradients vanish and, as a consequence, we consider only the streamwise velocity component $u_b(y)$. Inserting this base flow field into (2.2-2.3), we get a PDE system whose coefficients are independent of the spatial coordinates x, z and time t. Thus, taking into account the translation invariance of the problem in those directions, we can express the perturbation by using the Fourier representation as:

$$\boldsymbol{q'}(x, y, z, t) = \frac{1}{2}\{\hat{\boldsymbol{q}}(y)\ exp[\gamma t - i\alpha x - i\beta z] + c.c.\}, \tag{2.5}$$

where $\hat{\boldsymbol{q}} = (\hat{u}, \hat{v}, \hat{w}, \hat{P})$, α and β are the spatial wavenumbers. Introducing the ansatz (2.5) in the resulting LNSE system (2.2-2.3) leads to a system of Ordinary Differential Equations (ODEs) usually named Orr-Sommerfeld equations[10]:

$$-i\alpha\hat{u} + \hat{v}_y - i\beta\hat{w} = 0, \tag{2.6a}$$

$$\gamma\hat{u} - i\alpha u_b\hat{u} + u_{b,y}\hat{v} - i\alpha\hat{P} - \frac{1}{Re}(\hat{u}_{yy} - \alpha^2\hat{u} - \beta^2\hat{u}) = 0, \tag{2.6b}$$

$$\gamma\hat{v} - i\alpha u_b\hat{v} + \hat{P}_y - \frac{1}{Re}(\hat{v}_{yy} - \alpha^2\hat{v} - \beta^2\hat{v}) = 0, \tag{2.6c}$$

$$\gamma\hat{w} - i\alpha u_b\hat{w} - i\beta\hat{P} - \frac{1}{Re}(\hat{w}_{yy} - \alpha^2\hat{w} - \beta^2\hat{w}) = 0, \tag{2.6d}$$

We note that the eigenfunction $\hat{\mathbf{q}}$ exists only for values of α, β and γ that satisfy the inherent dispersion relation:

$$D(\alpha, \beta, \gamma, Re) = 0. \tag{2.7}$$

In simple cases, we can analytically calculate this relation. Otherwise, we obtain this relation by discretizing the Orr-Sommerfeld equations. We can consider an initial value problem, where we impose an initial disturbance and investigate its *temporal* growth. Such disturbance is represented, in the Fourier analysis, by a sum of modes (2.5) with real α and β and complex γ. The value of $\gamma = \sigma + i\omega$, provided by the dispersion relation, will indicate if the disturbance grows in time. The real part σ of γ represents the temporal growth rate of the perturbation and the imaginary part ω its frequency. For $\sigma > 0$, the flow is unstable whereas for $\sigma < 0$ it is stable.

On the other hand, we can consider a spatial problem where we impose a sinusoidal wave in space and investigate the *spatial* growth of such a wave. The inherent Fourier representation will have a real β, an imaginary γ and a complex α provided by the dispersion relation. This problem is also known as the *signaling* problem [13]. Such a *spatial analysis* is, for example, used to investigate the stability of the Blasius boundary layer. However, in the case of a generic unsteady flow, a theory able to describe the propagation of disturbance wave trains is still lacking. In the following section we will show how to investigate the stability of a generic unsteady flow.

2.4 Ray Theory

In this section, we present the ray theory in the case of the flow over a flat plate. However, the theory discussed herein can be applied to a generic steady or unsteady flow configuration. We choose for convenience the x axis in the streamwise direction, the y axis normal to the wall and the z axis orthogonal to the first two. As discussed in the previous sections, the

fluid motion is described by the usual Navier-Stokes system of equations. We choose to study the onset of instability within the framework of linear theory like the case of local stability analysis. Thus, the perturbed field is solution of the linearized Navier-Stokes equations (2.2-2.3). Let us focus our attention on the evolution of the disturbances on a known base flow.

In particular, we assume that the characteristic length scale ℓ_{bf} on which the base flow evolves is much larger than the perturbation length scale ℓ_{pert}. Thus, we consider the base flow as a function of (X, y, Z, T):

$$X = \epsilon x, \;\; Z = \epsilon z, \;\; T = \epsilon t. \tag{2.8}$$

where the small parameter $\epsilon << 1$ is the ratio between the two characteristic length scales. We *do not make* any additional assumption on the motivation why the base flow has different scales in the streamwise and wall-normal direction. This implies that ϵ and the Reynolds number Re are independent parameters.

In order to describe the evolution of the instability, even in the case of an unsteady base flow, a multiple-scale approximation is adopted as in Gaster[24]. Following the classical Wentzel-Kramers-Brillouin (WKB) [26] asymptotic expansion, the perturbation is expressed as follows:

$$\boldsymbol{q}'(X, y, Z, T) = e^{i\frac{\Theta(X,Z,T)}{\epsilon}} \sum_{k=0}^{\infty} \hat{\boldsymbol{q}}_k(X, y, Z, T)\epsilon^k \tag{2.9}$$

where $\hat{\boldsymbol{q}}_k = [\hat{u}_k, \hat{v}_k, \hat{w}_k, \hat{p}_k]$ and Θ is named the eikonal function; its spatial and temporal derivatives respectively represent the local wavenumber components and the frequency of the perturbation. Furthermore, we adopt the following notation:

$$\alpha = -\frac{\partial\Theta}{\partial X}, \;\; \beta = -\frac{\partial\Theta}{\partial Z}, \;\; \omega = \frac{\partial\Theta}{\partial T}. \tag{2.10}$$

Substituting the above expansion (2.9) into the perturbation equations (2.2), taking into account the relation (2.8) and grouping terms multiplied by the same power of ϵ, a hierarchy of equations is obtained. The leading-order approximation is governed by a differential problem formally identical to the one corresponding to the parallel-flow case (2.6) ***but for non-constant*** α, β and ω.

The linear system (2.6) admits a non-trivial solution if and only if the dispersion relation:

$$\mathcal{D}\left(X, Z, T, \alpha, \beta, \omega\right) = 0, \tag{2.11}$$

is satisfied.

We recall that after the discretization procedure (in y direction), the dispersion relation can be simply obtained by equating to zero the determinant of the resulting algebraic system. The dispersion relation of the differential problem can be considered as the limit of this determinant.

Inserting the definition of the local frequency and local wavenumber (2.10) in the dispersion relation, we obtain a first-order PDE for the complex eikonal function Θ:

$$\mathcal{D}\left(X, Z, T, -\frac{\partial\Theta}{\partial X}, -\frac{\partial\Theta}{\partial Z}, \frac{\partial\Theta}{\partial T}\right) = 0. \tag{2.12}$$

This equation is analogous to the Hamilton-Jacobi equation of analytical mechanics [27]; once the values of the eikonal function are assigned on a non-characteristic strip, then a unique solution of the Cauchy problem exists.

Characteristic lines in the parametric form $X = X(\sigma)$, $Z = Z(\sigma)$, $T = T(\sigma)$, $\alpha = \alpha(\sigma)$, $\beta = \beta(\sigma)$, $\omega = \omega(\sigma)$ are the solutions of the following system of ordinary differential equations:

$$\frac{dX}{d\sigma} = -\frac{\partial\mathcal{D}}{\partial\alpha}, \quad \frac{dZ}{d\sigma} = -\frac{\partial\mathcal{D}}{\partial\beta}, \quad \frac{dT}{d\sigma} = \frac{\partial\mathcal{D}}{\partial\omega}, \tag{2.13a}$$

$$\frac{d\alpha}{d\sigma} = \frac{\partial\mathcal{D}}{\partial X}, \quad \frac{d\beta}{d\sigma} = \frac{\partial\mathcal{D}}{\partial Z}, \quad \frac{d\omega}{d\sigma} = -\frac{\partial\mathcal{D}}{\partial T}, \tag{2.13b}$$

$$\frac{d\Theta}{d\sigma} = \frac{\partial\mathcal{D}}{\partial\alpha}\alpha + \frac{\partial\mathcal{D}}{\partial\beta}\beta + \frac{\partial\mathcal{D}}{\partial\omega}\omega. \tag{2.14}$$

The differential equations (2.13) are called *ray equations*. Equation (2.14), on the other hand, is directly derived from the definition of Θ; it can be used to compute the value of the eikonal function along the ray.

As previously mentioned, there is a strong analogy between the Hamiltonian equations of mechanics and the ray equations (2.13). Just as for the trajectory of a material point in mechanics, we can select a ray both by its initial location and wave vector $(X_0, Z_0, T_0, \alpha_0, \beta_0, \omega_0)$ (leading to an IVP) or by its initial and final positions $(X_0, Z_0, T_0, X_1, Z_1, T_1)$ (leading to a BVP).

Further details can be found in **paper 4** where we discuss also an application to a two-dimensional time-periodic flow (arising in oscillating airfoil problems) that, in addition, allows us to estimate the error introduced using a quasi-steady approach in the stability analysis.

2.5 Two-dimensional and three-dimensional global stability analysis

When the base flow is homogeneous and stationary in the spanwise direction only, a generic perturbation can be decomposed into Fourier modes of spanwise wavenumber β. The three-dimensional perturbations are expressed as

$$\boldsymbol{q}'(x,y,z,t) = \frac{1}{2}\{\hat{\boldsymbol{q}}(x,y)\ exp[\gamma t - i\beta z] + c.c.\}, \tag{2.15}$$

where $\gamma = \sigma + i\omega$ is the complex growth rate and *c.c.* stands for complex conjugate. Introducing the ansatz (2.15) in the LNSE (2.2-2.3), we obtain the *two-dimensional* generalized eigenvalue problem

$$\mathscr{A}\hat{\mathbf{q}}(x,y) + \gamma\mathscr{B}\hat{\mathbf{q}}(x,y) = 0, \tag{2.16}$$

where $\mathscr{A}$ is the complex linearized evolution operator. The operators $\mathscr{A}$ and $\mathscr{B}$, have the following expressions:

$$\mathscr{A} = \begin{pmatrix} \mathscr{C} - \mathscr{M} + \partial_x u_b & \partial_y u_b & 0 & \partial_x \\ \partial_x v_b & \mathscr{C} - \mathscr{M} + \partial_y v_b & 0 & \partial_y \\ 0 & 0 & \mathscr{C} - \mathscr{M} & ik \\ \partial_x & \partial_y & ik & 0 \end{pmatrix},$$

$$\mathscr{B} = \begin{pmatrix} 1 & 0 & 0 & 0 \\ 0 & 1 & 0 & 0 \\ 0 & 0 & 1 & 0 \\ 0 & 0 & 0 & 0 \end{pmatrix}, \tag{2.17}$$

where $\mathscr{M} = Re^{-1}(\partial_{x^2} + \partial_{y^2} - \beta^2)$ and $\mathscr{C} = u_b\partial_x + v_b\partial_y$ describe the viscous diffusion of the perturbation and its advection by the base flow. The boundary conditions associated with the eigenproblem (2.16) can be derived from those used for the base flow.

Finally, we note that the complex conjugate pairs $(\sigma + i\omega; \hat{\mathbf{q}})$ and $(\sigma - i\omega; \hat{\mathbf{q}}^*)$ are both solutions of the eigenproblem (2.16) for a real base flow $\boldsymbol{Q_b}$. Thus, the eigenvalues are complex conjugates and the spectra are symmetric with respect to the real axis in the (σ, ω) plane.

In the real world, however, we can observe flow configurations without any homogeneous spatial direction. The flow past a sphere (**paper 7,10**) or the flow over a hemispherical roughness element (**paper 5**) are examples where the velocity and the pressure fields have strong variations in all

directions. In case of full 3D analysis, the normal mode ansatz is

$$\boldsymbol{q}'(x,y,z,t) = \frac{1}{2}\{\hat{\boldsymbol{q}}(x,y,z)\ exp[\gamma t] + c.c.\}. \tag{2.18}$$

We refer to Chapter 5 for further details about the numerical methods developed to solve such eigenvalue problems.

2.6 Zero-dimensional asymptotic analysis

In the previous sections, we used the translational invariance (local or two-dimensional analysis) or the scale separation (WKBJ) to reduce the full 3D stability equations to a lower dimensional problem. However, in several flow configurations, it is possible to consider a scale separation in all directions: this leads to a zero-dimensional asymptotic analysis. These techniques have originally been developed to study inviscid instabilities. In particular, we present the asymptotic theory developed by Bayly [17]. He proposed to adopt a short-wavelength approximation (WKBJ) to describe the evolution of the perturbations along closed streamlines. This approach is shortly outlined here; for a more detailed presentation the reader is referred to [18, 19]. The solution of the linearized Navier–Stokes equations is sought in the form of a rapidly oscillating and localized wave-packet, evolving along the *Lagrangian trajectory* $\mathbf{X}(t)$ and characterized by a *wave-vector* $\mathbf{k}(t) = \nabla\phi(\mathbf{X},t)$ and an *envelope* $\mathbf{a}(\mathbf{X},t)$ such that:

$$\mathbf{u}(\mathbf{X},t) = \mathrm{e}^{i\phi(\mathbf{X},t)/\epsilon}\mathbf{a}(\mathbf{X},t,\epsilon) = \mathrm{e}^{i\phi(\mathbf{X},t)/\epsilon}\sum_n \mathbf{a}_n(\mathbf{X},t)\epsilon^n \tag{2.19}$$

$$p(\mathbf{X},t) = \mathrm{e}^{i\phi(\mathbf{X},t)/\epsilon}b(\mathbf{X},t,\epsilon) = \mathrm{e}^{i\phi(\mathbf{X},t)/\epsilon}\sum_n b_n(\mathbf{X},t)\epsilon^{n+1} \tag{2.20}$$

where $\epsilon \ll 1$ and $\mathbf{X} = \epsilon\mathbf{x}$ is a slowly varying variable. In the limit of vanishing viscosity ($Re \to \infty$) and large wavenumbers ($||\mathbf{k}|| \to \infty$), the theory provides the leading order term for the growth rate associated with a localized perturbation. This is obtained by integrating the following set of ordinary differential equations

$$\frac{D\mathbf{k}}{Dt} = -\mathcal{H}^t(\mathbf{X})\mathbf{k}, \tag{2.21}$$

$$\frac{D\mathbf{a}}{Dt} = \left(\frac{2\mathbf{k}\mathbf{k}^T}{|\mathbf{k}|^2} - \mathcal{I}\right)\mathcal{H}(\mathbf{X})\mathbf{a}, \tag{2.22}$$

along the Lagrangian trajectories defined by the ODE

$$\frac{D\mathbf{X}(t)}{Dt} = \mathbf{u}_b(X(t), t) \ . \tag{2.23}$$

In the equations above $\mathcal{H} = \nabla \mathbf{u}_b$ is the base-flow velocity gradient tensor and $\mathcal{I}$ the identity matrix. Since the flow under investigation is steady, the Lagrangian trajectory corresponds to the streamlines of the base flow. Three initial conditions have to be assigned to solve the problem above: $\mathbf{k}(t=0) = \mathbf{k}_0$, $\mathbf{a}(t=0) = \mathbf{a}_0$ and $\mathbf{x}(t=0) = \mathbf{x}_0$. The last condition imposes the Lagrangian origin of the streamline and thereby entirely identifies it.

Lifschitz & Hameiri [18] proved that a sufficient condition for inviscid instability is that the system of eqs. (2.21), (2.22) and (2.23) has at least one solution for which $\|\mathbf{a}(t)\| \to \infty$ as $t \to \infty$. This theory has been successfully applied in the past to study elliptic, hyperbolic and centrifugal instabilities of two-dimensional stationary base flows [20]. We apply this theory to characterize the instability mechanism arising inside an open cavity as discussed in **paper 3**. For this flow configuration, a central role is played by the closed Lagrangian trajectories (closed streamlines in **paper 3**), i.e. orbits described by material points which return to their initial positions after a given time T (the period of revolution of a material particle). These closed trajectories play a special role in the dynamics of the instability: on the closed orbits, local instability waves propagate and feedback on themselves leading to a self-excited unstable mode.

As discussed above, the theory implies that both equations (2.21) and (2.22) must be integrated along these closed orbits. In the case investigated in **paper 3**, the base flow is steady and the streamlines are closed: eq. (2.21) is a linear ODE with periodic coefficients whose general solution can be written in terms of Floquet modes. In particular, the solution can be found by building the fundamental Floquet matrix $\mathcal{M}(T)$, solution of the system

$$\frac{D\mathcal{M}}{Dt} = -\mathcal{H}^t(\mathbf{X})\mathcal{M} \quad with \quad \mathcal{M}(0) = \mathcal{I} \ , \tag{2.24}$$

and extracting its eigenvalues and the corresponding eigenvectors. Using these eigenvectors as initial conditions, it is possible to retrieve the temporal evolution of $\mathbf{k}$ during a lap around the closed streamline. Equation (2.21) admits three independent solutions related to the 3 eigenvectors of the fundamental Floquet matrix $\mathcal{M}(T)$. In the case of two-dimensional base flows, there exists for each orbit one eigenvalue equal to 1 with the corresponding eigenvector that remains constant in time and orthogonal to the

base flow. In other words, since the third column of $\mathcal{H}$ and the third line of $\mathcal{H}^t$ are zero, the transverse component of $\mathbf{k}$ remains constant as time evolves. On the contrary, the in-plane components evolve under the action of the deformation tensor. Once equation (2.21) is solved, the amplitude $\mathbf{a}$ can be found by integrating equation (2.22). One can use any linear combination of the Floquet modes from equation (2.24) to set the specific $\mathbf{k}$ in equation (2.22).

Since we are trying to determine a self-excited mode, we need only to consider solutions of (2.21) that are periodic in time, i.e. solutions such that $\mathbf{k}(0) = \mathbf{k}(T)$. Here, as in Bayly [17], only eigenvectors orthogonal to the base flow are considered. With this choice, eq. (2.22) reduces to an ordinary linear differential equation with periodic coefficients. According to Floquet theory, its solution can be written in terms of Floquet modes

$$\mathbf{a}(t) = \bar{\mathbf{a}}(t)\ \exp(\sigma t)\ , \tag{2.25}$$

where $\bar{\mathbf{a}}(t)$ is a periodic function (same period T as the material point moving along the selected closed streamline) and $\Re\{\sigma\} = \sigma_r$ is the growth rate of the perturbation.

As for eq. (2.21), the fundamental Floquet matrix $\mathcal{A}$ corresponding to equation (2.22) is built by integrating the system

$$\frac{D\mathcal{A}}{Dt} = \left(\frac{2\mathbf{k}\mathbf{k}^T}{|\mathbf{k}|^2} - \mathcal{I}\right)\mathcal{H}(\mathbf{X})\mathcal{A}, \tag{2.26}$$

$$\mathcal{A}(0) = \mathcal{I}; \tag{2.27}$$

along each orbit. The eigenvalues $\mu_i(x_0)$ and the corresponding eigenvectors of $\mathcal{A}(T)$ can be easily extracted.

As mentioned above, in case of two-dimensional base flows and in case in which the wavevector $\mathbf{k}$ is orthogonal to the $x-y$ plane, we expect one eigenvalue of $\mathcal{A}$ to be 1. The other two, for the incompressibility constrain, must multiply to 1, i.e. $\mu_1(x_0)\ \mu_2(x_0) = 1$. The Floquet exponent $\sigma(x_0)$ of the perturbation on the selected orbit ψ_0 is obtained from the Floquet multiplier $\mu(x_0)$ of $\mathcal{A}$ by the simple relation

$$\sigma^{\{n\}}(\psi_0) = \sigma_r(\psi_0) + i\sigma_i^{\{n\}}(\psi_0) = \frac{\log(\mu)}{T(\psi_0)} + i\frac{2n\pi}{T(\psi_0)} \ \text{ with } n \in \mathbb{N} \tag{2.28}$$

where $T(\psi_0)$ is the period of revolution.

The growth rate of each WKBJ mode is simply given by the real part of $\sigma^{\{n\}}$. The frequency is related to the imaginary part and is not unique. According to the formula (2.28), modes with the same growth rate (at leading order) but different frequencies are admissible: in particular the admissible frequencies are integer multiple of the frequency of revolution along the same streamline.

Finally, in order to have a quantitative estimation of the leading eigenvalue, we adopt the following formula proposed by Gallaire et al.[21]:

$$s = \sigma(\psi_0) - \frac{A}{k} - \frac{k^2}{Re}. \tag{2.29}$$

They considered the viscous correction term [22] and the correction term relative to finite wavenumber effects.

Chapter 3

Adjoint problem and Structural sensitivity

3.1 Adjoint equations

The adjoint of a linear operator is a very powerful and useful concept in the field of functional analysis. The use of the adjoint in the context of hydrodynamic stability analysis has been recently reviewed by Luchini & Bottaro [28]. The adjoint solution can be used when one is looking for some outputs of a system for a large range of possible inputs. There are hundreds of applications of the adjoint in fluid mechanics like the receptivity of boundary layer flows or the identification of self-sustained thermoacoustic oscillations and a feedback mechanism efficient at suppressing them[29]. Furthermore, the adjoint is a fundamental tool in the control theory.

In the framework of hydrodynamic stability theory, the adjoint equations can be used to evaluate the effects of a generic initial condition or forcing terms on the behaviour of the long time solution.

The derivation of the adjoint Navier-Stokes equations is based on the generalized Lagrange identity. Integrating over space and time such relation and using the divergence theorem provides the final system of equations that reads:

$$\frac{\partial \boldsymbol{u}^\dagger}{\partial t} + \mathcal{L}^\dagger\{\boldsymbol{u}_b, Re\}\boldsymbol{u}^\dagger + \boldsymbol{\nabla} P^\dagger = \boldsymbol{0}, \tag{3.1}$$

$$\nabla \cdot \boldsymbol{u}^\dagger = 0, \tag{3.2}$$

where $\mathcal{L}^\dagger$ is the linear *adjoint* Navier-Stokes operator defined as:

$$\mathcal{L}^\dagger\{\boldsymbol{u}_b, Re\}\boldsymbol{u}^\dagger = \boldsymbol{u}_b \cdot \boldsymbol{\nabla}\boldsymbol{u}^\dagger - \boldsymbol{\nabla}\boldsymbol{u}_b \cdot \boldsymbol{u}^\dagger + \frac{1}{Re}\boldsymbol{\nabla}^2\boldsymbol{u}^\dagger \tag{3.3}$$

In the present thesis we are interested in the global adjoint eigenmodes; thus, we express the adjoint perturbation field $(\boldsymbol{u}^\dagger, P^\dagger)$ as a normal mode:

$$\mathbf{q}^\dagger(x, y, z, t) = \hat{\mathbf{q}}^\dagger(x, y, z)\ exp\{-\gamma t\}. \tag{3.4}$$

Inserting (3.4) into equations (3.1-3.2) leads to an adjoint eigenvalue problem. Further details about the procedure adopted to obtain the adjoint system of equations (3.1-3.2) can be found in [35].

3.2 Classical sensitivity analysis

3.2.1 Structural sensitivity

The concept of structural sensitivity is general and can be applied to any dynamical system. Chomaz [31] investigated the stability features of the Ginzburg-Landau equation. He suggested to compute both direct and adjoint eigenvectors to determine the *wavemaker* region, i.e. the flow region giving rise to self-excited oscillations. Subsequently, Giannetti & Luchini [35] considered the flow past a circular cylinder. They underlined the large difference existing between the spatial distribution of the direct global mode and the adjoint one due to the non-normality of the linearized Navier-Stokes operator. This fact suggests that the study of the direct global mode, without considering the adjoint field, cannot correctly identify the instability mechanism. Therefore, they performed a structural sensitivity analysis of the governing operator. In particular, the analysis focused on the variations of the eigenvalue induced by a generic structural modification of this operator. The key idea of their approach is to model the feedback mechanism driving the instability by a local force proportional to the perturbation velocity which acts as a momentum source in the equations governing the evolution of the disturbance. This procedure leads to the definition of a new tensor defined as the product between the direct and adjoint fields:

$$\mathbf{S}(x, y, z) = \frac{\hat{\mathbf{u}}^\dagger \hat{\mathbf{u}}}{\int_D \hat{\mathbf{u}}^\dagger \cdot \hat{\mathbf{u}} dV} \tag{3.5}$$

A spatial map is then constructed by computing the spectral norm of this matrix. The function $\mathbf{S}(x, y, z)$ can be used to determine the locations

where the feedback is stronger, identifying in this way the regions where the instability mechanism acts.

This technique can take into account also strong non-parallel effects and it can be adopted to investigate the instability mechanism of complex flows.

3.2.2 Sensitivity to base flow modifications

In an experimental set up a possible way to introduce a structural perturbation is to add a small obstacle in the flow field. As an example, Strykowski & Sreenivasan[32] discussed where the placement of a small cylindrical obstacle is able to delay the onset of vortex shedding in the wake of a circular cylinder. In their case, the presence of such obstacle produces both a modification of the equations at the perturbation level and a modification of the base flow.

The sensitivity analysis described in the previous section is based on a structural perturbation that acts only on the evolution of the perturbation field. This approach provides the right tool to investigate the wavemaker but does not take into account the structural perturbations that can act at the base-flow level. A generic perturbation, in fact, can induce also modifications to the base flow that, in turn, produce changes in the coefficients of the linearized Navier-Stokes operator.

The so-called *sensitivity to base flow variations* is a concept introduced by Corbett et al.[33], and Marquet et al.[34]. In their analysis a small velocity-based perturbation can act at the base flow level: the effect of the base flow modifications on the leading eigenvalue of the stability problem allowed them to study the different mechanisms that can suppress or enhance the instability. The spatial structure of the so-called *adjoint base flow* [34] can be used to identify the features of the base flow that provide the main contribution to the instability dynamics and the regions where to locate effective passive control devices.

This analysis leads to a definition of the tensor $\mathbf{S}_b$ which expresses the sensitivity of the flow to base flow modifications:

$$\mathbf{S_b} = \frac{\hat{\mathbf{u_b}}^{\dagger}\mathbf{u_b}}{\int_D \hat{\mathbf{u}}^{\dagger} \cdot \hat{\mathbf{u}} dV}. \tag{3.6}$$

As for the structural sensitivity, the spatial map can be obtained by selecting a suitable norm of $\mathbf{S_b}$.

3.3 Second-order sensitivity

Sensitivity analysis has successfully located the most efficient regions in which to apply passive control in many globally unstable flows. As discussed in **paper 2**, the standard sensitivity analysis introduced in section (3.2.1) is linear with respect to the perturbation amplitude. Here, we introduce the second-order sensitivity analysis that allows us to predict also the effect of steady spanwise wavy alternating modification on the flow stability. In fact, the standard analysis predicts that this kind of stationary wavy modifications has no net effect on the stability of planar flows. We generalize sensitivity analysis by including $2nd$ order terms in the computation of the eigenvalue drift.

We focus our attention on a generic eigenproblem of form:

$$\mathcal{L}\hat{\mathbf{q}}_\mathbf{0} = \gamma_\mathbf{0}\hat{\mathbf{q}}_\mathbf{0}, \tag{3.7}$$

where $\mathcal{L}$ is the linearized Navier-Stokes operator, $\hat{\mathbf{q}}_\mathbf{0}$ a global linear temporal eigenmode, and $\gamma_0 = \sigma_0 + i\omega_0$ its eigenvalue. We now denote a structural perturbation of the governing operator by $\delta\mathcal{L}$. Following Hinch[23], the problem can be expanded in powers of the perturbation amplitude ϵ:

$$\begin{aligned}(\mathcal{L} + \epsilon\delta\mathcal{L})\left\{\hat{\mathbf{q}}_\mathbf{0} + \epsilon\hat{\mathbf{q}}_\mathbf{1} + \epsilon^\mathbf{2}\hat{\mathbf{q}}_\mathbf{2} + \mathbf{O}(\epsilon^\mathbf{3})\right\} = \\ \left(\gamma_0 + \epsilon\gamma_1 + \epsilon^2\gamma_2 + O(\epsilon^3)\right)\left\{\hat{\mathbf{q}}_\mathbf{0} + \epsilon\hat{\mathbf{q}}_\mathbf{1} + \epsilon^\mathbf{2}\hat{\mathbf{q}}_\mathbf{2} + \mathbf{O}(\epsilon^\mathbf{3})\right\}\end{aligned} \tag{3.8}$$

Here, γ_j is the j^{th} order correction to the eigenvalue, and $\hat{\mathbf{q}}_\mathbf{i}$ $(i > 0)$ is the i^{th} order correction to the eigenmode.

- At the 0^{th} order in ϵ, the original eigenvalue problem is recovered.
- At the 1^{st} order in ϵ, we obtain, after rearrangement:

  $$(\mathcal{L} - \gamma_0\mathcal{I})\{\hat{\mathbf{q}}_1\} = -\delta\mathcal{L}\{\hat{\mathbf{q}}_0\} + \gamma_1\hat{\mathbf{q}}_0, \tag{3.9}$$

  where $\mathcal{I}$ is the identity operator. Equation (3.9) admits solution only if a suitable compatibility condition is satisfied. This condition can be expressed through the *adjoint* eigenmode $\hat{\mathbf{q}}_0^\dagger$, defined in Sec. 3 (see also [28]).

  Such adjoint field $\hat{\mathbf{q}}_0^\dagger$ satisfies the left eigenvalue problem. Thus, the product of the left hand side of (3.9) by $\hat{\mathbf{q}}_0^\dagger$ vanishes. Hence, the right hand side also must be orthogonal to $\hat{\mathbf{q}}_\mathbf{0}^\dagger$ (Fredholm alternative), giving $0 = \langle\hat{\mathbf{q}}_0^\dagger, -\delta\mathcal{L}\{\hat{\mathbf{q}}_0\} + \gamma_1\hat{\mathbf{q}}_0\rangle$, which can be rearranged as:

  $$\gamma_1 = \langle\hat{\mathbf{q}}_\mathbf{0}^\dagger, \delta\mathcal{L}\{\hat{\mathbf{q}}_\mathbf{0}\}\rangle. \tag{3.10}$$

This 1^{st} order eigenvalue drift is a linear function of the operator perturbation, contains the direct and adjoint eigenmode, and lead to the standard sensitivity expressions (see section 3.2.1).

- At the 2^{nd} order in ϵ, we obtain from Eq. (3.8):

$$(\mathcal{L} - \gamma_0 \mathcal{I})\{\hat{\mathbf{q}}_2\} = -\delta\mathcal{L}\{\hat{\mathbf{q}}_1\} + \gamma_2 \hat{\mathbf{q}}_0 + \gamma_1 \hat{\mathbf{q}}_1.$$

By the same argument as for the 1^{st} order, both left and right sides are orthogonal to $\hat{\mathbf{q}}_0$, giving $\gamma_2 = \langle \hat{\mathbf{q}}_0^\dagger, (\delta\mathcal{L} - \gamma_1\mathcal{I})\{\hat{\mathbf{q}}_1\}\rangle$.

We observe that an arbitrary component of $\hat{\mathbf{q}}_0$ can always be added to $\hat{\mathbf{q}}_1$ [23], and that Eq. (3.9) would still remain valid. Note that γ_2 remains unaffected by the choice of this component, since $\langle \hat{\mathbf{q}}_0^\dagger, \delta\mathcal{L}\{C\hat{\mathbf{q}}_0\}\rangle - \gamma_1\langle \hat{\mathbf{q}}_0^\dagger, C\hat{\mathbf{q}}_0\rangle = 0$ for any constant C. The choice of C only corresponds to a normalization of the total perturbed eigenvector. A simple choice to guarantee uniqueness and remove the singularity of left-hand side in equation (3.9) is:

$$\langle \hat{\mathbf{q}}_0^\dagger, \hat{\mathbf{q}}_1\rangle = C = 0, \tag{3.11}$$

leading to:

$$\gamma_2 = \langle \hat{\mathbf{q}}_0^\dagger, \delta\mathcal{L}\{\hat{\mathbf{q}}_1\}\rangle. \tag{3.12}$$

Note that *the 2^{nd} order eigenvalue drift has exactly the same expression as the 1^{st} order drift*, but with the eigenmode $\hat{\mathbf{q}}_0$ replaced with the 1^{st} order eigenmode correction $\hat{\mathbf{q}}_1$. This means that all the sensitivity expressions derived in the literature can be used straight away to obtain 2^{nd} order corrections, if $\hat{\mathbf{q}}_0$ is replaced by $\hat{\mathbf{q}}_1$.

3.4 Inviscid Sensitivity analysis

There are several flow configurations in which it is possible to investigate the stability features by using the geometrical optics approximation. Physically, the resulting short-wave instabilities can be explained by local vorticity stretching. Three different types of instabilities exist: *elliptic*, *hyperbolic* and *centrifugal*. These inviscid mechanisms were studied in detail by Sipp et al. [20], Godeferd et al.[36]. They focussed their attention on closed streamlines that play a special role in the dynamics of the instability: on these orbits, local instability waves propagate and feedback on themselves leading to a self-excited unstable mode (see section 2.6 for the WKBJ analysis along the streamlines). In this context, our key idea is to isolate the effect of the inviscid mechanism by increasing only the Reynolds

number in the global stability equations. In this way, we can use the resulting *inviscid structural sensitivity* map to determine the flow regions where the inviscid mechanism acts. The resulting sensitivity tensor is function of both base-flow Reynolds number Re_{BF} and the stability Reynolds number Re_{STB}:

$$\mathbf{S}(Re_{BF}, Re_{STB}) = \frac{\hat{\mathbf{u}}^{\dagger}(\mathbf{u_b}(Re_{BF}); Re_{STB})\ \hat{\mathbf{u}}(\mathbf{u_b}(Re_{BF}); Re_{STB})}{\int_D \hat{\mathbf{u}}^{\dagger} \cdot \hat{\mathbf{u}} dV} \tag{3.13}$$

In **paper 3**, we showed that in the case of open cavity flow the resulting spatial map is very localized around a critical orbit inside the cavity. This orbit is the same identified by the WKBJ analysis and has a revolution period which is strictly related to the leading frequencies arising at higher Reynolds numbers.

3.5 Error Sensitivity to Refinement (ESR): an indicator for optimal grid adaptation

The strategy we are going to describe is inspired by the structural sensitivity analysis introduced in section 3.2.1. A similar procedure, consisting in combining information between the direct and adjoint solutions, can also be used to derive an effective indicator for grid refinement strategies. Grid refinement is a powerful tool that can be used in intensive and memory demanding applications to reduce the computational costs and, at the same time, retain and even improve the accuracy of the numerical problem. Reducing both errors and costs in a numerical simulation is a general and fundamental problem in computational sciences and is strictly related to uncertainty quantifications analysis. Further details about the proposed approach can be found in **paper 9**.

We focus our attention on a differential problem on a domain Ω with given b.c. on $\partial\Omega$. Let's consider an algebraic operator N_h obtained through a discretization of the continuous problem on a mesh with characteristic spacing h. If u_h is a solution of the discrete problem then

$$\mathbf{N}_h(\mathbf{u}_h) = \mathbf{0} \tag{3.14}$$

while the exact solution of the continuous problem u_{ex} satisfies

$$\mathbf{N}_h(\mathbf{u}_{ex}) = \mathbf{r}_h \tag{3.15}$$

where the term r_h is named *residual*. We measure the error between the approximate and exact solution using the E_2 definition of the error:

$$E_2 = \left(\int_\Omega |u_{ex}(\mathbf{x}) - u(\mathbf{x})|^2 dS \right)^{1/2}. \tag{3.16}$$

Replacing the integral by its numerical approximation, we can express the equation (3.16) as:

$$E_2^2 = \sum_i w_i \left(u_{h,i} - u_{ex,i} \right)^2 \tag{3.17}$$

where w_i are suitable weights composing a numerical quadrature formula. We want now to determine the sensitivity of the error E_2 to a small variation in the residual δr_h (its *gradient* v_h), or in other terms the gradient of E_2 with respect to δr_h.

A small variation δu_h in the numerical solution u_h produces a variation in the error of the form:

$$E_2 \delta E_2 = \mathbf{y} \cdot \delta \mathbf{u}_h \tag{3.18}$$

where y is the vector with components $y_i = w_i(u_{h,i} - u_{ex,i})$. By applying the adjoint analysis, we now write E_2 as a linear function of the residual. In order to achieve this, we first note that a small variation in the solution produces a small change in the residual according to

$$\mathbf{A}\, \delta \mathbf{u}_h = \delta \mathbf{r}_h \tag{3.19}$$

where $\mathbf{A} = \frac{\partial \mathbf{N}_h}{\partial \mathbf{u}}$ is the Jacobian of the differential operator in (3.14). By multiplying (3.19) by a vector $\mathbf{v}_h$ and using the definition of the adjoint operator we can write

$$\mathbf{v}_h \cdot \mathbf{A}_h \delta \mathbf{u}_h = \delta \mathbf{u}_h \cdot \mathbf{A}_h^T \mathbf{v}_h = \mathbf{v}_h \cdot \delta \mathbf{r}_h \tag{3.20}$$

If we now choose the adjoint vector $\mathbf{v}_h$ such to satisfy

$$\mathbf{A}_h^{\mathrm{T}}\, \mathbf{v}_h = \mathbf{y}/E_2 \tag{3.21}$$

we can rewrite the variation of the error in terms of a small residual change as

$$E_2 \delta E_2 = \mathbf{y} \cdot \delta \mathbf{u}_h = E_2 \mathbf{v}_h \cdot \mathbf{A}_h \delta \mathbf{u}_h = E_2 \mathbf{v}_h \cdot \delta \mathbf{r}_h. \tag{3.22}$$

Assume now that, asymptotically for small h, $r_h \sim h^p$ for some integer exponent p (the order of the discretization). A variation in h (a grid refinement) by a factor m (say $1/2$) will then induce a variation in the residual proportional (with opposite sign) to the residual itself, i.e.

$$\delta \mathbf{r}_h = \mathbf{r}_{mh} - \mathbf{r}_h \simeq (m^p - 1)\mathbf{r}_h. \tag{3.23}$$

This is, in fact, the rationale behind recovery-based methods: refining where the residual is largest produces the maximum reduction in the residual. We may also notice that, when the residual is related to the truncation error of a differential operator, the relationship between residual and refinement is a *local* one.

Such relation is still not what we really look for: in fact our aim is to know what happens when we refine the grid, which is not the same as changing the residual. To get the complete answer to our problem we need to consider what happens to the residual when we refine the grid.

Recalling now that the spatial map of the residuals indicates where a local refinement will mostly decrease the residual itself. On the other hand, the spatial map of the adjoint provides information on the location where a change in the residual will mostly affect the error. These two quantities can be compared with the direct and adjoint solution of the structural sensitivity analysis for fluid flow problems with self-exciting instabilities discussed above. As for those cases, we can now make a step forward and combine the information provided by the two maps by taking the local product between the residual and the adjoint field. In this way we define the Error Sensitivity to Refinement (ESR)

$$s_i = E_2^{-2} v_{h,i}\, r_{h,i} \tag{3.24}$$

where no implicit summation is assumed. This quantity indicates where a local refinement (by a fixed factor m) will mostly affect the error E_2 and it is therefore a natural indicator to really minimize (3.16). In general, both error and residual require a knowledge of the exact solution. Just as for all the other mesh-adaptation indicators, the latter can be estimated and replaced by a solution on a finer mesh. In particular, if both the error and the residual asymptotically decrease like h^p, we obtain the following relation

$$\mathbf{u}_{2h} - \mathbf{u}_h \simeq (1 - 2^{-p})(\mathbf{u}_{2h} - \mathbf{u}_{ex}) \simeq (2^p - 1)(\mathbf{u}_h - \mathbf{u}_{ex}) \tag{3.25}$$

between the error on grid h and the error of the solution with respect to a finer grid. Furthermore, considering that u_{2h} is the discrete solution on the course mesh, it is also possible to write

$$\mathbf{N}_{2h}(\mathbf{u}_h) - \underbrace{\mathbf{N}_{2h}(\mathbf{u}_{2h})}_{=0} \simeq$$

$$(1 - 2^{-p})(\mathbf{N}_{2h}(\mathbf{u}_{ex}) - \underbrace{\mathbf{N}_{2h}(\mathbf{u}_{2h})}_{=0}) \simeq (2^p - 1)\mathbf{N}_h(\mathbf{u}_e x) \tag{3.26}$$

which gives an estimate of the residual using the solution on a finer mesh. As a final remark we note that the error sensitivity $s_i = E_2^{-2} v_{h,i}\, r_{h,i}$ tends

to a grid-independent limit for $h \to 0$ so that sensitivity maps obtained on different grids will be similar provided the mesh spacing h is sufficiently small.

Chapter 4

Stabilization of the solution of the Navier-Stokes equations

The solution of the Navier-Stokes equations can change from stable to unstable with a variation of a control parameter. A classical example of such process is the instability occurring in the wake of a circular cylinder: at low Reynolds number, i.e. for $Re < 46.7$, the flow is steady and symmetric, but for larger values of Re a global instability arises in the flow field leading to the well-known von Kármán vortex street [35]. In order to perform stability computations beyond the critical threshold we need a numerical method able to track the base flow across and beyond the critical point. Unfortunately, we cannot use a standard time integration of the governing equations just because it is unstable.
The discretization of the governing equations, especially for fluid dynamic applications, often leads to very large discrete systems. As a consequence, matrix based methods, like for example the Newton-Raphson algorithm coupled with a direct inversion of the Jacobian matrix, lead to computational costs too large in terms of both memory and execution time.

In the case of high-dimensional systems, few computations have been performed in the literature. The most popular method to stabilize an unstable procedure was proposed by Shroff & Keller[37]. Their Recursive Projection Method (RPM) stabilizes an unstable algorithm by using the Newton method only on a small subspace. Another popular stabilization algorithm was presented by Akervik et al.[38]. The details of both methods will be provided in section 4.2 and 4.3 respectively. However, these methods

present some drawbacks.

A new stabilization algorithm is proposed in **paper 8**. This method, named `BoostConv`, can stabilize a pre-existing numerical procedure used to integrate any dynamical system without negatively impacting on its computation time. Moreover, it can be easily inserted in the pre-existing relaxation (integration) procedure with a call to a single black-box subroutine.

4.1 Iterative solution of a linear system

The study of a dynamical system described by a set of partial differential equations (PDEs) usually involves the solution of a linear system:

$$\mathbf{A}\mathbf{x} = \mathbf{b}, \tag{4.1}$$

where $\mathbf{A}$ is a $\mathbb{R}^{N\times N}$ matrix and $\mathbf{x}$, $\mathbf{b}$ are $\mathbb{R}^N$ vectors representing respectively the solution and the known term of the system. A generic linear iteration for the solution of the linear system (4.1) can be expressed as:

$$\mathbf{x}_{n+1} = (\mathbf{I} - \mathbf{B}\mathbf{A})\mathbf{x}_n + \mathbf{B}\mathbf{b} = \mathbf{x}_n + \mathbf{B}\mathbf{r}_n. \tag{4.2}$$

In the previous expression $\mathbf{r}_n = \mathbf{b} - \mathbf{A}\mathbf{x}_n$ is the residual and $\mathbf{B}$ is a matrix representing the particular iterative scheme used to solve the problem (see e.g. Ch.4 [39]). The convergence of procedure (4.2) is governed by the eigenvalues of the iteration matrix $\mathbf{M} = \mathbf{I} - \mathbf{B}\mathbf{A}$: the algorithm converges if and only if the spectral radius of the iteration matrix is less than 1. The asymptotic convergence rate is essentially governed by the slowly decaying modes.

4.2 The Recursive Projection Method (RPM)

The recursive projection method was initially developed for extending the domain of convergence of iterative procedures in the context of stability and bifurcation analysis. As discussed above, the convergence of a generic iterative procedure (4.2) is related to the eigenvalues of $\mathbf{M}$. In order to illustrate the RPM method, we suppose that the iteration (4.2) diverges because of s unstable eigenvalues. Shroff & Keller introduced a small subspace $\mathcal{P} \in \mathbb{R}^s$ spanned by the eigenvectors associated with the unstable eigenvalues (i.e. the eigenvalues that have a modulus larger than 1) and $\mathcal{Q}$ that is the orthogonal complement of the former subspace. Thus, the sum between these two spaces provides the whole $\mathbb{R}^N$: $\mathbf{x}^{TOT} = \mathbf{x}_p + \mathbf{x}_q$. The projectors

$\tilde{P}$ and $\tilde{Q}$ associated to $\mathcal{P}$ and $\mathcal{Q}$ can be defined by an orthonormal basis $\tilde{V}$ for $\mathcal{P}$ as:

$$\tilde{P} = \tilde{V}\tilde{V}^T, \quad \tilde{Q} = I - \tilde{V}\tilde{V}^T, \tag{4.3}$$

where superscript T represents the transpose operator.

The resulting RMP procedure can be written as follows:

$$\mathbf{x}_q^{n+1} = \tilde{Q}\left[\mathbf{M}\mathbf{x}_n + \mathbf{B}\mathbf{b}\right]; \tag{4.4}$$

$$\mathbf{x}_p^{n+1} = \mathbf{x}_p^n + (\mathbf{I} - \tilde{P}\mathbf{M}\tilde{P})^{-1}\{\tilde{P}\left[\mathbf{M}\mathbf{x}_n + \mathbf{B}\mathbf{b}\right] - \mathbf{x}_p^n\}; \tag{4.5}$$

$$\mathbf{x}^{n+1} = \mathbf{x}_p^{n+1} + \mathbf{x}_q^{n+1}. \tag{4.6}$$

Thus, at each step, only the projection of equation (4.2) onto the subspace $\mathcal{Q}$ is solved with the original iteration. The iteration on the low-dimensional subspace $\mathcal{P}$ is solved with Newton's method. Shroff & Keller [37] discussed the effectiveness of the algorithm proving the effective convergence even in case of unstable procedures. However, the RPM can be inefficient in the case of large linear systems due to the existence of modes with large negative real parts. In such cases, the resulting asymptotic convergence rate of the RPM algorithm is reduced.

4.3 SFD

Akervik et al.[38] presented the Selective Frequency Damping method. They showed that an existing time integration procedure for the solution of N-S problem, can be coupled with the SFD algorithm to reach a steady state by damping the unstable temporal frequencies. This is achieved by adding a dissipative relaxation term proportional to the high-frequency content of the velocity fluctuations. Here, we briefly describe the method; we refer to the original paper [38] for further details.

Let us consider a generic non-linear dynamical system, e.g. the Navier-Stokes system, that reads:

$$\frac{\partial}{\partial t}\mathbf{q} = \mathscr{L}\{\mathbf{q}\}, \tag{4.7}$$

where $\mathbf{q}$ is the state of the system and $\mathscr{L}$ is the differential operator. The key idea of the SFD algorithm is to add to the right-hand side a linear term forcing towards a target solution $\tilde{\mathbf{q}}$: $-\chi(\mathbf{q} - \tilde{\mathbf{q}})$. Here, the coefficient χ represents the amplitude of the control. Since the target solution is not available, they decided to approximate $\tilde{\mathbf{q}}$ as a modification of the current state $\mathbf{q}$ but with reduced temporal fluctuations. Thus, to obtain this aim,

the target solution is obtained as $\tilde{\mathbf{q}} = \mathbf{T} * \mathbf{q}$, where $\mathbf{T}$ is the temporal filter kernel; i.e. they adopted a temporal low-pass filter on $\mathbf{q}$. The resulting modified dynamical system reads:

$$\frac{\partial}{\partial t}\mathbf{q} = \mathscr{L}\{\mathbf{q}\} - \chi(\mathbf{I} - \mathbf{T}) * \mathbf{q}, \tag{4.8}$$

where $\mathbf{I}$ is the identity operator. Note that if $\mathbf{q} = \mathbf{q}_s$, the forcing term vanishes. The computed steady state of (4.8) is also a solution of the original problem. However, the SFD algorithm needs an *estimate* of the global mode frequency and it cannot be applied to compute unstable states in presence of stationary bifurcations.

4.4 BoostConv

The aim of the present section is to present a new algorithm, inspired by Krylov-subspace methods, able to compute efficiently such unstable states of a high-dimensional dynamical system. This method is based on the minimization of the norm of the residual at each integration step and can be applied as a black-box procedure in any iterative or time marching algorithm without negatively impacting the computational time of the original code.

The main idea which inspired the proposed algorithm is similar to the one at the basis of GMRES[39], but in a reverse logic sequence. We start from an existing iterative algorithm that is modified to Boost the Convergence of the overall procedure.

To obtain this stabilization, we focus our attention on the evolution of the residual. We can simply obtain the homogeneous equation for the propagation of the residual by applying $\mathbf{A}$ to (4.2) and successively adding $\mathbf{b}$:

$$\mathbf{b} - \mathbf{A}\mathbf{x}_{n+1} = \mathbf{b} - \mathbf{A}\left[\mathbf{x}_n + \mathbf{B}(\mathbf{b} - \mathbf{A}\mathbf{x}_n)\right], \text{i.e.}$$

$$\mathbf{r}_{n+1} = \mathbf{r}_n - \mathbf{A}\mathbf{B}\mathbf{r}_n. \tag{4.9}$$

Now, in order to improve the existing procedure (4.2), we replace the residual vector $\mathbf{r}_n$ with a modified residual $\boldsymbol{\xi}_n$ such that the improved algorithm reads

$$\mathbf{x}_{n+1} = \mathbf{x}_n + \mathbf{B}\boldsymbol{\xi}_n(\mathbf{r}_n). \tag{4.10}$$

In the previous equation $\boldsymbol{\xi}_n$ is a suitable function of $\mathbf{r}_n$ and can be interpreted as the feedback term of a closed loop control algorithm or a structural

perturbation to the original iteration matrix. We note that to guarantee the consistence of the modified algorithm, it is sufficient that $\boldsymbol{\xi}_n$ goes to zero when $\mathbf{r}_n$ does. The introduction of the vector $\boldsymbol{\xi}_n$ modifies equation (4.9) leading to the new residual equation

$$\mathbf{r}_{n+1} = \mathbf{r}_n - \mathbf{AB}\boldsymbol{\xi}_n, \tag{4.11}$$

or equivalently

$$\mathbf{r}_n - \mathbf{r}_{n+1} = \mathbf{AB}\boldsymbol{\xi}_n. \tag{4.12}$$

We now minimize $\mathbf{r}_{n+1}$ by choosing a suitable function $\boldsymbol{\xi}_n = \boldsymbol{\xi}_n(\boldsymbol{r}_n)$. If we knew $(\mathbf{AB})^{-1}$, we could exactly annihilate $\mathbf{r}_{n+1}$ by computing $\boldsymbol{\xi}_n(\mathbf{r}_n)$ as

$$\boldsymbol{\xi}_n = (\mathbf{AB})^{-1}\mathbf{r}_n. \tag{4.13}$$

However, for large systems, the exact inversion of $\mathbf{AB}$ is out of reach or too expensive to be performed. Therefore, we approximate the solution of (4.13) by using a classical least-square method.

The action of the operator $\mathbf{AB}$ can be represented by storing a set of N vector pairs $(\mathbf{u}_i, \mathbf{v}_i)$, where the second member is produced by the action of $\mathbf{AB}$ on the first. Least-squares method is then adopted to approximate the solution of the algebraic linear system $\mathbf{AB}\boldsymbol{\xi}_n = \mathbf{r}_n$ as

$$\boldsymbol{\xi}_n = \sum_{i=1}^{N} c_i \mathbf{u}_i. \tag{4.14}$$

In our case the vectors $\mathbf{u}_i$ and $\mathbf{v_i}$ are related by

$$\mathbf{v_i} = \mathbf{ABu_i} \quad \text{for } i = 1, .., N. \tag{4.15}$$

while the coefficients c_i are chosen to minimize $|\mathbf{r}_n - \mathbf{AB}\boldsymbol{\xi}_n|^2$. The standard least-squares procedure leads to a system of equations for the coefficients c_i of the form

$$D_{kl}\, c_l = t_k \tag{4.16}$$

where $t_k = \mathbf{v}_k \cdot \mathbf{r}_n$ and $D_{kl} = \mathbf{v}_k \cdot \mathbf{v}_l$ is a small $N \times N$ matrix. Matrix $\mathbf{D}$ is usually ill-conditioned and an orthogonalization procedure (QR decomposition) is usually needed to find the solution. However, when N is small, as for the cases we are considering, the solution can be simply found with a classical LU decomposition. This least-square solution is not exact and produces a residual $\boldsymbol{\rho} = \mathbf{r_n} - \mathbf{AB}\xi_\mathbf{n}$ which can be expressed in terms of $\mathbf{v_i}$ as

$$\boldsymbol{\rho} = \mathbf{r_n} - \mathbf{AB}\xi_\mathbf{n} = \mathbf{r_n} - \mathbf{AB}\left(\sum_{i=1}^{N} c_i \mathbf{u_i}\right) = \mathbf{r_n} - \sum_{i=1}^{N} c_i \mathbf{ABu_i} = \mathbf{r_n} - \sum_{i=1}^{N} c_i \mathbf{v_i}. \tag{4.17}$$

However, inserting the so calculated $\boldsymbol{\xi}_n$ in (4.10) is not yet sufficient to produce a converging algorithm because $\boldsymbol{\xi}_n$ could converge to zero even when the residual $\mathbf{r}_n$ is not identically zero, but simply orthogonal to the leading N (basis-)vectors $\mathbf{u}_i$. Remembering that the original iterative algorithm (4.2) simply had $\boldsymbol{\xi}_n = \mathbf{r}_n$, we restore a convergent procedure by adding the residual $\boldsymbol{\rho} = \mathbf{r}_n - \sum_i c_i \mathbf{v}_i$ to $\boldsymbol{\xi}_n$, so that the complete algorithm now reads

$$\boldsymbol{\xi}_n = \sum_i c_i \mathbf{u}_i + \mathbf{r}_n - \sum_i c_i \mathbf{v}_i \tag{4.18}$$

The rationale behind this procedure is to invert exactly the part of the problem represented by the dominant, slower decaying modes, while letting the original iterative algorithm to handle the remaining modes. We now go back to the issue of selecting a convenient set of vectors $\mathbf{u_i}$. In the case of `BoostConv`, both $\mathbf{u}_i$ and $\mathbf{v}_i$ can be conveniently calculated by observing that, according to (4.11), for each n we have

$$\mathbf{r}_n - \mathbf{r}_{n+1} = \mathbf{AB}\boldsymbol{\xi}_n. \tag{4.19}$$

For a given N, in a cyclic fashion, at the beginning of a new iteration, we add a new vector pair by selecting $\mathbf{u}_N = \boldsymbol{\xi}_{n-1}$ and $\mathbf{v}_N = \mathbf{r}_n - \mathbf{r}_{n-1}$. In order to keep the size of the basis constant, another pair must be discarded which typically will be the oldest. Such choice is dictated by the fact that applying the algorithm to a nonlinear system it is beneficial to use the freshest information on the system dynamics in order to account for the change of the system Jacobian (in our case represented by the linear operator $\mathbf{A}$). We also note that in matrix D_{kl} of (4.16) only the row and the column involving a new pair need to be updated. Such selection procedure works when we already have N vector pairs. At the beginning of the algorithm (for $n < N$) we can still use the same procedure but continuously increasing the basis dimension from 1 to the chosen value of N. In this first stage, no vector pairs are discharged.

From a programming viewpoint, the `BoostConv` algorithm can be encapsulated in a black-box procedure, where the only input is $\mathbf{r}_n$ and the only output is $\boldsymbol{\xi}_n$. If $\boldsymbol{\xi}_n$ is returned in the same vector where $\mathbf{r}_n$ was provided, the only modification necessary to boost the convergence of the pre-

existing iterative algorithm (4.2) is a single line of code containing the call to `BoostConv`.

In **paper 8**, we report numerical results obtained with this new procedure. We started from the classical case of the two-dimensional lid-driven cavity flow where we show that `BoostConv` is able to accelerate the convergence of the existing time integration procedure. Then, we consider the case of the two-dimensional flow past an infinitely long circular cylinder. For this case, we show, with several different codes, that `BoostConv` is able to drive the iterative procedure to the exact base flow (computed using a Newton method). A three-dimensional case is also considered to examine the application of `BoostConv` to a high-dimensional problem. In particular, we discuss the results obtained from the application of `BoostConv` to the case of boundary layer flow past a hemisphere reported in **paper 5**. In this case we checked also that the whole algorithm (time integration by using Nek5000+ `BoostConv`) has a computational burden very similar to the original iteration.

Chapter 5

Numerical methods

In the present thesis, three different codes have been used to perform the stability analyses presented in the papers (pert II). In the following, we briefly describe each approach, further details about $Freefem++$ can be found in [40]; for $Nek5000$ we refer to [44] while the multigrid code is described in **paper 7**.

5.1 $Freefem++$

$Freefem++$ is a free software based on the Finite Element Method; it has its own high level programming language. It has been adopted to investigate many phenomena involving different systems of PDE like *e.g.* fluid-structure interactions, Lorentz forces for aluminum casting and ocean-atmosphere coupling. We used this software to solve both the base flow problem and the stability eigenvalue problems.

5.1.1 Base flow

The variational formulation of the Navier-Stokes equations is derived. We used the classical $P2 - P1$ Taylor-Hood elements for the spatial discretization. The resultant nonlinear system of algebraic equations, along with the boundary conditions, is solved by a Newton-Raphson procedure: given an initial guess $\mathbf{w_b}^{(0)}$, the linear system

$$\mathbf{NS}(Re, \mathbf{W_b}^{(n)}) \cdot \mathbf{w_b}^{(n)} = -\mathbf{rhs}^{(\mathbf{n})} \tag{5.1}$$

is solved at each iteration step using the MUMPS-Multifrontal Massively Parallel sparse direct Solver [41] for the matrix inversion. The base flow is

Mesh	σ	ω	$n_{d.o.f.}$	n_t	Source
$\mathcal{M}\mathbf{1}$	0.0007590	7.4931	998668	221045	Present
$\mathcal{M}\mathbf{2}$	0.0008344	7.4937	1416630	313791	Present
$\mathcal{M}\mathbf{3}$	0.0009122	7.4943	2601757	576887	Present
$\mathcal{D}\mathbf{1}$	0.0007401	7.4930	880495	194771	[45]
$\mathcal{D}\mathbf{2}$	0.0008961	7.4942	1888003	418330	[45]

Table 5.1: Comparison of the results obtained with the present $FreeFem++$ code and those reported by [45] for the flow over an open cavity. The eigenfrequency ω and the growth rate σ have been calculated for the first two-dimensional unstable eigenmode at $Re = 4140$. $n_{d.o.f.}$ and n_t indicate the total number of degrees of freedom of the linearized problem and the number of triangles for each of the unstructured meshes used.

then updated as

$$\mathbf{W_b}^{(n+1)} = \mathbf{W_b}^{(n)} + \mathbf{w_b}^{(n)}. \tag{5.2}$$

The initial guess is usually chosen to be the solution of the Stokes equations and the process is continued until the L^2-norm of the residual of the governing equations becomes smaller than a given tolerance. The tests about the convergence of the resulting code has been performed for the case of the open cavity. We used three different meshes $\mathcal{M}\mathbf{1}$, $\mathcal{M}\mathbf{2}$ and $\mathcal{M}\mathbf{3}$ (see Table 5.1). These are generated by the Bidimensional Anisotropic Mesh Generator (Bamg) that is part of the Freefem++ package. The base flow computations are also validated using a variant of the second-order finite-difference code described in [35].

5.1.2 Direct and Adjoint eigenvalue solver

Once the base flow is determined, the system of equations (2.16) is used to perform the stability analysis. After spatial discretization, the governing equations and their boundary conditions are recast in the following standard form

$$[\mathbf{A}(Re, \mathbf{W_b}(Re)) + \gamma \mathbf{B}] \cdot \mathbf{w} = \mathbf{0}, \tag{5.3}$$

where $\mathbf{w}$ is the right (or direct) eigenvector. As methods based on the QR decomposition are not feasible for solving large scale problems as those associated to the matrix $\mathbf{A}$ obtained for our problem, we adopt an efficient matrix-free iterative method based on the Arnoldi algorithm [42] . We use the state-of-the-art ARPACK package [43], with implicit restarts to limit

memory requirements. The solution of the linear system built by the Arnoldi iterations on the Krylov subspace is obtained with the same sparse solver [41] used for the base flow calculations. The adjoint modes are computed as left eigenvectors of the discrete system derived from the discretization of the linearized equations and the sensitivity function is then computed by the product of the direct and the adjoint fields.

The code is validated against the results reported by [45]. These authors investigate the stability of a newtonian fluid in the same geometrical configuration of **paper 3** and report the first instability of a two-dimensional eigenmode to occur at Re=4140. In Table 5.1 we present the comparison between our results and the results in [45] for different meshes. In these tests, 50 eigenvalues were obtained, with an initial Krylov basis of dimension 150; the convergence criterion for the Arnoldi iterations is based on a tolerance of 10^{-9}. To independently check the accuracy of the results we *a posteriori* computed the residual $max_i|(A_{ij}+\gamma B_{ij})w_j|$: this turns out to be always below 10^{-9} for the results reported in this paper, typically less than 10^{-12} for the least stable modes.

5.2 $Nek5000$

$Nek5000$ is a computer software used to simulate fluid flow and heat transfer for steady and unsteady two-dimensional and three-dimensional geometries. The code includes: *i*) $PRENEK$ as a pre-processor; *ii*) $NEKTON$ as solver and *iii*) $POSTNEK$ as a post processor. $PRENEK$ is a preprocessor in which is possible to specify the mesh and the boundary and initial conditions. $NEKTON$ is a parallel spectral element solver that computes the velocity and pressure fields. These results can then be analyzed in the post processor $POSTNEK$. The code is written in f77 and the parallelization is achieved by using the MPI interfaces.

$Nek5000$ is based upon the spectral element method [46] which combines the high-order accuracy of spectral methods with the geometric flexibility of traditional finite-element methods.

The computational domain is divided into non-overlapping quadrangles; the unknown is approximated by high-order polynomial expansions. In particular, the unknown vector (u, v, w, P) is spatially discretized onto $P_N - P_{N-2}$ spectral elements using Lagrange orthogonal polynomials in the Gauss-Lobatto-Legendre (GLL) nodes. For the temporal discretization of momentum equation, a semi-implicit splitting scheme has been used because it allows high-order temporal accuracy. The time advancement is divided in 3 independent subproblems: convective, viscous, and pressure problem.

These last two elliptic subproblems are solved efficiently by using the overlapping Schwarz method. This code has been used to perform the stability analysis in **papers 1,2,5,7,11**.

As discussed previously, we recall that some complex flows cannot be assumed as quasi- parallel. Thus, in such cases, we need to adopt a full three-dimensional analysis to investigate the stability of fluid flow.

We cannot adopt a matrix-based method to solve the resulting eigenproblem. The inherent matrix $\mathscr{A}$, indeed, cannot even be stored in computer memory; for the case of **paper 5**, for example, it would require several Pbytes of storage for the considered mesh resolution. Hence, the only possible choice is to use a time-stepper method.

The time-stepper technique is usually based on the orthogonal projection of the large matrix $\mathscr{A}$ onto a lower-dimensional subspace. This operation will result in a significantly smaller system that can be solved by using direct methods. The Krylov subspace is usually chosen to build the basis; it is spanned by snapshots taken from flow fields $\boldsymbol{q}'$ separated by a constant Δt. The time advancement of the perturbation field is achieved by using the linearized time-stepper available in $Nek5000$. The construction of the Krylov basis and the inherent eigenvalue computations are obtained using a variant of the famous Arnoldi method [42]. In particular, we used ARPACK in which is implemented the Implicitely Restarted Arnoldi Method (IRAM), introduced by Lehoucq & Sorensen [15]. Further details about such approaches can be found in the textbook of Antoulas [16].

5.3 Finite-Difference Multigrid

The finite-difference immersed boundary multigrid code is based on a classical second-order conservative discretization of the Navier-Stokes equations on a staggered non-uniform Cartesian mesh. In particular, we used this code to investigate the zero-torque solution of the flow past a rotating sphere discussed in **paper 7**. In order to achieve high accuracy and save computation time, a grid clustering near the sphere has been adopted. The boundary conditions on the sphere are imposed through a second-order accurate immersed-boundary scheme, in which the stencil of the finite-difference operators near the body are modified using appropriate interpolation-extrapolation procedure. The interpolation was performed using the point closest to the body surface (which can be either an internal or an external point) and the nearest point on the exterior of the cylinder. The interpolation is performed either in the streamwise or transverse direction according to which one is closest to the local normal. The discretized

three-dimensional problem is then solved by using an in-house linear multigrid solver coupled to a Newton global linearization [47]. In order to obtain good convergence in the presence of highly stretched grids, a Collective Line Gauss-Seidel (CLGS) smoother was used. Such relaxation procedure considers a row (column) of computational cells as a main block of a Gauss-Seidel-type iteration, which leads to a banded six-diagonal system of linear equations to be solved at each sub-iteration of the multigrid algorithm. This procedure is the line version of the more classical block Vanka smoother ([48]) and has been used with a classical V cycle [47]. In our version, the matrix entries are calculated by a local linearization of the governing equations. More details on the characteristics of this kind of smoothers can be found in Feldman & Gelfgat [49]. The discretization of the convective terms can be problematic since the classical second-order centered discretization is not h-elliptic and can lead to a severe degradation and failure of the iterative procedure. In our code, the convective terms are discretized with a standard first-order upwind discretization while the second order precision is recovered through a standard deferred-correction procedure based on classical centered discretization implemented at the smoother level. The Immersed-boundary technique with a second order interpolation is applied only on the finest level while, for simplicity, at coarser levels, a stair- step geometry is considered. Such procedure does not alter the overall convergence speed of the multigrid algorithm and considerably simplifies the coding and the computation time. Textbook multigrid efficiency [47] is achieved far from the bifurcation thresholds. As true for other iterative procedures, a severe performance degradation occurs when the neutral point is approached. This is due to one or more eigenvalues of the iteration matrix that move across the imaginary line: in this situation the whole iterative procedure diverges. In order to avoid this problem, we used `BoostConv` (see Sec. 4.4) to accelerate the convergence of our multigrid. The code was tested for the case of the flow past a fixed sphere. It provided the critical Reynolds number for the first bifurcation equal to $Re_{cr} = 212$. The value agrees very well with those reported in literature [50].

Chapter 6

Conclusions

The stability and transition of open shear flows, such as the flow over an open cavity, the flow past a sphere or a hemispherical roughness element, was investigated by modal analysis, asymptotic techniques, adjoint-based tools and weakly nonlinear (WNL) expansions. In the open-cavity case, we identified the critical conditions and studied the instability mechanism by means of a WKBJ approximation along the closed streamlines inside the cavity. We showed that the *inviscid structural sensitivity* can accurately predict the particle orbit that provides the main contribution to the instability. The stability of the flow past a rotating sphere was also considered. In particular, for such a configuration, we investigated both the case of imposed rotation and the freely moving sphere. A full three-dimensional stability analysis was performed and a WNL approach was adopted to clarify the system dynamics for small values of the angular velocity. We showed that the asymmetric state, prior to the vortex shedding, verifies the normal form of an imperfect pitchfork bifurcation whose threshold is the critical Re beyond which the non-rotating sphere flow loses its axisymmetry. We also studied the full three-dimensional instability mechanism past a hemispherical roughness element immersed in a laminar Blasius boundary layer. The roughness-induced transition was found to be linked to a global instability in case of large protrusion height. The effect of the variation of the ratio between the obstacle height and the boundary layer thickness was also considered. A limit regime was obtained in which the only important parameter identifying the bifurcation was the unperturbed (i.e., without the roughness element) velocity slope at the wall.

The bifurcations of the flow in an X mixer was investigated via linear stability analysis and direct numerical simulations. This study revealed the instability mechanisms in a symmetric channel junction and showed how

these can be stabilized or destabilized by boundary modification. We observed two bifurcations as the Reynolds number increases; both bifurcations appeared when the recirculation zones reach a critical length.

Further, we generalized the structural sensitivity analysis by including second-order terms. We applied the proposed approach to a confined wake and showed how it is possible to take into account the spanwise wavy baseflow modifications to control the instability.

A general procedure was also developed to study the stability of unsteady boundary layers using complex-ray theory. The propagation of small disturbances was described by a high-frequency (optical) approximation similar to the one adopted for wave propagation in nonuniform media. The ray trajectories were described by a system of first-order differential equations.

Finally, we developed two new numerical tools related to the study of hydrodynamic instabilities: `BoostConv` and the Error Sensitivity to Refinement (ESR). The `BoostConv` procedure is a novel iterative algorithm, inspired by Krylov-subspace methods, which is able to compute unstable steady states and/or accelerate the convergence to stable configurations. Such new algorithm is based on the minimization of the residual norm at each iteration step with a projection basis updated at each iteration rather than at periodic restarts like in the classical GMRES method. The algorithm can stabilize any dynamical system without negatively impacting on the computation time of the numerical procedure originally used to solve the governing equations. The ESR is a new indicator, related to the sensitivity map of global stability problems, suitable for an optimal grid refinement that minimizes the global solution error. The new criterion was derived from the properties of the adjoint operator and provided a map of the sensitivity of the global error (or its estimate) to a local mesh refinement.

Bibliography

[1] Landau, L. D., Lifshitz, E. M., *Fluid Mechanics*, Course of Theoretical Physics **6** (1959)

[2] Lyapunov, A. M., *The General Problem of the Stability of Motion* (In Russian), Doctoral dissertation, Univ. Kharkov (1892)

[3] Poincaré, H., *Les Methodes Nouvelles de la Mecanique Celeste*, **1**, Gauthier Villars, Paris (1892)

[4] Helmholtz, H., *Úber discontinuirliche Flússigkeitsbewegungen*, Monats. Königl. Preuss. Akad. Wiss. Berlin **23**, 215–228 (1868)

[5] Kelvin, L., *Hydrokinetic solutions and observations*, Phil. Mag. **42**, 362–377; Mathematical and Physical Papers **4**, 69–85 (1871)

[6] Rayleigh, L., *On the instability of jets*, Proc. London. Math. Soc. **10**, 4–13 (1879)

[7] Reynolds, O., *An experimental investigation of the circumstances which determine whether the motion of water shall be directed or sinuous and of the law of resistance in parallel channels*, Phil. Trans. Roy. Soc. London, **174** 935–982 (1883)

[8] Orr, W. M., *The stability of instability of the steady motions of a perfect liquid and of a viscous liquid*, Proc. Roy. Irish Acad. A, **27**, 9–68, 69–138 (1907)

[9] Sommerfeld, A., *Ein Beitrag zur hydrodynamischen Erklrung der turbulenten Flssigkeitenewegungen*, Atti del 4 Congresso Internazionale dei Matematici, Ser. **I 3**, 116-124 (1908)

[10] Schmid, P. J., Henningson, D. S., *Stability and transition in shear flows*, Springer Science & Business Media, (2012)

[11] Charru, F., *Hydrodynamic Instabilities*, Vol. **37**, Cambridge University Press, (2011)

[12] Theofilis, V., *Global linear instability*, Annu. Rev. Fluid Mech. **43** 319–352, (2011)

[13] Huerre, P., Monkewitz, P. A., *Local and global instabilities in spatially developing flows*, Annu. Rev. Fluid Mech. **22** 473–537, (1990)

[14] Drazin, P., Reid, W., *Hydrodynamic Stability*, Cambridge University Press, (1981)

[15] Lehoucq, R.B., Sorensen D.C., Yang C., *ARPACK users' guide: solution of large-scale eigenvalue problems with implicitly restarted Arnoldi methods*, SIAM, Philadelphia (1998)

[16] Antoulas, A. C., *Approximation of large-scale dynamical systems*. Society for Industrial and Applied Mathematics (SIAM), 2005.

[17] Bayly, B. *Three-dimensional centrifugal-type instabilities in inviscid two-dimensional flows*, Phys. Fluids, **31**, 56-64.

[18] Lifschitz, A., Hameiri, E., *Local stability conditions in fluid dynamics*, Phys. Fluids A, **3**, 2644–2651 (1991)

[19] Lifschitz, A., *On the instability of certain motions of an ideal incompressible fluid*, Adv. Appl. Maths, **15**, 404–436 (1994)

[20] Sipp, D., Lauga, E., Jacquin, L., *Vortices in rotating systems: Centrifugal, elliptic and hyperbolic type instabilities* Phys. Fluids, **11**, 3716 (1999)

[21] Gallaire, F., Marquillie, M., Ehrenstein, U., *Three-dimensional transverse instabilities in detached boundary layers* J. Fluid Mech., **571** 221–233 (2007).

[22] Landman, M. J., Saffman, P., *The three-dimensional instability of strained vortices in a viscous fluid*. Phys. Fluids **30**, 2339–2342 (1987)

[23] Hinch, E. J., *Perturbation Methods*, Cambridge University Press (1991)

[24] Gaster M., *On the effects of boundary-layer growth on flow stability*, J. Fluid Mech., **66** 465–480 (1974)

[25] Whitham, G. B., *Linear and Nonlinear Waves*, Wiley, (1974)

[26] Bender, C. M., Orszag, S. A. *Advanced mathematical methods for scientists and engineers* Springer Science & Business Media, (1999)

[27] Goldstein, H.,*Classical Mechanics*, Addison-Wesley P.C., (1957)

[28] Luchini, P., Bottaro, A., *Adjoint equations in stability analysis* Annu. Rev. Fluid Mech. **46**, 493–517 (2014)

[29] Magri, L., Juniper, M. P., *Sensitivity of a time-delayed thermo-acoustic system via an adjoint-based approach*, J. Fluid Mech. **719**, 183–202 (2013)

[30] Ince, E. L. *Ordinary Differential Equations*, Dover (1926)

[31] Chomaz, J. M., *Global instabilities in spatially developping flows: non-normality and nonlinearity*, Annu. Rev. Fluid Mech. **37**, 357–392 (2005)

[32] Strykowski, P. J., Sreenivasan, K. R., *On the formation and suppression of vortex 'shedding' at low Reynolds number*, J. Fluid Mech. **218**, 71–107 (1990)

[33] Bottaro, A., & Corbett, P., Luchini, P., *The effect of base flow variation on flow stability*, J. Fluid Mech. **476**, 293–302 (2003)

[34] Marquet, O., Sipp, D., Jacquin, L., *Sensitivity analysis and passive control of cylinder flow* J. Fluid Mech. **615**, 221–252 (2008)

[35] Giannetti, F. & Luchini, P. *Structural sensitivity of the first instability of the cylinder wake*, J. of Fluid Mech. **581**, 167–197 (2007)

[36] Godeferd, F. S., Cambon, C., Leblanc, S., *Zonal approach to centrifugal, elliptic and hyperbolic instabilities in Stuart vortices with external rotation*, J. Fluid Mech. **449**, 1-37 (2001)

[37] Shroff, G. M. & Keller, H. B. *Stabilization of unstable procedures: the recursive projection method*, SIAM J. Numer. anal., **30**, 1099–1120 (1993)

[38] Akervik, E., Brandt, L., Henningson, D. S., Hoepffner, J., Marxen, O., Schlatter, P. *Steady solutions of the Navier-Stokes equations by selective frequency damping*, Phys. of Fluids, **18**, 068102 (2006)

[39] Saad, Y. *Iterative Methods for Sparse Linear Systems (2nd edn)*, SIAM, 2003

[40] Hecht, F. *New development in FreeFem++*, J. Numer. Math., **20**, 251–265 (2012)

[41] Amestoy, P. R., Duff, I. S., Koster, J., L'Excellent, J.-Y. *A fully asynchronous multifrontal solver using distributed dynamic scheduling.* SIAM. J. Matrix Anal. & Appl., **23**, 15–41 (2001)

[42] Arnoldi, W. E. *The principle of minimized iteration in the solution of the matrix eigenproblem.* Quart. Appl. Math., **9**, 17–29 (1951)

[43] Lehoucq, R., Maschhoff, K., Sorensen, D., Yang, C. *Arpack software. website: http://www.caam.rice.edu/software/arpack/* (2007)

[44] Fischer, P. F., *An overlapping schwarz method for spectral element solution of the incompressible Navier-Stokes equations*, J. Comput. Phys., **133**, 84–101 (1997)

[45] Sipp, D., Lebedev, A. *Global stability of base and mean flows: a general approach and its applications to cylinder and open cavity flows.* J. Fluid Mech. **593**, 333–358 (2007)

[46] Patera, A. T. *A spectral element method for fluid dynamics - Laminar flow in a channel expansion.* J. of Comp. Phys. **54**, 468–488, (1984)

[47] Trottenberg, U., Oosterlee, C. W., Schüller, A., *Multigrid*, Academic Press (2001)

[48] Vanka, S. P., *Block-implicit multigrid solution of navier-stokes equations in primitive variables* J. Comput. Phys. **65**, 138–158 (1986)

[49] Feldman, Y., Gelfgat, A. Y., *On pressure-velocity coupled time-integration of incompressible Navier-Stokes equations using direct inversion of Stokes operator or accelerated multigrid technique* Comput. Struct. **87**, 710–720 (2009)

[50] Meliga, P., Chomaz, J.-M., Sipp, D., *Unsteadiness in the wake of disks and spheres: instability, receptivity and control using direct and adjoint global stability analyses* J. Fluid Struct., **25** 601–616 (2009)

Part II

Papers

Paper

١

J. Fluid Mech. (2014), *vol.* 753, *pp.* 1–28.
doi:10.1017/jfm.2014.364

The planar X-junction flow: stability analysis and control

Iman Lashgari[1], Outi Tammisola[2,†], Vincenzo Citro[3], Matthew P. Juniper[2] and Luca Brandt[1]

[1]Linné FLOW Centre and SeRC (Swedish e-Science Research Centre), KTH Mechanics, SE-100 44 Stockholm, Sweden

[2]DIIN, University of Salerno, via Ponte don Melillo, 84084 Fisciano (SA), Italy

[3]Department of Engineering, University of Cambridge, Trumpington Street, Cambridge CB2 1PZ, UK

(Received 24 May 2013; revised 22 April 2014; accepted 24 June 2014)

The bifurcations and control of the flow in a planar X-junction are studied via linear stability analysis and direct numerical simulations. This study reveals the instability mechanisms in a symmetric channel junction and shows how these can be stabilized or destabilized by boundary modification. We observe two bifurcations as the Reynolds number increases. They both scale with the inlet speed of the two side channels and are almost independent of the inlet speed of the main channel. Equivalently, both bifurcations appear when the recirculation zones reach a critical length. A two-dimensional stationary global mode becomes unstable first, changing the flow from a steady symmetric state to a steady asymmetric state via a pitchfork bifurcation. The core of this instability, whether defined by the structural sensitivity or by the disturbance energy production, is at the edges of the recirculation bubbles, which are located symmetrically along the walls of the downstream channel. The energy analysis shows that the first bifurcation is due to a lift-up mechanism. We develop an adjustable control strategy for the first bifurcation with distributed suction or blowing at the walls. The linearly optimal wall-normal velocity distribution is computed through a sensitivity analysis and is shown to delay the first bifurcation from $Re = 82.5$ to $Re = 150$. This stabilizing effect arises because blowing at the walls weakens the wall-normal gradient of the streamwise velocity around the recirculation zone and hinders the lift-up. At the second bifurcation, a three-dimensional stationary global mode with a spanwise wavenumber of order unity becomes unstable around the asymmetric steady state. Nonlinear three-dimensional simulations at the second bifurcation display transition to a nonlinear cycle involving growth of a three-dimensional steady structure, time-periodic secondary instability and nonlinear breakdown restoring a two-dimensional flow. Finally, we show that the sensitivity to wall suction at the second bifurcation is as large as it is at the first bifurcation, providing a possible mechanism for destabilization.

Key words: flow control, instability, wakes/jets

† Email address for correspondence: outi@mech.kth.se

1. Introduction

In this study, we examine the stability and control of the flow in a planar two-dimensional X-junction, which comprises three inlet channels and one outlet channel. We employ three-dimensional direct numerical simulation (DNS) and global linear stability analysis to discover the nature of the first and second bifurcations. Finally we use adjoint-based sensitivity analysis to control the flow by applying apply optimal steady suction or blowing at the wall.

The present study is mostly fundamental in nature. The flow in the X-junction is a complex wall-bounded separated flow. Understanding the bifurcation mechanisms of this flow and designing control strategies to influence them is interesting in its own right, and adds to the physical understanding of a more general class of separated flows, in particular channel junctions and similar configurations (e.g. Chiang & Sheu 2002; Poole, Alves & Oliveira 2007; Lanzerstorfer & Kuhlmann 2012; Oliveira, Pinho & Alves 2012). In the present paper we show that the critical parameter for the onset of both two- and three-dimensional instabilities of the X-junction is the length of the recirculation bubble(s) rather than the Reynolds number. This indicates that similar instabilities can be found at lower or higher Reynolds flows, which develop a similar topology to these recirculation zones.

X-junctions exist in many natural phenomena, such as river junctions, and in industrial applications, such as micromixers and flow focusing devices. Even though the typical Reynolds number in river engineering is higher than that in the present study (of the order of 1000–100 000), the mean flow streamlines and the recirculation zone downstream of the junction are qualitatively similar (see e.g. Best 1987). The structure of the recirculation zone of a river is directly connected to sediment transport and accumulation (river bed formations) (Best & Reid 1984; Shabayek, Steffler & Hicks 2002). Conversely, the Reynolds number for micromixers and flow focusers is often low ($Re < 10$), except for inertial micromixers (at $Re = 100$–1000), where the formation of the recirculation zone downstream of the junction is evident even without non-Newtonian effects.

Micromixers are designed to mix two fluids as efficiently as possible at small length scales, most often at low Reynolds numbers and in the absence of turbulence (Nguyen & Wu 2005). Flow focusers are often used to produce controlled-size droplets (Joanicot & Ajdari 2005), and have been tested for the purpose of creating thread-like fibres in materials processing (Kinahan *et al.* 2011; Håkansson 2012; Håkansson *et al.* 2014). In the present work we propose a control strategy by fluid injection or removal (steady suction or blowing), which could be applicable for recirculatory flows in mixers and focusers despite the low Reynolds number.

Both mixing and focusing of the flow in X- and T-shaped junctions have been investigated in previous studies. However, there have been only a few studies in the area of inertia-driven hydrodynamic instabilities. Oliveira *et al.* (2012) numerically and experimentally studied the vortical structure of a Newtonian fluid through an X-junction. Their numerical study was two-dimensional. They defined the velocity ratio, V_r, as the ratio of the maximum velocity in the side channel to that in the main channel, and the width ratio, W_r, similarly. They found that the critical Reynolds number, based on the exit channel quantities, is about $Re \approx 140$ for $V_r = 50$. They showed that the instabilities take the form of central vortices in the exit channel.

Mixers have been studied in more detail. Flow regimes in a T-mixer with a rectangular cross-section are reported in the numerical study by Kockmann, Foll & Woias (2003). As they increased the Reynolds number, they observed laminar flow, then vortical flow and then engulfment flow, in which the streamlines in the

mixing channel are asymmetric. Tomas, Ameel & Guilkey (2010) experimentally studied a Newtonian fluid within a T-junction with a rectangular cross-section. They observed that the flow first bifurcates to a steady asymmetric state at Reynolds number $Re = 105$, and then a highly oscillatory asymmetric flow occurs in the range $190 < Re < 240$. At higher Re, the flow regains its symmetric state and the rate of mixing decreases. Recently, Fani, Camarri & Salvetti (2013) studied the engulfment regime in a three-dimensional T-mixer with a quadratic cross-section by DNS and a global stability analysis. The mechanism of engulfment was found to be the tilting of the vortical structures at the beginning of the exit channel. They also studied the sensitivity to the perturbation inlet velocity and reported that the flow with non-fully developed inflow condition tends to be more stable.

Other studies in planar X-junction geometries (Poole *et al.* 2007; Poole, Rocha & Oliveira 2014) considered rheology measurements. These authors recently extended their studies to the inertial regime (Poole *et al.* 2014). In their DNS of Newtonian inertial fluids on the same two-dimensional configuration as ours, but with a different inflow–outflow structure, they find a very similar symmetry-breaking bifurcation at the same length of the recirculation bubbles ($L \approx 6$) as ours (but at much higher Re).

The stability analysis and control of the inertia-dominated flow in an X-junction is also interesting from a fundamental point of view because the flow contains confined jet-like structures and recirculation regions. The flow in a planar X-junction exhibits two bifurcations as the Reynolds number is increased from zero. A similar bifurcation pattern has been observed in a channel with a sudden expansion (Fearn, Mullin & Cliffe 1990; Fani, Camarri & Salvetti 2012), contraction (Chiang & Sheu 2002), or both (Mizushima & Shiotani 2000). The flow first bifurcates to an asymmetric steady state through a pitchfork bifurcation. On further increasing the Reynolds number, the flow develops a time-dependent nonlinear cycle, initiated by a stationary global instability of a single recirculation bubble. Similar instabilities are observed in the flow behind a bump (Gallaire, Marquillie & Ehrenstein 2007; Passaggia, Leweke & Ehrenstein 2012), behind a backward-facing step (Barkley, Gomes & Henderson 2002; Marquet *et al.* 2009; Lanzerstorfer & Kuhlmann 2011), in boundary layer recirculation bubbles (Rodriguez & Theofilis 2010) and in a lid-driven cavity (Albensoeder, Kuhlmann & Rath 2001; Haque *et al.* 2012).

Adjoint-based sensitivity analysis of flows was first introduced by Hill (1992) and has been used extensively to examine the receptivity to internal and external modifications (Sipp *et al.* 2010; Luchini & Bottaro 2014). In this study, we use a global stability and a structural sensitivity analysis to investigate the dynamics of instabilities in a planar X-junction flow. Structural sensitivity analysis was introduced by Chomaz (2005) and Giannetti & Luchini (2007) to identify the origin of instabilities in open shear flows. The structural sensitivity is defined as the region of the flow where a force–velocity feedback results in the largest drift of the eigenvalue. In this paper, we also seek the most efficient control strategy to delay or promote the first pitchfork bifurcation. We use the sensitivity to boundary velocity modification, introduced by Hill (1992) and used among others in Marquet & Sipp (2010), to obtain an optimal suction or blowing distribution at the wall. Furthermore, we map the control effect on the flow by using the base flow sensitivity (Marquet, Sipp & Jacquin 2008; Pralits, Brandt & Giannetti 2010). Similar techniques were used by Meliga & Chomaz (2011) on the flow in a confined impinging jet. They employed an adjoint-based method to control the global modes by optimal body and wall forcing on a broadly comparable geometry to that in the present work. Promoting the first and second bifurcations is useful in order to increase mixing by large-scale structures,

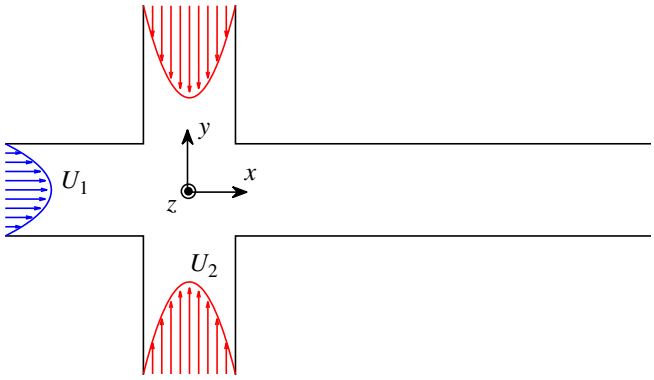

FIGURE 1. (Colour online) Schematic of the geometrical configuration and coordinate system.

e.g. in inertial micromixers, while delaying the first bifurcation is useful in order to obtain mixing by diffusion or to maintain symmetric flow, e.g. in flow focusers for fibre fabrication. We also aim to shed further light on the physical mechanisms behind the first bifurcation, and proposed control strategies.

This paper is organized as follows. We describe the flow configuration, the governing equations and the stability formulations in § 2. We introduce the numerical methods and validation in § 3. We report the results of the stability analysis and control of the first bifurcation in § 4, and the results of the second bifurcation in § 5. The conclusions are presented in § 6.

2. Configuration and problem formulation

The flow set-up and coordinate system are shown in figure 1. The geometry consists of a main channel aligned with the x-axis, and two identical side channels attached perpendicularly to the main channel at the same position, forming a cross. The origin of the coordinate system is located at the centre of the cross. The mean flow is homogeneous in the spanwise direction (z). The geometry comprises three inlets (one for the main channel and two for the side channels) and one outlet (for the main channel). The side channels have the same inflow conditions. The flow is governed by the non-dimensional incompressible Navier–Stokes and continuity equations,

$$\frac{\partial \boldsymbol{u}}{\partial t} + \boldsymbol{u}\cdot\boldsymbol{\nabla}\boldsymbol{u} = -\boldsymbol{\nabla}p + \frac{1}{Re}\nabla^2\boldsymbol{u}, \tag{2.1}$$

$$\boldsymbol{\nabla}\cdot\boldsymbol{u} = 0, \tag{2.2}$$

where $\boldsymbol{u} = (u, v, w)$ is a vector of non-dimensional velocity components, and p is the non-dimensional pressure. Two non-dimensional parameters define the characteristics of the flow: the Reynolds number (Re) and the velocity ratio (V_r). The Reynolds number is defined as

$$Re = \frac{U_1 h}{\nu}, \tag{2.3}$$

where U_1 is the maximum inflow velocity of the main channel, h is the half-width of the channels and ν is the kinematic viscosity. The velocity ratio is defined as

$$V_r = \frac{U_2}{U_1}, \tag{2.4}$$

where U_2 is the maximum inflow velocity of the side channels. In this paper, we study the stability of the X-junction flow in the Reynolds number regime $60 < Re < 700$ and for velocity ratio $0.5 < V_r < 4$. The choice of the value of V_r is based on the experiments by Tomas *et al.* (2010) and Håkansson (2012).

2.1. *Linear stability analysis*

In order to perform a linear stability analysis, we decompose the flow into a two-dimensional steady base flow and an infinitesimal three-dimensional unsteady perturbation. The base flow and perturbation velocities and pressure are denoted by $Q = (\boldsymbol{U}_b, P_b)$ and $q = (\boldsymbol{u}', p')$, respectively. The perturbation q takes the form of two-dimensional global modes,

$$\boldsymbol{u}'(x, y, z, t) = \hat{\boldsymbol{u}}(x, y)\exp(\sigma t + \mathrm{i}\beta z), \tag{2.5}$$

$$p'(x, y, z, t) = \hat{p}(x, y)\exp(\sigma t + \mathrm{i}\beta z), \tag{2.6}$$

where the spanwise wavenumber, β, exploits the homogeneity of the base flow in the spanwise direction. For a given β, the complex frequency, σ, can be computed by solving the linearized eigenvalue problem,

$$\sigma\hat{\boldsymbol{u}} + \hat{\boldsymbol{u}}\cdot\nabla\boldsymbol{U}_b + \boldsymbol{U}_b\cdot\nabla\hat{\boldsymbol{u}} = -\nabla\hat{p} + \frac{1}{Re}\nabla^2\hat{\boldsymbol{u}}, \tag{2.7}$$

$$\nabla\cdot\hat{\boldsymbol{u}} = 0. \tag{2.8}$$

To compute the base flow, we set up parabolic inflow conditions for all the inlets and a stress-free outflow condition for the outlet. For the stability analysis, we set a Dirichlet boundary condition for all the inlets and traction-free boundary condition for the outlet as suggested by Barkley, Blackburn & Sherwin (2008). The total field (the base flow plus the perturbation) satisfies the outlet boundary condition. The real and imaginary parts of the eigenvalue σ are the growth rate and oscillation frequency of the corresponding global mode. If there exists any eigenvalue with $\mathrm{Re}\{\sigma\} > 0$, the flow is linearly unstable. Conversely, if all eigenvalues have $\mathrm{Re}\{\sigma\} < 0$, the flow is linearly stable and infinitesimal perturbations eventually decay to zero.

2.2. *Structural sensitivity*

The generalized Lagrange identity is used to derive the adjoint equations. We introduce a similar ansatz for the non-trivial solution of the adjoint system:

$$\boldsymbol{u}'^{+}(x, y, z, t) = \hat{\boldsymbol{u}}^{+}(x, y)\exp(-\sigma t + \mathrm{i}\beta z), \tag{2.9}$$

$$p'^{+}(x, y, z, t) = \hat{p}^{+}(x, y)\exp(-\sigma t + \mathrm{i}\beta z), \tag{2.10}$$

where $\boldsymbol{u}'^{+} = (u'^{+}, v'^{+}, w'^{+})$ and p'^{+} are the adjoint velocity and pressure perturbation fields. The adjoint eigenvalue problem is

$$-\sigma\hat{\boldsymbol{u}}^{+} - \nabla\boldsymbol{U}_b\cdot\hat{\boldsymbol{u}}^{+} + \boldsymbol{U}_b\cdot\nabla\hat{\boldsymbol{u}}^{+} = -\nabla\hat{p}^{+} - \frac{1}{Re}\nabla^2\hat{\boldsymbol{u}}^{+}, \tag{2.11}$$

$$\nabla\cdot\hat{\boldsymbol{u}}^{+} = 0. \tag{2.12}$$

We calculate the direct and adjoint global modes to construct the structural sensitivity (Giannetti & Luchini 2007). This gives the core of the instability, defined as the region

where a local feedback force proportional to the velocity results in the largest drift of the leading eigenvalue. The sensitivity tensor is

$$\boldsymbol{S}(x_0, y_0) = \frac{\hat{\boldsymbol{u}}^+(x_0, y_0)\hat{\boldsymbol{u}}(x_0, y_0)}{\int_D \hat{\boldsymbol{u}}^+ \cdot \hat{\boldsymbol{u}}\, \mathrm{d}A}. \tag{2.13}$$

The core of the instability can be identified by different norms of the tensor $\boldsymbol{S}$. Here we use the spectral norm, which measures the effect of the maximum possible coupling among the velocity components.

2.3. *Base flow sensitivity*

The sensitivity to generic base flow modifications, $\boldsymbol{S}_{BF}$, where the modified base flow is not necessarily a solution to the steady Navier–Stokes equations, represents the variation of the complex eigenvalue, $\delta\sigma$, with respect to the small modification of base flow, $\delta\boldsymbol{U}$. The sensitivity to base flow modification is given by (see Marquet *et al.* 2008)

$$\boldsymbol{S}_{BF} = \frac{-(\nabla\hat{\boldsymbol{u}})^{\mathrm{H}} \cdot \hat{\boldsymbol{u}}^* + \nabla\hat{\boldsymbol{u}}^+ \cdot \hat{\boldsymbol{u}}^*}{\int_D \hat{\boldsymbol{u}}^+ \cdot \hat{\boldsymbol{u}}\, \mathrm{d}A}, \tag{2.14}$$

where * and $^{\mathrm{H}}$ stand for complex conjugate and transpose conjugate, respectively. We denote the horizontal and vertical components of the sensitivity to base flow modification by S_U and S_V. Note that, for a zero-frequency mode, $\boldsymbol{S}_{BF}$ is a real quantity. This is because two-dimensional modifications of the two-dimensional base flow can only change the growth rate of the mode, while the frequency remains zero.

2.4. *Sensitivity to boundary velocity modification*

The sensitivity to boundary velocity modification, $\boldsymbol{S}_b$, can be derived by explicitly including the boundary condition as a constraint in the Lagrangian functional, and considering the boundary velocity $\boldsymbol{U}_B$ as a control variable. A procedure similar to that of Marquet *et al.* (2008) and Marquet & Sipp (2010) then gives

$$\boldsymbol{S}_b = P^+\boldsymbol{n} + Re^{-1}\nabla\boldsymbol{U}^+ \cdot \boldsymbol{n}, \tag{2.15}$$

where $\boldsymbol{U}^+$ and P^+ are the adjoint base flow velocity and pressure. The eigenvalue drift is obtained by integrating $\boldsymbol{S}_b$ over the domain boundary B:

$$\delta\sigma = \int_B \boldsymbol{S}_b \cdot \delta\boldsymbol{U}_B. \tag{2.16}$$

3. Numerical methods

We compute the base flows with the spectral element method (SEM), implemented in the code Nek5000 (see Tufo & Fischer 1999). In this approach, the computational domain is divided into quadrilateral spectral elements. The equations are cast into weak form and discretized following the $\mathbb{P}_N$–$\mathbb{P}_{N-2}$ SEM discretization by Maday & Patera (1989). The velocity space consists of Nth-order Lagrange polynomial interpolants, $h_i^N(x)$, based on tensor-product arrays of Gauss–Lobatto–Legendre (GLL)

Reynolds number	Coarser mesh	Finer mesh	Relative error (%)
80	$0.0 - 0.0626\mathrm{i}$	$0.0 - 0.0633\mathrm{i}$	0.0111
90	$0.0 + 0.0476\mathrm{i}$	$0.0 + 0.0472\mathrm{i}$	0.0084
100	$0.0 + 0.1288\mathrm{i}$	$0.0 + 0.1285\mathrm{i}$	0.0023

TABLE 1. Influence of the grid resolution on the growth rate of the leading eigenvalues.

Code	Inlet length	Outlet length	Growth rate
Nek5000	4	40	0.0476
Nek5000	8	40	0.0811
Nek5000	16	40	0.0815
Nek5000	8	80	0.0811
DOG	8	40	0.0807
FreeFEM++	8	40	0.0813

TABLE 2. Influence of the domain size on the growth rate of the leading eigenvalues at $Re = 90$.

quadrature points in a local element, Ω^e, $e = 1, \ldots, E$, satisfying $h_i^N(\xi_j^N) = \delta_{ij}$, where $\xi_j^N \in [-1, 1]$ denotes one of the $N + 1$ GLL quadrature points and δ_{ij} is the Kronecker delta. SEM combines the geometrical flexibility of finite elements with the high accuracy of spectral methods. It results in exponential convergence of the solution when the polynomial order is increased, called p-refinement (see Patera 1984). It can also be used for localized refinement by increasing the number of elements, called h-refinement.

We use the stability solver DOG (Barkley *et al.* 2008) to investigate three-dimensional instabilities about the two-dimensional base flows. The perturbation fields are considered as Fourier modes and dealt with in Fourier-transformed space. A time stepping technique is used to calculate the evolution of the direct and adjoint equations. A built-in library, together with ARPACK, calculates the eigensolution of the stability problem.

The three-dimensional global modes ($\beta \neq 0$), discussed in § 4.2.4, are computed using the FreeFEM++ open-source finite element software (Pironneau, Hecht & Morice 2013), validated in § 3.1 against Nek5000 and DOG. For this we use $\mathbb{P}_2$–$\mathbb{P}_1$ Taylor–Hood elements.

3.1. *Validation*

In this section, we show the effect of the resolution and domain length on the stability of the flow in order to validate the numerical methods. We ensure that the leading eigenvalue does not vary when the number of elements and the polynomial order, N_p, are increased, and also when the inlet and outlet channels are lengthened. These results are summarized in tables 1 and 2. In the first study, we compare two meshes: a coarser mesh with 1072 elements and $N_p = 8$, and a finer mesh with 2544 elements and $N_p = 8$. The inlet and outlet lengths are 4 and 40, respectively, while the widths of the main and side channels are both 2. Table 1 shows that the growth rate of the leading eigenvalue changes by less than 0.1 %, so we choose the coarser mesh for the rest of this study. In the second study, documented in table 2, we quantify the effect of

the domain length on the stability, employing three different numerical codes. Based on this result, we choose the inlet lengths to be 8 and the outlet length to be 40. These tests shows a very good agreement between the results obtained with the three different stability solvers.

4. First bifurcation

4.1. *Linear stability analysis*

For $V_r = 3$ and Reynolds number $Re < 82.5$, the DNS converges to a steady and stable symmetric flow in the X-junction (see figure 2*a*). At the beginning of the outlet channel, a symmetric jet forms and establishes two recirculating regions. Further downstream, the flow recovers the Poiseuille channel flow profile owing to the action of viscous dissipation. As the Reynolds number increases, a steady and stable asymmetric state appears (see figure 2*b*). At the start of the outlet channel, the jet tilts towards one of the walls and the two recirculation regions have unequal sizes. There is an equal probability for the jet to tilt towards the upper or lower wall. The same phenomenon has been observed in similar flow configurations (see the experimental studies by Cherdron, Durst & Whitelaw (1978) and Fearn *et al.* (1990) on the laminar flow over a planar symmetric sudden expansion). We define the Reynolds number at which the flow changes its state, from steady symmetric to steady asymmetric, as the critical Reynolds number of the first bifurcation, Re_{c1}. The attachment of a jet to the adjacent wall, the Coanda effect, has been studied for some time (see the early work by Bourque & Newman (1960)). It is understood as a consequence of the pressure difference established in the cross-stream direction (see e.g. Sobey & Drazin 1986). To better understand the nature of the first bifurcation, we perform a global stability analysis around the symmetric base flow. In order to obtain the steady but unstable symmetric base flow at $Re > Re_{c1}$, we simulate the flow in only half of the domain, imposing the symmetry boundary condition on the axis of symmetry. The global analysis in the full domain around this symmetric flow at $Re > Re_{c1}$ has stationary unstable modes for all velocity ratios. In the linear framework, the flow therefore becomes globally unstable through a pitchfork bifurcation. In figure 3(*a*), we show the growth rate of the leading global modes as a function of the spanwise wavenumber, β, for the symmetric base flows at $Re = 82.5$, 90 and 115 and for $V_r = 3$. The most unstable mode has zero spanwise wavenumber, i.e. the first bifurcation is two-dimensional, and the critical Reynolds number for the first bifurcation is 82.5. The eigenvalue spectrum of the flow at $Re = 82.5$ is shown in figure 3(*b*) for a zero spanwise wavenumber. The distribution of the eigenvalues is symmetric around the zero frequency axis, and the least stable eigenvalues are discrete (well separated from the continuous spectrum further down in the figure).

Figure 4 shows the spatial structure of the most unstable global mode for $Re = 90$ and $\beta = 0$. Only part of the domain is shown; the domain size is larger in the simulations. The global modes have highest amplitude around the recirculation bubble and the u-perturbation is the strongest. This increases the speed at the outer edge of the bottom bubble and decreases the speed at the outer edge of the top bubble. The v-perturbation moves the flow down around $x = 2$ and up around $x = 6$. The p-perturbation shows that the pressure decreases in the bottom bubble around $x = 4$ and increases in the top bubble. The structure of the global modes suggests that the streamwise acceleration leads to lower pressure at the lower recirculation zone (the opposite for the top bubble), which in turn induces a cross-stream pressure gradient that helps to maintain the asymmetry. This effect is similar to the asymmetric

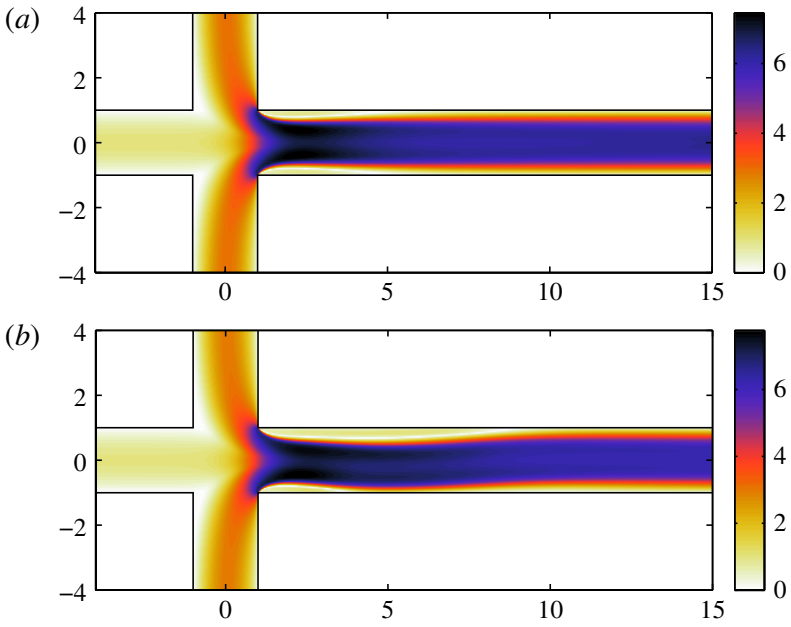

FIGURE 2. (Colour online) Total velocity distribution for $V_r = 3$: (*a*) symmetric steady state at $Re = 80$; (*b*) asymmetric steady state at $Re = 110$.

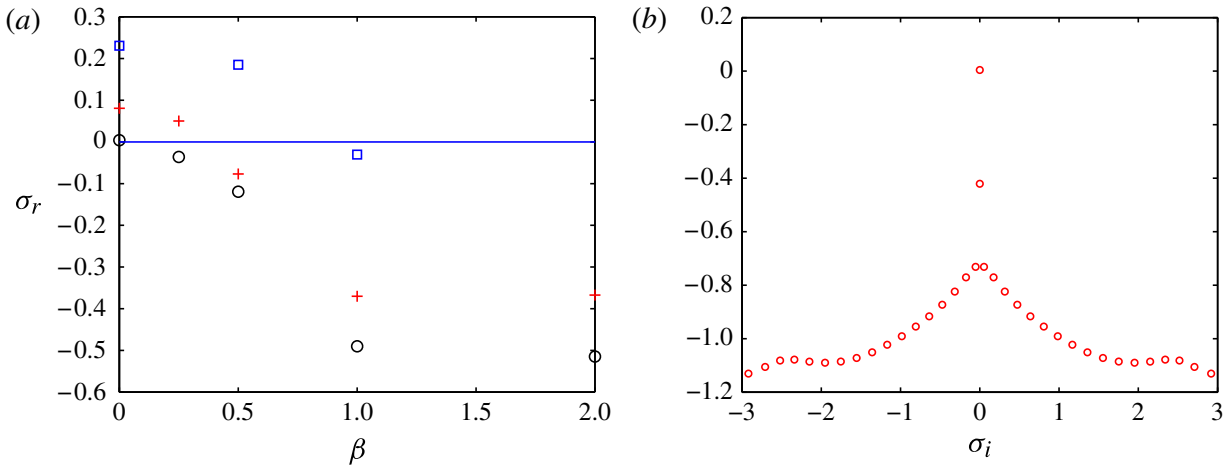

FIGURE 3. (Colour online) (*a*) Growth rate of the leading eigenvalues about the symmetric base flows for $V_r = 3$ and $Re = 82.5$ (black circles), 90 (red crosses) and 115 (blue squares). (*b*) Eigenvalue spectrum for $V_r = 3$, $Re = 82.5$ and $\beta = 0$.

attachment in stenotic flow, which is described in the work by Sherwin & Blackburn (2005): 'the axial perturbation velocities induce a weak cross-flow pressure gradient and flow ... Therefore the perturbation flow tends to deflect the centreline of the enclosed jet away from the tubes axis of symmetry, promoting a mild Coanda-type attachment'. The growth of the *u*-perturbation itself can be explained by a lift-up mechanism, as will be detailed in a later paragraph.

The region with the highest structural sensitivity, which is also known as the core of the instability, is the region of the flow in which force–velocity feedback has the greatest influence on the eigenvalue. This core is found by overlapping the direct and adjoint global modes and is shown in figure 5(*a*). It is localized at the edge of the recirculation bubble(s), suggesting that the instability can be controlled by

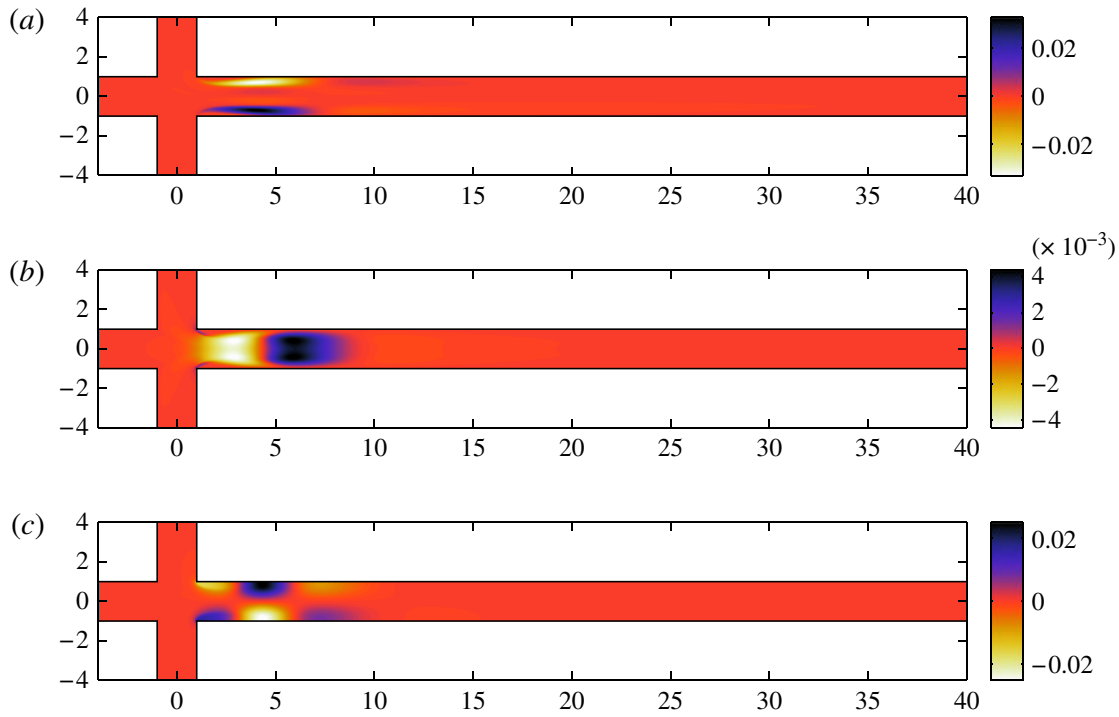

FIGURE 4. (Colour online) Spatial structure of the direct global modes: (*a*) horizontal velocity, (*b*) vertical velocity, and (*c*) pressure around the symmetric base flow at $Re = 90$, $V_r = 3$ and $\beta = 0$.

manipulating the bubble. This will be confirmed in § 4.2, where passive control by optimal suction or blowing at the wall is examined.

Here we depict only the spectral norm of the sensitivity tensor. The u^+u component of the sensitivity tensor is significantly stronger than the other components and has the same structure as the spectral norm.

In figure 5(*b*), we present the spatial map of the production of the perturbation kinetic energy for the same flow. The production term is normalized by the overall perturbation kinetic energy in the domain. The regions of largest transfer of the kinetic energy from the base state to the perturbations are found in the shear layer at the edge of recirculation bubbles. Interestingly, the core of the instability corresponds to the region of maximum positive and negative production.

More specifically, we compute the contribution of the term $uv\,\mathrm{d}U/\mathrm{d}y$ in the production of the perturbation kinetic energy. The spatial map of this term is depicted in figure 5(*c*), and can be compared to the map of total energy production in figure 5(*b*). We observe that total energy production and energy production by the term $uv\,\mathrm{d}U/\mathrm{d}y$ are almost identical in amplitude and shape, from which we conclude that the instability growth is due to this term.

The disturbance extracts energy from the base flow through the $uv\,\mathrm{d}U/\mathrm{d}y$ term in several shear flow instabilities, most notably the Kelvin–Helmholtz instability, Tollmien–Schlichting waves and the lift-up effect. To determine the instability mechanism in our flow, we note that the present instability is stationary, the mode shape is streamwise-elongated and the streamwise velocity component is an order of magnitude larger than the vertical component (figure 4 *a*,*b*). This strongly indicates a lift-up mechanism, where a small initial v-perturbation induces a strong u-perturbation (for a review on lift-up, see Brandt (2014)).

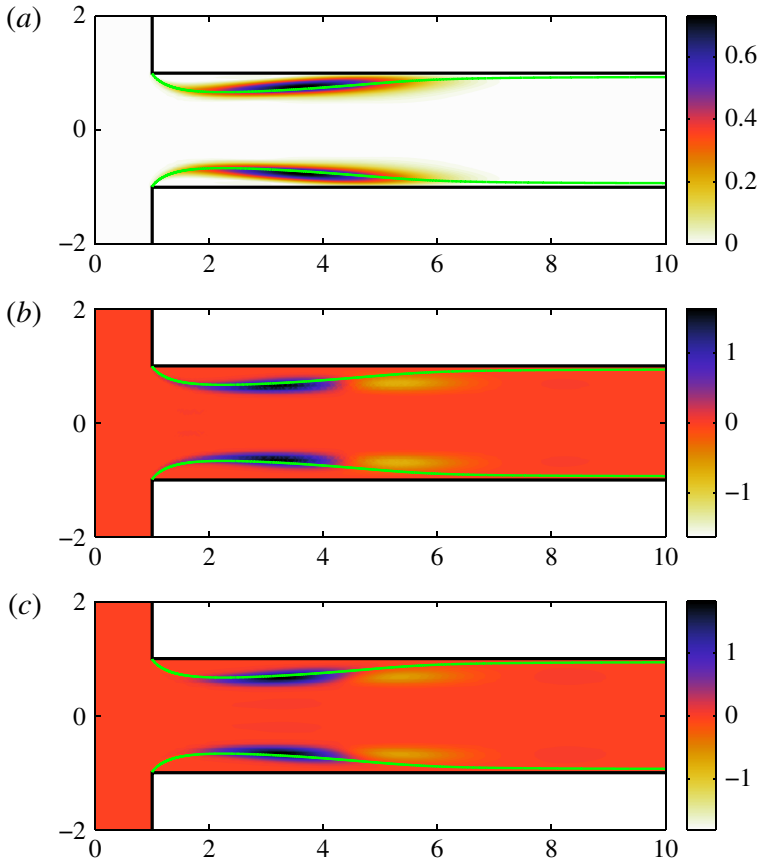

FIGURE 5. (Colour online) (*a*) Spatial map of structural sensitivity, (*b*) production of the perturbation kinetic energy and (*c*) lift-up perturbation kinetic energy around the symmetric base flow at $Re = 90$, $V_r = 3$ and $\beta = 0$. (The solid pale green lines show the edge of recirculation regions.)

This instability is different from the lift-up in parallel flows due to the feedback provided by the recirculation region, which leads to a self-sustained mechanism. This is similar to the finding of Lanzerstorfer & Kuhlmann (2011), who notes that the instability behind a backward-facing step is caused by a lift-up effect, which gains its exponential growth through recirculation for some specific value of the step height. The present configuration with two symmetric bubbles is more unstable than the case of a single bubble, because the two-dimensional asymmetric instability mode sets in at lower Reynolds numbers. This can also be explained by the energy budget: the antisymmetric global mode involving two bubbles allows the v-perturbation to be constant in the vertical direction, minimizing $\mathrm{d}v/\mathrm{d}y$, and thereby minimizing the global dissipation.

The critical Reynolds number for the first bifurcation depends significantly on V_r. Figure 6(*a*) shows that the critical Reynolds number decreases monotonically from $\sim$530 for $V_r = 0.5$ to $\sim$60 for $V_r = 4$. Nonlinear simulations on the two-dimensional domain give the same result for the first bifurcation (not shown here). If we define the Reynolds number based on the maximum velocity at the side channels, however, the neutral curve for the first bifurcation is almost independent of the velocity ratio: $Re_c = 262.5$–245 for $V_r = 0.5$–4. We also examine two extreme cases: $V_r = 10$ and $V_r = 0.2$. For $V_r = 10$, $Re_c \approx 260$ based on U_2, similarly to the previous cases. For $V_r = 0.2$, however, $Re_c \approx 310$, i.e. the flow is more stable when the side flow is

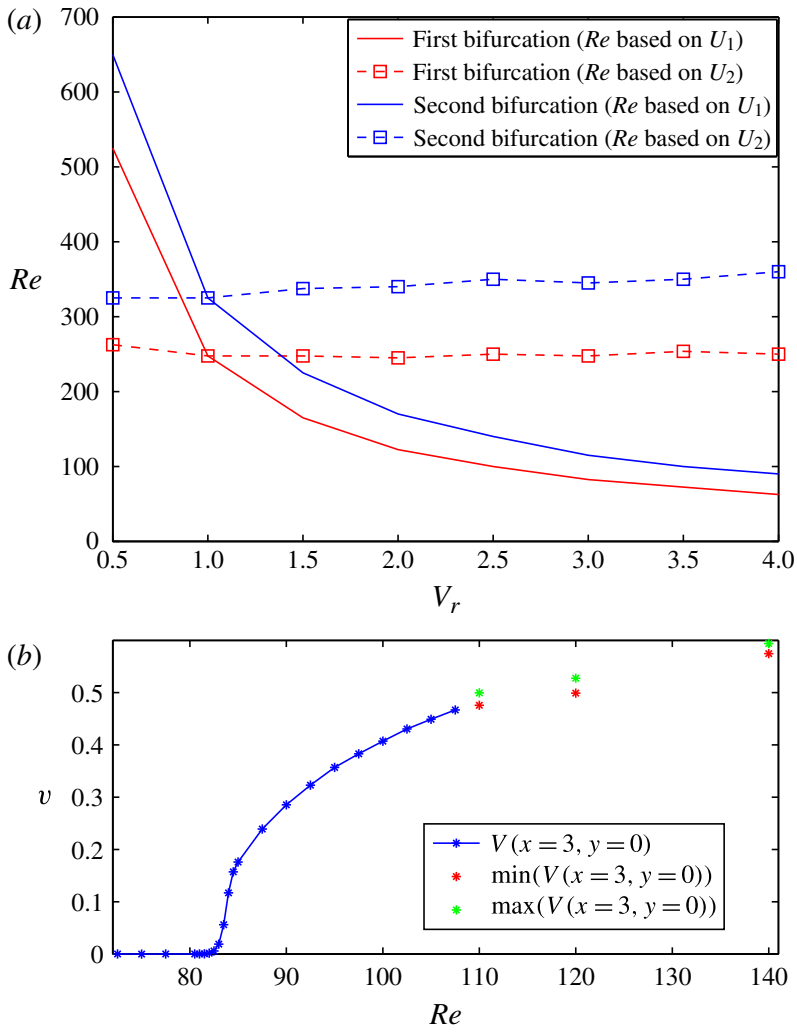

FIGURE 6. (Colour online) (*a*) Critical Reynolds number for the first and second bifurcations versus velocity ratio. (*b*) Bifurcation diagram of the X-junction flow with velocity ratio $V_r = 3$.

weaker. This shows that the critical Reynolds number of the first bifurcation is mainly determined by the inlet velocity of the side channels.

To visualize the bifurcation of the flow in the X-junction quantitatively, we introduce a measure of the deviation from the symmetric flow: the v-velocity at $(x, y) = (3, 0)$, on the centreline. In figure 6(*b*), we show the maximum and minimum value (in time) of this measure as a function of the Reynolds number. Up to $Re = 110$, the flow is steady and v is constant. The first bifurcation is evident at $Re = 82.5$. We will return to this figure when examining the second bifurcation.

For this flow, the point of first bifurcation seems to be determined by the size of the recirculation region. Figure 7 shows the stagnation streamline that starts from the upper right corner, $(x, y) = (1, 1)$, and separates the recirculating bubble from the flow that passes through the X-junction. For a fixed velocity ratio $V_r = 3$, figure 7(*a*), the bubble elongates as the Reynolds number increases. For the cases along the neutral curve, figure 7(*b*), the bubble has almost the same size for various velocity ratios and Reynolds numbers. It seems therefore that the first bifurcation occurs when the bubble reaches a critical length, which is approximately 6.1.

This result also provides a physical explanation for the scaling found in figure 6(*a*). The shape of the recirculating region at the critical conditions is unaffected by the

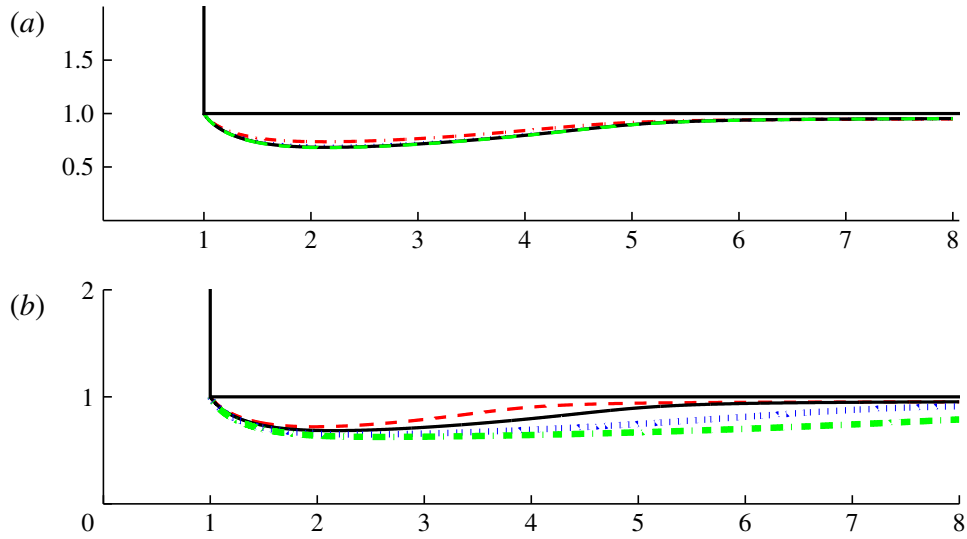

FIGURE 7. (Colour online) (*a*) Recirculation bubble of symmetric base flows for a fixed velocity ratio $V_r = 3$ and $Re = 60$ (red dashed line), $Re = 80$ (black full line), $Re = 115$ (blue dotted line) and $Re = 162.5$ (green dot-dashed line). (*b*) Some cases along the neutral curve for $Re = 520$, $V_r = 0.5$ (red dashed line), $Re = 162.5$, $V_r = 1.5$ (blue dotted line), $Re = 80$, $V_r = 3$ (black full line) and $Re = 60$, $V_r = 4$ (green dot-dashed line).

main stream when $V_r > 0.5$. This is because the side flows force the horizontal stream to flow down the middle of the exit channel without affecting the dynamics of the bubbles. This explains the dependence of the bifurcation thresholds on the velocity of the side channels. For low velocity ratios, however, i.e. $V_r = 0.2$, the stability boundary is different and Re_c is higher. Based on these principles, we anticipate that the critical condition for the T-junction will be very similar to that for the X-junction.

To investigate whether the bifurcation is supercritical or subcritical, we have performed nonlinear simulations with various amplitudes of initial noise and have observed that the final steady symmetric solution is attained for all cases when $Re < Re_{c1}$. This is also true when we simulate the flow using an asymmetric solution as the initial condition. We conclude therefore that the first bifurcation is supercritical.

4.2. *Control of the first bifurcation*

A traditional way to control globally unstable open shear flows is by a control cylinder. However, for a complex wall-bounded geometry, small-amplitude suction or blowing at the walls presents a more versatile option because the amplitude distribution can be varied more easily. We therefore try to control the first bifurcation of the X-junction by small-amplitude steady (time-independent) suction or blowing at the walls.

4.2.1. *Sensitivity to wall suction*

The sensitivity $\boldsymbol{S}_b(x, y)$ represents the change in the growth rate due to a localized velocity change of amplitude $A = 1$ at the boundary location (x, y), in the linear limit. The eigenvalue drift for different amplitudes and finite actuation areas can be obtained from $\boldsymbol{S}_b$ by integrating equation (2.16). Figure 8(*a*) shows the real part of $S_{b,n}$, which is the change in the growth rate σ_r due to control in the horizontal channel. By 'suction', we mean a velocity at the wall in the direction of the outgoing normal. We show the sensitivity for two different Reynolds numbers: $Re = 90$ (just above bifurcation) and $Re = 150$ (far from bifurcation). The main observation is that the

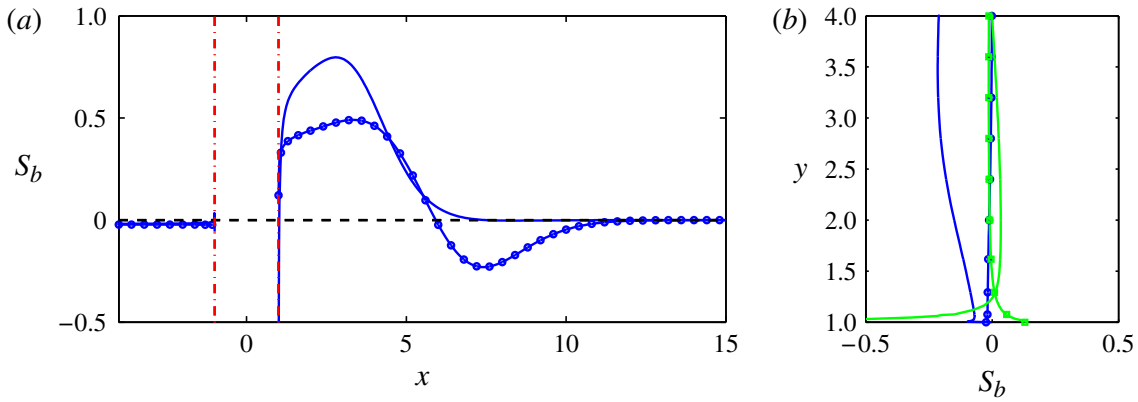

FIGURE 8. (Colour online) Sensitivity of the growth rate to suction at the main channel walls: (*a*) horizontal channel (versus x) and (*b*) vertical channel (versus y); left wall (darker, blue) and right wall (paler, green); $Re = 90$ (plain solid line) and $Re = 150$ (solid line with circles). Sensitivity to blowing is the negative of the same curve. The sensitivities to suction at both side channels are equal and are the same at the upper and lower walls of the horizontal channel. The minimum value of the solid line in the downstream corner is outside the axis in both panels: it is $\mathrm{Re}(S_{b,n}) = -1.8$.

sensitivity to suction is largest just downstream of the junction, around $x = 3$, and that suction there increases the instability growth rate, for both $Re = 90$ and $Re = 150$. Therefore, suction in this location is destabilizing.

The sensitivity is lower at $Re = 150$ than at $Re = 90$, and both stabilizing and destabilizing effects are observed for the same actuation. This indicates that a lower amplitude is needed to control the flow at $Re = 90$ than at $Re = 150$. Also, at $Re = 150$ the departure from the steady symmetric solution will be greater than it is for the $Re = 90$ flow, suggesting that the sensitivity at $Re = 150$ might be less relevant for control of the bifurcated flow.

Figure 8(*b*) shows the sensitivity along the upstream and downstream walls of the vertical channel at $Re = 90$ and $Re = 150$. The sensitivity is generally lower in the vertical channel than in the horizontal channel, apart from at the corners, where it is the same. The sensitivity is large and negative close to the downstream corner, which means that suction there is stabilizing. However, this region where suction is stabilizing is very small, making control near the corner difficult. Comparing the results at the same height y in the upstream and downstream channel, it is interesting to note that the sensitivity is higher on the upstream wall, except at the corner.

4.2.2. *Passive control by distributed suction and blowing*

The sensitivity distributions, such as the curves in figure 8, are also gradient distributions. This means that $\mathrm{Re}(S_{b,n})$ gives the suction distribution that increases the eigenvalue growth rate most, of any suction distribution with a given L^2-norm (and with a low enough amplitude so that the linear analysis is valid). Correspondingly, $-\mathrm{Re}(S_{b,n})$ gives the distribution that decreases the eigenvalue growth rate most. If $-\mathrm{Re}(S_{b,n})$ is applied at the boundary, the critical Reynolds number should increase.

We therefore test how far the linearly optimal distribution can increase the critical Reynolds number. The procedure is as follows. We choose a suction amplitude A and first compute the base flow and modes at bifurcation. Then we extract the optimal stabilizing suction distribution $-\mathrm{Re}(S_{b,n})$ and scale it so that the ratio of the absolute value of the maximal suction velocity, and the maximal inflow velocity, is equal to A.

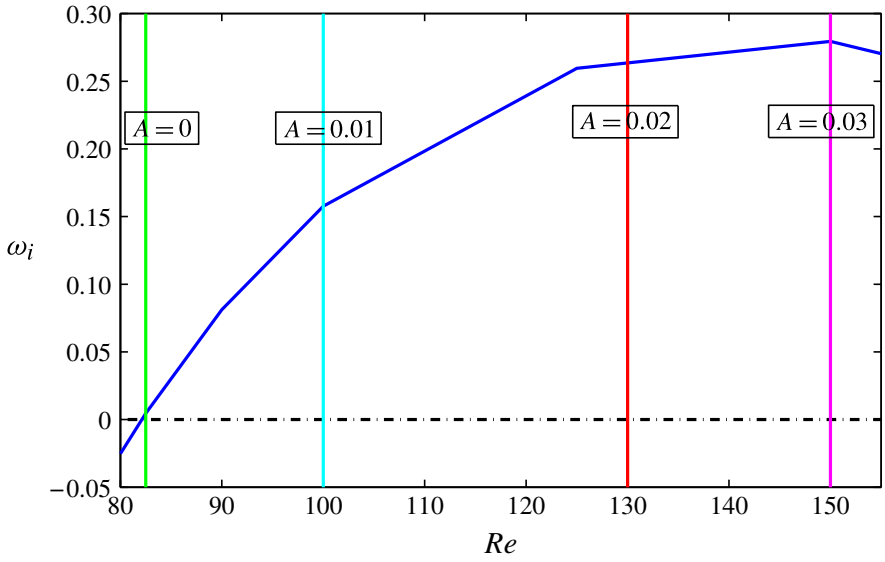

FIGURE 9. (Colour online) The effect of optimal boundary suction or blowing. The curve (blue online) gives the global mode growth rate of the uncontrolled base flow. The vertical lines (colour online, labelled) give the stability limits at different values of suction.

Next, we apply the optimal suction distribution at the boundary, and recompute the base flow and the global modes. If all global modes now have negative growth rates, then all steps are repeated at higher Re. We keep increasing the Reynolds number until the growth rate of the leading mode is positive despite the control. In this way, we have found the new critical Reynolds number corresponding to the suction amplitude A.

The critical Reynolds numbers for $A = 0$, 0.01, 0.02 and 0.03 are shown by vertical lines in figure 9. First, it is remarkable that suction of such a small maximal amplitude as 3 % of the inflow velocity can stabilize the flow until $Re = 150$, which is almost double the critical Reynolds number of the uncontrolled case. Higher suction amplitudes were also tested but did not result in any further increase of the critical Reynolds number. The change of the flow rate due to suction or blowing in the configuration with $A = 0.03$ is also around 3 %, which is small. Changes in the total flow rate due to control could be adjusted for by applying suction or blowing in the region downstream ($x > 10$), if desired. In this region, the instability is not sensitive to suction or blowing, and hence the flow rate adjustment would not interfere with the control effect.

The linear growth rate without suction is also shown in the same figure and reaches values up to $\sigma_r = 0.27$ at $Re = 150$. The growth rate with the linearly optimal suction still becomes negative at this Re (the flow is stabilized). Therefore suction or blowing is a robust and efficient way to control the X-junction flow. Next, we will investigate how the control works in more detail.

4.2.3. *Physical interpretation of suction control*

The optimal suction distribution has several simultaneous effects on the base flow. We cannot create arbitrary base flow changes because the base flow has to satisfy the Navier–Stokes equations. Some of the changes induced by the optimal suction might have a large effect on the growth rate, and some might have no effect at all but be merely a consequence of the fact that the base flow has to satisfy the Navier–Stokes equations. To find out where the effective base flow changes induced by suction are

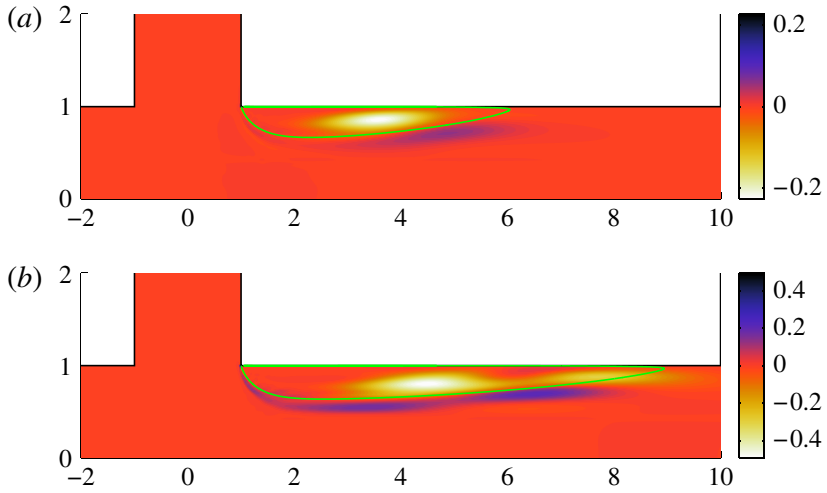

FIGURE 10. (Colour online) Spatial map of the control effect obtained by wall suction, $\int_B \mathrm{Re}(\boldsymbol{S}_{BF}) \cdot (\boldsymbol{U}_s - \boldsymbol{U}_0)$, for (*a*) $Re = 90$ and (*b*) $Re = 150$. The thin pale green line shows the boundary of the recirculation bubble in each case.

located, we investigate the product of the base flow sensitivity (2.14) and the base flow change, $\int_B \boldsymbol{S}_{BF} \cdot (\boldsymbol{U}_s - \boldsymbol{U}_0)$, where $\boldsymbol{U}_s$ is the base flow velocity vector with suction, and $\boldsymbol{U}_0$ the base flow velocity vector without suction. This product gives a spatial map of the control effect, and the real part, displaying stabilization, is shown in figure 10 for $Re = 90$ and $Re = 150$. Inside and just outside the recirculating region, the suction induces stabilizing and destabilizing base flow modifications, respectively. It can be seen that the stabilizing influence occurs almost entirely inside the recirculation bubble, where the wavemaker defined by the structural sensitivity (figure 5) is located. This is true for both $Re = 90$ and $Re = 150$, although the optimal suction distributions themselves (figure 8) are qualitatively different. Hence, in line with the stability results, we find the suction to be optimal because of its effect on the most influential region of the flow: the recirculation bubble.

To quantify in more detail how the control changes the recirculation bubble, we investigate three base flows at $Re = 90$: (*a*) without suction or blowing, (*b*) with optimal stabilizing suction or blowing $-\mathrm{Re}(S_{b,n})$, and (*c*) with optimal destabilizing suction or blowing $\mathrm{Re}(S_{b,n})$ (see figure 11). The most stable flow has the fewest streamlines with reverse flow and the smallest recirculation bubble – i.e. there is both weaker and less recirculation. By looking at $-\mathrm{Re}(S_{b,n})$ (the negative of the curve in figure 8*a*), we observe that this is achieved by blowing from the wall in the location of the recirculation bubble. The attenuation of the instability can be attributed to two factors. Firstly, blowing decreases the velocity gradient between the main stream and the bubble, decreasing $v\,\mathrm{d}U/\mathrm{d}y$ and hence weakening the energy production by lift-up. Secondly, blowing also counteracts the recirculation, which is needed to produce exponential growth of the otherwise algebraic lift-up mechanism.

4.2.4. *Control of three-dimensional modes*

Previously, we showed that the optimal wall suction distribution can be computed for the leading two-dimensional eigenmode, and stabilizes that mode up to $Re = 150$. However, to confirm that the flow is indeed stabilized by suction, we also need to stabilize all three-dimensional eigenmodes, $\beta \neq 0$. It is impossible to experimentally design different controls for different wavenumbers. Therefore we proceed to examine

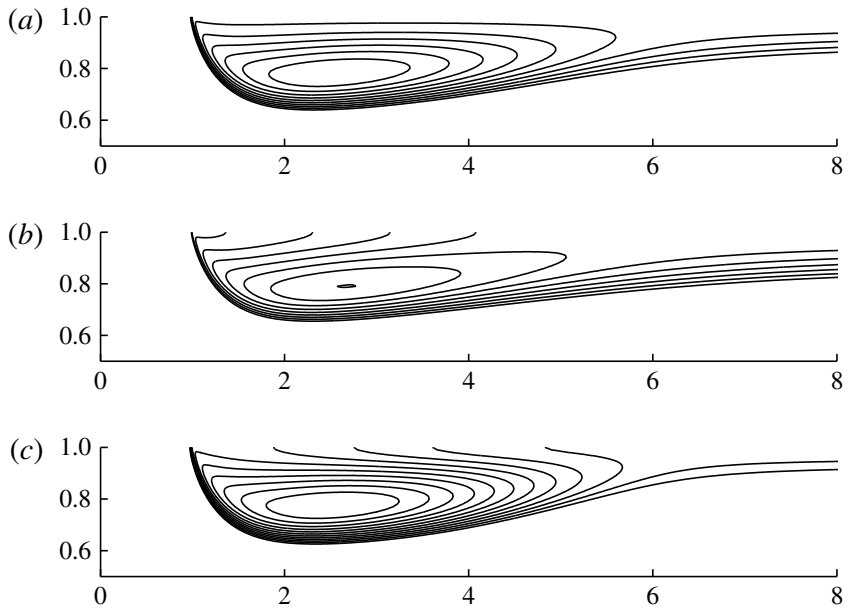

FIGURE 11. Streamlines around the recirculation bubble of the base flow: (*a*) base flow with zero wall velocity; (*b*) base flow with optimal stabilizing suction or blowing distribution at the wall, magnitude 1 %; (*c*) base flow with optimal destabilizing suction or blowing distribution at the wall, magnitude 1 %.

Re	β	Production	Dissipation
90	0	0.474	−0.325
90	0.5	0.296	−0.377
150	0	0.536	−0.257
150	0.5	0.599	−0.254

TABLE 3. Perturbation kinetic energy budget.

whether the two-dimensionally optimal suction stabilizes all modes, whether optimal or not, for $\beta \neq 0$.

The leading eigenvalues for different values of β are shown in figure 12 for the case $Re = 150$, with suction and without suction. Interestingly, for the cases without suction, spanwise-periodic modes become gradually less and less stable by increasing the Reynolds number. The spanwise wavenumber of the least stable mode becomes different from zero at $Re \approx 120$, and approaches $\beta = 0.5$ when $Re = 150$. To understand this effect, we analyse the perturbation energy budget for the cases $Re = 90$ and $Re = 150$ at $\beta = 0$ and $\beta = 0.5$. The production and dissipation of the perturbation kinetic energy, normalized by the kinetic energy, are shown in table 3. The wavenumber selection only depends on which wavenumbers experience most energy production by the lift-up effect. Dissipation does not vary significantly with β, whereas the production grows with Re for $\beta = 0.5$. Thus lift-up is more effective at finite β despite the presence of a spanwise velocity component in the dissipation term.

When applying control by optimal suction, we see that the eigenvalues become stable for all β. Results for Reynolds numbers lower than 150 also show the same behaviour. This confirms that the control works well for two- and three-dimensional modes, and the flow is indeed stabilized up to $Re = 150$. Furthermore, we observe that

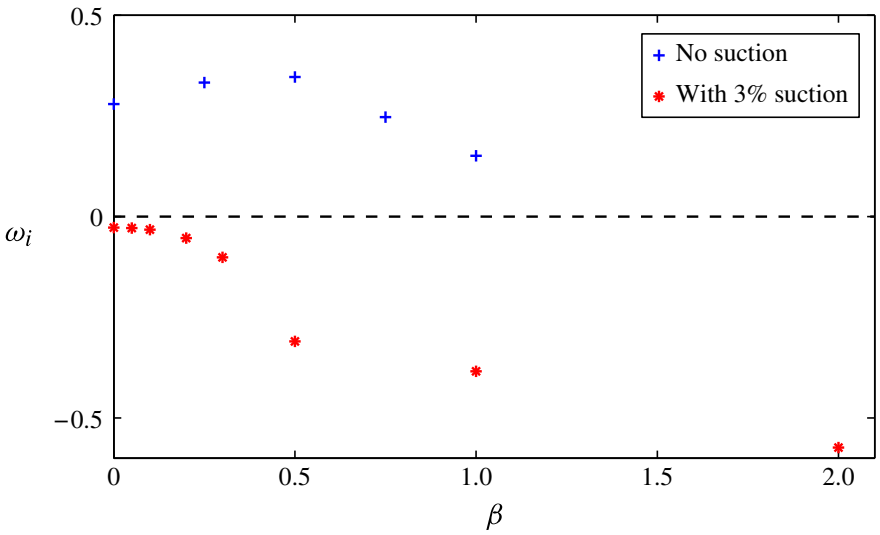

FIGURE 12. (Colour online) At $Re = 150$, the growth rate of the most unstable eigenvalue as a function of β, with (red stars) and without (blue crosses) two-dimensional optimal suction.

the modes at non-zero spanwise wavenumbers are more affected by suction than the two-dimensional mode, and the controlled flow is characterized again by a least stable mode of $\beta = 0$.

5. Second bifurcation

5.1. *Linear analysis*

When the Reynolds number is increased beyond the first bifurcation, the flow maintains its steady asymmetric state until $Re = Re_{c2}$, the critical Reynolds number for the second bifurcation. For $Re > Re_{c2}$, it bifurcates again owing to the action of stationary global modes around the steady asymmetric base flow. For $V_r = 3$, a global stability analysis gives an unstable global mode with $\beta = 1$ for $Re = 115$. In figure 13(*a*), we show the leading eigenvalues as a function of the spanwise wavenumber at $Re = 115$ and 120. The second bifurcation is also of the pitchfork type. Figure 13(*b*) shows the eigenvalue spectrum of the asymmetric base flow at $Re = 115$. The spectrum is discrete and symmetric, as for the symmetric base flows.

We present the features of the most unstable global mode around the asymmetric base flow in figure 14. The structure of the modes illustrates the asymmetry of the underlying base flow; in this case, the jet is tilted towards the lower wall. The u-component is the strongest and is maximal at the larger recirculation bubble, close to the upper wall of the outlet channel. The v- and w-perturbation modes also display their maximum amplitude next to the larger bubble. The strong u-perturbation of the global direct mode, together with the strong v^+-perturbation of the global adjoint mode (not shown here), suggests that the lift-up mechanism is active in the shear layer associated with the largest recirculating region (see Marquet *et al.* 2009). The perturbation transports the base flow momentum from the regions of low speed to those with higher speeds and creates a large u-perturbation.

Figure 15 shows the overlap of the direct and adjoint global modes, which is the core of the instability at the second bifurcation. The core is located in the larger recirculation bubble. Note that the core of the instability at the second bifurcation is in the middle of the bubble and extends over the whole bubble, while the core of the

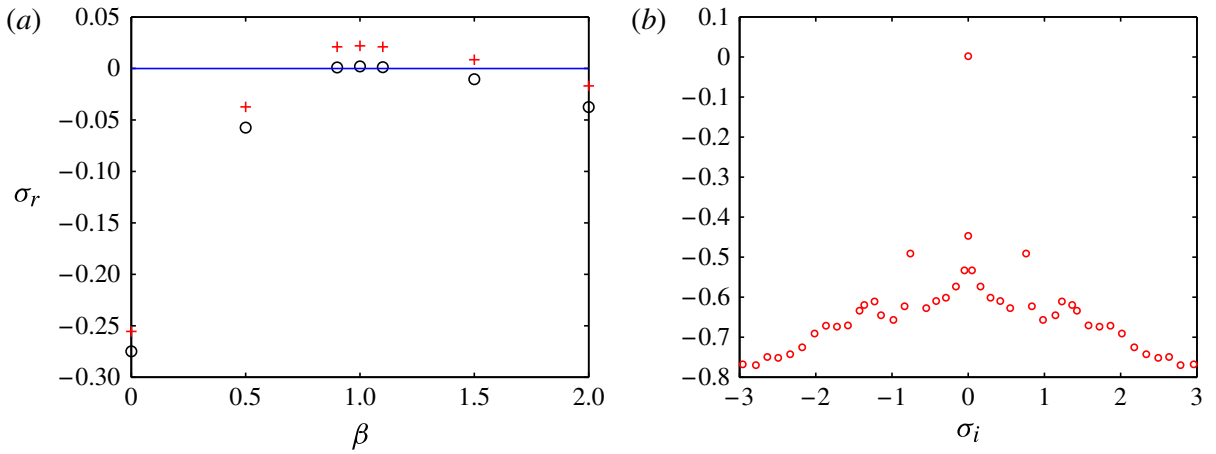

FIGURE 13. (Colour online) (*a*) Growth rate of the leading eigenvalues around the asymmetric base flows for $V_r = 3$ at $Re = 115$ (black circles) and 120 (red crosses). (*b*) Eigenvalue spectrum at $Re = 115$, $V_r = 3$ and $\beta = 1$.

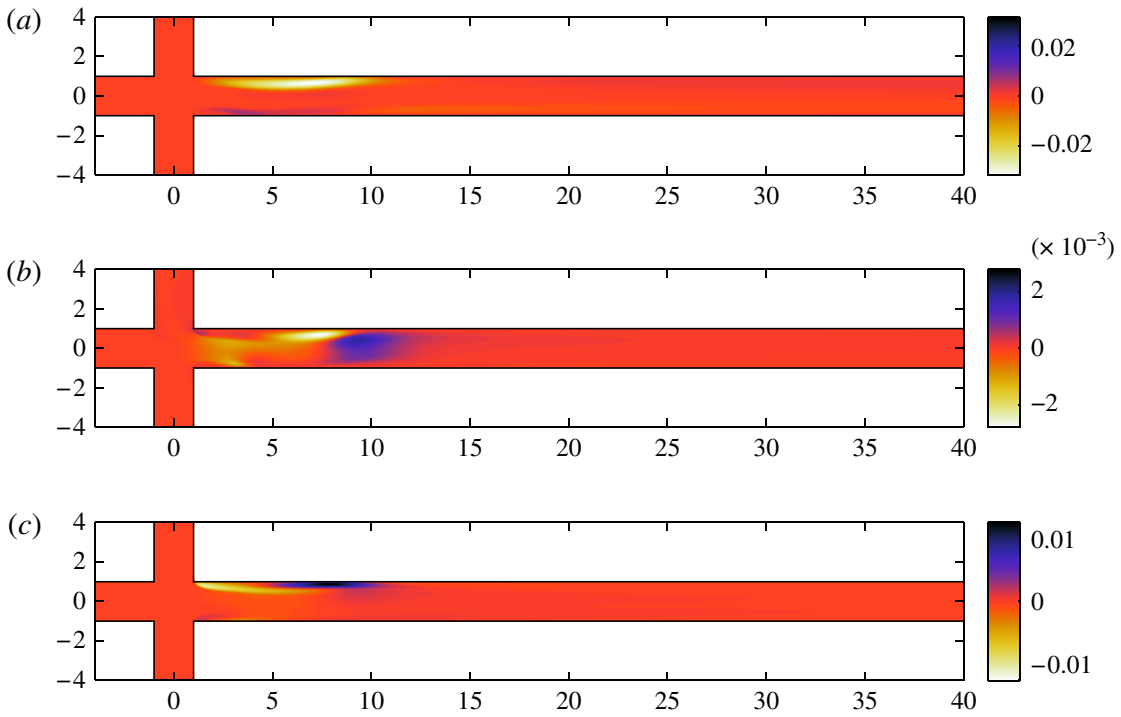

FIGURE 14. (Colour online) Spatial structure of the direct global modes: (*a*) horizontal velocity, (*b*) vertical velocity and (*c*) spanwise velocity around the asymmetric base flow at $Re = 120$, $V_r = 3$ and $\beta = 1$.

instability at the first bifurcation was localized at the downstream edges of the two bubbles (see § 5.1). The instability is three-dimensional and steady, which is similar to the instabilities that develop along the streamlines in the flow behind a bump or in a cavity (see e.g. Albensoeder *et al.* 2001; Gallaire *et al.* 2007; Rodriguez & Theofilis 2010) and at the recirculation region over a backward-facing step (see e.g. Marquet *et al.* 2009; Lanzerstorfer & Kuhlmann 2011). Lanzerstorfer & Kuhlmann (2011) used the energy production, together with the flow streamlines, to distinguish between three types of instability for the backward-facing step: centrifugal, elliptic and lift-up mechanism. We shall attempt to do the same for the second bifurcation.

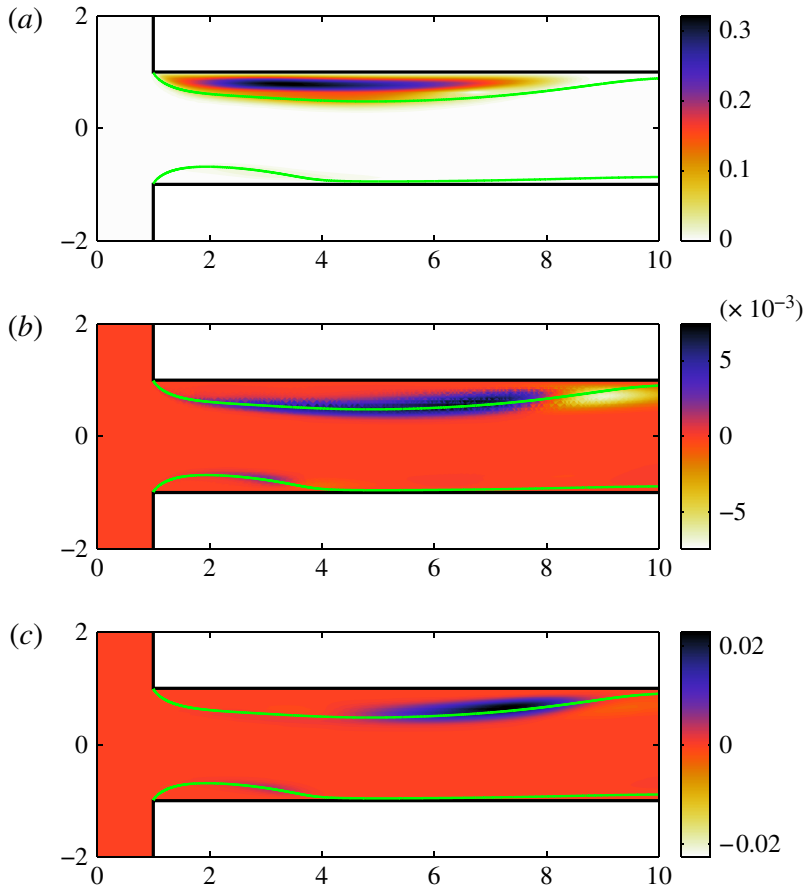

FIGURE 15. (Colour online) (*a*) Spatial map of the structural sensitivity, (*b*) production of the perturbation kinetic energy and (*c*) lift-up perturbation kinetic energy around the asymmetric base flow at $Re = 120$, $V_r = 3$ and $\beta = 1$. (The solid pale green lines show the edge of recirculation regions.)

The energy production for the instability leading to the second bifurcation is shown in figure 15(*b*). The maximum of the production is in an area of curved streamlines, but the velocity increases radially outwards (to the middle stream), which precludes centrifugal instability. Furthermore, elliptic instability would be indicated by a maximum production in the centre of a vortex, while in our case the maximum is at the outer edge of the recirculation region. Similarly to the analysis of the first bifurcation, we present the spatial structure of the lift-up term ($uv\,\mathrm{D}U/\mathrm{D}y$) in the production of the perturbation kinetic energy in figure 15(*c*). The lift-up term presents a structure relatively similar to the total production, both with a localized maximum at the downstream edge of the larger recirculation bubble where the base flow shear is strongest. We conclude that also the second bifurcation is due to the lift-up mechanism (Lanzerstorfer & Kuhlmann 2011), and the vertical velocity perturbation extracts energy from the base flow shear ($\mathrm{d}U/\mathrm{d}y$) to produce in this case streamwise-elongated low- and high-speed streaks. We also show that the structural sensitivity (figure 15*a*) is the largest in the middle of the bubble, indicating that velocity perturbations initiated there participate in the streamline displacement and the lift-up.

In figure 6(*a*), we show the critical Reynolds number for the second bifurcation. This neutral curve has the same behaviour as that of the first bifurcation. The second bifurcation is also almost independent of the velocity ratio if the Reynolds number

is based on the maximum velocity in the side channel. For all velocity ratios greater than unity, the most dangerous mode is found to have spanwise wavenumber $\beta = 1$. However, for $V_r = 0.5$, the mode with $\beta = 1.4$ is the most unstable.

5.2. *Nonlinear analysis*

In order to further understand the results of the linear analysis about the second bifurcation, we perform nonlinear simulations on a three-dimensional periodic geometry with spanwise length, $L_z = 2\pi$, corresponding to $\beta = 1$. We use three, six and nine spectral elements in the spanwise direction (the polynomial order is eight, as in the two-dimensional simulations) to ensure that the final results are mesh-independent. We construct an initial condition for the DNS consisting of the asymmetric base solution combined with the spanwise periodic perturbation leading to the strongest transient energy growth (computed separately by standard direct-adjoint iterations). The initial condition is scaled to have maximum spanwise velocity, the strongest component, equal to unity. The nonlinear evolution of the initial condition shows that the spanwise velocity decays to zero and a two-dimensional steady state is obtained asymptotically for all $Re \leqslant 105$ (below the second bifurcation). Interestingly, once all the disturbances have travelled out of the computational domain, the larger recirculation bubble may have moved to the opposite side with respect to the initial condition. We therefore find two possible steady two-dimensional solutions for $Re \leqslant 105$ once the convective instabilities have travelled out of the domain.

At $Re \geqslant 110$ and $V_r = 3$, the nonlinear flow becomes time-dependent and three-dimensional. To ensure that this behaviour is independent of the outlet length, we have run also a three-dimensional nonlinear simulation at $Re = 110$ where the outlet length is increased from $L_{out} = 40$ to $L_{out} = 60$. The flow has the same nonlinear cycle as in the simulations with the shorter outlet length described below. In figure 16 we present the time evolution of the spanwise velocity for the case $Re = 120$. Similar behaviour is observed for $Re \in [110–140]$. The nonlinear evolution of the flow displays a cyclic behaviour with a period of approximately 50 time units, where t_0 in the figure is the initial time of the cycle. The spanwise velocity first grows in time up to a critical threshold, where the maximum non-dimensional spanwise velocity becomes $w \approx 0.85$ (see figure 16*a*). Above this threshold, the flow develops instabilities at the end of the large recirculation region, figure 16(*b*). These instabilities prevent the three-dimensional flow structure from saturating nonlinearly to a stationary state. Instead, they break down the structure and produce a convective packet travelling downstream, as shown in figure 16(*c*). Once the instabilities have been convected out of the domain, the flow returns to a nearly two-dimensional state, the spanwise velocity starts to grow again at the end of the recirculation region, and the cycle repeats, figure 16(*d*). The behaviour of the flow is similar at higher Reynolds number. In figure 17 we present the history of the v-velocity extracted from the probe signals for $Re = 110$ and $Re = 120$ when $V_r = 3$. The cyclic behaviour of the nonlinear simulation is evident. Upstream, the velocity varies smoothly in time. Downstream, the flow shows rapid oscillations at the end of each cycle, which correspond to the secondary instability and the formation of the travelling packet. The period of each cycle for $Re = 120$ is shorter and not constant in time with respect to the one for $Re = 110$.

In summary, we observe a steady two-dimensional flow at $Re \leqslant 105$ and an unsteady three-dimensional final state at $Re \geqslant 110$. This behaviour is also shown in figure 6(*b*). The appearance of the nonlinear cycle is evident at $Re = 110$ where the v-velocity at the centreline becomes time-dependent. This critical Reynolds number agrees

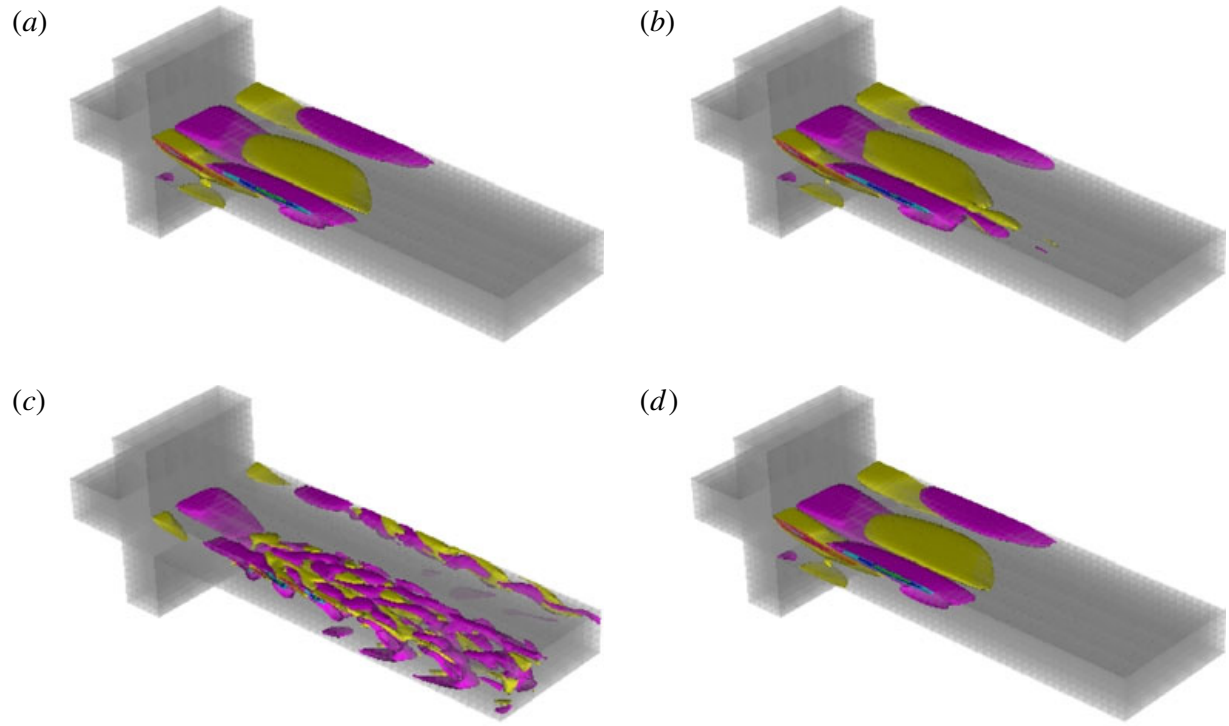

FIGURE 16. (Colour online) Time evolution of the spanwise velocity at $Re = 120$ and $V_r = 3$: (*a*) initial amplification of velocity, at $t = t_0 + 32$; (*b*) onset of instability at $w \approx 0.85$, at $t = t_0 + 44$; (*c*) convective instabilities, at $t = t_0 + 48$; and (*d*) re-establishment of the spanwise velocity, at $t = t_0 + 50 + 32$.

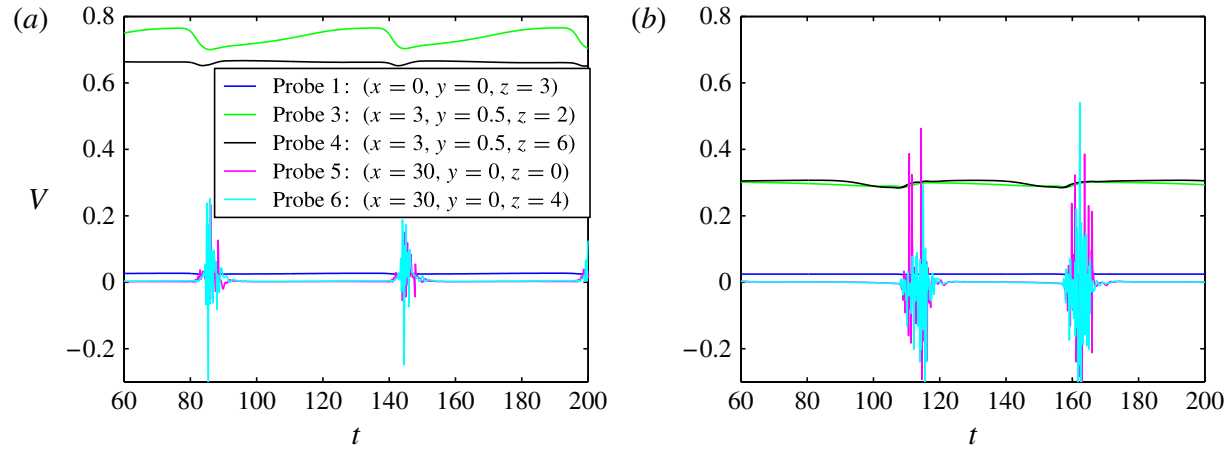

FIGURE 17. (Colour online) The v-velocity of the probe signal for $V_r = 3$ and (*a*) $Re = 110$ and (*b*) $Re = 120$.

qualitatively but not quantitatively with the results of the linear stability analysis, where the asymmetric base flow results in an unstable stationary global mode at $Re \geqslant 115$. DNS of the three-dimensional configuration with different initial conditions indicates that the second bifurcation is weakly subcritical. In the subcritical case the cycle is initiated by similar flow structures. The observed spanwise modulation growing at the beginning of the cycle (figure 16*a* for $Re = 120$) resembles the leading global mode at the same Reynolds number. This is also true for $Re = 110$. Hence, although the bifurcation is weakly subcritical, we assume that the physical mechanism behind the nonlinear cycle at $Re = 110$ is the same as global instability at $Re > 115$.

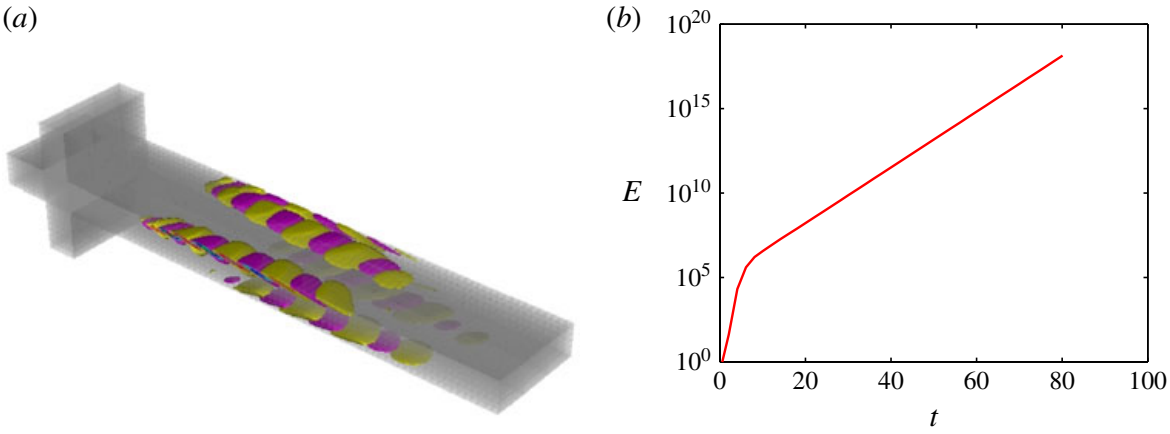

FIGURE 18. (Colour online) (*a*) Spatial structure and (*b*) exponential growth of the energy of the unstable travelling mode about the fictitious flow with $w = 0.85$ at $Re = 120$ and $V_r = 3$.

We further analyse the nonlinear cyclic behaviour of the flow by using the linearized Navier–Stokes solver on a three-dimensional base flow. We create an artificial base flow by adding the unstable spanwise-dependent global mode to the two-dimensional base flow at $Re = 120$. The amplitudes of the unstable mode are chosen to produce a maximum spanwise velocity of the new base flow in the range $0 < w < 1$. Marching the linearized Navier–Stokes solver about this fictitious flow, we observe, for $w \geqslant 0.85$, the appearance of an oscillatory mode that preserves its shape while growing exponentially in time. If the maximum of w is less than 0.85, the non-stationary mode eventually decays – i.e. the flow is stable. We depict the structure of the spanwise velocity component of the oscillatory mode in figure 18(*a*). It emerges at the end of the larger recirculation bubble and disappears downstream at a streamwise location approximately 25. The frequency of the oscillatory mode is approximately 1.25, which is close to the frequency of breakdown in the nonlinear simulation (approximately 1). Figure 18(*b*) presents the energy growth of the oscillatory mode. A significant transient growth of energy is evident for $0 < t < 5$, followed by exponential growth. The presence of this oscillatory unstable mode, which grows exponentially, reduces the spanwise modulation of the flow. Our hypothesis is that, in the nonlinear DNS, this oscillatory mode leads to chaotic flow and nonlinear breakdown to a nearly two-dimensional flow at the end of each cycle. After breakdown, the spanwise modulation caused by the global mode ($\beta = 1$) starts to grow again and a new cycle starts.

5.3. *Sensitivity to wall suction*

The second bifurcation is caused by a three-dimensional stationary global mode around the asymmetric steady state. Here we examine the sensitivity of the second bifurcation to wall suction or blowing.

The sensitivity to wall suction at both walls is shown in figure 19, for asymmetric flow at $Re = 115$. Blowing away from the wall at the streamwise location of the two asymmetric recirculation bubbles is stabilizing, and suction destabilizing, as for the first bifurcation in § 4.2.1. The sensitivity at the second bifurcation is highest at the side of the larger recirculation bubble.

Some general observations about the control of the second bifurcation can be made. First of all, the magnitudes of the sensitivity to the wall suction are nearly twice as

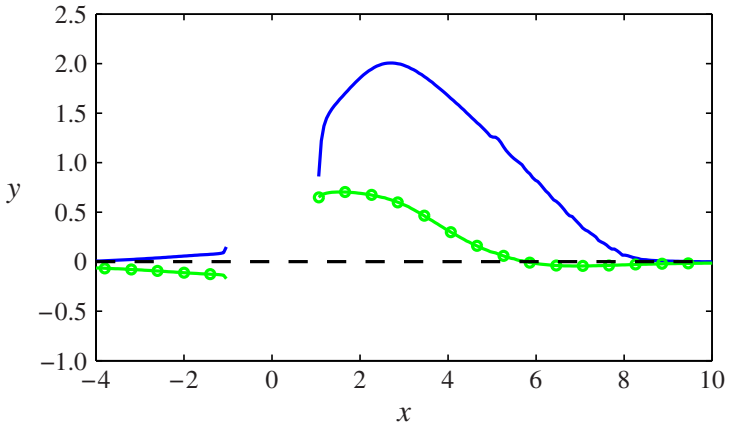

FIGURE 19. (Colour online) Sensitivity of the second bifurcation to wall suction ($Re = 115$), at the adjacent wall of the largest bubble (solid blue line) and at the opposite wall (green line with circles).

large as for the first bifurcation. This means that control of the second bifurcation is likely to be efficient. One should note that, in order to obtain the best control effect, one would need to know at which wall the larger bubble is. Since the pitchfork bifurcation might lead to a larger bubble on either wall, the control needs to be adjustable.

Stabilizing control of the second bifurcation at $Re = 115$ is probably of limited interest because we have shown that the critical Reynolds number for the first bifurcation can be increased as far as $Re = 150$ with control. However, destabilizing control of the second bifurcation could be interesting for inertial micromixers, for which a time-dependent state causes enhanced mixing.

6. Conclusions

In this paper, we have investigated the hydrodynamic instabilities of the flow in an X-junction using three-dimensional DNS, linear global stability and sensitivity analysis.

For all the velocity ratios considered in this study, the X-junction exhibits two bifurcations as the Reynolds number is increased. The destabilization first occurs through a pitchfork bifurcation to a two-dimensional asymmetric steady state at $Re \approx 82.5$ for velocity ratio $V_r = 3$. Global stability analysis around a symmetric flow at $Re > 82.5$ detects the zero-frequency unstable two-dimensional global mode, which is responsible for this first bifurcation. The core of the instability, in terms of both the structural sensitivity and the disturbance energy production, is localized symmetrically at the edges of the two recirculation bubbles. The kinetic energy budget of the perturbation is analysed, and the structure and amplitude of the lift-up term in the energy budget is shown to be almost identical to the total production. This together with the mode shapes, stationary streamwise-elongated modes with strong streamwise velocity, shows that the lift-up mechanism causes the perturbation energy growth. This is similar to the finding of Lanzerstorfer & Kuhlmann (2011) for the backward-facing step, where, at a certain parameter range, the vertical velocity perturbation extracts energy from the base flow shear to produce streamwise-elongated low- and high-speed streaks. The first bifurcation in the X-junction is, however, two-dimensional, as was the original lift-up mechanism identified by Landahl (1975). The presence of two

recirculation bubbles makes it possible to form antisymmetric modes, which induces a cross-stream pressure difference promoting asymmetry, and also minimizes the dissipation by vertical velocity gradients.

We show that the shape of the recirculating region at the critical condition is unaffected by the velocity of the main channel and is determined only by the velocity of the side channels. Therefore, the value of the critical Reynolds number based on the velocity of the side channels is found to be almost constant for the range of velocity ratios studied. Our hypothesis is that the instability appears at a critical size of the recirculation zones (around six channel half-widths for the first bifurcation), which are more affected by the side flows than by the main flow. Also in a previous study, an instability in a junction with different inflow–outflow structure appeared at the same length of the recirculation zone (Poole *et al.* 2014).

An adjustable control strategy for the first bifurcation is proposed in the form of distributed suction or blowing at the walls. This proves to be an efficient means to maintain a symmetric flow. In the sensitivity distribution, the positive values represent suction and the negative values represent blowing. This wall-normal velocity is then applied at both walls symmetrically in actual computations, at different small amplitudes, and the stability recalculated. The optimal stabilizing wall-normal velocity increases the critical Reynolds number for the first bifurcation from $Re = 82.5$ to $Re > 150$, with normalized amplitude of only 3 % in terms of both maximum velocity and flow rate. The main stabilizing effect is due to blowing from the wall, which reduces both the backflow and the velocity gradient responsible for the lift-up mechanism.

The second bifurcation has more intricate dynamics. Linear stability of the steady asymmetric base flow, obtained after nonlinear saturation of the first instability, reveals that a new instability appears at $Re \approx 115$ for $V_r = 3$, again as a zero-frequency global mode. This unstable mode has a spanwise wavenumber $\beta \approx 1$ for all velocity ratios $V_r \geqslant 1$. As for the first bifurcation, the Reynolds number for the second bifurcation is dictated by the side channel velocities only or, physically, the size of the larger recirculation bubble. The structural sensitivity is localized in the middle of the bubble but the maximum perturbation kinetic energy is localized at the edge of the bubble. The lift-up term of the production of the perturbation kinetic energy is dominating and its structure is similar to the total production. This suggests that the second bifurcation is also due to the lift-up instability mechanism similar to the findings of Marquet *et al.* (2009) and Lanzerstorfer & Kuhlmann (2011).

The behaviour at the second bifurcation is clearly defined by means of nonlinear simulations. These three-dimensional simulations show that the flow is steady and two-dimensional, regardless of the initial condition, for $Re \leqslant 105$. However, for $Re \geqslant 110$, we observe a nonlinear cycle: a two-dimensional asymmetric flow, the growth of a spanwise modulation, a time-dependent chaotic flow, travelling wavepacket and return to a nearly two-dimensional asymmetric flow. We use the linearized Navier–Stokes solver to explain the nonlinear breakdown of the flow by a secondary instability: we identify an oscillatory unstable mode that grows exponentially about an artificial base flow, constructed by combining the steady asymmetric base flow with the unstable three-dimensional steady mode, when the amplitude of the spanwise modulation reaches a critical value. The frequency of the oscillatory unstable mode is found to be similar to that of the nonlinear breakdown. The DNS indicates that the second bifurcation is weakly subcritical because it occurs at $Re = 110$, while a three-dimensional global mode destabilizes first at $Re = 115$. However, the structure of the growing spanwise modulation resembles the leading

global mode (at $Re = 110$, it is marginally stable), and we conclude that the same physical mechanism is active for $Re \geqslant 110$. The sketch representing the bifurcations versus the Reynolds number for the flow with velocity ratio $V_r = 3$ is presented in figure 6(*b*).

Finally, we show that the sensitivity to wall suction at the second bifurcation is twice as large as at the first bifurcation – i.e. that this control is efficient. Given that the critical Reynolds number for the first bifurcation can be increased as far as $Re = 150$ by boundary blowing or suction, stabilization of the second bifurcation should be studied at higher Reynolds number. Destabilization of the second bifurcation with control could be useful in order to trigger instabilities that increase mixing in micromixers.

Acknowledgements

We would like especially to thank Hugh Blackburn for providing us with the linear stability solver, DOG. We also thank K. Håkansson, D. Söderberg and F. Lundell for discussions about the flow geometry and Flavio Giannetti for his comments and suggestions. This work was performed on the computational facilities provided by SNIC (Swedish National Infrastructure for Computing), and the Darwin Supercomputer of the University of Cambridge High Performance Computing Service (http://www.hpc.cam.ac.uk/). The financial support for O.T. and M.P.J. from the European Research Council through Project ALORS 2590620 is gratefully acknowledged. Travel support for O.T. was provided by Wallenberg Wood Science Center, Sweden.

REFERENCES

ALBENSOEDER, S., KUHLMANN, H. C. & RATH, H. J. 2001 Three-dimensional centrifugal-flow instabilities in the lid-driven-cavity problem. *Phys. Fluids* **13**, 121–135.

BARKLEY, D., BLACKBURN, H. M. & SHERWIN, S. J. 2008 Direct optimal growth analysis for timesteppers. *Intl J. Numer. Meth. Fluids* **57**, 1435–1458.

BARKLEY, D., GOMES, G. M. & HENDERSON, R. D. 2002 Three-dimensional instability in flow over a backward-facing step. *J. Fluid Mech.* **473**, 167–190.

BEST, J. L. 1987 Flow dynamics at river channel confluences: implications for sediment transport and bed morphology. In *Recent Developments of Fluvial Sedimentology*, pp. 27–35. Society of Economic Paleontologists and Mineralogists.

BEST, J. L. & REID, I. 1984 Separation zone at open-channel junctions. *J. Hydraul. Engng ASCE* **110**, 1588–1594.

BOURQUE, C. & NEWMAN, B. G. 1960 Reattachment of a two-dimensional, incompressible jet to an adjacent flat plate. *Aeronaut. Q.* **11**, 201–232.

BRANDT, L. 2014 The lift-up effect: the linear mechanism behind transition and turbulence in shear flows. *Eur. J. Mech. (*B*/Fluids)* **47**, 80–96.

CHERDRON, W., DURST, F. & WHITELAW, J. H. 1978 Asymmetric flows and instabilities in symmetric ducts with sudden expansion. *J. Fluid Mech.* **84**, 13–31.

CHIANG, T. & SHEU, T. W. H. 2002 Bifurcations of flow through plane symmetric channel contraction. *Trans. ASME: J. Fluids Engng* **124**, 444–451.

CHOMAZ, J. M. 2005 Global instabilities in spatially developing flows: non-normality and nonlinearity. *Annu. Rev. Fluid Mech.* **37**, 357–392.

FANI, A., CAMARRI, S. & SALVETTI, M. V. 2012 Stability analysis and control of the flow in a symmetric channel with a sudden expansion. *Phys. Fluids* **24**, 084102.

FANI, A., CAMARRI, S. & SALVETTI, M. V. 2013 Investigation of the steady engulfment regime in a three-dimensional T-mixer. *Phys. Fluids* **25**, 064102.

FEARN, R. M., MULLIN, T. & CLIFFE, K. A. 1990 Nonlinear flow phenomena in a symmetric sudden expansion. *J. Fluid Mech.* **211**, 595–608.

GALLAIRE, F., MARQUILLIE, M. & EHRENSTEIN, U. 2007 Three-dimensional transverse instabilities in detached boundary layer. *J. Fluid Mech.* **571**, 221–223.

GIANNETTI, F. & LUCHINI, P. 2007 Structural sensitivity of the first instability of the cylinder wake. *J. Fluid Mech.* **581**, 167–197.

HÅKANSSON, K. 2012 Orientation of elongated particles in shear and extensional flow. Licentiate thesis in Engineering Mechanics, Stockholm, Sweden.

HÅKANSSON, K., FALL, A., LUNDELL, F., YU, S., KRYWKA, C., ROTH, S. V., SANTORO, G., KVICK, M., PRAHL-WITTBERG, L., WÅGBERG, L. & SÖDERBERG, L. D. 2014 Hydrodynamic alignment and assembly of nanofibrils resulting in strong cellulose filaments. *Nat. Commun.* **5**, 4018.

HAQUE, S., LASHGARI, I., GIANNETTI, F. & BRANDT, L. 2012 Stability of fluids with shear-dependent viscosity in the lid-driven cavity. *J. Non-Newtonian Fluid Mech.* **173**, 49–61.

HILL, D. C. 1992 A theoretical approach for analyzing the re-stabilization of wake. *AIAA Paper* 92-0067.

JOANICOT, M. & AJDARI, A. 2005 Droplet control for microfluidics. *Science* **309**, 887–888.

KINAHAN, M. E., FILIPPIDI, E., KÖSTER, S., HU, X., EVANS, H. M., PFOHL, T., KAPLAN, D. L. & WONG, J. 2011 Tunable silk: using microfluidics to fabricate silk fibers with controllable properties. *Biomacromolecules* **12**, 1504–1511.

KOCKMANN, N., FOLL, C. & WOIAS, P. 2003 Flow regimes and mass transfer characteristics in static micromixers. *Proc. SPIE* **4982**, 319–329.

LANDAHL, M. T. 1975 Dynamics and control of global instabilities in open flows: a linearized approach. *SIAM J. Appl. Maths* **28**, 735–756.

LANZERSTORFER, D. & KUHLMANN, H. 2011 Global stability of the two-dimensional flow over a backward-facing step. *J. Fluid Mech.* **693**, 1–27.

LANZERSTORFER, D. & KUHLMANN, H. C. 2012 Global stability of multiple solutions in plane sudden-expansion flow. *J. Fluid Mech.* **702**, 378–402.

LUCHINI, P. & BOTTARO, A. 2014 Adjoint equations in stability analysis. *Annu. Rev. Fluid Mech.* **46**, 493–517.

MADAY, Y. & PATERA, A. T. 1989 Spectral element methods for the Navier–Stokes equations. In *State-of-the-Art Surveys in Computational Mechanics* (ed. A. K. Noor), vol. 18, pp. 71–143. ASME.

MARQUET, O., LOMBARDI, M., CHOMAZ, J. M., SIPP, D. & JACQUIN, L. 2009 Direct and adjoint global modes of a recirculation bubble: lift-up and convective non-normalities. *J. Fluid Mech.* **622**, 1–21.

MARQUET, O. & SIPP, D. 2010 Active, steady control of vortex shedding: an adjoint-based sensitivity approach. In *Seventh IUTAM Symposium on Laminar–Turbulent Transition*, IUTAM Bookseries, vol. 18, pp. 259–264. Springer.

MARQUET, O., SIPP, D. & JACQUIN, L. 2008 Sensitivity analysis and passive control of cylinder flow. *J. Fluid Mech.* **615**, 221–252.

MELIGA, P. & CHOMAZ, J. M. 2011 Global modes in a confined impinging jet: application to heat transfer and control. *Theor. Comput. Fluid Dyn.* **25**, 179–193.

MIZUSHIMA, J. & SHIOTANI, Y. 2000 Transitions and instabilities of flow in a symmetric channel with a suddenly expanded and contracted part. *J. Fluid Mech.* **434**, 355–369.

NGUYEN, N. G. & WU, Z. 2005 Micromixers – a review. *J. Micromech. Microengng* **15**, R1.

OLIVEIRA, M. S. N., PINHO, F. T. & ALVES, M. A. 2012 Divergent streamlines and free vortices in Newtonian fluid flows in microfluidic flow-focusing devices. *J. Fluid Mech.* **711**, 171–191.

PASSAGGIA, P. Y., LEWEKE, T. & EHRENSTEIN, U. 2012 Transverse instability and low-frequency flapping in incompressible separated boundary layer flows: an experimental study. *J. Fluid Mech.* **703**, 363–373.

PATERA, A. T. 1984 A spectral element method for fluid dynamics: laminar flow in a channel expansion. *J. Comput. Phys.* **54**, 468–488.

PIRONNEAU, O., HECHT, F. & MORICE, J. 2013 FreeFEM++. Available at: http://www.freefem.org.

POOLE, R. J., ALVES, M. A. & OLIVEIRA, P. J. 2007 Purely elastic flow asymmetries. *Phys. Rev. Lett.* **99**, 164503.

POOLE, R. J., ROCHA, G. N. & OLIVEIRA, P. J. 2014 A symmetry-breaking inertial bifurcation in a cross-slot flow. *Comput. Fluids* **93**, 164503.

PRALITS, J. O., BRANDT, L. & GIANNETTI, F. 2010 Instability and sensitivity of the flow around a rotating circular cylinder. *J. Fluid Mech.* **650**, 513–536.

RODRIGUEZ, D. & THEOFILIS, V. 2010 Structural changes of laminar separation bubbles induced by global linear instability. *J. Fluid Mech.* **655**, 280–305.

SHABAYEK, S., STEFFLER, P. & HICKS, F. 2002 Dynamic model for subcritical combining flows in channel junctions. *J. Hydraul. Engng ASCE* **128**, 821–828.

SHERWIN, S. J. & BLACKBURN, H. M. 2005 Three-dimensional instabilities and transition of steady and pulsatile axisymmetric stenotic flows. *J. Fluid Mech.* **533**, 297–327.

SIPP, D., MARQUET, O., MELIGA, P. & BARBAGALLO, A. 2010 Dynamics and control of global instabilities in open flows: a linearized approach. *Appl. Mech. Rev.* **63**, 030801.

SOBEY, I. J. & DRAZIN, P. G. 1986 Bifurcations of the two-dimensional channel flows. *J. Fluid Mech.* **171**, 263–287.

TOMAS, S., AMEEL, T. & GUILKEY, J. 2010 Mixing kinematics of moderate Reynolds number flows in a T-channel. *Phys. Fluids* **22**, 013601.

TUFO, H. M. & FISCHER, P. F. 1999 Terascale spectral element algorithms and implementations. In *Proceedings of the 1999 ACM/IEEE Conference on Supercomputing*. ACM.

Paper

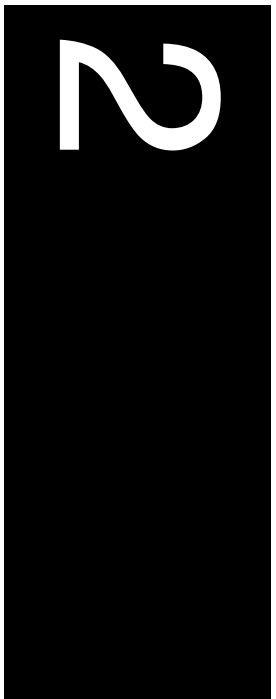

J. Fluid Mech. (2014), *vol.* 755, *pp.* 314–335.
doi:10.1017/jfm.2014.415

Second-order perturbation of global modes and implications for spanwise wavy actuation

O. Tammisola[1,†], F. Giannetti[2], V. Citro[2] and M. P. Juniper[1]

[1]Department of Engineering, University of Cambridge, Trumpington Street, Cambridge CB2 1PZ, UK

[2]DIIN, University of Salerno, via Ponte don Melillo, 84084 Fisciano (SA), Italy

(Received 20 January 2014; revised 24 May 2014; accepted 16 July 2014;
first published online 18 August 2014)

Sensitivity analysis has successfully located the most efficient regions in which to apply passive control in many globally unstable flows. As is shown here and in previous studies, the standard sensitivity analysis, which is linear (first order) with respect to the actuation amplitude, predicts that steady spanwise wavy alternating actuation/modification has no effect on the stability of planar flows, because the eigenvalue change integrates to zero in the spanwise direction. In experiments, however, spanwise wavy modification has been shown to stabilize the flow behind a cylinder quite efficiently. In this paper, we generalize sensitivity analysis by examining the eigenvalue drift (including stabilization/destabilization) up to second order in the perturbation, and show how the second-order eigenvalue changes can be computed numerically by overlapping the adjoint eigenfunction with the first-order global eigenmode correction, shown here for the first time. We confirm the prediction against a direct computation, showing that the eigenvalue drift due to a spanwise wavy base flow modification is of second order. Further analysis reveals that the second-order change in the eigenvalue arises through a resonance of the original (2-D) eigenmode with other unperturbed eigenmodes that have the same spanwise wavelength as the base flow modification. The eigenvalue drift due to each mode interaction is inversely proportional to the distance between the eigenvalues of the modes (which is similar to resonance), but also depends on mutual overlap of direct and adjoint eigenfunctions (which is similar to pseudoresonance). By this argument, and by calculating the most sensitive regions identified by our analysis, we explain why an in-phase actuation/modification is better than an out-of-phase actuation for control of wake flows by spanwise wavy suction and blowing. We also explain why wavelengths several times longer than the wake thickness are more efficient than short wavelengths.

Key words: absolute/convective instability, instability control, wakes/jets

1. Introduction

Control of wake instability by spanwise alternating suction and blowing was studied with direct numerical simulation (DNS) by Kim & Choi (2005). (The alternating

† Email address for correspondence: olot2@cam.ac.uk

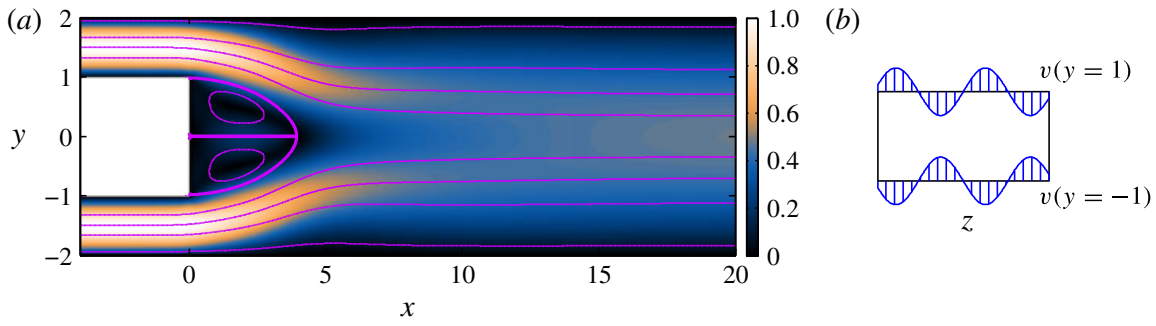

FIGURE 1. (Colour online) (*a*) Base flow: velocity magnitude and streamlines. The boundary of the recirculation bubble is shown by a thick line. (*b*) Illustration of in-phase suction.

suction and blowing will be called 'suction' in the rest of this paper.) Through steady spanwise wavy suction, they shifted the Hopf bifurcation point of the wake behind a cylinder from a Reynolds number of $Re \approx 45$ to $Re = 140$. This degree of stabilization cannot be achieved with any known 2-D open-loop control strategies. Only certain spanwise wavelengths of the actuation were successful in suppressing the instability, however. These wavelengths were approximately 5–6 cylinder diameters. Control at other wavelengths was less effective. The suction was applied from two slots placed on the top and bottom of the cylinder. The configuration in which the suction through the upper slot was in phase with that through the lower slot (figure 1*b*) was found to be much more effective than the antiphase configuration.

In order to explain these effects, Hwang, Kim & Choi (2013) examined the local absolute instability of a fixed streamwise base flow profile (a wake profile), modified sinusoidally in the spanwise direction. The absolute instability was suppressed by spanwise wavy modifications at medium to long wavelengths, while short wavelengths had a strongly destabilizing effect, the latter not observed in the DNS (Kim & Choi 2005). The suppression of absolute instability at medium to long wavelengths was proposed to be based on the interaction of the von Kármán street with vortex tilting.

Very recently, Del Guercio, Cossu & Pujals (2014) examined the effect of streaks in suppressing temporal and absolute instability of wakes. Streamwise streaks were chosen as they are the streamwise uniform perturbations that experience most transient growth around a parallel 2-D wake profile taken as a base flow. The optimal initial condition to create the streaks was shown to be streamwise vortices, as in many shear flows. These optimally amplified streaks were then applied as base flow modifications of the local wake profile, and the temporal and absolute growth rates were recalculated. Del Guercio *et al.* (2014) found that the dependence of the absolute growth rate on the streak amplitudes was quadratic. Furthermore, they suggested that the spanwise wavy modifications are particularly effective as stabilizers because they experience strong transient growth in wake flows. This means that high-amplitude streaks can be created from low-amplitude vortices.

The aim of the present study is to revisit the effect of spanwise wavy steady actuation on stability, using full global analysis of the spatially developing base flow. We explain the findings using a novel generalized sensitivity analysis, which is applicable to spanwise wavy modifications of the base flow and of the linear operator in general. We demonstrate this method on the confined wake behind a flat plate (figure 1). Some of the theoretical results are expected to be directly applicable to the cylinder wake configuration. However, this is not our only aim. The framework

presented and verified here permits analysis of the effect of spanwise wavy flow perturbations in general (such as streaks), inflow asymmetries in axisymmetric geometries, and control by spanwise wavy actuation.

The second-order terms have not been considered in modal stability studies so far (local or global), to the best of the authors' knowledge. A similar perturbation approach was successfully used in a non-modal study quantifying the effect of streamwise travelling waves on the transient energy growth in a channel flow (Lieu, Moarref & Jovanovic 2010; Moarref & Jovanovic 2010).

2. Perturbation analysis

Let us consider a general eigensystem of the form

$$\mathcal{L}\boldsymbol{q}_0 = \sigma_0 \boldsymbol{q}_0, \tag{2.1}$$

where $\boldsymbol{q}_0$ is an eigenvector and σ_0 is an eigenvalue. We will now perturb the governing operator by another operator $\delta\mathcal{L}$, so that the problem remains a linear eigenvalue problem. Following a standard perturbation approach (e.g. Baumgärtel 1984; Hinch 1991), the problem can be expanded in powers of the perturbation amplitude ϵ:

$$\begin{aligned}(\mathcal{L} + \epsilon\delta\mathcal{L})\{\boldsymbol{q}_0 + \epsilon\boldsymbol{q}_1 + \epsilon^2\boldsymbol{q}_2 + O(\epsilon^3)\} \\ = (\sigma_0 + \epsilon\sigma_1 + \epsilon^2\sigma_2 + O(\epsilon^3))\{\boldsymbol{q}_0 + \epsilon\boldsymbol{q}_1 + \epsilon^2\boldsymbol{q}_2 + O(\epsilon^3)\}.\end{aligned} \tag{2.2}$$

Here, σ_j is the jth order correction to the eigenvalue and $\boldsymbol{q}_j$ ($j > 0$) is the ith order correction to the eigenmode. By grouping the terms at the same order in ϵ, and solving this equation, we will obtain these corrections at different orders.

At the zeroth order in ϵ, the original eigenvalue problem is recovered, satisfied by definition. At the first order in ϵ, we obtain, after rearrangement,

$$(\mathcal{L} - \sigma_0\mathcal{I})\,\{\boldsymbol{q}_1\} = -\delta\mathcal{L}\{\boldsymbol{q}_0\} + \sigma_1\boldsymbol{q}_0, \tag{2.3}$$

where $\mathcal{I}$ is the identity operator. To solve (2.3), we will use the *adjoint* eigenmode $\boldsymbol{q}_0^+$, defined based on an inner product $\langle , \rangle$ such that $\langle \boldsymbol{q}_0^+, \boldsymbol{q}_0 \rangle = 1$. The adjoint is found by solving the eigenproblem for the adjoint operator, $\mathcal{L}^+\boldsymbol{q}_0^+ = \sigma_0^*\boldsymbol{q}_0^+$ (see, e.g., Luchini & Bottaro (2014) for details). The left-hand side has no component in the direction of $\boldsymbol{q}_0$, which can be seen by projecting it onto $\boldsymbol{q}_0$ by $\boldsymbol{q}_0^+$:

$$\langle \boldsymbol{q}_0^+, (\mathcal{L} - \sigma_0\mathcal{I})\,\{\boldsymbol{q}_1\}\rangle = \langle \mathcal{L}^+\{\boldsymbol{q}_0^+\}, \boldsymbol{q}_1\rangle - \langle \boldsymbol{q}_0^+, \sigma_0\boldsymbol{q}_1\rangle = \langle \sigma_0^*\boldsymbol{q}_0^+, \boldsymbol{q}_1\rangle - \langle \boldsymbol{q}_0^+, \sigma_0\boldsymbol{q}_1\rangle = 0, \tag{2.4}$$

where * denotes the complex conjugate. Hence, the right-hand side also must be orthogonal to $\boldsymbol{q}_0^+$ (Fredholm alternative), giving $0 = \langle \boldsymbol{q}_0^+, -\delta\mathcal{L}\{\boldsymbol{q}_0\} + \sigma_1\boldsymbol{q}_0\rangle$, which can be rearranged as

$$\sigma_1 = \langle \boldsymbol{q}_0^+, \delta\mathcal{L}\{\boldsymbol{q}_0\}\rangle. \tag{2.5}$$

This first-order eigenvalue drift is a linear function of the operator perturbation, contains the direct and adjoint eigenmodes, and will lead to the standard sensitivity expressions.

At the second order in ϵ, we obtain from (2.2)

$$(\mathcal{L} - \sigma_0\mathcal{I})\,\{\boldsymbol{q}_2\} = -\delta\mathcal{L}\{\boldsymbol{q}_1\} + \sigma_2\boldsymbol{q}_0 + \sigma_1\boldsymbol{q}_1. \tag{2.6}$$

By the same argument as for the first order, both the left and the right sides are orthogonal to $\boldsymbol{q}_0$, giving $\sigma_2 = \langle \boldsymbol{q}_0^+, (\delta\mathcal{L} - \sigma_1\mathcal{I})\{\boldsymbol{q}_1\}\rangle$. This leads to

$$\sigma_2 = \langle \boldsymbol{q}_0^+, \delta\mathcal{L}\{\boldsymbol{q}_1\}\rangle. \tag{2.7}$$

We observe that an arbitrary component of $\boldsymbol{q}_0$ can always be added to $\boldsymbol{q}_1$ (Hinch 1991), and that (2.3) would still remain valid. It should be noted that σ_2 remains unaffected by the choice of this component, since $\langle \boldsymbol{q}_0^+, \delta\mathcal{L}\{C\boldsymbol{q}_0\}\rangle - \sigma_1\langle \boldsymbol{q}_0^+, C\boldsymbol{q}_0\rangle = 0$ for any constant C. The choice of C only corresponds to a normalization of the total perturbed eigenvector. A convenient choice to guarantee uniqueness and remove the singularity of the left-hand side in (2.3) is

$$\langle \boldsymbol{q}_0^+, \boldsymbol{q}_1\rangle = C = 0. \tag{2.8}$$

It should be noted that the second-order eigenvalue drift has exactly the same expression as the first-order drift, but with the eigenmode $\boldsymbol{q}_0$ replaced with the first-order eigenmode correction $\boldsymbol{q}_1$. This means that all the sensitivity expressions derived in the literature can be used straight away to obtain second-order corrections, if $\boldsymbol{q}_0$ is replaced by $\boldsymbol{q}_1$. To do this, one of course needs to solve for $\boldsymbol{q}_1$, which can be performed numerically as described in § 4.

2.1. *Application to base flow modifications*

The theory of second-order perturbations up to now is not limited to a particular set of equations. Hereafter, we will limit our consideration to perturbations around a steady state (base flow) of the Navier–Stokes equations, leading to an operator perturbation $\delta\mathcal{L}(\delta\boldsymbol{U})$. A full derivation of the first-order base flow sensitivity can be found in previous works (e.g. Marquet, Sipp & Jacquin 2008), and just a brief version is included here in order for the paper to be self-contained. The total flow field is governed by the incompressible Navier–Stokes and continuity equations,

$$\frac{\partial \boldsymbol{u}_{tot}}{\partial t} + \boldsymbol{u}_{tot}\cdot\boldsymbol{\nabla}\boldsymbol{u}_{tot} = -\boldsymbol{\nabla}p_{tot} + \frac{1}{Re}\nabla^2\boldsymbol{u}_{tot}, \tag{2.9}$$

$$\boldsymbol{\nabla}\cdot\boldsymbol{u}_{tot} = 0, \tag{2.10}$$

where $\boldsymbol{u}_{tot} = (u_{tot}, v_{tot}, w_{tot})$ is a velocity vector, with non-dimensional streamwise (u_{tot}), vertical (v_{tot}) and spanwise (w_{tot}) components, and p_{tot} is the non-dimensional pressure.

In the following, let us denote by capital letters the planar two-dimensional base flow $\boldsymbol{U}(x, y) = [U(x, y), V(x, y)]$, which is obtained by solving the steady two-dimensional Navier–Stokes equations. Around this base flow we consider linear perturbations, denoted by $\boldsymbol{u} = [u, v, w]$. Around a planar base flow, a decomposition into BiGlobal eigenmodes of the following form applies (Theofilis 2003):

$$\begin{aligned}\boldsymbol{u}_0(x, y, z, t) &= \left[\hat{u}_0(x, y, z), \hat{v}_0(x, y, z), \hat{w}_0(x, y, z)\right]\exp(\sigma_0 t)\\ &= \left[\tilde{u}_0(x, y), \tilde{v}_0(x, y), \tilde{w}_0(x, y)\right]\exp(\mathrm{i}\beta_0 z + \sigma_0 t),\end{aligned} \tag{2.11}$$

$$p_0(x, y, z, t) = \hat{p}_0(x, y, z)\exp(\sigma_0 t) = \tilde{p}_0(x, y)\exp(\mathrm{i}\beta_0 z + \sigma_0 t), \tag{2.12}$$

where $\boldsymbol{u}_0 = (u_0, v_0, w_0)$ is a velocity field of the eigenmode, p_0 is its pressure, β_0 is its spanwise wavenumber and σ_0 is its complex temporal eigenfrequency. It should be stressed for later that throughout this paper the superscript $\hat{}$ refers to the whole spatial

part of the eigenmode including the z-dependence, and $\tilde{}$ is used for the 2-D part. This distinction is important when taking gradients.

By introducing this ansatz into Navier–Stokes equations, and linearizing them, we obtain the BiGlobal generalized eigenvalue problem:

$$\sigma_0 \hat{\boldsymbol{u}}_0 = -\hat{\boldsymbol{u}}_0 \cdot \nabla \boldsymbol{U} - \boldsymbol{U} \cdot \nabla \hat{\boldsymbol{u}}_0 - \nabla \hat{p}_0 + \tfrac{1}{Re} \nabla^2 \hat{\boldsymbol{u}}_0, \tag{2.13}$$

$$\nabla \cdot \hat{\boldsymbol{u}}_0 = 0, \tag{2.14}$$

which we solve with homogeneous Dirichlet boundary conditions for the velocity at all boundaries. The formalism presented for standard eigenvalue problems in the previous section still applies, since it is known that the pressure can be eliminated and hence the generalized eigenvalue problem can be recast into a standard eigenvalue problem. However, the above generalized eigenvalue formulation is convenient to solve numerically.

In what follows, the mode $(\boldsymbol{u}_0, p_0)$ being perturbed will be called the original eigenmode, and its spanwise wavenumber will be denoted by β_0. The spanwise wavenumber of the base flow modification is β_B. The inner product for two velocity vectors $\hat{\boldsymbol{u}}_a$ and $\hat{\boldsymbol{u}}_b$ is here defined as

$$\begin{aligned} \langle \hat{\boldsymbol{u}}_a, \hat{\boldsymbol{u}}_b \rangle &= \lim_{L_Z \to \infty} L_Z^{-1} \int_{-L_Z/2}^{L_Z/2} \int_{D(x,y)} \hat{\boldsymbol{u}}_a^{*\mathrm{T}} \hat{\boldsymbol{u}}_b \, \mathrm{d}x\mathrm{d}y\mathrm{d}z \\ &= \lim_{L_Z \to \infty} L_Z^{-1} \int_{-L_Z/2}^{L_Z/2} \int_{D(x,y)} \left(\hat{u}_a^* \hat{u}_b + \hat{v}_a^* \hat{v}_b + \hat{w}_a^* \hat{w}_b \right) \mathrm{d}x\mathrm{d}y\mathrm{d}z, \end{aligned} \tag{2.15}$$

where $D(x, y)$ is the 2-D flow domain and T denotes the transpose. The adjoint linearized Navier–Stokes operator is defined using the generalized Lagrange identity based on this inner product, with homogeneous boundary conditions for the perturbation, and the adjoint system becomes

$$\sigma_0^+ \hat{\boldsymbol{u}}_0^+ = (\nabla \boldsymbol{U})^{\mathrm{T}} \cdot \hat{\boldsymbol{u}}_0^+ - \boldsymbol{U} \cdot \nabla \hat{\boldsymbol{u}}_0^+ - \nabla \hat{p}_0^+ - \tfrac{1}{Re} \nabla^2 \hat{\boldsymbol{u}}_0^+, \tag{2.16}$$

$$\nabla \cdot \hat{\boldsymbol{u}}_0^+ = 0, \tag{2.17}$$

where it can be shown that $\sigma_0^+ = -\sigma_0^*$, while T denotes a transpose of the nine-component gradient matrix (in tensor notation $[\nabla \boldsymbol{U}^{\mathrm{T}}]_{ij} = \partial U_j / \partial x_i$). The adjoint eigenproblem also has homogeneous Dirichlet boundary conditions.

By imposing a base flow perturbation $\delta \boldsymbol{U}$ onto (2.13) we obtain

$$\sigma_1 = \langle \boldsymbol{q}_0^+, \delta \mathcal{L}(\delta \boldsymbol{U}) \boldsymbol{q}_0 \rangle = \langle \hat{\boldsymbol{u}}_0^+, -\hat{\boldsymbol{u}}_0 \cdot \nabla \delta \boldsymbol{U} - \delta \boldsymbol{U} \cdot \nabla \hat{\boldsymbol{u}}_0 \rangle. \tag{2.18}$$

By integration by parts, and with the homogeneous boundary conditions, the first-order drift is found to be

$$\sigma_1 = \langle \boldsymbol{q}_0^+, \delta \mathcal{L}(\delta \boldsymbol{U}) \boldsymbol{q}_0 \rangle = \langle -\nabla \hat{\boldsymbol{u}}_0^{\mathrm{T}*} \hat{\boldsymbol{u}}_0^+ + \nabla \hat{\boldsymbol{u}}_0^+ \hat{\boldsymbol{u}}_0^*, \delta \boldsymbol{U} \rangle. \tag{2.19}$$

Here, the expression $-\nabla \hat{\boldsymbol{u}}_0^{\mathrm{T}*} \hat{\boldsymbol{u}}_0^+ + \nabla \hat{\boldsymbol{u}}_0^+ \hat{\boldsymbol{u}}_0^*$ is precisely the (first-order) sensitivity to base flow modifications (Marquet *et al.* 2008).

The second-order eigenvalue change with respect to base flow modifications is correspondingly

$$\sigma_2 = \langle \boldsymbol{q}_0^+, \delta \mathcal{L}(\delta \boldsymbol{U}) \boldsymbol{q}_1 \rangle = \langle -\nabla \hat{\boldsymbol{u}}_1^{\mathrm{T}*} \hat{\boldsymbol{u}}_0^+ + \nabla \hat{\boldsymbol{u}}_0^+ \hat{\boldsymbol{u}}_1^*, \delta \boldsymbol{U} \rangle, \tag{2.20}$$

where $\hat{\boldsymbol{u}}_1$ is the first-order correction to the velocity eigenmode, which can be obtained from

$$-\hat{\boldsymbol{u}}_1 \cdot \nabla \boldsymbol{U} - \boldsymbol{U} \cdot \nabla \hat{\boldsymbol{u}}_1 - \nabla \hat{p} + \frac{1}{Re}\nabla^2 \hat{\boldsymbol{u}}_1 - \sigma \hat{\boldsymbol{u}}_1 = \hat{\boldsymbol{u}}_0 \cdot \nabla \delta \boldsymbol{U} + \delta \boldsymbol{U} \cdot \nabla \hat{\boldsymbol{u}}_0, \quad (2.21)$$

$$\nabla \cdot \boldsymbol{u}_1 = 0. \quad (2.22)$$

2.2. *Wavy base flow modifications*

The first-order eigenvalue correction vanishes for spanwise wavy modifications of 2-D base flows, because the first-order eigenvalue correction is linear with respect to the base flow modification, and hence the total contribution from a z-alternating base flow modification integrates to zero in the z direction. To see this, we consider example base flow modifications of the form $\delta \boldsymbol{U} = \delta \tilde{\boldsymbol{U}}(x, y)\cos(\beta_B z) = \delta \tilde{\boldsymbol{U}}(x, y)[\exp(\mathrm{i}\beta_B z) + \exp(-\mathrm{i}\beta_B z)]/2$. Using (2.15) and (2.19) we obtain

$$\sigma_1 = \left(\lim_{L_Z \to \infty} L_Z^{-1} \int_{-L_Z/2}^{L_Z/2} \cos(\beta_B z)\mathrm{d}z\right) \int_{D(x,y)} \left(-\nabla \hat{\boldsymbol{u}}_0^{\mathrm{T}} \hat{\boldsymbol{u}}_0^{+*} + \nabla \hat{\boldsymbol{u}}_0^{+*} \hat{\boldsymbol{u}}_0\right) \cdot \delta \hat{\boldsymbol{U}}(x, y)\mathrm{d}x\mathrm{d}y = 0, \quad (2.23)$$

because the z-integral vanishes.

The second-order correction σ_2 remains finite, however, because the first-order eigenmode correction is of the form $\boldsymbol{u}_1 = \hat{\boldsymbol{u}}_{1+}(x, y)\exp(\mathrm{i}(\beta + \beta_B)z) + \hat{\boldsymbol{u}}_{1-}(x, y)\exp(\mathrm{i}(\beta - \beta_B)z)$. The reason for this form is that (2.21)–(2.22) are linear, and the wavenumber is uniquely set by the eigenmode and base flow modification through the right-hand side terms. After some algebra we obtain (one should note the inclusion of spanwise gradients)

$$\sigma_2 = 1/2 \int_{D(x,y)} \left(-\nabla \hat{\boldsymbol{u}}_1^{\mathrm{T}} \hat{\boldsymbol{u}}_0^{+*} + \nabla \hat{\boldsymbol{u}}_0^{+*} \hat{\boldsymbol{u}}_1\right) \cdot \delta \tilde{\boldsymbol{U}}(x, y)\mathrm{d}x\mathrm{d}y. \quad (2.24)$$

3. Physical conclusions from the perturbation theory

One can conclude from § 2 that the second-order eigenvalue correction is proportional to the first-order eigenmode correction. Hence, qualitatively, base flow modifications that induce a large eigenmode correction will induce a large second-order eigenvalue drift.

The eigenmode correction is given by (2.21)–(2.22). The left-hand side operator is reminiscent of a resolvent operator. As for a resolvent, there are two ways to obtain a large eigenmode correction: (i) The base flow modification is such that $\hat{\boldsymbol{u}}_1$ is close to an eigenmode of the system (which is similar to modal resonance) or (ii) the base flow modification invokes a large non-modal response (which is similar to pseudoresonance). These properties become obvious when expanding $\hat{\boldsymbol{u}}_1$ in the basis of the original eigenmodes following Hinch (1991): $\boldsymbol{u}_1 = \sum_{N \neq 0} \left[\sigma_0 - \sigma_{(N)}\right]^{-1} \langle \hat{\boldsymbol{u}}_{(N)}^{+}, \delta \mathcal{L} \hat{\boldsymbol{u}}_0 \rangle \hat{\boldsymbol{u}}_{(N)} + C\hat{\boldsymbol{u}}_0$, where N represents a mode index in the original eigenmode basis and C is an arbitrary constant. It should be observed that again $\hat{\boldsymbol{u}}_{(N)}$ refers to the spatial part of the Navier–Stokes eigenmode number N, excluding its time-varying part. It is easily verified that this solution satisfies (2.3), and leads to the following second-order eigenvalue correction:

$$\sigma_2 = \sum_{N \neq 0} [\sigma_0 - \sigma_{(N)}]^{-1} \langle \hat{\boldsymbol{u}}_{(N)}^{+}, \delta \mathcal{L} \hat{\boldsymbol{u}}_0 \rangle \langle \hat{\boldsymbol{u}}_0^{+}, \delta \mathcal{L} \hat{\boldsymbol{u}}_{(N)} \rangle. \quad (3.1)$$

Two restrictions need to be mentioned relating to this expansion.

First, the expansion does not provide physical results in the limit $\epsilon[\sigma_0 - \sigma_{(N)}]^{-1} \approx O(1)$, being in fact singular when $\sigma_{(N)} \to \sigma_0$.

The singularity occurs because when $\sigma_{(N)} \to \sigma_0$, then $\langle \hat{\boldsymbol{u}}^+_{(N)}, \delta\mathcal{L}\hat{\boldsymbol{u}}_0\rangle\langle \hat{\boldsymbol{u}}^+_0, \delta\mathcal{L}\hat{\boldsymbol{u}}_{(N)}\rangle \to \langle \hat{\boldsymbol{u}}^+_0, \delta\mathcal{L}\hat{\boldsymbol{u}}_0\rangle^2$, which is finite, whereas $[\sigma_0 - \sigma_{(N)}]^{-1} \to \infty$, and therefore $\sigma_2 \to \infty$. In fact, it can be shown that if higher-order corrections are formed, the sum of all eigenvalue corrections will diverge when $\epsilon[\sigma_0 - \sigma_{(N)}]^{-1} \gtrapprox O(1)$. A similar situation occurs, for example, when predicting orbits in a three-planet system (Kolmogorov 1954), yielding a similar expansion with respect to distance. If the orbits of two planets are too close, the perturbation approach becomes invalid and other approaches such as the Kolmogorov–Arnold–Moser (KAM) theory need to be applied. In our case the restriction has the following meaning: the expansion, as well as the perturbation approach itself, is valid as long as the perturbation amplitude is not too large to satisfy $\epsilon[\sigma_0 - \sigma_{(N)}]^{-1} < O(1)$. If two eigenvalues are very close, the perturbation approach is valid only for small perturbation amplitudes.

In the special case of spanwise wavy base flow modifications, this means that when β_B is very close to zero, the sensitivities become arbitrarily large; however, the expansion itself is valid for smaller and smaller amplitudes, and hence conclusions derived from it are of less practical interest in that regime. The reason for the singularity lies in the structure of the eigenmode spectrum for different β. When β is varied, the most unstable eigenvalue is a smooth continuous function of β. Only eigenmodes with wavelength $\beta = \beta_0 \pm \beta_B$ contribute to the sum (3.1). When $\beta_B \to 0$, then $\sigma \to \sigma_0$ for the most unstable mode with $\beta = \beta_0 \pm \beta_B$. The following can be taken as a practical guideline: when the base flow modification amplitude ϵ has been chosen, the theory can be applied for β_B large enough (spanwise wavelength small enough) so that

$$|\sigma_0 - \sigma_{(N)}(\beta_B)| > \epsilon \quad \forall N. \tag{3.2}$$

For $\epsilon = 0.01$ in § 5.3, this translates to the following lower limit for spanwise wavenumber: $\beta_B > 0.15$, whereas for $\epsilon = 0.1$, the upper limit would be approximately $\beta_B > 0.4$.

Second, the eigenvalue that is perturbed needs to belong to the discrete spectrum for the chosen β_0, and a rigorous treatment of the continuous branches in the above sum would require their decomposition into a finite number of discrete 'leaky modes' (Pralits *et al.* 2007).

Despite the two restrictions, the above expansion gives significant insights into the physics of general second-order perturbations, and wavy perturbations in particular, as detailed in § 5.2. Base flow perturbations invoke at the second order a linear resonance between different eigenmodes, similar to the linear frequency response. The eigenvalue drift induced by another eigenmode depends on how close the eigenvalue is to the one being perturbed (modal resonance), and mutual products between adjoint and direct eigenmodes (non-modal effect/pseudoresonance). The two integrands could be large in two different regions of space, and could be affected by two different physical mechanisms, which creates possibilities for rich dynamics. In other words, a non-local base flow modification is not a simple integral of many local base flow modifications. This property is not a consequence of approximations but an inherent physical property of wavy actuation or modification (due to their second-order nature).

4. Numerical solution

The numerical results discussed in the present paper are carried out using two different codes: the finite-element software FreeFem++ (see http://www.freefem.org) and the spectral-element solver (SEM) Nek5000. Three different problems are

addressed from a numerical point of view: base flow computations (FreeFem++ and Nek5000), eigenmode computations (FreeFem++ and Nek5000) and the computation of the first-order eigenvector correction (FreeFem++).

In FreeFem++, the finite-element method is used to solve the base flow, eigenmode and eigenmode correction equations in § 2. The spatial domain is discretized by a triangular finite-element mesh using a Delaunay–Voronoi algorithm, leading to a mesh with 213 620 triangles and 108 486 vertices. We employ the pair $P2-P1$, consisting of piecewise quadratic velocities and piecewise linear pressure (Taylor–Hood elements), leading to 10^6 degrees of freedom. After derivation of the variational formulation of the governing equations (§ 2), the associated sparse matrices are built by means of the FreeFem++ software.

In FreeFem++, the steady version of (2.9)–(2.10) is solved by the Newton–Raphson iterative procedure to compute the steady base flow for the stability analyses. Second, the direct and adjoint eigenproblems (2.13)–(2.14) and (2.16)–(2.17) are solved using the implicitly restarted Arnoldi method implemented in the ARPACK library (Lehoucq, Sorensen & Yang 1998). Third, the numerical solution of the eigenvector correction $\boldsymbol{q}_1$ is performed, as detailed in a separate section below. All the required matrix inversions are performed using the sparse LU solver UMFPACK (Davis 2004). The iterative procedure is stopped when the L_2 norm of the residual (the latest correction of the Newton iterations) of the governing equations is less than 10^{-7}.

The code chosen for the computation of 3-D (suction-modified) base flows and for the TriGlobal linear stability analysis used for method verification purposes is Nek5000 (Fischer 1997). TriGlobal stability means that the eigenmodes are computed directly from the ansatz $\boldsymbol{u}(x, y, z, t) = \hat{\boldsymbol{u}}(x, y, z)\exp(\sigma t)$, without setting a spanwise wavenumber. For these verification cases, since the aim is to compare stability characteristics, the unmodified 2-D base flow is also computed in Nek5000 and subsequently interpolated into FreeFem++. The spatial discretization for the TriGlobal stability problem (the verification points in figures 3 and 8, and the eigenmode correction verification in figure 6*d–f*) consists of 43 200 spectral elements, with a gradually refined element distribution in the streamwise direction around the downstream edge of the flat plate, and a finer distribution near the walls in the vertical direction. The spanwise direction is discretized by 12 uniformly distributed elements.

Nek5000 is chosen because it allows a highly accurate matrix-free solution of the TriGlobal stability problems in the present work. As for the finite-element method, the incompressible Navier–Stokes equations are cast into a weak form and integrated over the computational domain. A classical Galerkin approximation is used to spatially discretize the governing equations, where each velocity field is related to polynomials two degrees higher than the pressure ($\mathbb{P}_N$–$\mathbb{P}_{N-2}$ formulation). In this work, the polynomial order $p = 5$ was chosen for 3-D computations, and $p = 8$ for the 2-D base flow. The space associated with the velocity is spanned by Nth-order Lagrange interpolants h_i^N, based on a tensor-product grid formed by Gauss–Lobatto–Legendre nodes in each coordinate direction.

The base flows are computed by time stepping the nonlinear Navier–Stokes equations on the same grid as for the stability problem, but using only the upper half of the flow domain. At the centreline, we set a symmetry condition, which eliminates the (antisymmetric) oscillatory modes, and the flow converges towards a steady state. The convergence is considered to be reached when two successive velocity fields, separated by 10 non-dimensional time units, have a maximum absolute difference of 10^{-6}.

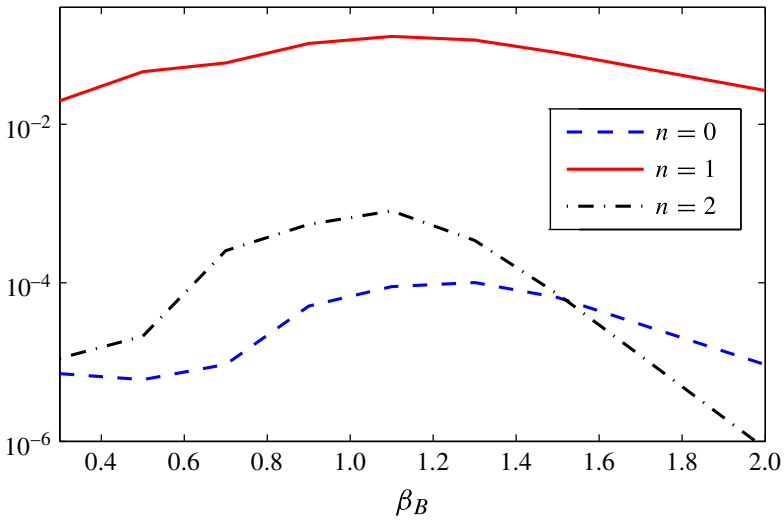

FIGURE 2. (Colour online) The L_2-norm of the first three spatial coefficients $\delta \boldsymbol{U}_n$ of the Fourier transform of the base flow difference $\delta \boldsymbol{U}$, at different suction wavelengths β_B. This shows that the $n = 1$ component ($\propto \exp(\mathrm{i}\beta_B z)$) dominates. The y-scale is logarithmic.

The full three-dimensional eigenpairs of the linearized Navier–Stokes operator are computed (as in Lashgari *et al.* 2014) using the linearized DNS time stepper (available in Nek5000) coupled with the implicit restart Arnoldi method implemented in PARPACK (Maschhoff & Sorensen 1996). Finally, for the 3-D cases, the base flows and base flow modifications (see § 4.1) are extracted from Nek5000 and interpolated into FreeFem++ as follows. To simplify the computational procedure, we assume the base flow modification to be linear with respect to the suction amplitude, and hence have the same wavenumber β_B. If the base flow modification is nonlinear (as it might be for high suction amplitudes), then the base flow modification might contain harmonics at multiples of β_B. Then, a rigorous treatment of these would require extracting the harmonics, and computing eigenvector corrections for each harmonic separately. In figure 2, we have extracted the L_2-norms of the amplitudes of $\exp(\mathrm{i}n\beta_B z)$, $n = 0, 1, 2$, at different β_B. This shows that the components for $n \neq 1$ are smaller by two orders of magnitude compared with $n = 1$, and, hence, it is a good approximation to assume that the base flow difference is of the form $\delta \boldsymbol{U}(x, y) \exp(\mathrm{i}\beta_B z)$. With this assumption, the base flow difference takes the following form:

$$\delta \boldsymbol{U} = \boldsymbol{F}(x, y) \cos(\beta_B z) + \boldsymbol{G}(x, y) \sin(\beta_B z), \tag{4.1}$$

where $\boldsymbol{F} = \delta \boldsymbol{U}(z = 0)$ and $\boldsymbol{G} = \delta \boldsymbol{U}(z = \pi/[2\beta_B])$.

Hence, we interpolate the Nek5000 base flow velocities at $z = 0$ and $z = \pi/(2\beta_B)$ into FreeFem++ and use the above form for the base flow difference. The interpolation proceeds as follows. First, all the $p = 5$ base flows are interpolated in Nek5000 to the Gauss–Lobatto–Legendre points of order $p = 8$ (used for the 2-D base flow). Second, a triangulation is built in FreeFem++ around these points. Third, the base flows are interpolated to the final finite-element grid inside FreeFem++.

4.1. *Second-order perturbation*

Since the solution of the second-order perturbation problem is new, it is worth mentioning the different ways to solve it numerically. There are two ways to obtain

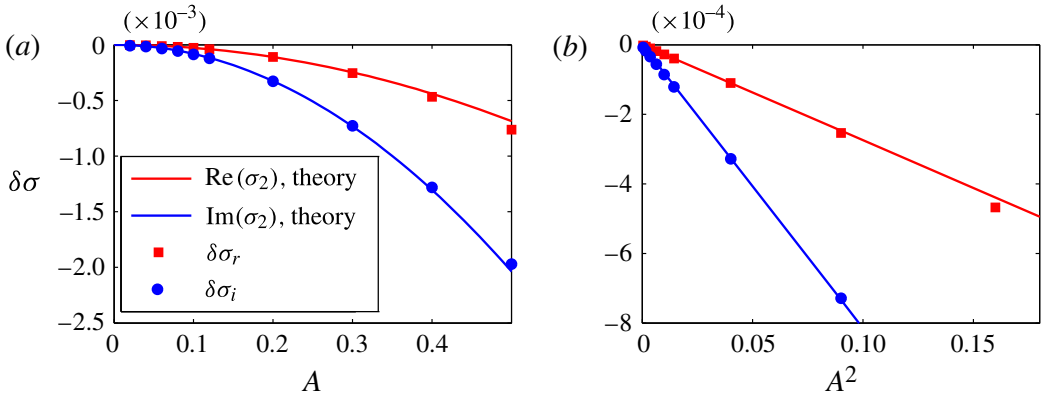

FIGURE 3. (Colour online) (*a*) Markers: the change of the global mode eigenvalue $\delta\sigma = \delta\sigma_r + \mathrm{i}\delta\sigma_i$ as a function of the amplitude A of a given base flow modification (5.1). Solid lines: the predicted eigenvalue perturbation at the second order (σ_2), real and imaginary part. (*b*) The same as (*a*), but as a function of A^2, demonstrating that $\delta\sigma \propto A^2$.

σ_2 for a known operator perturbation (e.g. base flow change). The first is to solve (2.21)–(2.22) directly for $\boldsymbol{u}_1$, and then compute σ_2 from (2.7). The second is to use the eigenmode expansion (3.1) by solving another 2-D global eigenvalue problem, and there is no general rule as to how many modes are needed for the sum to converge.

The choice between the two methods depends on what kind of information is requested. If the exact form of the desired base flow change is known (as in § 5.3, where the base flow change by suction was computed explicitly), then it is clearly preferable to compute the eigenvector correction. If the exact form of the base flow change is unknown, forming the first few terms in the expansion may provide the desired physical insights. In fact, the first term in the sum is a more computationally efficient way to approximate the sensitivity core than traversing a Dirac delta function over the x–y-plane, which will be carried out in § 5.2.

The left-hand side of (2.3) and its specific form (2.21)–(2.22) are singular, as discussed in § 2, which does not affect σ_2 but may place a requirement on the solver. To prevent singularity, we wish to impose the condition $\langle \hat{\boldsymbol{u}}_0^+, \hat{\boldsymbol{u}}_1 \rangle = 0$. This is true whenever $\hat{\boldsymbol{u}}_1$ has a spanwise wavenumber different from β_0. As mentioned in § 2.2, the correct way is to assume that $\boldsymbol{u}_1$ must have the same wavelength as $-\delta\mathcal{L}\{\boldsymbol{u}_0\}$: $\beta_1 = \beta_0 \pm \beta_B$. By replacing $\partial/\partial z$ with $\mathrm{i}\beta_1$ in the equations, we hence automatically impose the above condition, and $(\mathcal{L}(\beta_1) - \sigma_o\mathcal{I})$ becomes non-singular.

The equation system derived from (2.3) becomes

$$\left.\begin{aligned}
&-\hat{\boldsymbol{u}}_{(1,+)}\cdot\nabla\boldsymbol{U} - \boldsymbol{U}\cdot\nabla\hat{\boldsymbol{u}}_{(1,+)} - \nabla\hat{p}_{1,+} + \frac{1}{Re}\nabla^2\hat{\boldsymbol{u}}_{(1,+)} - \sigma\hat{\boldsymbol{u}}_{(1,+)} \\
&\quad = \hat{\boldsymbol{u}}_{(1,+)}\cdot\nabla\delta\boldsymbol{U}_+ + \delta\boldsymbol{U}_+\cdot\nabla\hat{\boldsymbol{u}}_{(1,+)}, \\
&\nabla\cdot\hat{\boldsymbol{u}}_{(1,+)} = 0, \\
&-\hat{\boldsymbol{u}}_{(1,-)}\cdot\nabla\boldsymbol{U} - \boldsymbol{U}\cdot\nabla\hat{\boldsymbol{u}}_{(1,-)} - \nabla\hat{p}_{(1,-)} + \frac{1}{Re}\nabla^2\hat{\boldsymbol{u}}_{(1,-)} - \sigma\hat{\boldsymbol{u}}_{(1,-)} \\
&\quad = \hat{\boldsymbol{u}}_{(1,-)}\cdot\nabla\delta\boldsymbol{U}_- + \delta\boldsymbol{U}_-\cdot\nabla\hat{\boldsymbol{u}}_{(1,-)}, \\
&\nabla\cdot\hat{\boldsymbol{u}}_{(1,-)} = 0,
\end{aligned}\right\} \tag{4.2}$$

where $\partial(\delta\boldsymbol{U}_\pm)/\partial z = \pm\mathrm{i}\beta_B\boldsymbol{U}$, and $\partial\hat{\boldsymbol{u}}_{1,\pm}/\partial z = \mathrm{i}(\beta_0 \pm \beta_B)\boldsymbol{U}$. The base flow change components are found by decomposing the base flow difference as follows:

$$\delta\boldsymbol{U} = \delta\boldsymbol{U}_+ \exp(\mathrm{i}\beta_B z) + \delta\boldsymbol{U}_- \exp(-\mathrm{i}\beta_B z)\,, \tag{4.3}$$

where $\delta \boldsymbol{U}_+$ and $\delta \boldsymbol{U}_-$ are obtained from (4.1) in a complex form. The above system is solved by the same Newton–Raphson algorithm as the base flow, but the algorithm converges at one iteration because the system is linear. Finally, the second-order perturbation of the eigenvalue was extracted by taking the following integral in FreeFem++:

$$\sigma_2 = \langle -\hat{\boldsymbol{u}}_0^+, \hat{\boldsymbol{u}}_{(1,+)} \cdot \nabla \delta \boldsymbol{U}_- + \delta \boldsymbol{U}_- \cdot \nabla \hat{\boldsymbol{u}}_{(1,+)} + \hat{\boldsymbol{u}}_{(1,-)} \cdot \nabla \delta \boldsymbol{U}_+ + \delta \boldsymbol{U}_+ \cdot \nabla \hat{\boldsymbol{u}}_{(1,-)} \rangle. \tag{4.4}$$

5. Results

To demonstrate the second-order perturbation method, we investigate as an example case the wake behind a flat plate with half-thickness h, confined in a channel of height $4h$. The inflow velocity is parabolic on both sides of the plate. The problem is non-dimensionalized with h and maximum inflow velocity U_{in}. The Reynolds number is fixed at $Re = 100$ for all results presented here. The numerical domain extends from $x = -10$ to $x = 60$ in the streamwise direction, and we employ a no-slip condition at the plate and the channel walls.

5.1. *Verification of quadratic behaviour*

First, we need to show that the eigenvalue drift indeed increases quadratically when the amplitude of the base flow modification is increased; that is, the eigenvalue sensitivity is of second order. Second, we want to compare our predicted eigenvalue drifts with the actual eigenvalue drifts when the base flow is modified and the eigenvalues are recomputed.

For the purpose of this test, we have chosen the same artificially modified 1-D base flow profile as Hwang *et al.* (2013), multiplied by a Gaussian in the streamwise direction:

$$\delta U = A \left[\exp(-(x^2 + 1/2(y-1)^2)) + \exp(-(x^2 + 1/2(y+1)^2)) \right] \cos(z). \tag{5.1}$$

This base flow modification results in a coflow at and around the trailing edge of the plate. It should be noted that this test base flow does not satisfy the Navier–Stokes equations, which is necessary for the sake of method validation. It is impossible to introduce base flow modifications that have exactly the same shape but at different amplitudes, so that the total flow satisfies the Navier–Stokes equations. The procedure is comparable with the addition of optimal streaks to the local base flow profile in Del Guercio *et al.* (2014), with the same shape, but at different amplitudes.

The amplitude of the base flow modification is varied from $A = 0.01$ (1 % of the maximum inlet velocity) to $A = 0.5$ (50 % of the maximum inlet velocity). There is no reason to expect a quantitative agreement at the highest amplitudes even from a second-order prediction. The results are shown in figure 3. The computed changes in both the frequency and the growth rate are clearly quadratic with respect to the amplitude. The quantitive agreement between prediction and computation is almost exact for $A < 0.4$, and as expected deviates more for larger amplitudes. Nevertheless, in particular the frequency component agrees very well even for the largest amplitudes.

5.2. *Sensitivity core for spanwise wavy base flow changes*

Next, we show how the theory can be used not only to predict, but also to physically understand, the influence of spanwise wavy perturbations. In the following, we aim to

generalize the concept of the wavemaker or the core of the instability for first-order sensitivities (Giannetti & Luchini 2007; Marquet *et al.* 2008), and compare this region for wavy and non-wavy modifications. To do this, we quantify the regions where localized modifications of the base flow similar to a Dirac delta function produce the largest eigenvalue drift. The analogy for first-order sensitivities should not be pushed too far, however. Considering the eigenvalue drift as a sum over eigenmodes as in (3.1), we see that the eigenvalue drifts for large and non-local changes are not obtained from a single integral over many small changes, but rather from a product of two integrals. For a specific global base flow modification, these two integrals could potentially be large in two different regions. Hence, unlike first-order sensitivity base flow modifications, for the second-order perturbations one cannot conclusively obtain all information about the effect of non-local base flow changes from a spatial map obtained for the Dirac delta function.

However, by applying the Dirac delta function we can identify regions where the local flow response for control with each spanwise wavelength is maximum, and hence which are always likely to provide a large contribution. To identify such regions in the flow, to be called 'the sensitivity core', we consider the following highly localized base flow modification:

$$\begin{aligned} \delta U &= B\cos(\beta_B z)\big[\exp(-500((x-x_0)^2+(y-y_0)^2)) \\ &\quad + \exp(-500((x-x_0)^2+(y+y_0)^2))\big], \qquad (5.2) \\ \delta V &= \delta W = 0. \qquad (5.3) \end{aligned}$$

The base flow change is then normalized to a unit area in the x–y-plane by setting the amplitude as

$$B = \left[\int \delta\tilde{U}(x, y)\mathrm{d}x\mathrm{d}y\right]^{-1}. \qquad (5.4)$$

This procedure approximates the effect of a Dirac delta function, but avoids discontinuities which could potentially cause numerical problems.

This base flow modification is traversed over the x–y-plane, and the eigenvalue drift is computed for each (x_0, y_0) pair. Only the streamwise velocity is shown here, but we tried a Gaussian modification of the vertical and spanwise velocities in a few positions too, and these tests indicated that the most efficient regions were similar. The resulting sensitivity core is shown in figure 4. Panel (a) shows the standard 2-D sensitivity, (b) shows the sensitivity core for $\beta_B = 1$ and (c) shows $\beta_B = 30$. This leads to two interesting observations. First, the longer spanwise wavelength ($\beta_B = 1$) causes a larger eigenvalue change than the 2-D modification by a factor of 60 (see the colourbars) and a larger eigenvalue change than the short spanwise wavelength ($\beta_B = 30$) by a factor of two. Second, all three sensitivities are localized along the recirculation bubble and have their maximum at $x \approx 3$–3.5.

A physical explanation for both phenomena – the efficiency of long wavelengths and the similar positions of maximum sensitivity for wavy and non-wavy modifications – is found from the eigenmode expansion (3.1). For spanwise wavy perturbations of wavenumber β_B around a 2-D flow, the base flow sensitivity arises through the mode interactions in the sum (3.1). These only involve modes with $\beta = \pm\beta_B$. No other modes contribute. For a wake behind a flat plate, the most unstable eigenvalue varies continuously as β varies. The eigenvalue spectra at two different values of β are shown in figure 5, together with the 2-D ($\beta = 0$) eigenvalue σ_0 that is being perturbed. At small β (long wavelengths), such as $\beta = 0.3$ ($\lambda = 21$) in figure 5, the leading

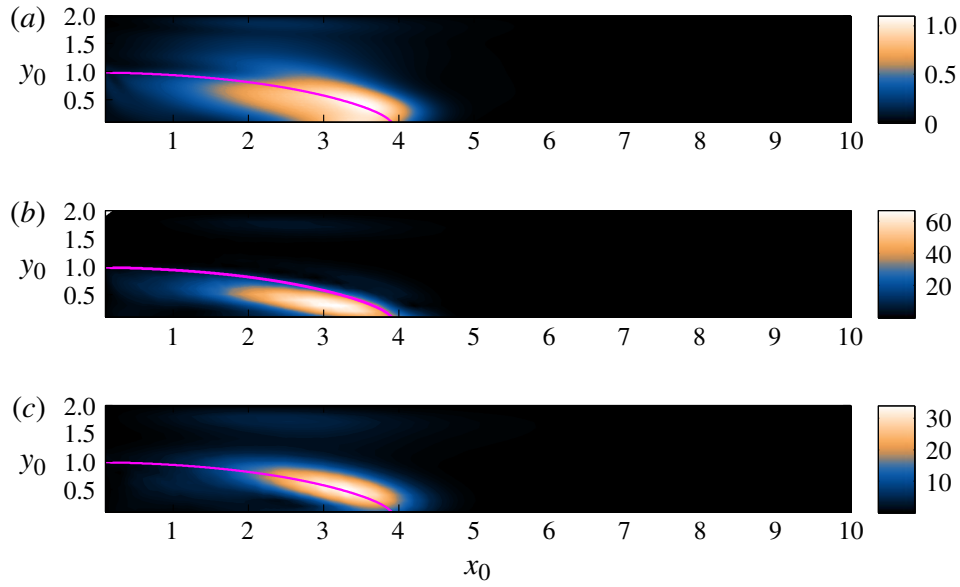

FIGURE 4. (Colour online) The sensitivity core for spanwise wavy base flow modifications estimated by a spatial mapping of the eigenvalue drifts induced by localized modifications approximating a Dirac delta function: (*a*) $\beta_B = 0$ (2-D), (*b*) $\beta_B = 1$, (*c*) $\beta_B = 30$. The eigenvalue drift is large inside the light-coloured region. This demonstrates that when the same base flow modification is applied at different spanwise wavelengths, long wavelengths are more efficient than short ones (see the colourbars) and much more efficient than 2-D suction, while the sensitivity cores have similar shapes to those in 2-D. The boundary of the recirculation zone is depicted by the solid line (magenta online).

eigenvalue is very close to the 2-D eigenvalue ($\beta = 0$), while the other eigenmodes are comparatively far away. Therefore, at small wavenumbers, the interaction between the most unstable mode at $\beta = \pm\beta_B$ and the original mode at $\beta = 0$ provides a large contribution. Qualitatively, the smaller the wavenumber is, the larger the effect on the eigenvalue is (keeping the restrictions of § 3 in mind). Furthermore, the most unstable mode does not change its spatial shape much between $\beta = 0$ and small non-zero β. This means that the sensitivity core remains similar for any small spanwise wavenumber. At slightly larger wavenumbers (such as $\beta_B = 1$ or $\lambda = 6.2$ in figure 5), corresponding to shorter wavelengths, the leading modes are further apart, which means that the effect on σ_0 from the mode interactions is smaller. In this case, other eigenmodes also contribute to the sum, and therefore to the spatial sensitivity distribution, in a similar proportion to the leading mode. However, the wake or shear layer modes that contribute most to the sum have similar frequencies to the wake mode, and these are not essentially different in their spatial distribution, which still gives rise to similar sensitivity regions, but at slightly lower amplitudes.

5.3. *Control effect of steady spanwise wavy suction*

Finally, we apply the theory to study and explain the effect of actual base flow modifications induced by suction on a wake behind a flat plate. A sinusoidal steady wall-normal suction is applied from a slot located near the trailing edge $-0.2 < x < -0.01$, similarly to Kim & Choi (2005): $\boldsymbol{U}_{wall} = (0, 0.01\cos(\beta_B z), 0)$. The suction distributions on the upper and lower surfaces of the plate are in phase with each other (see figure 1*b* for illustration).

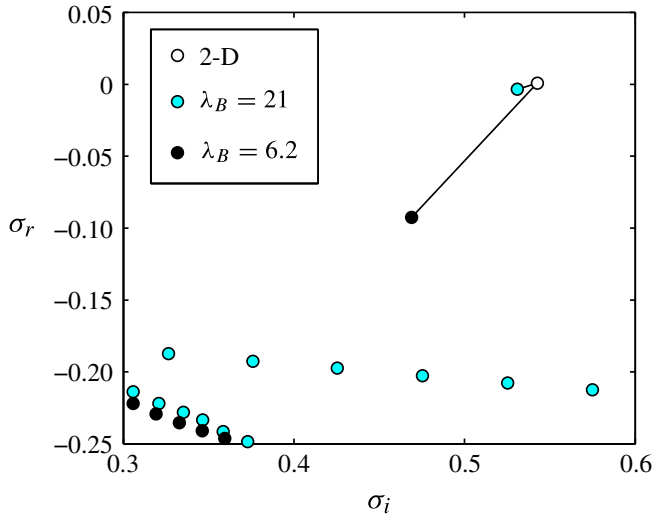

FIGURE 5. (Colour online) Unperturbed eigenvalue spectra for two different spanwise wavelengths ($\lambda_B = 21$ which gives $\beta_B = 0.3$, and $\lambda_B = 6.2$ which gives $\beta_B = 1$), shown together with the unstable 2-D eigenvalue ($\beta = 0$). The solid lines are added to illustrate the distances between the most unstable eigenvalue and the 2-D eigenvalue (white circle). The mode resonance effect (§ 3) is inversely proportional to the distance between eigenvalues.

The choice of an in-phase suction distribution (rather than out-of-phase) is worth mentioning, since this choice turns out to be well grounded in the present theory. In earlier works (Kim & Choi 2005; Hwang *et al.* 2013), in-phase distribution was observed to be much more efficient in stabilizing the flow than out-of-phase distribution, but this effect was not explained. The σ_2 derived in the present work (3.1) contains an integral product of the mode, its adjoint and the base flow change over y. In order for this integral not to vanish, in-phase perturbations may only invoke a resonance of the original mode with sinuous modes, while antiphase perturbations invoke a resonance with varicose modes. The global eigenvalues for varicose modes in wakes are very damped, so the distance between the original eigenvalue and varicose eigenvalues is long. On the other hand, the eigenvalue distance between the original mode and the leading sinuous mode is short, if the spanwise wavelength for suction $\lambda_B = 2\pi/\beta_B$ is long, by the arguments in the previous section. Therefore, the theory shows that long-wavelength in-phase base flow modifications induce the largest eigenvalue drift through the resonance of the original mode with the leading spanwise wavy sinuous mode with wavenumber $\pm\beta_B$.

This in-phase suction is implemented as a boundary condition in the base flow computations for 12 different wavenumbers: β_B = (0(2-D), 0.3, 0.5, 0.7, 0.9, 1.1, 1.3, 1.5, 1.7, 1.9, 2, 30). The difference between the base flows with and without suction is then extracted, as described in § 4. From this point, we proceed in two ways: (i) by computing the eigenvalue change σ_2 based on our theory and (ii) by recomputing the stability around the 3-D modified base flow, to get a reference result. For the computation of σ_2, $\delta\hat{\boldsymbol{U}}(x, y)$ is extracted from the 3-D base flow as described in § 4. The 2-D non-wavy base flow modification is normalized to have the same L_2-norm as the spanwise wavy ones, to ensure a similar suction effort.

The first-order eigenvector correction $\hat{\boldsymbol{u}}_1$ is computed in the process, and this quantity is shown for the first time for linear global modes in figure 6(*a–c*). Both the real and the imaginary parts are computed, and $\hat{\boldsymbol{u}}_1$ is observed to have the following

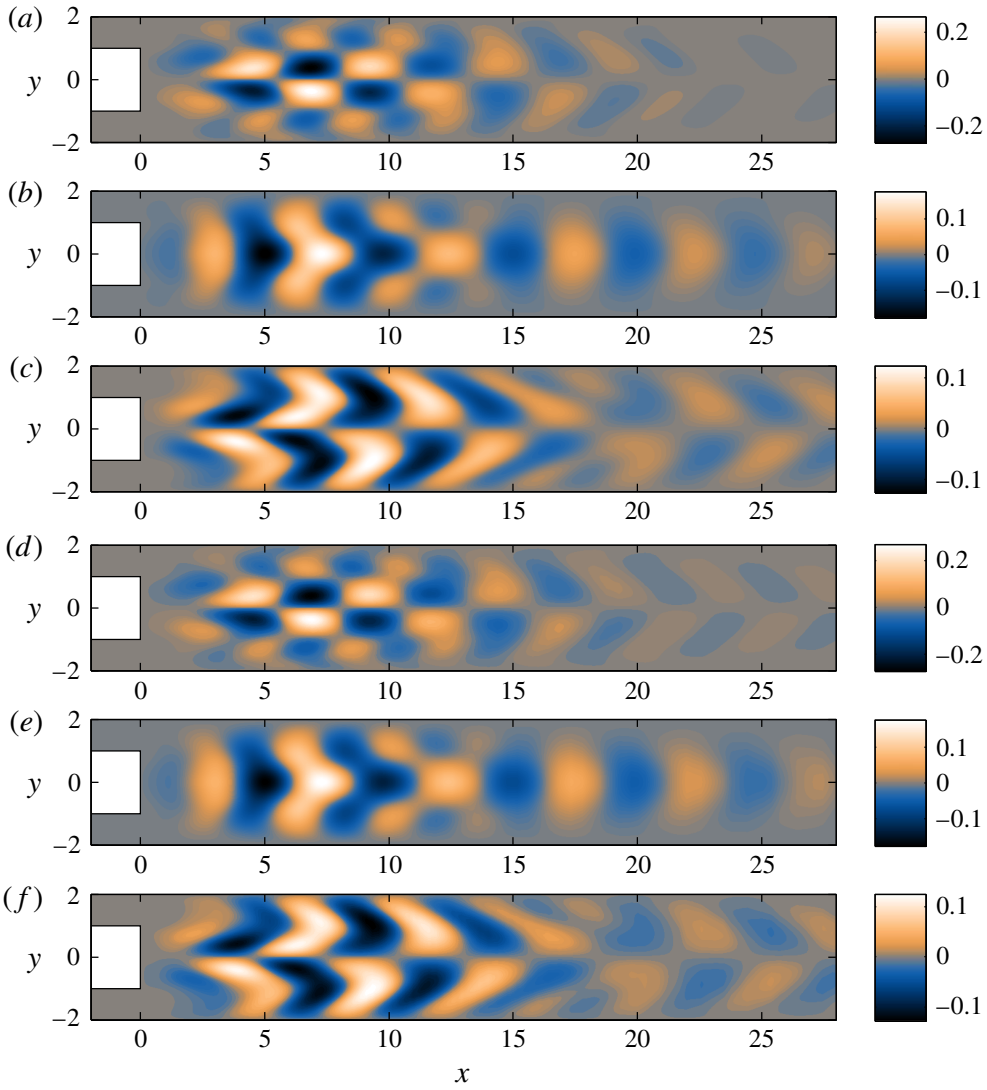

FIGURE 6. (Colour online) (*a–c*) The first-order eigenfunction correction computed from (2.3) with suction wavelength $\beta_B = 1.1$, $\hat{\boldsymbol{u}}_1 = [\tilde{u}_1(x, y)\cos(\beta_B z),\ \tilde{v}_1(x, y)\cos(\beta_B z),\ \tilde{w}_1(x, y)\sin(\beta_B z)]$: (*a*) $\tilde{u}_1$, real part; (*b*) $\tilde{v}_1$, real part; (*c*) $\tilde{w}_1$, real part. (*d–f*) The same as (*a–c*), but where a true eigenfunction correction is extracted from a computed 3-D eigenfunction with suction $\boldsymbol{u}_s$ by subtracting the component in the direction of the unperturbed eigenfunction. Both correction fields are normalized to a unit L_2-norm.

form: $\boldsymbol{u}_1 = \tilde{\boldsymbol{u}}_1(x, y)\cos(\beta_B z)$, $\boldsymbol{v}_1 = \tilde{\boldsymbol{u}}_1(x, y)\cos(\beta_B z)$, $\boldsymbol{w}_1 = \tilde{\boldsymbol{w}}_1(x, y)\sin(\beta_B z)$, following the same symmetry in z as the suction, and the induced base flow modification. The different velocity components are shown in figure 6(*a–c*), for $\beta_B = 1.1$, and these are reminiscent of eigenfunctions of confined wakes, as expected. To further validate our method of computing the eigenvector correction, a true eigenmode correction extracted from a computed 3-D eigenmode is shown in figure 6(*d–f*). The latter result was obtained from a 3-D eigenmode with suction, $\boldsymbol{u}_s$, by subtracting the component in the direction of the original eigenmode: $\boldsymbol{u}_s - \langle \boldsymbol{u}_0^+, \boldsymbol{u}_s \rangle$. The result is nearly indistuingishable from the one computed from our theory. Both corrections are normalized to a unit L_2-norm.

The norm of $\boldsymbol{u}_1$ which will be obtained in an actual computation of an experiment is arbitrary. The reason is worth discussing in some depth. The norm of $\boldsymbol{u}_1$ is uniquely determined by the norm of the unperturbed (original) eigenvector $\boldsymbol{u}_0$. Conversely, when

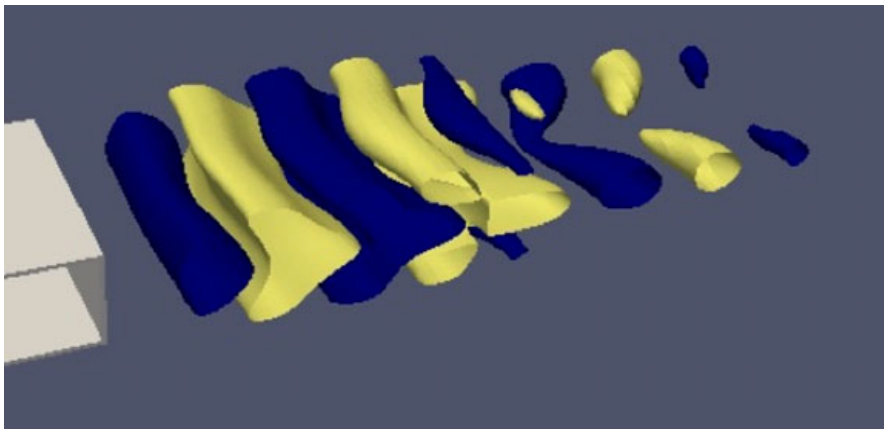

FIGURE 7. (Colour online) The computed triglobal eigenmode with suction, $A = 0.01$ and $\beta_B = 1.1$; positive (dark, blue online) and negative (light, yellow online) contours of the vertical disturbance velocity $\hat{v}_0(x, y, z)$. The edge of the flat plate, extending from $y = -1$ to $y = 1$, is also shown in pale grey.

$\boldsymbol{u}_1$ is known, so that $\langle \boldsymbol{u}_0^+, \boldsymbol{u}_1 \rangle = 0$, then $\boldsymbol{u}_0$ can be determined uniquely by inverting (2.3). However, as mentioned in § 2, an arbitrary component $C\boldsymbol{u}_0$ can always be added to $\boldsymbol{u}_1$ to obtain (non-unique) solutions to (2.3). The actual eigenmode returned from a 3-D computation or an experiment may therefore have any value of C. The value of C can be found from $\boldsymbol{u}_1$, by inverting (2.3), if desired. Importantly, the eigenvalue correction σ_2 remains independent of C, as shown in § 2.

The eigenmode correction has its largest amplitude at $x \approx 5$. However, the relative amplitude of the correction and the original eigenmode determine the final shape, and this depends on the (arbitrary) value of C. Hence, the eigenmode correction observed in computation or experiments might be either small or large, while the observed eigenvalue correction is unique. Figure 7 shows a computed TriGlobal eigenmode with suction. In the shape of the eigenmode, the spanwise variation only shows further downstream (around $x = 8$), where the amplitude of the original 2-D eigenmode is small.

When it comes to changing the eigenvalue, however, neither the shape of the correction nor the original eigenmode can indicate which region in the flow has most influence on the eigenvalue change. To know this, we need to overlap the eigenmode correction with the adjoint original eigenmode and the base flow change induced by suction, as explained in § 2, and as demonstrated later in this section.

Now we turn to the comparison between predicted and computed second-order eigenvalue changes, and the efficiency of different suction wavelengths β_B in influencing the stability of the wake flow. The predicted and computed second-order eigenvalue changes for all but the shortest wavelength are shown in figure 8, demonstrating good qualitative agreement and the same value of the most stabilizing wavelength. The shortest wavelength that we tested, $\beta_B = 30$ ($\lambda_B = 0.2$), is far outside the figure and caused an unobservable change in the eigenvalue for both methods. There are quantitative differences between the computed and the predicted results which were hard to avoid, since they are computed with two different numerical tools, and the base flow difference had to be interpolated from one grid to another. The absolute difference between prediction and computation is small, less than 10^{-3}, and therefore easily influenced by numerics. The eigenvalue difference increases quadratically with suction amplitude, and the growth rate decrease is predicted

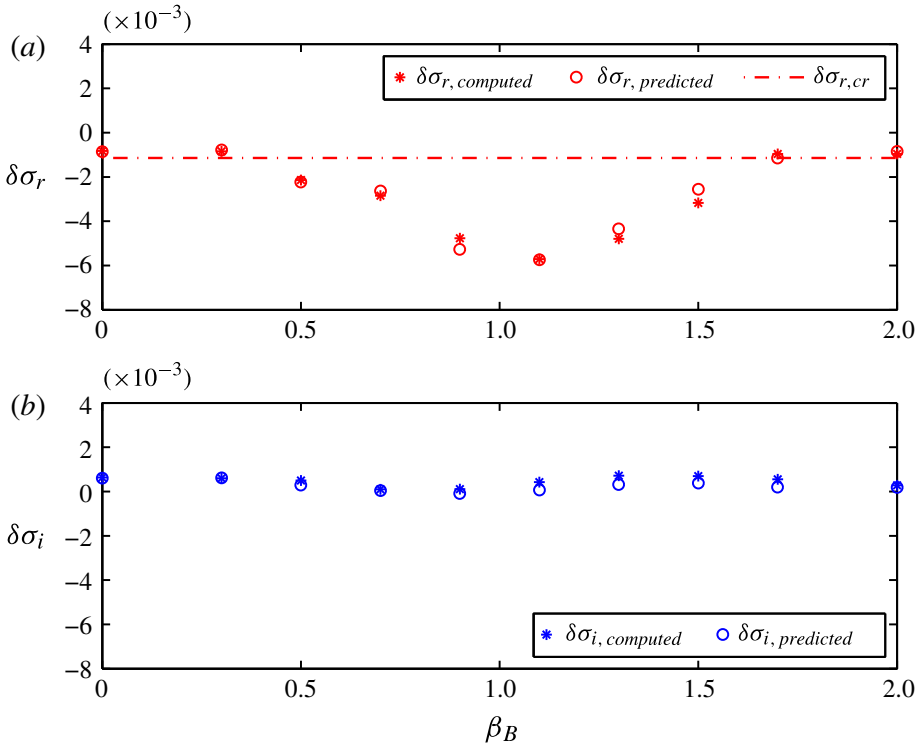

FIGURE 8. (Colour online) The eigenvalue drift for different suction wavenumbers, β_B, for a wake with steady suction where the base flow satisfies the Navier–Stokes equation. Computed and predicted eigenvalue change (see legends): (*a*) change in the real part; (*b*) change in the imaginary part. The value where the growth rate of the suction-modified eigenvalue is zero (neutral stability point) is marked with a dot–dash line in (*a*).

to be $\delta\sigma_r = -0.024$ for only 2 % suction amplitude ($A = 0.02$), and $\delta\sigma_r = -0.15$ for 5 % suction amplitude ($A = 0.05$). We expect the difference between the two numerical tools to be an absolute difference due to the finite accuracy of solution and interpolation, and hence we expect that the relative difference between prediction and computation will be smaller for even slightly larger suction amplitudes.

The growth rate of the eigenvalue decreases slightly for all cases with suction, in both the prediction and the computation. The eigenvalue is stabilized for a wide range of β_B, approximately $0.4 < \beta_B < 1.6$. The maximal stabilization is reached at $\beta_B = 1.1$. This corresponds to a wavelength of approximately 6. The observed optimal wavelengths for a cylinder flow are longer: Kim & Choi (2005) obtained 10–12 in our non-dimensional coordinates, and Hwang *et al.* (2013) 12 in our coordinates. The physical reason for the difference between optimal wavelengths in these two configurations could be the confinement. In previous works (Juniper, Tammisola & Lundell 2011; Tammisola *et al.* 2011), confinement was shown to alter the base flow as well as the structure of the eigenmode at similar Reynolds numbers. Figure 6 indeed seems to show that the eigenmode correction extends all the way to the surrounding walls, as well as the base flow modification induced by suction (figure 9*a–c*), so they might be affected by confinement. However, the principles behind the wavelength selection that we present next are general, and not tied to the specific wake flow in question. First of all, figure 8 shows that the stabilizing influence only occurs for relatively long suction wavelengths, and short wavelengths ($\beta_B > 1.7$) have no effect on the eigenvalue. This is consistent with the results in § 5.2, where a fixed base flow modification $\delta\boldsymbol{U}(x, y)$ was applied with

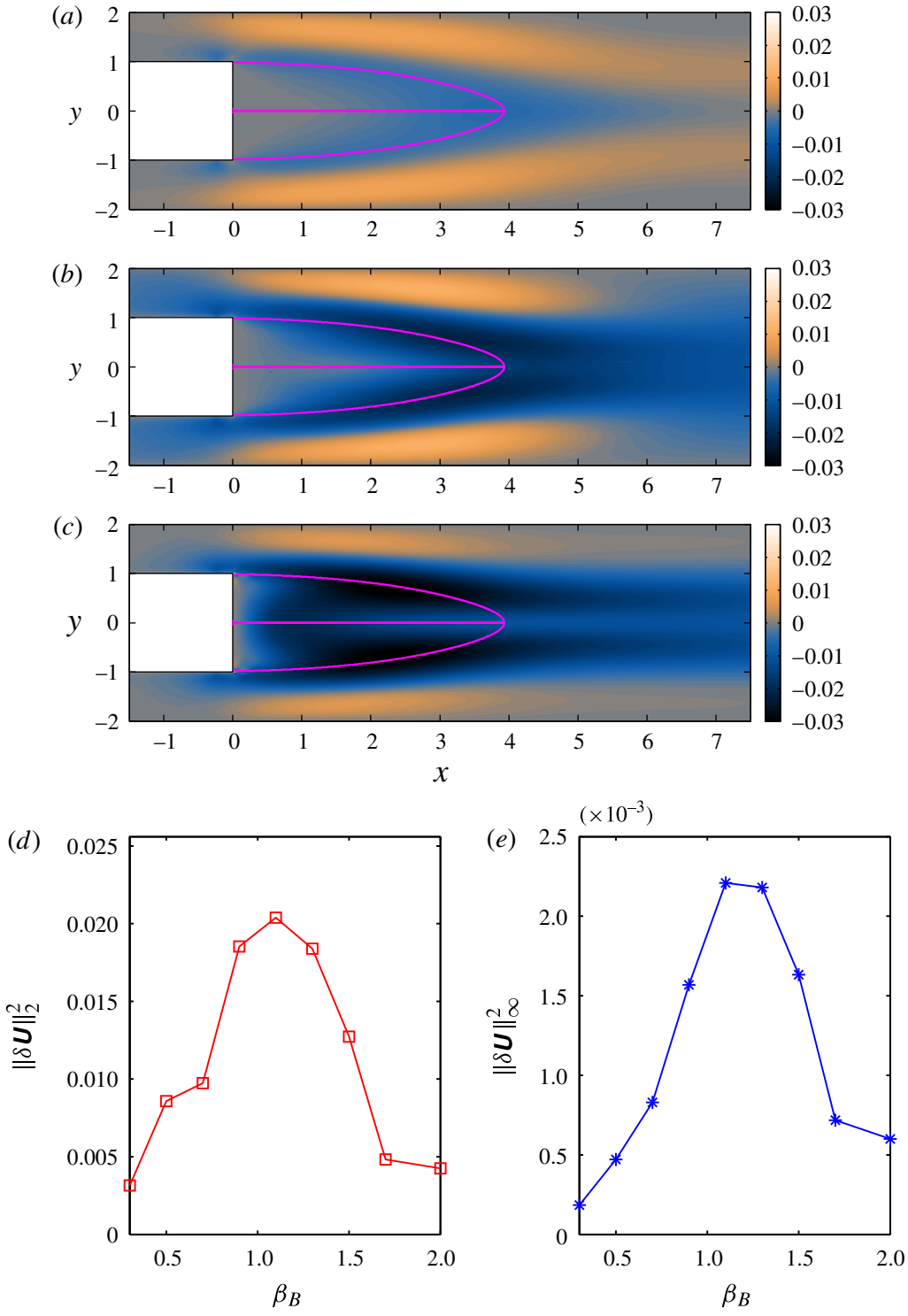

FIGURE 9. (Colour online) The difference between the base flows with and without suction: (*a*) streamwise velocity difference at $\beta_B = 0$ (2-D); (*b*) streamwise velocity difference at $\beta_B = 0.5$ at $z = \pi/(2\beta_B)$; (*c*) streamwise velocity difference at $\beta_B = 2$, $z = \pi/(2\beta_B)$; (*d*) L_2-norm squared as a function of β_B; (*e*) L_∞-norm squared as a function of β_B.

different β_B, and the effect on the eigenvalue decreased with increasing β_B. This also supports the argument presented in § 3 that second-order eigenvalue change can occur due to a resonance between unperturbed eigenmodes at $\beta = 0$ and β_B, when their eigenvalues are close to each other (for illustration see figure 5). The inverse of

the difference between the most unstable eigenvalues at $\beta = 0$ and β_B is depicted in figure 10(*f*), and explains the general trend that long wavelengths are efficient while short wavelengths are not. However, this argument does not explain why the longest wavelength studied here ($\beta_B = 0.3$) is not stabilizing, and why some slightly shorter wavelengths are performing better. To understand the latter, we consider the structure of the base flow modifications induced by suction.

An important effect was pointed out by Del Guercio *et al.* (2014): the amplitude of the actual base flow change induced by suction is a function of β_B. In figure 9(*a–c*), the streamwise velocity difference between suction and no-suction base flows is shown for $\beta_B = 0$ (*a*), $\beta_B = 0.5$ (*b*) and $\beta_B = 2$ (*c*). Two things can be immediately observed. First, spanwise wavy suction (*b–c*) is clearly more efficient in modifying the base flow than a spanwise invariant suction (*a*). Second, the maximal modification is larger for $\beta_B = 2$ than for $\beta_B = 0.5$. To quantify how efficiently the base flow is modified by suction as a function of β_B, the square of the L_2-norm and the square of the L_∞-norm (maximum norm) of the base flow change are shown for different β_B in figure 9 (the reason for taking the square is that we expect the eigenvalue drift to be proportional to the square of the base flow change). We can see that both base flow changes are maximal at $\beta_B = 1.1$. In particular, the square of the L_2-norm of the base flow change seems to be qualitatively proportional to the growth rate change in figure 8, confirming that this effect plays an important role in selecting the optimal stabilizing wavelength.

It would now be tempting to conclude that the L_2-norm of the base flow change induced by suction, integrated over the whole domain, determines the stability. The region where eigenvalue changes actually occur (where the base flow modification interacts with the eigenmode correction and the adjoint eigenmode) can be shown by plotting the integrand of σ_2, (2.7) or (4.4). In figure 10(*a–d*), this quantity is shown for different β_B. The eigenvalue is only affected by the base flow changes inside the narrow dark region (blue online) in these figures, which follows the edge of the recirculation bubble. For all four suction wavelengths, the base flow changes are seen to influence the flow along the outer edge of the recirculation zone for the 2-D base flow (shown in solid line, magenta online). This effectively coincides with the sensitivity cores shown in § 5.2. The maximum negative value of the integrands (the location in space that contributes to the most stabilizing effect) is in the same location ($x \approx 3.0$, $y \approx 0.6$) for all four wavelengths. In figure 10, we show how the base flow change at the location of maximum sensitivity develops with β_B. This shows the expected trend, with the strongest base flow modification at $\beta_B = 1.1$.

Our conclusion is that two factors combine to determine the optimal wavelength for stabilization of this flow. (i) The eigenmode resonance occurs at long wavelengths. (ii) Medium wavelengths induce largest base flow change inside the sensitivity core region. These competing factors are shown in figure 10(*e*,*f*). Regarding how the base flow change due to suction is created, the reader is referred to the recent paper of Del Guercio *et al.* (2014), where the influence on the cylinder wake base flow is explained to be due to amplification of streaks through the lift-up effect. We expect the same mechanism to be present in this flow, while the base flow changes are slightly modified by confinement.

Finally, it is worth pointing out that the effects described here are based on a global stability analysis, in which the most sensitive region to spanwise wavy perturbations ('sensitivity core') has been identified in the (x, y)-plane, and its location has been related to where the base flow modifications by suction are acting. This was carried out by mapping the effect of a localized base flow modification in the form of a Dirac delta function. Next, by computing the actual base flow modification induced

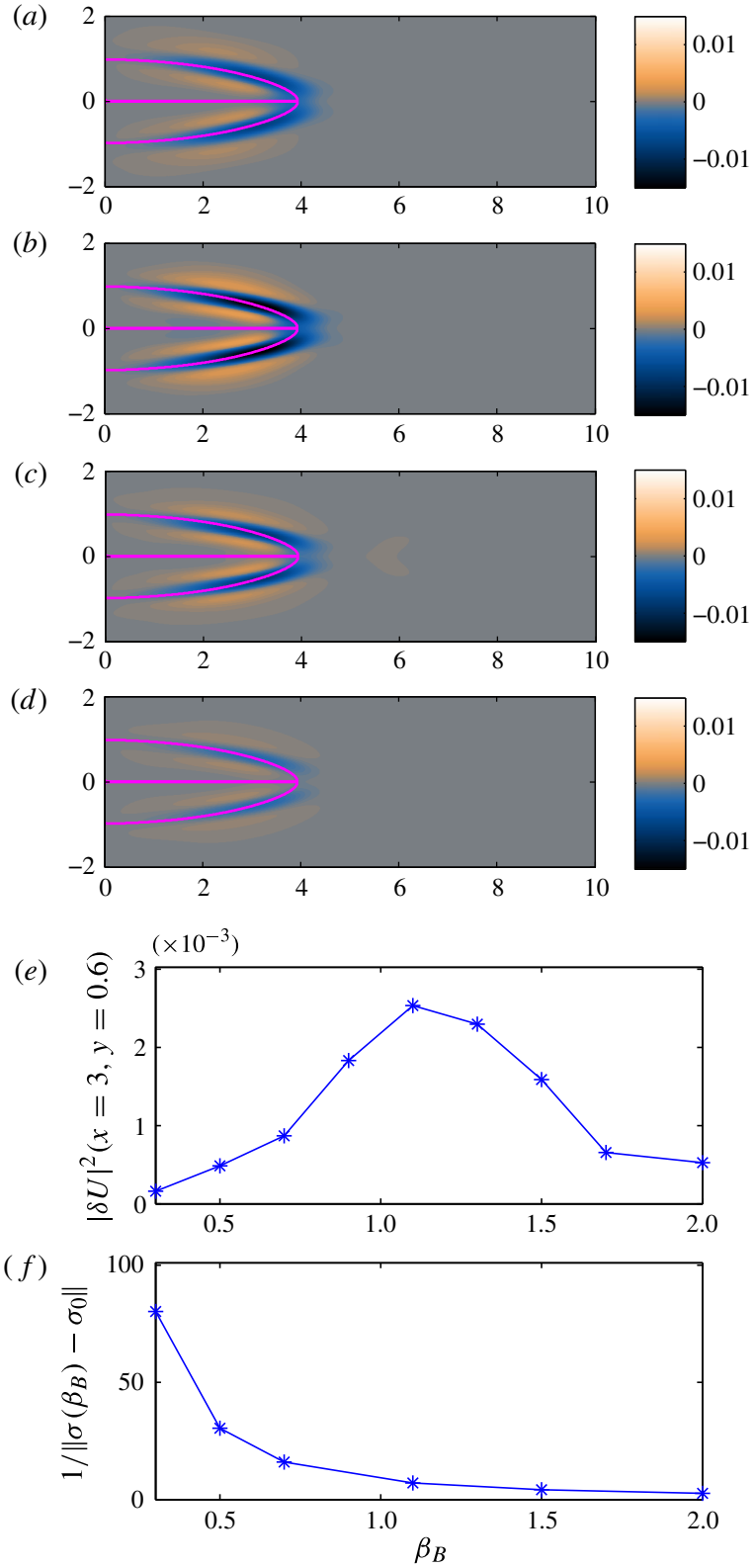

FIGURE 10. (Colour online) (*a*)–(*d*) Integrand of the eigenvalue growth rate change (2.7). Suction wavelengths: (*a*) $\beta_B = 0.7$, (*b*) $\beta_B = 1.1$, (*c*) $\beta_B = 1.5$, (*d*) $\beta_B = 1.7$. A dark colour indicates a stabilizing contribution. The boundary of the recirculation zone of the 2-D base flow is shown by the solid line (magenta online). (*e*) The amplitude of base flow modification at $x = 3.0$, $y = 0.6$, near the maximum negative of the integrands. (*f*) Inverse of the distance from σ_0 to the closest unperturbed eigenvalue at $\beta = \beta_B$.

by suction, and overlapping this with the product of the adjoint eigenmode and eigenmode correction, we found out where the eigenvalue changes due to suction originate. This turned out to coincide well with the sensitivity core. We did not separate the effects of modifying any specific term in the Navier–Stokes equations. Our arguments for spanwise wavelength selection are hence slightly different from the ones described in the local analysis of Hwang *et al.* (2013), detailing the stabilizing mechanism of a fixed velocity profile. However, the two analyses are not contradictory, as these two mechanisms might coexist in a real flow. Del Guercio *et al.* (2014) point out that spanwise wavy perturbations introduce a base flow change of a large amplitude through the creation of streaks by the lift-up effect. We observe that indeed a 2-D suction induces a smaller global base flow modification than a 3-D spanwise wavy suction, in agreement with Del Guercio *et al.* (2014). However, we extend the previous arguments by identifying the most sensitive region in the x–y-plane, and investigating when the base flow modifications induced by suction are inside this most sensitive region.

The vortex-tilting mechanism described in Hwang *et al.* (2013) might be examined by separating our sensitivities into different components, but this is out of the scope of the present paper. The primary aim here is to present and verify theoretical findings applicable to a much wider class of flow problems involving asymmetric perturbations or control.

6. Conclusions

The sensitivity of global mode eigenvalues has been generalized by considering the eigenproblem perturbation expansion up to the second order. The theory and numerical solution of the derived BiGlobal equation system have been used to shed light on how globally unstable flows are influenced by spanwise wavy actuation, for which the standard sensitivity theory predicts no effect. The computational methods presented for computation of the second perturbations are two-dimensional, except for the base flow with suction which was computed in 3-D (but could also be computed in 2-D as long as the base flow changes linearly with suction amplitude). The 2-D predictions were verified by 3-D computations. The theoretically predicted eigenvalue drift due to spanwise wavy actuation agrees well with the directly computed one. Based on this theory, we argue that the second-order effects on the eigenvalue arise from a resonance between the von Karman eigenmode at infinite spanwise wavelength (2-D) and the same mode at the actuation wavelength. This explains two observations from previous studies: in-phase suction distribution is more efficient than an out-of-phase distribution, and short wavelengths are less efficient than long wavelengths. The optimal wavelength selection is qualitatively explained by showing that the base flow changes induced by suction must be large inside the region most sensitive to spanwise wavy perturbations, called the sensitivity core. From our analysis, this is seen to occur for medium wavelengths. The theory and the eigenmode resonance effect may be relevant to a wide class of problems, for example, the effect of asymmetric inflow profiles on the stability of axisymmetric flows, or flow–acoustics interactions.

Acknowledgements

This work was supported by the European Research Council through Project ALORS 2590620. The work was performed on the computational facilities provided by the Darwin cluster of the University of Cambridge High Performance Computing Service (http://www.hpc.cam.ac.uk/).

REFERENCES

BAUMGÄRTEL, H. 1984 *Perturbation Theory for Matrices and Operators*, Licensed edition by Birkhäuser Verlag edn. Akademie Verlag.

DAVIS, T. A. 2004 Algorithm 832: UMFPACK, an unsymmetric-pattern multifrontal method. *Trans. Math. Software* **30** (2), 196–199.

FISCHER, P. F. 1997 An overlapping Schwarz method for spectral element solution of the incompressible Navier–Stokes equations. *J. Comput. Phys.* **133**, 84–101.

GIANNETTI, F. & LUCHINI, P. 2007 Structural sensitivity of the first instability of the cylinder wake. *J. Fluid Mech.* **581**, 167–197.

DEL GUERCIO, G., COSSU, C. & PUJALS, G. 2014 Stabilizing effect of optimally amplified streaks in parallel wakes. *J. Fluid Mech.* **739**, 37–56.

HINCH, E. J. 1991 *Perturbation Methods*. Cambridge University Press.

HWANG, Y., KIM, J. & CHOI, H. 2013 Stabilization of absolute instability in spanwise wavy two-dimensional wakes. *J. Fluid Mech.* **727**, 346–378.

JUNIPER, M., TAMMISOLA, O. & LUNDELL, F. 2011 The local and global stability of confined planar wakes at intermediate Reynolds number. *J. Fluid Mech.* **686**, 218–238.

KIM, J. & CHOI, H. 2005 Distributed forcing of flow over a circular cylinder. *Phys. Fluids* **17**, 033103.

KOLMOGOROV, A. N. 1954 On the conservation of conditionally periodic motions under small perturbation of the Hamiltonian. *Dokl. Akad. Nauk SSSR* **74**, 527–530.

LASHGARI, I., TAMMISOLA, O., CITRO, V., BRANDT, L. & JUNIPER, M. P. 2014 The planar *X*-junction flow: stability and control. *J. Fluid Mech.* **753**, 1–28.

LEHOUCQ, R. B., SORENSEN, D. C. & YANG, C. 1998 *ARPACK Users' Guide: Solution of Large-Scale Eigenvalue Problems with Implicitly Restarted Arnoldi Methods*. SIAM.

LIEU, B. K., MOARREF, R. & JOVANOVIC, M. R. 2010 Controlling the onset of turbulence by streamwise travelling waves. Part 2. Direct numerical simulation. *J. Fluid Mech.* **663**, 100–119.

LUCHINI, P. & BOTTARO, A. 2014 Adjoint equations in stability analysis. *Annu. Rev. Fluid Mech.* **46**, 493–517.

MARQUET, O., SIPP, D. & JACQUIN, L. 2008 Sensitivity analysis and passive control of cylinder flow. *J. Fluid Mech.* **615**, 221–252.

MASCHHOFF, K. J. & SORENSEN, D. C. 1996 PARPACK: an efficient portable large scale eigenvalue package for distributed memory parallel architectures. In *Proceedings of the Third International Workshop on Applied Parallel Computing, Industrial Computation and Optimization*, pp. 478–486. Springer.

MOARREF, R. & JOVANOVIC, M. R. 2010 Controlling the onset of turbulence by streamwise travelling waves. Part 1. Receptivity analysis. *J. Fluid Mech.* **663**, 70–99.

PRALITS, J. O., BYSTRÖM, M., HANIFI, A. & HENNINGSON, D. S. 2007 Optimal disturbances in three-dimensional boundary-layer flows. *Ercoftac Bulletin* **74**, 23–31.

TAMMISOLA, O., LUNDELL, F., SCHLATTER, P., WEHRFRITZ, A. & SÖDERBERG, L. D. 2011 Global linear and nonlinear stability of viscous confined plane wakes with co-flow. *J. Fluid Mech.* **675**, 397–434.

THEOFILIS, V. 2003 Advances in global linear instability analysis of nonparallel and three-dimensional flows. *Prog. Aerosp. Sci.* **39**, 249–315.

Paper

3

J. Fluid Mech. (2015), *vol.* 768, *pp.* 113–140.
doi:10.1017/jfm.2015.72

Linear three-dimensional global and asymptotic stability analysis of incompressible open cavity flow

Vincenzo Citro[1,†], Flavio Giannetti[1], Luca Brandt[2] and Paolo Luchini[1]

[1]DIIN, University of Salerno, Via Giovanni Paolo II, 84084 Fisciano (SA), Italy

[2]Linné Flow Centre and SeRC (Swedish e-Science Research Centre), KTH Mechanics, S-100 44 Stockholm, Sweden

(Received 21 May 2014; revised 19 December 2014; accepted 1 February 2015)

The viscous and inviscid linear stability of the incompressible flow past a square open cavity is studied numerically. The analysis shows that the flow first undergoes a steady three-dimensional bifurcation at a critical Reynolds number of 1370. The critical mode is localized inside the cavity and has a flat roll structure with a spanwise wavelength of about 0.47 cavity depths. The adjoint global mode reveals that the instability is most efficiently triggered in the thin region close to the upstream tip of the cavity. The structural sensitivity analysis identifies the wavemaker as the region located inside the cavity and spatially concentrated around a closed orbit. As the flow outside the cavity plays no role in the generation mechanisms leading to the bifurcation, we confirm that an appropriate parameter to describe the critical conditions in open cavity flows is the Reynolds number based on the average velocity between the two upper edges. Stabilization is achieved by a decrease of the total momentum inside the shear layer that drives the core vortex within the cavity. The mechanism of instability is then studied by means of a short-wavelength approximation considering pressureless inviscid modes. The closed streamline related to the maximum inviscid growth rate is found to be the same as that around which the global wavemaker is concentrated. The structural sensitivity field based on direct and adjoint eigenmodes, computed at a Reynolds number far higher than that of the base flow, can predict the critical orbit on which the main instabilities inside the cavity arise. Further, we show that the sub-leading unstable time-dependent modes emerging at supercritical conditions are characterized by a period that is a multiple of the revolution time of Lagrangian particles along the orbit of maximum growth rate. The eigenfrequencies of these modes, computed by global stability analysis, are in very good agreement with the asymptotic results.

Key words: bifurcation, instability, separated flows

1. Introduction

Flow separation and recirculation are of great interest as they play an important role in the phenomena involved in transport and mixing processes. The flow past open

† Email address for correspondence: vcitro@unisa.it

cavities is a prototype of geometrical configurations characterized by a finite region of separated flow. The identification of the flow characteristics related to instability mechanisms (e.g. coherent structures) is also of practical importance since these may lead to resonances, acoustic noise or structural vibrations. Rockwell & Naudascher (1978) classified the unstable behaviour of this kind of flow into fluid-dynamic, fluid-resonant, and fluid-elastic.

Acoustic resonance (i.e. fluid-resonant behaviour) has received a remarkable amount of attention in the past due its relation with the noise generation process (Rossiter 1964; Yamouni, Sipp & Jacquin 2013). In this case, there exists a feedback mechanism between the unstable shear layer susceptible to Kelvin–Helmholtz instability and the pressure waves (Rowley, Colonius & Basu 2002). Gharib & Roshko (1987) observed experimentally that the increase of the cavity length to depth ratio (L/D) led to a different kind of instability, the so-called 'wake mode'. This global instability relies on a purely hydrodynamic mechanism (the oscillation Strouhal number is weakly dependent on the Mach number) and is characterized by a large-scale vortex shedding.

1.1. *Experimental and numerical investigations of three-dimensional instabilities*

Three-dimensional structures in cavities with large span-to-chord ratios were first reported by Maull & East (1963) using oil flow and static-pressure measurements. These authors observed stable cell formations inside open rectangular cavities of different aspect ratios (L/D). Rockwell & Knisely (1980) observed a strong coupling between the growth of the primary vortices and the increase of the vorticity of the longitudinal vortices past the downstream edge of the cavity. They concluded that, because of this interaction, the cavity core vortex presents an ordered spanwise modulation. These coherent structures were analysed in detail in the laminar regime by Faure *et al.* (2007, 2009) in cavities with an aspect ratio varying between 0.5 and 2. Using smoke visualizations, Faure *et al.* (2007) report mushroom-like counter-rotating vortical structures and suggest that the resulting inherent flow is the consequence of a centrifugal instability related to the cavity core vortex.

Brés & Colonius (2007*b*) performed numerical simulations of the linearized compressible Navier–Stokes equations to investigate the instability features in open cavity flows. These authors identify the onset of the first bifurcation over a wide range of Mach numbers and cavity aspect ratios and discuss the variations of the spanwise modulation with the cavity depth. Brés & Colonius (2007*a*) showed, furthermore, that the full nonlinear results, computed by direct numerical simulation (DNS), agree very well with the features of the three-dimensional global mode provided by linear stability analysis. Brés & Colonius (2008) accurately discuss the properties, the structure and the nature of such instability. Using the generalized Rayleigh criterion (Bayly 1988), they show that the instability is a centrifugal instability associated with the closed streamlines inside the cavity.

Faure *et al.* (2009) performed an experimental investigation aimed at understanding the three-dimensional flow topology inside cavities of different shapes and for several Reynolds numbers. These authors also performed a secondary instabilities analysis and identified the relevant shear-layer and inner-cavity flow scales. Zhang & Naguib (2006, 2008, 2011) carried out a systematic study of the effect of the sidewalls on the unsteady open cavity flow at low Mach number. The presence of the sidewalls is shown to lead to strong amplifications of the pressure fluctuations inside the cavity. Lasagna *et al.* (2011) investigated the effects of a trapped vortex cell (TVC) on the

aerodynamic performance of a wing model and found a three-dimensional organization of the flow inside the cell according to the value of the angle of attack and the Reynolds number. di Cicca *et al.* (2013) reported time-resolved tomographic particle image velocimetry (PIV) measurements in rectangular cavities having the length-to-depth ratio equal to 2, 3 and 4.

Very recently, de Vicente *et al.* (2014) examined both experimentally and numerically the instabilities over a rectangular open cavity of aspect ratio $L/D = 2$. These authors compared the linear three-dimensional instability results with the spatial structure of the experimental fields, showing qualitative agreement for the main flow characteristics. Furthermore, they also show that modifications of the spanwise boundary conditions can cause significant alterations of the flow field due to nonlinear effects. Finally, Meseguer-Garrido *et al.* (2014) present a systematic study of the onset of the first instability, varying the Reynolds number, the incoming boundary-layer thickness and the cavity aspect ratio.

Experimental studies on the formation of three-dimensional structures in the start-up flow inside a lid-driven cavity (LDC) can be found in Migeon, Texier & Pineau (2000), Guermond *et al.* (2002) and Migeon, Pineau & Texier (2003). These three-dimensional modulations inside the cavities are also documented by de Vicente *et al.* (2010) and Gonzalez *et al.* (2011) who considered complex cross-sectional shapes.

1.2. *Short-wave asymptotic analysis*

Instabilities in open and closed cavities, as well as in separated flows, are interpreted as centrifugal instabilities. Centrifugal short-wave instabilities were first considered by Bayly (1988) who used the geometrical optics approximation and Flouquet theory to extend the classical Rayleigh theory for centrifugal instabilities to general inviscid planar flows. Bayly proposed diagonalizing the convective operator of the linearized Euler equations (LEes) and constructing linear asymptotic eigenmodes in the limit of large spanwise wavenumber using a Wentzel–Kramers–Brillouin–Jeffreys (WKBJ) expansion, localized on the closed orbit characterized by the maximum Floquet exponent. Later, the same author showed qualitative agreement between the results obtained with the linearized Navier–Stokes equations and the asymptotic predictions (Bayly 1989). Lifschitz & Hameiri (1991) investigated the asymptotic instability features, considering the initial value problem for the LEes and for the linearized equations of gas dynamics. Their more general approach was able to include both exponential and algebraic growth in time. Many efforts have since been made to quantitatively link the short-wave asymptotics and the normal-mode analysis: Sipp, Lauga & Jacquin (1999) showed agreement between the optimal streamline (i.e. the streamline where the inviscid growth rate is maximum) and the spatial distribution of the unstable eigenmodes, and between the inviscid and viscous amplification rate of an elliptic instability. Gallaire, Marquillie & Ehrenstein (2007) examined the centrifugal instability of the separated region behind a bump and were able to make a composite estimation of the growth rate taking into account the viscous effects (see also Landman & Saffman 1987) and the short-wave inviscid asymptotic limit. Recently, Giannetti (2015) applied a WKBJ approach to investigate the nature of the secondary instability arising in the periodic wake of a cylinder.

In this context, the main goal of the present work is to characterize the instabilities of the flow past an open cavity, develop an asymptotic approach to understand the instability mechanisms and finally relate the results of the global and local asymptotic analysis. The specific aims of the work, defining the outline of the article, are to:

(i) provide an accurate estimation of the critical Reynolds number and the spanwise wavenumber of the first three-dimensional bifurcation in incompressible open cavity flows;
(ii) determine the instability core by means of the adjoint-based structural sensitivity analysis;
(iii) investigate the sensitivity of the leading instability to base flow modifications induced by a perturbation of the inflow profile or wall blowing/suction;
(iv) provide a quantitative prediction of the onset of the instability by means of the short-wave asymptotic theory;
(v) show that the inviscid structural sensitivity (i.e. structural sensitivity based on direct and adjoint eigenmodes computed at a Reynolds number higher than that of the base flow) is able to accurately predict the particle orbit that provides the main contribution to the instability;
(vi) suggest a generalization of the expression used to calculate the instability growth rate from the Floquet exponent to predict the frequency of the time-dependent modes emerging at supercritical conditions.

2. Theoretical framework

2.1. *Geometrical configuration and base flow*

We investigate the stability and sensitivity of the flow over a spanwise-uniform square open cavity exposed to a uniform stream. The geometry, the frame of reference and the notation adopted in this work are all displayed in figure 1. The origin of the Cartesian reference system is located on the left edge of the cavity with x, y and z denoting the streamwise, wall-normal and spanwise directions. The fluid motion is described by the unsteady incompressible Navier–Stokes equations,

$$\boldsymbol{\nabla}\cdot\boldsymbol{u}=0, \tag{2.1a}$$

$$\frac{\partial \boldsymbol{u}}{\partial t}+(\boldsymbol{u}\cdot\boldsymbol{\nabla})\boldsymbol{u}=-\boldsymbol{\nabla}P+\frac{1}{Re_{BF}}\nabla^2\boldsymbol{u}, \tag{2.1b}$$

where $\boldsymbol{u}$ is the velocity vector with components $\boldsymbol{u}=(u, v, w)$ and P is the reduced pressure. Equations (2.1) are made dimensionless using the cavity depth D as the characteristic length scale and the velocity of the incoming uniform stream U_∞ as the reference velocity. The Reynolds number is thus defined as $Re_{BF}=U_\infty D/\nu$ (here the subscript BF means base flow Reynolds number) with ν the fluid kinematic viscosity. To ease comparisons, we have chosen the same boundary conditions as Sipp & Lebedev (2007) and Barbagallo, Sipp & Schmid (2009). The system of differential equations (2.1) is closed by the following Dirichlet boundary conditions at the inflow $\partial\mathscr{D}_{in}$ and stress-free conditions at the outflow $\partial\mathscr{D}_{out}$:

$$\boldsymbol{u}=1\cdot\boldsymbol{e}_x, \quad x\in\partial\mathscr{D}_{in}; \qquad P\boldsymbol{n}-Re^{-1}(\boldsymbol{\nabla u})\cdot\boldsymbol{n}=\boldsymbol{0}, \quad x\in\partial\mathscr{D}_{out}, \tag{2.2a,b}$$

where e_x is the unit vector in the direction of the x axis, n is the normal vector (in this case, it is the vector perpendicular to the outlet of the computational domain). Symmetric conditions (i.e. $\partial_y u=0$ and $v=0$) are imposed at the free-stream upper boundary of the computational domain $\partial\mathscr{D}_{ext}$ and no-slip conditions $\boldsymbol{u}=\boldsymbol{0}$ at the solid walls $\partial\mathscr{D}_w$. Note that a free-slip condition with zero tangential stress (i.e. $\partial_y u=0$ and $v=0$) is used on the walls close to the inflow and outflow $\partial\mathscr{D}_{fs}=\partial\mathscr{D}_{fs}^1\cup\partial\mathscr{D}_{fs}^2$.

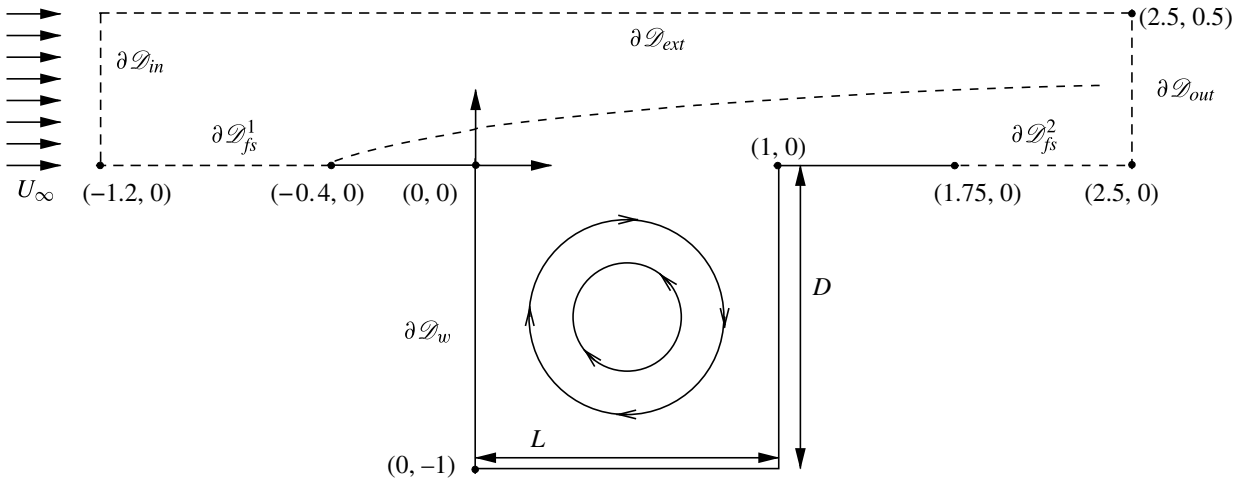

FIGURE 1. Flow configuration, frame of reference and computational domain $\mathscr{D}$. The main features of the flow are also sketched in the figure, i.e. the boundary layer developing over the walls, the shear layer above the cavity and the recirculation forming inside the cavity of length L and depth $D = L$.

2.2. *Global stability analysis*

The flow linear instability is studied with a classical normal-mode analysis. The analysis relies on the existence of a steady solution about which infinitesimal perturbations are superimposed. The velocity and pressure fields are decomposed into a two-dimensional base flow, $\boldsymbol{Q}_b(x, y) = (\boldsymbol{u}_b, P_b)^{\mathrm{T}} = (u_b, v_b, 0, P_b)^{\mathrm{T}}$, and a three-dimensional disturbance flow denoted by $\boldsymbol{q}'(x, y, z, t) = (\boldsymbol{u}', P')^{\mathrm{T}} = (u', v', w', P')^{\mathrm{T}}$ of small amplitude ϵ. Introducing this decomposition into (2.1) and linearizing the equations governing the disturbance evolution, we obtain the two systems describing the spatial structure of the base flow and the behaviour of generally unsteady perturbations. In particular, the base flow is governed by the steady version of (2.1), whereas the perturbation field is described by the linearized unsteady Navier–Stokes equations (LNSE)

$$\frac{\partial \boldsymbol{u}'}{\partial t} + \boldsymbol{L}\{\boldsymbol{u}_b(Re_{BF}), Re_{STB}\}\boldsymbol{u}' = -\boldsymbol{\nabla} P', \tag{2.3}$$

$$\boldsymbol{\nabla} \cdot \boldsymbol{u}' = 0, \tag{2.4}$$

with the linearized Navier–Stokes operator $\boldsymbol{L}$ (Re_{STB} indicates the Reynolds number used for stability computations)

$$\boldsymbol{L}\{\boldsymbol{u}_b, Re_{STB}\}\boldsymbol{u}' = \boldsymbol{u}_b \cdot \boldsymbol{\nabla}\boldsymbol{u}' + \boldsymbol{u}' \cdot \boldsymbol{\nabla}\boldsymbol{u}_b - \frac{1}{Re_{STB}}\nabla^2 \boldsymbol{u}'. \tag{2.5}$$

As the base flow is homogeneous and stationary in the spanwise direction, a generic perturbation can be decomposed into Fourier modes of spanwise wavenumber k. The three-dimensional perturbations are expressed as

$$\boldsymbol{q}'(x, y, z, t) = \tfrac{1}{2}\{(\hat{u}, \hat{v}, \hat{w}, \hat{P})(x, y) \ \exp[\mathrm{i}kz + \gamma t] + \mathrm{c.c.}\}, \tag{2.6}$$

where $\gamma = \eta + \mathrm{i}\omega$ is the complex growth rate and c.c. stands for complex conjugate. The real part η of γ represents the temporal growth rate of the perturbation and the

imaginary part ω its frequency. For $\eta > 0$, the flow is unstable whereas for $\eta < 0$ it is stable. Introducing the ansatz (2.6) in the LNSE (2.3)–(2.4), we obtain the generalized eigenvalue problem

$$\boldsymbol{A}\hat{\boldsymbol{q}} + \gamma \boldsymbol{B}\hat{\boldsymbol{q}} = 0, \tag{2.7}$$

in which $\hat{\boldsymbol{q}} = (\hat{u}, \hat{v}, \hat{w}, \hat{P})^{\mathrm{T}}$ and $\mathscr{A}$ is the complex linearized evolution operator. The operators $\mathscr{A}$ and $\mathscr{B}$, have the following expressions:

$$\boldsymbol{A} = \begin{pmatrix} \mathscr{C} - \mathscr{M} + \partial_x u_b & \partial_y u_b & 0 & \partial_x \\ \partial_x v_b & \mathscr{C} - \mathscr{M} + \partial_y v_b & 0 & \partial_y \\ 0 & 0 & \mathscr{C} - \mathscr{M} & \mathrm{i}k \\ \partial_x & \partial_y & \mathrm{i}k & 0 \end{pmatrix}, \quad \boldsymbol{B} = \begin{pmatrix} 1 & 0 & 0 & 0 \\ 0 & 1 & 0 & 0 \\ 0 & 0 & 1 & 0 \\ 0 & 0 & 0 & 0 \end{pmatrix}, \tag{2.8a,b}$$

where $\mathscr{M} = {Re_{STB}}^{-1}(\partial_{x^2} + \partial_{y^2} - k^2)$ and $\mathscr{C} = u_b\partial_x + v_b\partial_y$ describe the viscous diffusion of the perturbation and its advection by the mean flow. The boundary conditions associated with the eigenproblem (2.7) are derived from those used for the base flow, i.e.

$$\hat{\boldsymbol{u}} = \boldsymbol{0}, \quad \text{on } \partial\mathscr{D}_{in} \cup \partial\mathscr{D}_{w} \text{ (inlet and wall)}, \tag{2.9a}$$

$$\hat{P}\boldsymbol{n} - {Re_{STB}}^{-1}(\boldsymbol{\nabla}\hat{\boldsymbol{u}}) \cdot \boldsymbol{n} = \boldsymbol{0}, \quad \text{on } \partial\mathscr{D}_{out} \text{ (outlet)}, \tag{2.9b}$$

$$\partial_y \hat{u} = \hat{v} = \hat{w} = 0, \quad \text{on } \partial\mathscr{D}_{ext} \cup \partial\mathscr{D}_{fs} \text{ (free stream and free-slip boundary)}. \tag{2.9c}$$

Finally, we note that the complex-conjugate pairs $(\eta + \mathrm{i}\omega; \hat{\boldsymbol{q}})$ and $(\eta - \mathrm{i}\omega; \hat{\boldsymbol{q}}^*)$ are both solutions of the eigenproblem (2.7) with the boundary conditions (2.9) for a real base flow $\boldsymbol{Q}_b$. Thus, the eigenvalues are complex conjugates and the spectra are in a symmetric plane with respect to the real axis in the (η, ω).

2.3. *Determination of the instability core: structural sensitivity*

In this section we present the structural sensitivity analysis following the framework in Pralits, Brandt & Giannetti (2010). The underlying idea is the concept of 'wavemaker', introduced by Giannetti & Luchini (2007) to identify the location of the core of a global instability. The wavemaker is the region in the flow where variations in the structure of the problem provide the largest drift of a specific eigenvalue. We first consider the perturbed eigenvalue problem

$$\gamma'\hat{\boldsymbol{u}}' + \boldsymbol{L}\{\boldsymbol{u}_b, Re_{STB}\}\hat{\boldsymbol{u}}' = -\boldsymbol{\nabla}\hat{P}' + \delta\boldsymbol{H}(\hat{\boldsymbol{u}}', \hat{P}'), \tag{2.10}$$

$$\boldsymbol{\nabla} \cdot \hat{\boldsymbol{u}}' = 0, \tag{2.11}$$

where $\delta\boldsymbol{H}$ is the generalized structural perturbation. It is assumed to be a momentum force localized in space and proportional to the local velocity perturbation through a (3×3) coupling matrix $\delta\boldsymbol{M}_0$ and a Dirac delta function:

$$\delta\boldsymbol{H}(\hat{\boldsymbol{u}}', \hat{P}') = \delta\boldsymbol{M}(x, y) \cdot \hat{\boldsymbol{u}}' = \delta(x - x_0, y - y_0)\delta\boldsymbol{M}_0 \cdot \hat{\boldsymbol{u}}'. \tag{2.12}$$

Neglecting higher-order terms, variations of the eigenvalue $\delta\gamma$ and of the corresponding eigenfunction $(\delta\hat{\boldsymbol{u}}, \delta\hat{P})$ satisfy the following expressions:

$$\gamma\delta\hat{\boldsymbol{u}} + \boldsymbol{L}\{\boldsymbol{u}_b, Re_{STB}\}\delta\hat{\boldsymbol{u}} = -\boldsymbol{\nabla}\delta\hat{P} + \delta\boldsymbol{M} \cdot \hat{\boldsymbol{u}} - \delta\gamma\hat{\boldsymbol{u}}, \tag{2.13}$$

$$\boldsymbol{\nabla} \cdot \delta\hat{\boldsymbol{u}} = 0. \tag{2.14}$$

Using then the Lagrange identity (see Luchini & Bottaro 2014), we can determine the equations governing the structure of the adjoint field: $\hat{\boldsymbol{g}}^{+}(x, y) = (\hat{\boldsymbol{f}}^{+}, \hat{m}^{+})$

$$-\gamma\hat{\boldsymbol{f}}^{+} + \boldsymbol{u}_b \cdot \nabla\hat{\boldsymbol{f}}^{+} - \nabla\boldsymbol{u}_b \cdot \hat{\boldsymbol{f}}^{+} + \frac{1}{Re_{STB}}\nabla^2\hat{\boldsymbol{f}}^{+} + \nabla\hat{m}^{+} = 0, \tag{2.15}$$

$$\nabla \cdot \hat{\boldsymbol{f}}^{+} = 0. \tag{2.16}$$

After integration over the domain $\mathscr{D}$, accounting for the boundary conditions and introducing the sensitivity tensor

$$\boldsymbol{S}(x_0, y_0; Re_{BF}, Re_{STB}) = \frac{\hat{\boldsymbol{f}}^{+}(x_0, y_0)\hat{\boldsymbol{u}}(x_0, y_0)}{\displaystyle\int_{\mathscr{D}} \hat{\boldsymbol{f}}^{+} \cdot \hat{\boldsymbol{u}}\,\mathrm{d}S}, \tag{2.17}$$

we can express the eigenvalue drift due to the local feedback as

$$\delta\gamma(x_0, y_0) = \frac{\displaystyle\int_{\mathscr{D}} \hat{\boldsymbol{f}}^{+} \cdot \delta\boldsymbol{M} \cdot \hat{\boldsymbol{u}}\,\mathrm{d}S}{\displaystyle\int_{\mathscr{D}} \hat{\boldsymbol{f}}^{+} \cdot \hat{\boldsymbol{u}}\,\mathrm{d}S} = \frac{\hat{\boldsymbol{f}}^{+} \cdot \delta\boldsymbol{M}_0 \cdot \hat{\boldsymbol{u}}}{\displaystyle\int_{\mathscr{D}} \hat{\boldsymbol{f}}^{+} \cdot \hat{\boldsymbol{u}}\,\mathrm{d}S} = \boldsymbol{S} : \delta\boldsymbol{M}_0 = \sum_{ij} S_{ij}\delta M_{0ij}. \tag{2.18}$$

Different norms of the tensor $\boldsymbol{S}$ can be used to build a spatial map of the sensitivity. The spectral norm is chosen here to study the worst possible case.

3. Numerical approach

3.1. *Base flow calculation*

The numerical computation of the base flow has been performed using a finite element method. The variational formulation of the Navier–Stokes equations (2.1) is implemented in the software package FreeFem++ (Hecht (2012); http://www.freefem.org) using classical *P*2–*P*1 Taylor–Hood elements for the spatial discretization. The resultant nonlinear system of algebraic equations, along with the boundary conditions, is solved by a Newton–Raphson procedure: given an initial guess $\boldsymbol{w}_b{}^{(0)}$, the linear system

$$NS(Re_{BF}, \boldsymbol{W}_b{}^{(n)}) \cdot \boldsymbol{w}_b{}^{(n)} = -rhs^{(n)} \tag{3.1}$$

is solved at each iteration step using the MUMPS (multifrontal massively parallel sparse direct solver) (Amestoy *et al.* 2001, 2006) for the matrix inversion. The base flow is then updated as

$$\boldsymbol{W}_b^{(n+1)} = \boldsymbol{W}_b{}^{(n)} + \boldsymbol{w}_b{}^{(n)}. \tag{3.2}$$

The initial guess is chosen to be the solution of the Stokes equations and the process is continued until the L^2-norm of the residual of the governing equations becomes smaller than 10^{-12}. To test the implementation and convergence, we used three different meshes M1, M2 and M3 (see table 1). These are generated by the bidimensional anisotropic mesh generator (Bamg) that is part of the Freefem++ package. The base flow computations are also validated using a variant of the second-order finite-difference code described in Giannetti & Luchini (2007). A typical steady flow over the open cavity is depicted in figure 2.

Mesh	η	ω	$n_{d.o.f.}$	n_t	Source
M1	0.0007590	7.4931	998 668	221 045	Present
M2	0.0008344	7.4937	1416 630	313 791	Present
M3	0.0009122	7.4943	2601 757	576 887	Present
D1	0.0007401	7.4930	880 495	194 771	Sipp & Lebedev (2007)
D2	0.0008961	7.4942	1888 003	418 330	Sipp & Lebedev (2007)

TABLE 1. Comparison of the results obtained with the present implementation and those reported by Sipp & Lebedev (2007) for the same configuration. The eigenfrequency ω and the growth rate η have been calculated for the first two-dimensional unstable eigenmode at $Re_{BF} = Re_{STB} = 4140$; $n_{d.o.f.}$ and n_t indicate the total number of degrees of freedom of the linearized problem and the number of triangles for each of the unstructured meshes used.

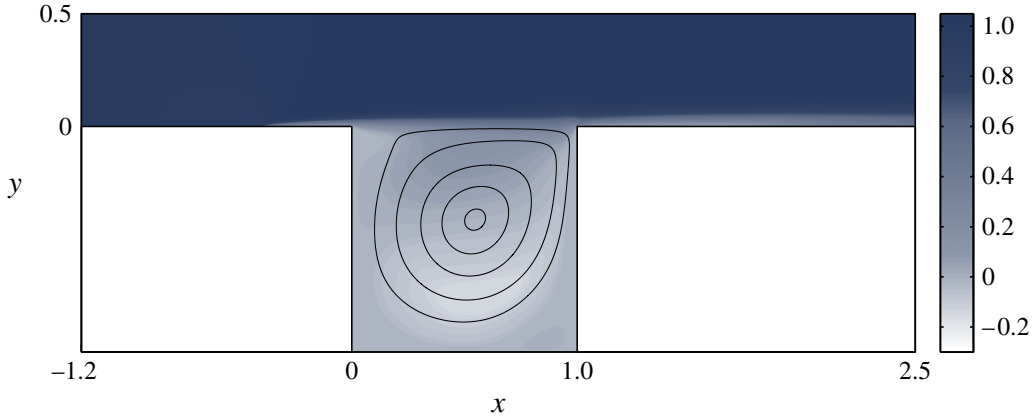

FIGURE 2. (Colour online) Visualization of the steady two-dimensional base flow for the Reynolds number $Re_{BF} = 1370$ at which a three-dimensional instability is first observed. The background shading displays the streamwise velocity whereas solid lines indicate the streamlines inside the cavity.

3.2. *Eigenvalue solver and adjoint field*

Once the base flow is determined, the system (2.7) is used to perform the stability analysis. After spatial discretization, the governing equations and their boundary conditions (2.9) are recast in the following standard form:

$$[\boldsymbol{A}(Re_{STB}, \boldsymbol{W}_b(Re_{BF})) + \gamma \boldsymbol{B}] \cdot \boldsymbol{w} = \boldsymbol{0}, \tag{3.3}$$

where $\boldsymbol{w}$ is the right (or direct) eigenvector. As methods based on the QR decomposition are not feasible for solving large-scale problems like those associated with the matrix $\boldsymbol{A}$ obtained for our problem, we adopt an efficient matrix-free iterative method based on the Arnoldi algorithm (Arnoldi 1951). We use the state-of-the-art ARPACK package (Lehoucq *et al.* 2007), with implicit restarts to limit memory requirements. The solution of the linear system built by the Arnoldi iterations on the Krylov subspace is obtained with the same sparse solver (Amestoy *et al.* 2001, 2006) as used for the base flow calculations. The adjoint modes are computed as left eigenvectors of the discrete system derived from the discretization of the linearized equations and the sensitivity function is then computed by the product of the direct

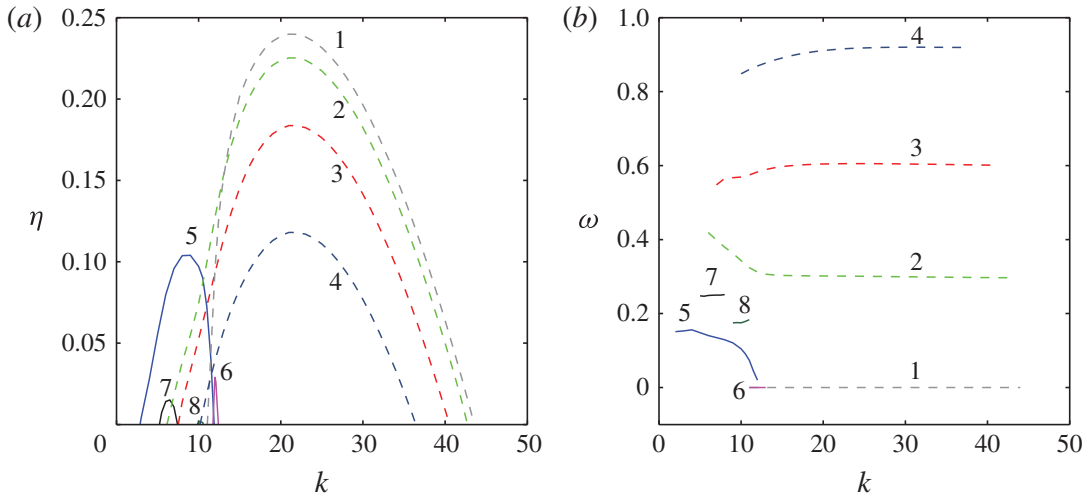

FIGURE 3. (Colour online) Stability analysis of the open cavity flow at $Re = 4140$, where an unstable two-dimensional mode first emerges. (*a*) Real and (*b*) imaginary part of the eigenvalue γ versus the spanwise wavenumber k. The different branches are numbered for future reference.

and the adjoint fields. The right (direct) and left (adjoint) eigenvectors are normalized by requiring

$$\max_{x,y\in\mathscr{D}}\{|\hat{u}(x,y)|\} = 1, \qquad \int_{\mathscr{D}} \hat{\boldsymbol{f}}^{+} \cdot \hat{\boldsymbol{u}} \mathrm{d}S = 1. \tag{3.4a,b}$$

The code is validated against the results reported by Sipp & Lebedev (2007). These authors investigate the stability of a Newtonian fluid in the same geometrical configuration and report the first instability of a two-dimensional eigenmode to occur at $Re = 4140$. In table 1 we present the comparison between our results and the results in Sipp & Lebedev (2007) for different meshes. In these tests, 50 eigenvalues were obtained, with an initial Krylov basis of dimension 150; the convergence criterion for the Arnoldi iterations is based on a tolerance of 10^{-9}. To independently check the accuracy of the results we *a posteriori* computed the residual $\max_i |(A_{ij} + \gamma B_{ij})w_j|$: this turns out to be always below 10^{-9} for the results reported in this paper, typically less than 10^{-12} for the least stable modes. The majority of the computations presented in the following are obtained using mesh M2. Henceforth whenever $Re_{BF} = Re_{STB}$ we will simply use Re.

4. Linear stability results

4.1. *Three-dimensional versus two-dimensional instability*

As the cavity is typically considered an example of centrifugal instability, we expect the first bifurcation to be characterized by the appearance of steady three-dimensional modes of relatively short wavelength in the spanwise direction (Albensoeder, Kuhlmann & Rath 2001). To verify this, we scan the k-axis seeking for unstable modes at the Reynolds number $Re = 4140$ where a two-dimensional mode first becomes unstable (Sipp & Lebedev 2007). The results in figure 3 clearly show that eight unstable branches can be found for this value of Re where the most unstable mode has wavenumber $k = 22$ and represents a steady disturbance ($\omega = 0$ in figure 3*b*). The flow over an open cavity is therefore characterized by a first bifurcation to a steady three-dimensional configuration.

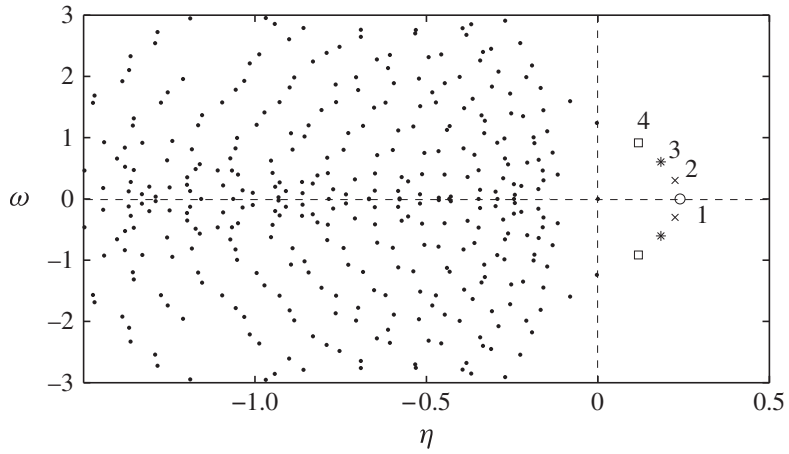

FIGURE 4. Eigenvalue spectrum for $Re = 4140$ and $k = 22$. The numbers in the figure relates to the branches identified in figure 3.

The full eigenvalue spectrum at $k = 22$ is shown in figure 4 where seven unstable modes appear (four branches with respect to k), placed symmetrically with respect to the real axis. It is interesting to highlight that the steady mode is the most unstable one, while the others are characterized by frequencies which are integer multiples of a fundamental one and arise (as explained in § 7) as results of resonances on a particular streamline.

In figure 5 we display the modulus of both the direct and adjoint eigenfunctions corresponding to the eigenvalues denoted by 1, 2, 3, and 4 in figure 4. The velocity perturbations are most evident in the circular region inside the cavity, with a tail in the shear region just above the downstream wall. The adjoint modes, indicating the region in the flow most receptive to forcing in the momentum equations, have a similar structure, except for the thin region close to the upstream tip of the cavity, where instability is most efficiently triggered. The unstable modes are spatially localized in the same region. The secondary flow generated by the leading instability can be described as a flat roll lying within the square cavity. The different resonances are associated with periodic oscillations again concentrated in the region inside the cavity.

To document the appearance of this two-to-three-dimensional bifurcation, we determine the critical Reynolds number at which the instability first occurs: as shown in figure 6 the critical value is about $Re_{cr} \approx 1370$ and the first mode to become unstable is associated with a wavenumber $k \approx 13.4$. All modes whose growth rate is reported in figure 6 have zero frequency; this stationary instability will be analysed in detail in the rest of the paper.

4.2. *Structural sensitivity of the first bifurcation*

We study the characteristics of the bifurcation by first showing the spatial structure of the fluctuation of the least stable mode at $Re = 1370$, $k = 13.4$. Like the modes at higher Reynolds number, the mode is localized along the external streamlines of the recirculation region inside the cavity (see figure 7). The level of fluctuations is largest in the streamwise component, the cross-stream and spanwise ones being respectively about 61 % and 88 % of the streamwise fluctuations. The adjoint of the critical mode is displayed in figure 7(*d–f*): its spatial structure closely resembles that of the direct mode, with a strong localization along the circular streamlines inside the cavity. As noted above, the direct mode presents a second region of noticeable amplitude near the

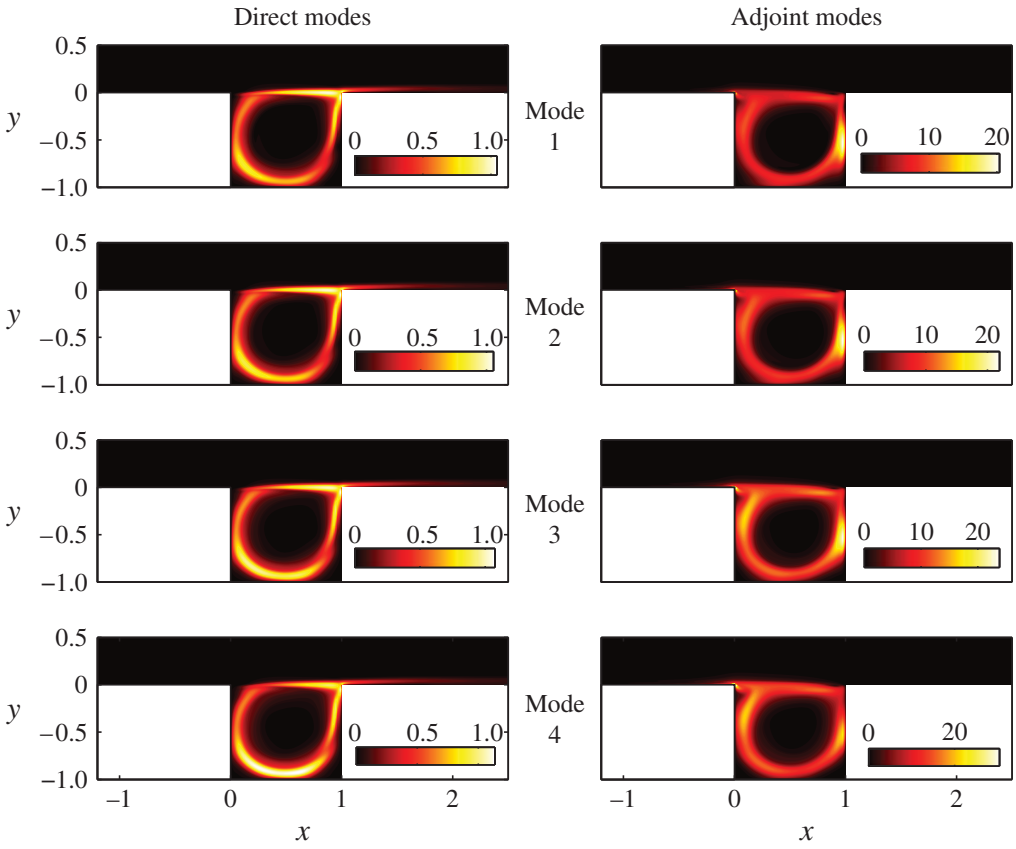

FIGURE 5. (Colour online) Contour plots of the absolute value of the direct and adjoint eigenfunctions of modes 1, 2, 3 and 4 as denoted in figure 4 for $Re = 4140$ and $k = 22$. Global mode 1 is stationary ($\omega = 0$), mode 2 has $\omega \approx 0.3$, mode 3 has $\omega \approx 0.6$ and mode 4 has $\omega \approx 0.9$.

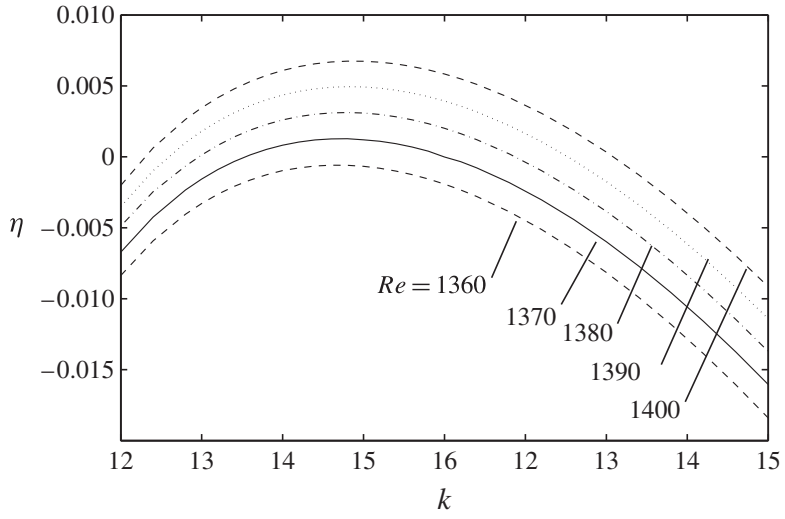

FIGURE 6. Leading eigenmode for cavity flow with $L/D = 1$. Growth rate of the most unstable mode versus the spanwise wavenumber k for the Reynolds numbers indicated. The circular frequency is zero for all modes displayed. Thus, the first instability of the flow over an open cavity is a three-dimensional steady mode.

downstream tip of the cavity and in the shear region just downstream of it, whereas the amplitude of the adjoint mode is not negligible near the upstream tip.

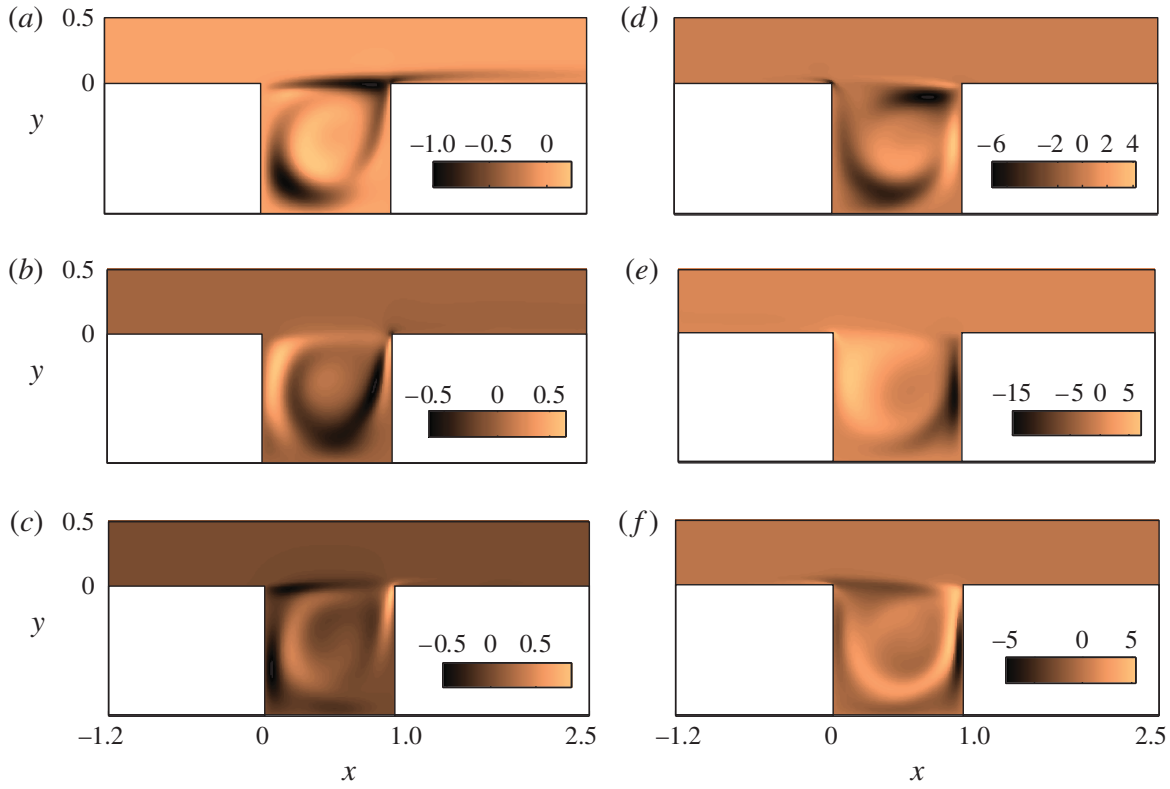

FIGURE 7. (Colour online) Contour plots of the streamwise (*a* direct; *d* adjoint), wall-normal (*b* direct; *e* adjoint) and spanwise (*c* direct; *f* adjoint) component of the direct and adjoint mode close to the critical Reynolds number $Re = 1370$, $k = 13.4$.

The structural sensitivity of this mode is displayed in figure 8. This quantity indicates the regions in the flow where a feedback forcing proportional to the local perturbation velocity most alters the eigenvalue, in other words the wavemaker of the instability. The sensitivity, product of the direct and adjoint mode, is largest inside the cavity, with no significant contributions from the regions of strong shear above it. It is interesting to note that the wavemaker is similar to that computed for a lid-driven square cavity (Giannetti, Luchini & Marino 2010; Haque *et al.* 2012).

5. Instabilities in cavity flows

5.1. *Open cavity and lid-driven cavity*

The sensitivity analysis performed in the previous section clearly shows that the core of the three-dimensional instability leading to the first bifurcation in a square open cavity is highly localized in space and completely contained inside the cavity. This is in contrast with the first 2D instability (Sipp & Lebedev 2007), arising at $Re = 4140$, which is more similar to a wake-type instability (Sipp 2012; Yamouni *et al.* 2013) and localized downstream near the second tip of the cavity.

Examining the results obtained from the stability analysis, it is clear that the external flow plays little role in the generation mechanism of the three-dimensional instability. It is thus reasonable to assume that the configuration studied here is subject to the same type of instabilities as those appearing in a LDC and discussed by Albensoeder *et al.* (2001) and Albensoeder & Kuhlmann (2006) among others. In the open cavity the shear layer detaching from the upstream corner has the same role as that of the lid in the formation of the vortical motion inside the LDC configuration.

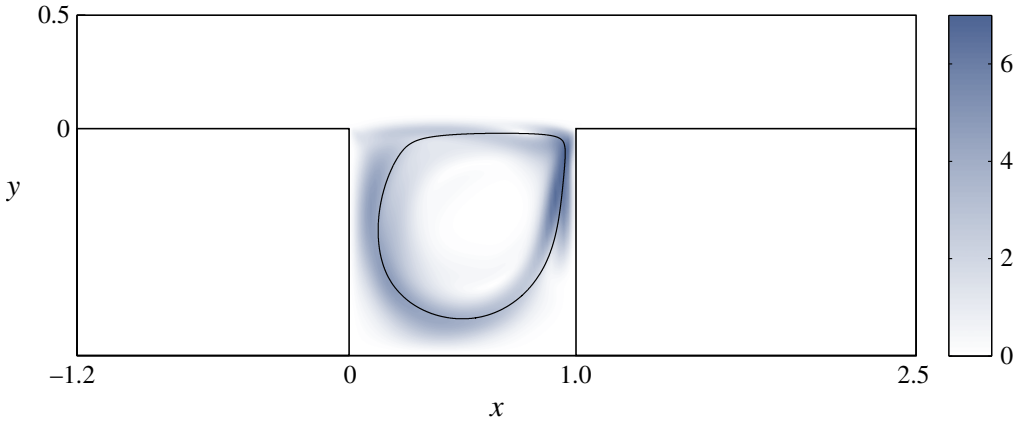

FIGURE 8. (Colour online) Structural sensitivity, the core of the instability, at the neutral conditions, $Re = 1370$, $k = 13.4$, for the flow over an open square cavity. The streamline where the asymptotic analysis predicts the maximum inviscid growth rate is also depicted (see § 7).

The velocity of the lid is uniform while in the present study the fluid velocity along the line connecting the two upper corners is not constant: the velocity starts from zero at the left corner, increases, reaches a maximum and then decreases again, vanishing at the downstream corner. In addition, the vertical velocity is different from zero, its magnitude being smaller than that of the horizontal component, however. As a result the flow field, although qualitatively similar, also has important differences with respect to that occurring in the lid-driven problem.

For the LDC the critical Reynolds number for the first bifurcation has been calculated independently by Theofilis (2000) and Albensoeder *et al.* (2001) (see also Ding & Kawahara 1998; Shatrov, Mutschke & Gerbeth 2003). The numerical three-dimensional linear stability analysis of Albensoeder *et al.* (2001) covers a wide range of cavity aspect ratios and presents the corresponding unstable modes, which appear to be qualitatively different when varying the cavity aspect ratio. These authors explain the centrifugal instability mechanism in terms of the perturbation energy budget and the criterion proposed by Sipp & Jacquin (2000).

As suggested by Brés & Colonius (2008) (see § 4.2 of their paper), if we introduce a (base flow) Reynolds number Re_{av} based on the cavity depth D and on the average velocity $\tilde{U}$ along the line connecting the two opposite corners, the critical Reynolds number for the first instability of the open cavity flow becomes

$$Re_{av} = \frac{\tilde{U}D}{\nu} \approx 490, \tag{5.1}$$

which is around 38 % lower than the value found by Albensoeder *et al.* (2001). Despite this difference in the value of the critical Reynolds number, the spanwise wavenumbers at which the instability first occurs are comparable, being $k_{lid} \approx 15.4$ in the LDC case and $k \approx 13.4$ in the present configuration. These qualitative similarities, both in terms of base flows and modes, suggest that the same kind of instability is acting in the two configurations.

5.2. *Link between open cavity flows*

Brés & Colonius (2008) performed DNS of open cavity flows for several Re_{δ^*}, where δ^* is displacement thickness, to investigate the effect of this parameter on the

instability properties. In the present configuration the shear layer starts developing at $x^{bl} = -0.4$ (we recall that the origin of our frame of reference is located on the left edge of the cavity) leading to a displacement thickness at the upstream edge of ($Re = 1370$)

$$\delta^*(x^{bl}) = \int_0^{0.5} \frac{u_b(x^{bl}, 0.5) - u_b(x^{bl}, y)}{u_b(x^{bl}, 0.5)} \mathrm{d}y \approx 0.029. \tag{5.2}$$

Thus, the critical Reynolds number based on this boundary-layer thickness is equal to $Re_{\delta^*} = U_\infty \delta^*(x^{bl})/\nu \approx 39.7$.

As discussed in Brés & Colonius (2008), the critical conditions for the instability are only weakly affected by the starting position of the upstream laminar boundary layer when the critical Reynolds number is appropriately defined. The main idea is that the dynamics inside the cavity is approximately driven by the average velocity between the two edges rather than by the shear-layer thickness, thus strengthening the connection to the LDC flow. Analysing the limiting case arising when the incoming free-stream velocity U_∞ is simply linear, i.e. when a Couette profile of velocity $U_\infty(y) = \boldsymbol{y} \cdot \boldsymbol{e_y}$ is imposed at the inlet, we found that the first bifurcation occurs at $Re^{Couette} \approx 20\,200$ for modes of spanwise wavenumber $k \approx 13.0$. Interestingly, the critical Reynolds number scaled with the cavity depth and average velocity, $Re_{av} \approx 470$, is in a very good agreement with the value obtained previously, (5.1), although the boundary-layer thickness of Couette flow is infinity. In the light of this result we confirm that the averaged Reynolds number Re_{av} is a relevant parameter to predict the onset of instability for open cavity flows.

6. Structural sensitivity to a velocity-based linear feedback

The so-called sensitivity to base flow variations is a concept introduced by Bottaro, Corbett & Luchini (2003) and Marquet, Sipp & Jacquin (2008) within the global framework. In this analysis a small structural velocity-based perturbation acts at the base flow level: the effect of the base flow modifications on the leading eigenvalue of the stability problem allows us to study the different mechanisms that can suppress or enhance the instability. The spatial structure of the so-called adjoint base flow can be used to identify the features of the base flow that provide the main contribution to the instability dynamics and the regions where to locate effective passive control devices. In other words, this modification of the structure of the Navier–Stokes operator causes a variation of the base flow which in turn produces a drift of the leading eigenvalue $\gamma = \eta + \mathrm{i}\omega$.

For the sake of brevity, only the main ingredients are outlined here; an extensive and detailed derivation can be found in Marquet *et al.* (2008) and Pralits *et al.* (2010). Using a formalism based on control theory, the eigenproblem (2.7) represents the state equation, the state vector is composed of the global mode $\hat{\boldsymbol{q}}$ and the complex eigenvalue γ, and the base flow $\boldsymbol{Q}_b$ is the control variable. As in Pralits *et al.* (2010) we express the eigenvalue drift $\delta\gamma$ as

$$\delta\gamma = \delta\eta + \mathrm{i}\delta\omega = \frac{\displaystyle\int_{\mathscr{D}} (\hat{\boldsymbol{u}} \cdot \nabla \hat{\boldsymbol{f}}^+ - \nabla \hat{\boldsymbol{u}} \cdot \hat{\boldsymbol{f}}^+) \cdot \delta \boldsymbol{u}_b \mathrm{d}S}{\displaystyle\int_{\mathscr{D}} \hat{\boldsymbol{f}}^+ \cdot \hat{\boldsymbol{u}} \mathrm{d}S}, \tag{6.1}$$

where $\delta\boldsymbol{u}_b$ is a generic modification of the base flow. The relation (6.1) provides the effect of a specified velocity distribution implying a dedicated computation for

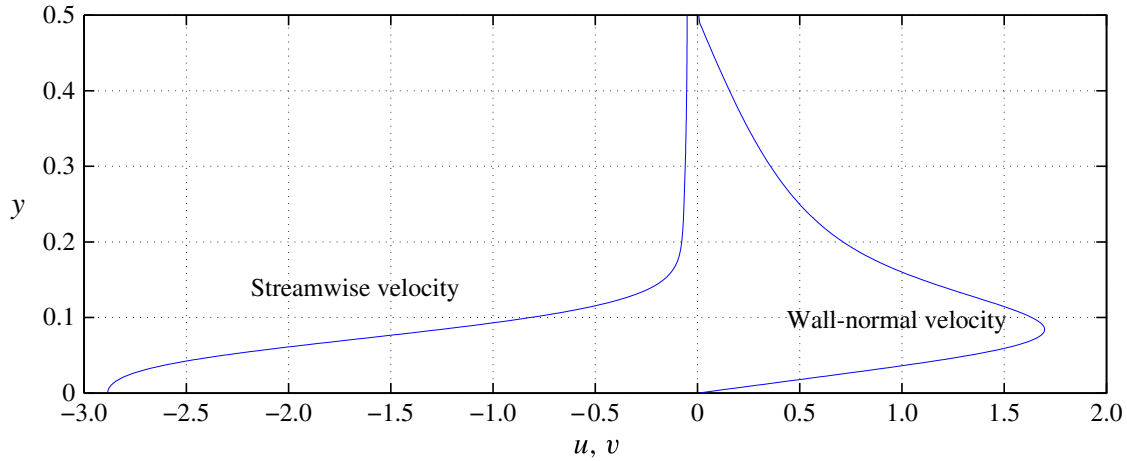

FIGURE 9. (Colour online) Sensitivity of the first bifurcation to streamwise and wall-normal mean velocity modifications at the inflow. The profile shown would provide the largest possible stabilization of the first bifurcation.

each specific actuation, e.g. wall blowing/suction. The optimal boundary velocity distribution, instead, can be directly found as follows (see Meliga & Chomaz 2011):

$$\delta\gamma = \frac{\displaystyle\int_{\partial\mathscr{D}_{w,i,fs}} \left[\left(m_b^+\boldsymbol{n} + \frac{1}{Re}\boldsymbol{n}^{\mathrm{T}}\cdot\boldsymbol{\nabla}\boldsymbol{f}_b^+\right)\cdot\delta\boldsymbol{U}_{w,i,fs}\right]\mathrm{d}l}{\displaystyle\int_{\mathscr{D}} \hat{\boldsymbol{f}}^+\cdot\hat{\boldsymbol{u}}\mathrm{d}S} \tag{6.2}$$

where m_b^+ and $\hat{\boldsymbol{f}}_b^+$ are the adjoint base flow pressure and the three-dimensional adjoint base flow velocity field and the subscripts w, i, fs indicate the boundaries (inlet, wall or free-slip) on which we calculate the integral $\mathrm{d}l$ is the length element along $\partial D_{w,i,fs}$. The adjoint base flow field $\boldsymbol{Q}_b^+$ must satisfy the following set of linear equations (Pralits *et al.* 2010):

$$\boldsymbol{u}_b\cdot\boldsymbol{\nabla}\boldsymbol{f}_b^+ - \boldsymbol{\nabla}\boldsymbol{u}_b\cdot\boldsymbol{f}_b^+ + \frac{1}{Re}\nabla^2\boldsymbol{f}_b^+ + \boldsymbol{\nabla}m_b^+ = \hat{\boldsymbol{u}}\cdot\boldsymbol{\nabla}\hat{\boldsymbol{f}}^+ - \boldsymbol{\nabla}\hat{\boldsymbol{u}}\cdot\hat{\boldsymbol{f}}^+, \tag{6.3}$$

$$\boldsymbol{\nabla}\cdot\boldsymbol{f}_b^+ = 0, \tag{6.4}$$

along with the adjoint base flow outlet condition $m_b^+\boldsymbol{n} - Re^{-1}\boldsymbol{n}\cdot\boldsymbol{\nabla}\boldsymbol{f}_b^+ = -(\boldsymbol{u_b}\cdot\boldsymbol{n})\boldsymbol{f}_b^+ + (\hat{\boldsymbol{u}}\cdot\boldsymbol{n})\hat{\boldsymbol{u}}^+$ at $\partial\mathscr{D}_{out}$ and zero-velocity conditions at the solid walls and at the inlet.

The sensitivity of the instability with respect to the incoming flow is examined first. Figure 9 shows the sensitivity to both the streamwise and the wall-normal components of the inflow velocity profile, where the profiles shown would provide the optimal decrease of the instability growth rate. The x-component is found to be always negative and attains significant values only near the wall. This fact is not surprising because the base flow modifications have effect only if related to the shear layer that drives the core vortex inside the cavity. Perturbations in the free stream do not affect the flow at the edge and inside the cavity, the regions where the instability is triggered. Negative modifications of the inlet velocity profile cause stabilization due to decrease of the momentum inside the shear layer. The effect of the wall-normal component is related to the same mechanism, decreasing of the total streamwise momentum at the cavity tip by normal advection.

In view of an active control of the first bifurcation, we depict the wall-normal component of the sensitivity along the cavity walls in figure 10; this corresponds to

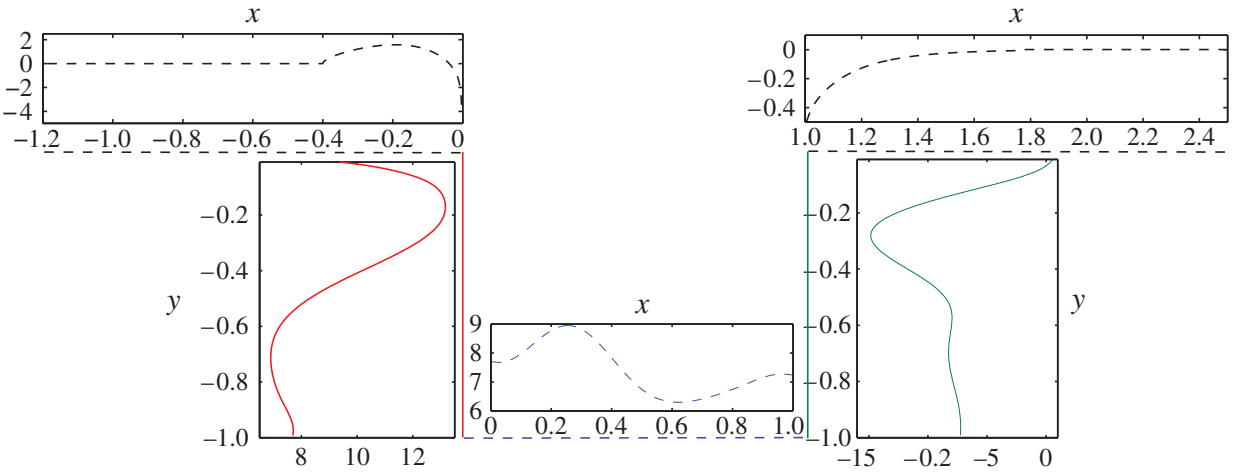

FIGURE 10. (Colour online) Sensitivity to wall-normal blowing and suction of the leading-mode growth rate at $Re = 1370$ and $k = 13.4$. Positive (negative) values indicate blowing (suction) and lead to stabilization (destabilization). The profiles shown on each wall provide the optimal decrease of the instability growth rate.

the optimal blowing/suction profiles giving the largest stabilization. We see that the sensitivity is vanishing along the first free-slip boundary just downstream of the inflow ($y = 0$; $-1.2 < x < -0.4$), while a combination of blowing and suction is found to be optimal on the wall upstream of the cavity ($y = 0$; $-0.4 < x < 0$). Inside the cavity, on both lateral walls, a stabilizing normal component is directed in the streamwise direction. The optimal blowing and suction on the lower wall would create a flow opposite to the vortex inside the cavity, thus trying to quench it. The analysis, finally, shows that it is not possible to significantly modify the instability by applying control on the downstream wall (lowest sensitivity magnitude).

7. Asymptotic inviscid stability theory

The spatial distribution of the structural sensitivity (that is spatially concentrated around a streamline inside the cavity) suggests the possibility of using the local theory to describe the evolution of the instability and provide more quantitative evidence for the mechanism from which it arises. An appealing approach in this context is offered by the short-wavelength approximation (WKBJ) developed by Bayly (1988).

This approach is briefly outlined here; for a more detailed presentation the reader is referred to Lifschitz & Hameiri (1991), Lifschitz (1994) and references therein. The solution of the linearized Navier–Stokes equations is sought in the form of a rapidly oscillating and localized wave-packet evolving along the Lagrangian trajectory $\boldsymbol{X}(t)$ and characterized by a wave-vector $\boldsymbol{k}(t) = \nabla\phi(\boldsymbol{X}, t)$ and an envelope $\boldsymbol{a}(\boldsymbol{X}, t)$ such that

$$\boldsymbol{u}(\boldsymbol{X}, t) = \mathrm{e}^{\mathrm{i}\phi(\boldsymbol{X},t)/\epsilon}\boldsymbol{a}(\boldsymbol{X}, t, \epsilon) = \mathrm{e}^{\mathrm{i}\phi(\boldsymbol{X},t)/\epsilon}\sum_n \boldsymbol{a}_n(\boldsymbol{X}, t)\epsilon^n, \tag{7.1}$$

$$p(\boldsymbol{X}, t) = \mathrm{e}^{\mathrm{i}\phi(\boldsymbol{X},t)/\epsilon}b(\boldsymbol{X}, t, \epsilon) = \mathrm{e}^{\mathrm{i}\phi(\boldsymbol{X},t)/\epsilon}\sum_n b_n(\boldsymbol{X}, t)\epsilon^{n+1}, \tag{7.2}$$

where $\epsilon \ll 1$ and $\boldsymbol{X} = \epsilon\boldsymbol{x}$ is a slowly varying variable. In the limit of vanishing viscosity ($Re \to \infty$) and large wavenumbers ($\|\boldsymbol{k}\| \to \infty$), the theory provides the leading-order term for the growth rate associated with a localized perturbation. This

is obtained by integrating the following set of ordinary differential equations (ODEs):

$$\frac{\mathrm{D}\boldsymbol{k}}{\mathrm{D}t} = -\boldsymbol{L}^t(\boldsymbol{X})\boldsymbol{k}, \tag{7.3}$$

$$\frac{\mathrm{D}\boldsymbol{a}}{\mathrm{D}t} = \left(\frac{2\boldsymbol{k}\boldsymbol{k}^{\mathrm{T}}}{|\boldsymbol{k}|^2} - \boldsymbol{I}\right)\boldsymbol{L}(\boldsymbol{X})\boldsymbol{a}, \tag{7.4}$$

along the Lagrangian trajectories defined by the ODE

$$\frac{\mathrm{D}\boldsymbol{X}(t)}{\mathrm{D}t} = \boldsymbol{u}_b(X(t), t). \tag{7.5}$$

In the equations above $\boldsymbol{L} = \nabla\boldsymbol{u}_b$ is the base flow velocity gradient tensor and $\boldsymbol{I}$ the identity matrix. Since the flow under investigation is steady, the Lagrangian trajectory corresponds to the streamlines of the base flow. Three initial conditions have to be assigned to solve the problem above: $\boldsymbol{k}(t=0) = \boldsymbol{k}_0$, $\boldsymbol{a}(t=0) = \boldsymbol{a}_0$ and $\boldsymbol{x}(t=0) = \boldsymbol{x}_0$. The last condition imposes the Lagrangian origin of the streamline and thereby entirely identifies it.

Lifschitz & Hameiri (1991) proved that a sufficient condition for inviscid instability is that the system (7.3)–(7.5) has at least one solution for which $\|\boldsymbol{a}(t)\| \to \infty$ as $t \to \infty$. This theory has been successfully applied in the past to study elliptic, hyperbolic and centrifugal instabilities of two-dimensional stationary base flows (Sipp *et al.* 1999; Godeferd, Cambon & Leblanc 2001). In order to characterize the instability mechanism arising inside the cavity with this local theory, the self-excited nature of the instability must be properly accounted for. In this context, a central role is played by closed Lagrangian trajectories (closed streamlines in our case), i.e. orbits described by material points which return to their initial positions after a given time T (the period of revolution of a material particle). These closed trajectories play a special role in the dynamics of the instability: on the closed orbits, local instability waves propagate and feed back on themselves leading to a self-excited unstable mode.

To apply the theory, both (7.3) and (7.4) must be integrated along the closed orbits existing inside the cavity. Since the base flow is steady and the streamlines are closed, (7.3) is a linear ODE with periodic coefficients whose general solution can be written in terms of Floquet modes. In particular, the solution can be found by building the fundamental Floquet matrix $\boldsymbol{M}(T)$, solution of the system

$$\frac{\mathrm{D}\boldsymbol{M}}{\mathrm{D}t} = -\boldsymbol{L}^t(\boldsymbol{X})\boldsymbol{M} \quad \text{with } \boldsymbol{M}(0) = \boldsymbol{I}, \tag{7.6}$$

and extracting its eigenvalues and the corresponding eigenvectors. Using these eigenvectors as initial conditions, it is possible to retrieve the temporal evolution of $\boldsymbol{k}$ during a lap around the closed streamline. Equation (7.3) admits three independent solutions related to the three eigenvectors of the fundamental Floquet matrix $\boldsymbol{M}(T)$. However, since the base flow is two-dimensional, there exists for each orbit one eigenvalue equal to one, with the corresponding eigenvector remaining constant in time and orthogonal to the base flow. In other words, since the third column of $\boldsymbol{L}$ and the third line of $\boldsymbol{L}^t$ are zero, the transverse component of $\boldsymbol{k}$ remains constant as time evolves. In contrast, the in-plane components evolve under the action of the deformation tensor. Once (7.3) is solved, the amplitude $\boldsymbol{a}$ can be found by integrating

(7.4). One can use any linear combination of the Floquet modes from (7.6) to set the specific $\boldsymbol{k}$ in (7.4).

Since we are trying to determine a self-excited mode, we need only to consider solutions of (7.3) that are periodic in time, i.e. solutions such that $\boldsymbol{k}(0) = \boldsymbol{k}(T)$. Moreover Bayly (1988), Lifschitz & Hameiri (1991) and Sipp & Jacquin (2000) have shown that centrifugal and hyperbolic instabilities attain their maximum growth rate for modes characterized by purely transverse wavenumbers. Therefore, only eigenvectors orthogonal to the base flow will be considered in the following analysis. Solutions of (7.4) associated with a $\boldsymbol{k}$ orthogonal to the plane of motion are usually termed pressureless modes (see also Godeferd *et al.* 2001). With this choice, (7.4) reduces to an ordinary linear differential equation with periodic coefficients. According to Floquet theory, its solution can be written in terms of Floquet modes

$$\boldsymbol{a}(t) = \bar{\boldsymbol{a}}(t)\exp(\sigma t), \tag{7.7}$$

where $\bar{\boldsymbol{a}}(t)$ is a periodic function (with the same period T as the material point moving along the selected closed streamline) and $\mathrm{Re}\{\sigma\} = \sigma_r$ is the growth rate of the perturbation. In order to make a quantitative comparison with the eigenvalues predicted by the global analysis, we have to compute the values of σ in (7.7) for each closed orbit inside the cavity. To this end, we parameterize each streamline, and the corresponding growth rate σ, with the distance along the horizontal line connecting the centre of the vortex to the left-hand wall of the cavity (see figure 11).

As for (7.3), the fundamental Floquet matrix $\boldsymbol{A}$ corresponding to (7.4) is built by integrating the system

$$\frac{\mathrm{D}\boldsymbol{A}}{\mathrm{D}t} = \left(\frac{2\boldsymbol{k}\boldsymbol{k}^{\mathrm{T}}}{|\boldsymbol{k}|^2} - \boldsymbol{I}\right)\boldsymbol{L}(\boldsymbol{X})\boldsymbol{A}, \tag{7.8}$$

$$\boldsymbol{A}(0) = \boldsymbol{I}, \tag{7.9}$$

along each orbit. The eigenvalues $\mu_i(x_0)$ and the corresponding eigenvectors of $\boldsymbol{A}(T)$ are then easily extracted.

As mentioned above, since the base flow is two-dimensional and the wave-vector $\boldsymbol{k}$ is orthogonal to the x–y plane, we expect one eigenvalue of $\boldsymbol{A}$ to be 1. The other two, for the incompressibility constrain, must multiply to 1, i.e. $\mu_1(x_0)\ \mu_2(x_0) = 1$. The Floquet exponent $\sigma(x_0)$ of the perturbation on the selected orbit ψ_0 is obtained from the Floquet multiplier $\mu(x_0)$ of $\boldsymbol{A}$ by the simple relation

$$\sigma^{\{n\}}(\psi_0) = \sigma_r(\psi_0) + \mathrm{i}\sigma_i^{\{n\}}(\psi_0) = \frac{\log(\mu)}{T(\psi_0)} + \mathrm{i}\frac{2n\pi}{T(\psi_0)} \quad \text{with } n \in \mathbb{N}, \tag{7.10}$$

where $T(\psi_0)$ is the period of revolution.

The growth rate of each WKBJ mode is simply given by the real part of $\sigma^{\{n\}}$. The frequency is related to the imaginary part and is not unique. According to the formula (7.10), modes with the same growth rate (at leading order) but different frequencies are admissible: in particular the admissible frequencies are integer multiple of the frequency of revolution along the same streamline.

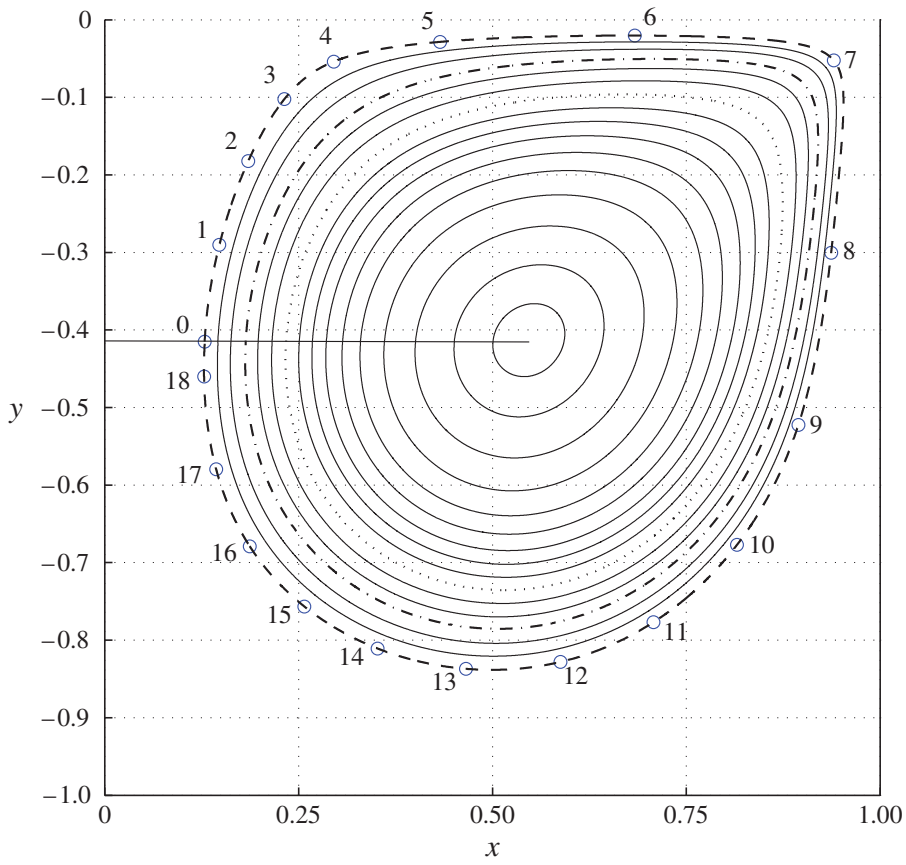

FIGURE 11. (Colour online) Streamlines for the flow inside the cavity at $Re = 1370$. The asymptotic inviscid stability theory identifies three streamlines along which three different WKBJ modes present their maximum growth rate: - - - -, orbit of the global maximum growth rate pertaining to the steady mode σ_∞ (see figure 12); — · —, orbit of the unsteady mode related to σ_2; · · · · · ·, orbit of the steady mode related to σ_3. The evolution of a particle along the streamline - - - - is also depicted. The revolution period of this streamline is $T = 18.3$. The horizontal line connecting the centre of the vortex to the left-hand wall of the cavity is used in the present work to parameterize the streamlines.

7.1. *Asymptotic estimate of the first bifurcation*

The numerical computations of the asymptotic stability are performed on the same base flow fields as used for the global stability analysis. Several numerical methods are available to solve the system of ODEs (7.5)–(7.8) along with their initial conditions. We chose a fourth-order Runge–Kutta method: starting from the points located on the horizontal line, connecting the centre of the vortex to the left-hand wall of the cavity (see figure 11), the algorithm marches along the orbits ensuring the spatial periodicity of each streamline. In the figure we also report the position of a material point along its trajectory at equal time intervals to give a visual impression of the local velocity along the streamline.

The asymptotic eigenpairs have been computed with several discretizations and only the eigenvalues with an accuracy of four significant digits are presented. In figure 12, we show the real and imaginary part of the eigenvalues obtained with the WKBJ approximation as function of the x coordinate defining the different orbits.

The asymptotic analysis reveals three maxima of the growth rates $\sigma_{r\infty}(=\sigma_{r1})$, which is also the global maximum, σ_{r2} and σ_{r3}. The first and the third branches (σ_1 and σ_3) are characterized by zero-frequency eigenvalues, while the second branch

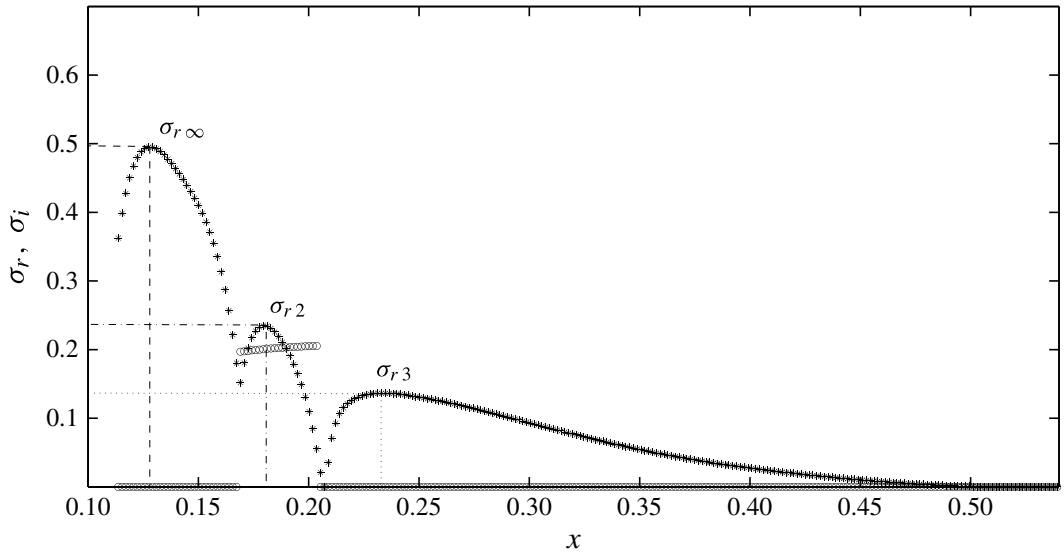

FIGURE 12. WKBJ growth rate σ_r ($*$) and eigenfrequency σ_i ($\bigcirc$) at $Re_{BF} = 1370$. Here the parameter x is the physical coordinate showed in figure 11. The lines denote the maximum of the different branches: - - - -, maximum inviscid growth rate $\sigma_{r\infty}$; — · —, maximum related to second branch σ_{r2}; · · · · · ·, third maximum σ_{r3}.

(σ_2) is associated with unstable oscillations with frequency of $\approx$0.2. As further discussed below, the closed streamline of maximum growth rate $\sigma_{r\infty}$ is located within the wavemaker of stationary unstable global mode.

However, despite this agreement, the viscous correction term and the correction term relative to finite wavenumber effects need to be taken into account for a correct prediction of the instability, see Landman & Saffman (1987) and Gallaire *et al.* (2007).

In figure 13(a) we report the growth rate of the unstable mode computed on the base flow at $Re_{BF} = 1370$ when increasing the Reynolds number in the linearized stability equations, Re_{STB}, and the growth rate obtained by integrating along the closed orbits with the corrections discussed in appendix A,

$$s = \sigma(\psi_0) - \frac{A}{k} - \frac{k^2}{Re_{BF}}. \tag{7.11}$$

The value of A above is not estimated by a least square fitting as in previous studies, but computed analytically using the information provided by the local adjoint and direct field on the streamline. The values obtained with this procedure are reported in table 2. Figure 13(a) shows that the scaling provided by the global stability analysis estimates correctly the asymptotic growth rate $\sigma_{r\infty}$. The corresponding optimal spanwise wavenumber k is depicted in 13(b) as a function of $Re_{STB}^{1/3}$. The spanwise wavenumber, like the maximal growth rate, follows the correct scaling laws, $\sigma_r \propto Re_{STB}^{-1/3}$ and $k_{opt} \propto Re_{STB}^{1/3}$ (Bayly 1988; Sipp *et al.* 1999).

Finally, we focus our attention on the spatial distribution of the structural sensitivity fields computed with the maximum Re_{STB} considered (equal to 300 000). Figure 14(a) shows the agreement between the critical streamline (i.e. the streamline ψ where the inviscid growth rate is maximum) and the sensitivity map. At large (stability) Reynolds numbers Re_{STB}, therefore, the sensitivity analysis indicates that the instability core is located on the orbit with maximum growth rate.

The global analysis performed at Re_{BF} also provides information about the sub-critical branches arising in the asymptotic computations. We depict the structural

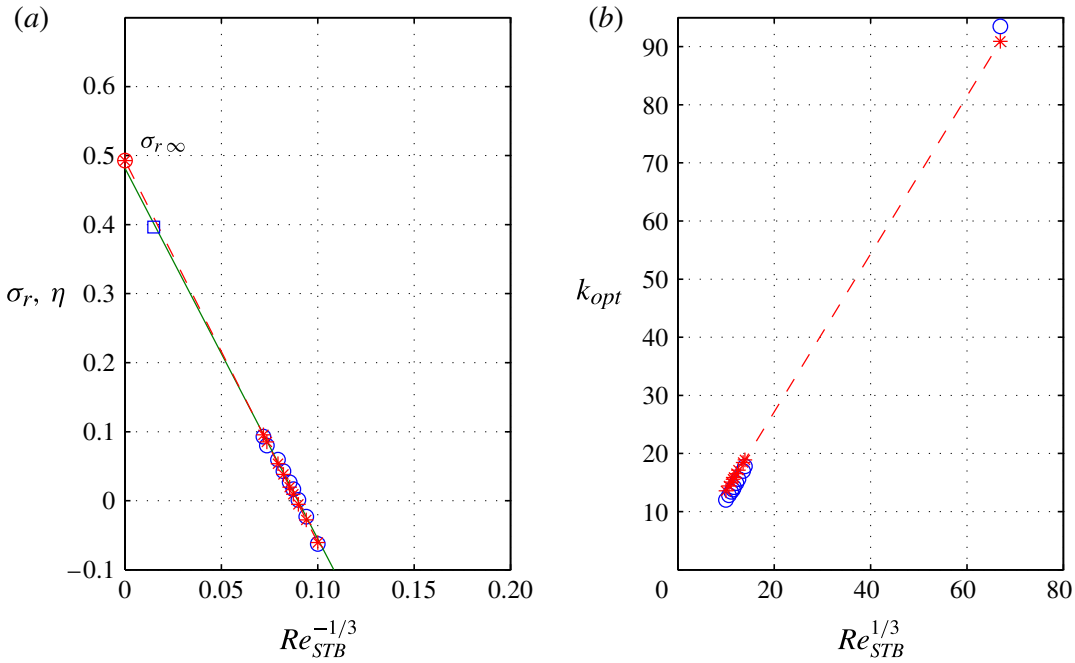

FIGURE 13. (Colour online) Global and asymptotic stability results. (*a*) Viscous growth rate η (○, □ $= Re_{STB} = 300\,000$) at $Re_{BF} = 1370$ and asymptotic estimate of growth rate σ_r (∗- - - -) according to the correction in appendix A. We also depict the regression line (——) related to the global growth rates. (*b*) Optimal global spanwise wavenumber k_{opt} (○) and prediction from the asymptotic theory (∗) as a function of $Re_{STB}^{1/3}$. The predicted optimal spanwise wavenumber is simply obtained by finding the maximum of the scaling law (A 6), i.e. $k = (Re_{STB}A/2)^{1/3}$.

Δt_{orbit}	k	$\mathscr{J}$	A
0.0050	13.4	0.00637	5.1143
0.0025	13.4	0.00678	5.0148
0.0010	13.4	0.00681	5.0078

TABLE 2. Convergence of parameters arising in the asymptotic estimation (see appendix A) of the viscous growth rate; Δt_{orbit} is the step used to discretize the critical orbit. (Here, $Re_{BF} = 1370$).

sensitivity extracted from the global analysis of these two sub-critical WKBJ eigenmodes in figure 14(*b*,*c*). As for the leading eigemode we observe an excellent correspondence between the sensitivity spatial map and the two critical orbits. Interestingly, we note also the agreement between the frequency of mode σ_2 (see figure 14*b*) and the frequency predicted by the WKBJ analysis. From a physical point of view, this matching can be associated with the fact that these eigenmodes are of centrifugal nature, i.e. inviscid, and therefore the inviscid structural sensitivity is able to isolate accurately the regions where each of the three instability branches presents the main contribution to the instability mechanism.

7.2. *Asymptotic results for* $Re_{BF} = 4140$

As previously discussed, when we consider the stability to three-dimensional perturbations at supercritical Reynolds numbers, we find several unstable branches

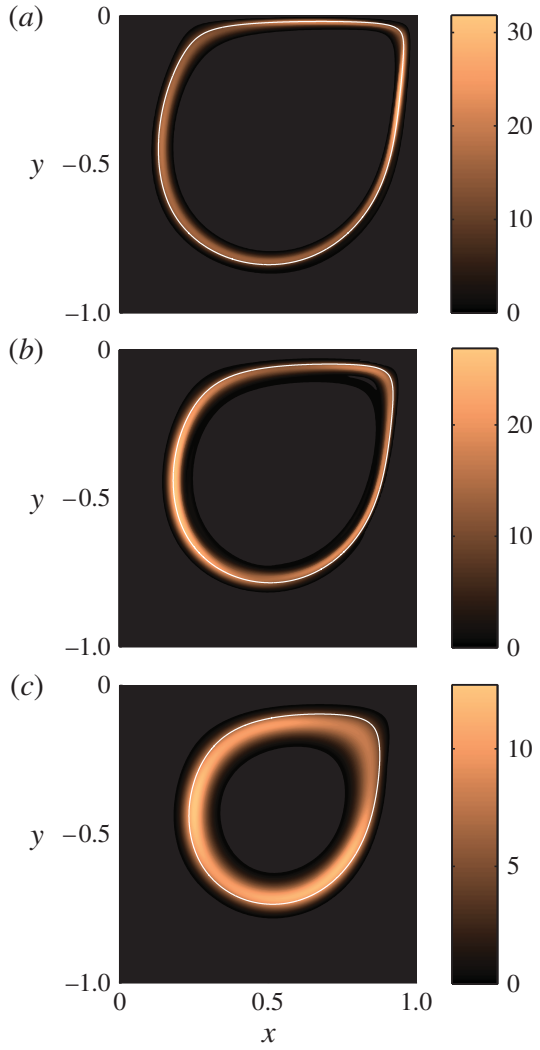

FIGURE 14. (Colour online) Comparison between the optimal streamline of WKBJ branches and sensitivity maps related to (global) eigenvalues: (*a*) $0.36 + \mathrm{i}0.00$; (*b*) $0.14 + \mathrm{i}0.20$; (*c*) $0.07 + \mathrm{i}0.00$. Parameter settings: $Re_{BF} = 1370$, $Re_{STB} = 300\,000$ and $k = 93.5$.

(see figure 3). If we consider the spanwise wavenumber $k = 22$ and $Re_{BF} = 4140$, we observe the occurrence of several harmonics of the fundamental leading eigenvalue. As shown in figure 3(*b*), these modes are characterized by a quantized eigenfrequency, $\omega \approx 0.32n$ with n integer. To show that the asymptotic analysis is also able to accurately predict the frequency of these harmonics, we carry out computations for the base flow at Reynolds number $Re_{BF} = 4140$ and report the results in figure 15, using the same conventions used for the onset of the bifurcation, for $Re_{BF} = 1370$, in figure 12. We first need to identify the closed streamlines and then calculate the instability properties along the orbit. We observe again three local maxima of the asymptotic growth rate, corresponding to two steady and one time-dependent modes.

The variation of the revolution period T as a function of the coordinate x, defining the different orbits, is depicted in the upper half of figure 16, while the corresponding orbits inside the cavity are displayed in the lower half. The main result we present here is that the period of the higher harmonics of the zero-frequency leading mode is selected by the period of revolution along the streamline of maximum growth rate. In table 3 we show that the frequencies obtained from the global stability analysis and

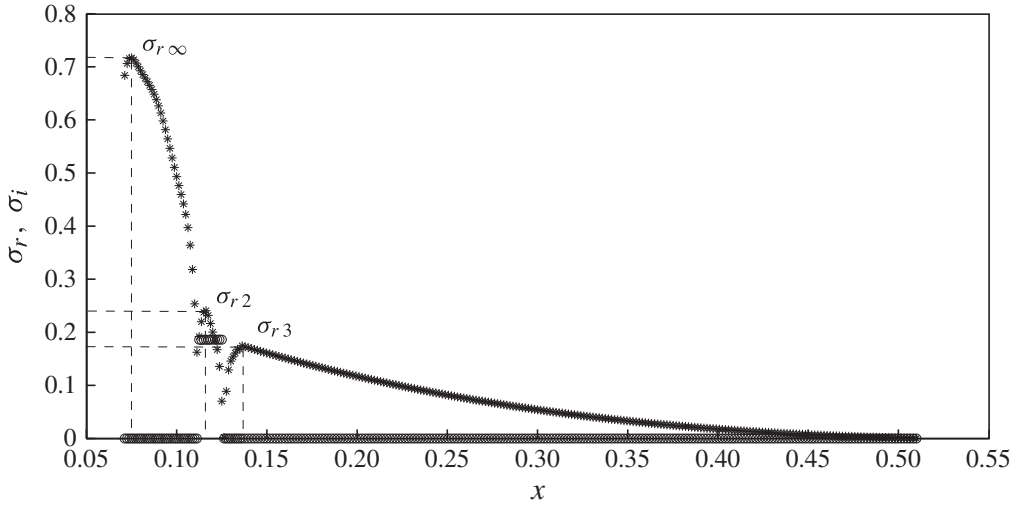

FIGURE 15. Asymptotic results for $Re_{BF} = 4140$. See figure 12 for details.

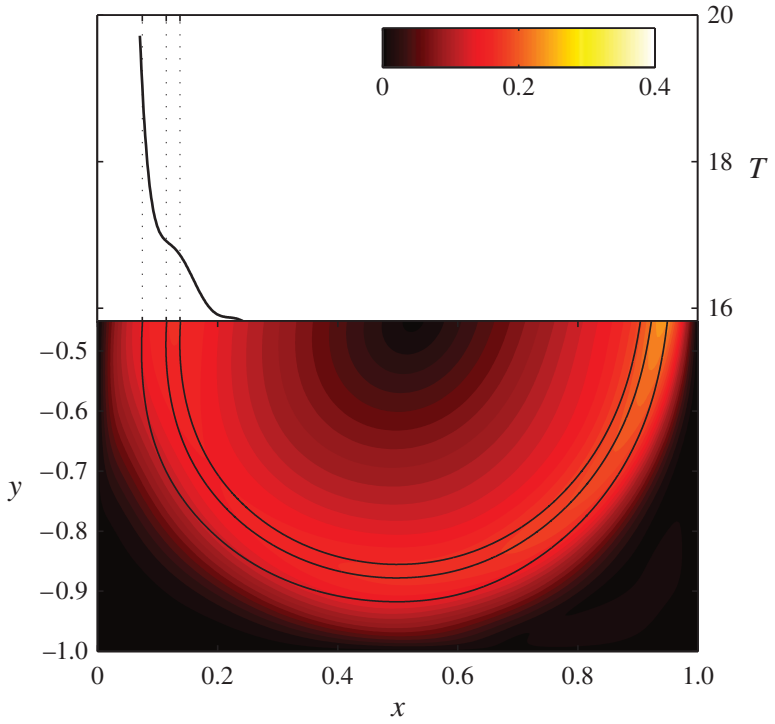

FIGURE 16. (Colour online) Revolution period of cavity orbits as a function of the abscissa x (upper half). Contour plot of the base flow modulus ($\|\boldsymbol{u}_b\|_2$) at $Re_{BF} = 4140$ and the three streamlines corresponding to the local maxima of the inviscid growth rate in figure 15 (lower half).

displayed in figure 3 do indeed correspond to the frequency computed by the local analysis (7.10). It is interesting to note that the global mode frequencies are uniquely related to the revolution period of a Lagrangian particle transported along the orbit. Thus, we conclude that the different frequencies of the multiple unstable branches are obtained as multiples n of the period of revolution along the critical (most unstable) orbit; the data in the table show an error lower than 5 %.

Harmonic n	Global mode frequency ω	Orbit period T	WKBJ frequency $\sigma_i^{\{n\}}(\psi_0) = 2n\pi/T$	Percentage error (%)
0	0.000	19.5	0.00	—
1	0.302	19.5	0.32	4.2
2	0.610	19.5	0.64	4.7
3	0.920	19.5	0.96	4.5

TABLE 3. Comparison of the results obtained using global stability analysis with those provided by the asymptotic analysis. We selected the orbit that has the maximum inviscid growth rate using a base flow characterized by $Re_{BF} = 4140$. The WKBJ frequencies are calculated according to (7.10).

8. Final remarks

In this work, we study the instability of the flow past an infinitely wide open square cavity. First, we identify the critical Reynolds number ($Re_{BF} = 1370$) at which the first bifurcation occurs. This instability drives the flow from a steady two-dimensional to a steady three-dimensional configuration characterized by a relatively short modulation in the spanwise direction, the spanwise scale of the modulation being of about 0.47 cavity depths.

The spatial structure of the direct and adjoint eigenmodes is examined to describe the features of the flow past the bifurcation. The direct mode is concentrated inside the cavity in a circular region with a tail on the shear region just above the downstream wall; the adjoint mode has a similar structure except for a small region near the upstream edge of the cavity where the flow is most receptive to momentum forcing. The overlapping of these two fields provides information about the instability mechanism (the so-called wavemaker) and is concentrated within the square cavity, suggesting that the generation of the instability mechanism is spatially concentrated around a closed streamline inside the cavity, around the core vortex.

We examine different types of cavity flows (i.e. characterized by different boundary conditions) and identify the corresponding critical Reynolds number at which the first bifurcation occurs. As proposed by Brés & Colonius (2008), we confirm that the mean velocity computed along the line connecting the two opposite edges allows us to roughly estimate the critical conditions at which the first bifurcation arises. The critical value of a Reynolds number based on this averaged velocity, the cavity depth and the fluid viscosity is found to be $Re_{av} \approx 470$.

The sensitivity to base flow modifications is then considered to study the mechanisms that can suppress or enhance the instability. We follow here the approach by Meliga & Chomaz (2011) and compute the optimal linear velocity distribution at the walls and at the inlet of the computational domain able to stabilize the flow. The resulting blowing/suction profiles show that each modification (when possible) is aimed at decreasing the total momentum of the cavity core vortex (identified above as the core of the instability).

The WKBJ approximation is then introduced to predict the first instability and its characteristics as suggested by Bayly (1988). Considering the asymptotic stability along the closed streamlines inside the cavity, we find three different branches of unstable orbits (two stationary branches and an unsteady branch) and select the three critical orbits ψ whose corresponding growth rates are local maxima ($\sigma_{r\infty}$, σ_{r2}, σ_{r3}). The asymptotic values of the growth rate and of the spanwise wavenumber of the

unstable modes show very good agreement with the global stability analysis once the correction for finite Reynolds number and spanwise length scale are applied to the inviscid asymptotic result. The three critical orbits detected by the asymptotic analysis are also shown to overlap with the structural sensitivity map of unstable modes at low viscosities, large Re_{STB} (we refer to this field as inviscid structural sensitivity). This procedure allows us to identify the spatial region where the core of the inviscid mechanism of the instability is located.

To identify a frequency selection mechanism for the time-dependent sub-leading unstable global modes emerging at supercritical conditions, we consider the stability of the flow at $Re_{BF} = 4140$ where the global analysis shows the occurrence of four branches of unstable modes characterized by frequencies that are multiples of a fundamental value ω_0. We show that the value of ω_0 corresponds to the period of revolution of Lagrangian fluid particles along the closed orbit of largest growth rate in the asymptotic limit. We thus conclude that the asymptotic theory is able to predict accurately the global stability results, enabling us to estimate the critical conditions leading to the instability. Furthermore, the inviscid structural sensitivity, discussed here, is a general concept that can be used whenever the instability is of inviscid type.

Appendix A. Construction of pressureless modes

In what follows we briefly recall the theory related to the dynamics of asymptotic modes (Bayly 1988). First of all, we express the evolution of the perturbation using the normal-mode ansatz

$$[\boldsymbol{u}', P'] = [\hat{\boldsymbol{u}}, \hat{P}] \exp\{\mathrm{i}kz + st\}. \tag{A 1}$$

The main idea is to use the eigenpairs of the fundamental Floquet matrix $\boldsymbol{M}(T)$ to build a vector basis $\boldsymbol{f}_i$ for the representation of the modes along the orbit:

$$\hat{\boldsymbol{u}}(\boldsymbol{x}) = \sum_{i=1}^{3} \hat{u}_i(\boldsymbol{x}) \boldsymbol{f}_i(\boldsymbol{x}). \tag{A 2}$$

This basis diagonalizes the nonlinear operator $\boldsymbol{u}_b \cdot \nabla(\,) + (\,) \cdot \nabla \boldsymbol{u}_b$ and can be computed as $\boldsymbol{f}_i = \mathrm{e}^{-\sigma t} \boldsymbol{M}(t) \boldsymbol{e}_i$. Considering the limit of $\|\boldsymbol{k}\| \to \infty$, we re-scale the WKBJ eigenmode as

$$[\hat{\boldsymbol{u}}, \hat{\boldsymbol{v}}, \hat{\boldsymbol{w}}, \hat{\boldsymbol{p}}](\tilde{\Psi}) = [\hat{\boldsymbol{U}}, \hat{\boldsymbol{V}}/k, \hat{\boldsymbol{w}}/\sqrt{k}, \hat{\boldsymbol{p}}/k\sqrt{k}](\tilde{\Psi}), \tag{A 3}$$

where the new streamfunction $\tilde{\Psi} = \sqrt{k}(\psi - \psi_0)$ allows us to magnify the region near the critical orbit ψ_0. Introducing the scaling (A 3) into the LEes, we get the equation of a quantum harmonic oscillator (see e.g. Bender & Orszag 1978)

$$\hat{\boldsymbol{U}}''(\tilde{\Psi}) + \left[\frac{A}{\mathscr{J}(\psi_0)} - \lambda^2 \tilde{\Psi}^2 \right] \hat{\boldsymbol{U}} = 0, \tag{A 4}$$

with $\hat{\boldsymbol{U}}(\pm\infty) = 0$, $\lambda^2 = -\sigma''(\psi_0)/(2\mathscr{J})$ and

$$\mathscr{J} = \frac{1}{T(\psi_0)} \int_0^{T(\psi_0)} (\boldsymbol{f}_1^{\dagger} \cdot \nabla\psi) \left[\sigma(\psi_0) + \frac{\mathrm{d}}{\mathrm{d}t} \right] \{\boldsymbol{f}_1 \cdot \nabla\psi\} \mathrm{d}t. \tag{A 5}$$

In (A 4), the constant A is the parameter that governs the scaling of the eigenvalue s (i.e. $s = \sigma(\psi_0) - A/k$) and the adjoint vector $\boldsymbol{f}_i^\dagger$ is normalized as $\boldsymbol{f}_i^\dagger \cdot \boldsymbol{f}_j = \delta_{ij}$.

A better quantitative estimate of the viscous growth rate can be achieved using the viscous correction introduced by Landman & Saffman (1987) (see also Gallaire *et al.* 2007). The composite estimation thus reads

$$s = \sigma(\psi_0) - \frac{A}{k} - \frac{k^2}{Re_{BF}}. \tag{A 6}$$

REFERENCES

ALBENSOEDER, S. & KUHLMANN, H. C. 2006 Nonlinear three-dimensional flow in the lid-driven square cavity. *J. Fluid Mech.* **569**, 465–480.

ALBENSOEDER, S., KUHLMANN, H. C. & RATH, H. J. 2001 Three-dimensional centrifugal-flow instabilities in the lid-driven-cavity problem. *Phys. Fluids* **13**, 121–136.

AMESTOY, P. R., DUFF, I. S., KOSTER, J. & L'EXCELLENT, J.-Y. 2001 A fully asynchronous multifrontal solver using distributed dynamic scheduling. *SIAM J. Matrix Anal. Applics.* **23** (1), 15–41.

AMESTOY, P. R., GUERMOUCHE, A., L'EXCELLENT, J.-Y. & PRALET, S. 2006 Hybrid scheduling for the parallel solution of linear systems. *Parallel Comput.* **32** (2), 136–156.

ARNOLDI, W. E. 1951 The principle of minimized iteration in the solution of the matrix eigenproblem. *Q. Appl. Maths* **9**, 17–29.

BARBAGALLO, A., SIPP, D. & SCHMID, P. J. 2009 Closed-loop control of an open cavity flow using reduced-order models. *J. Fluid Mech.* **641**, 1–50.

BAYLY, B. J. 1988 Three-dimensional centrifugal-type instabilities in inviscid two-dimensional flows. *Phys. Fluids* **31**, 56–64.

BAYLY, B. J. 1989 Computations of broad-band instabilities in a class of closed-streamline flows. In *Mathematical Aspects of Vortex Dynamics* (ed. R. E. Caflisch), Society for Industrial and Applied Mathematics.

BENDER, C. M. & ORSZAG, S. A. 1978 *Advanced Mathematical Methods For Scientists and Engineers*. McGraw-Hill.

BOTTARO, A., CORBETT, P. & LUCHINI, P. 2003 The effect of base flow variation on flow stability. *J. Fluid Mech.* **476**, 293–302.

BRÉS, G. A. & COLONIUS, T. 2007*a* Direct numerical simulations of three-dimensional cavity flows. *AIAA Paper* 2007-3405.

BRÉS, G. A. & COLONIUS, T. 2007*b* Three-dimensional linear stability analysis of cavity flows. *AIAA Paper* 2007-1126.

BRÉS, G. A. & COLONIUS, T. 2008 Three-dimensional instabilities in compressible flow over open cavities. *J. Fluid Mech.* **599**, 309–339.

DI CICCA, G. M., MARTINEZ, M., HAIGERMOSER, C. & ONORATO, M. 2013 Three-dimensional flow features in a nominally two-dimensional rectangular cavity. *Phys. Fluids* **25**, 097101.

DING, Y. & KAWAHARA, M. 1998 Linear stability of incompressible flow using a mixed finite element method. *J. Comput. Phys.* **139**, 243–273.

FAURE, T. M., ADRIANOS, P., LUSSEYRAN, F. & PASTUR, L. 2007 Visualization of the flow inside an open cavity at medium range Reynolds numbers. *Exp. Fluids* **42**, 169–184.

FAURE, T. M., PASTUR, L., LUSSEYRAN, F., FRAIGNEAU, Y. & BISCH, D. 2009 Three-dimensional centrifugal instabilities development inside a parallelepipedic open cavity of various shape. *Exp. Fluids* **47**, 395–410.

GALLAIRE, F., MARQUILLIE, M. & EHRENSTEIN, U. 2007 Three-dimensional tranverse instabilities in detached boundary layers. *J. Fluid Mech.* **571**, 221–233.

GHARIB, M. & ROSHKO, A. 1987 The effect of flow oscillations on cavity drag. *J. Fluid Mech.* **177**, 501–530.

GIANNETTI, F. 2015 WKBJ analysis in the periodic wake of a cylinder. *Theor. Appl. Mech. Lett.*; accepted for publication.

GIANNETTI, F. & LUCHINI, P. 2007 Structural sensitivity of the first instability of the cylinder wake. *J. Fluid Mech.* **581**, 167–197.

GIANNETTI, F., LUCHINI, P. & MARINO, L. 2010 Characterization of the three-dimensional instability in a lid-driven cavity by an adjoint based analysis. In *Seventh IUTAM Symposium on Laminar-Turbulent Transition* (ed. P. Schlatter & D. S. Henningson), IUTAM Bookseries, vol. 18, pp. 165–170. Springer.

GODEFERD, F. S., CAMBON, C. & LEBLANC, S. 2001 Zonal approach to centrifugal, elliptic and hyperbolic instabilities in Stuart vortices with external rotation. *J. Fluid Mech.* **449**, 1–37.

GONZALEZ, L. M., AHMED, M., KÜHNEN, J., KUHLMANN, H. C. & THEOFILIS, V. 2011 Three-dimensional flow instability in a lid-driven isosceles triangular cavity. *J. Fluid Mech.* **675**, 369–396.

GUERMOND, J. L., MIGEON, C., PINEAU, G. & QUARTAPELLE, L. 2002 Start-up flows in a three-dimensional rectangular driven cavity of aspect ratio 1:1:2 at $Re = 1000$. *J. Fluid Mech.* **450**, 169–199.

HAQUE, S., LASHGARI, I., GIANNETTI, F. & BRANDT, L. 2012 Stability of fluids with shear-dependent viscosity in the lid-driven cavity. *J. Non-Newtonian Fluid Mech.* **173–174**, 49–61.

HECHT, F. 2012 New development in freefem++. *J. Numer. Maths* **20**, 251–265.

LANDMAN, M. J. & SAFFMAN, P. 1987 The three-dimensional instability of strained vortices in a viscous fluid. *Phys. Fluids* **30**, 2339–2342.

LASAGNA, D., DONELLI, R., GREGORIO, F. D. & IUSO, G. 2011 Effect of a trapped vortex cell on a thick wing airfoil. *Exp. Fluids* **51**, 1369–1384.

LEHOUCQ, R., MASCHHOFF, K., SORENSEN, D. & YANG, C. 2007 Arpack software. website: http://www.caam.rice.edu/software/arpack/.

LIFSCHITZ, A. 1994 On the instability of certain motions of an ideal incompressible fluid. *Adv. Appl. Maths* **15**, 404–436.

LIFSCHITZ, A. & HAMEIRI, E. 1991 Local stability conditions in fluid dynamics. *Phys. Fluids* A **3**, 2644–2651.

LUCHINI, P. & BOTTARO, A. 2014 Adjoint equations in stability analysis. *Annu. Rev. Fluid Mech.* **46** (1), 493–517.

MARQUET, O., SIPP, D. & JACQUIN, L. 2008 Sensitivity analysis and passive control of cylinder flow. *J. Fluid Mech.* **615**, 221–252.

MAULL, D. J. & EAST, L. F. 1963 Three-dimensional flow in cavities. *J. Fluid Mech.* **16**, 620–632.

MELIGA, P. & CHOMAZ, J. M. 2011 Global modes in a confined impinging jet: application to heat transfer and control. *Theor. Comput. Fluid Dyn.* **25**, 179–193.

MESEGUER-GARRIDO, F., DE VICENTE, J., VALERO, E. & THEOFILIS, V. 2014 On linear instability mechanism in incompressible open cavity flow. *J. Fluid Mech.* **752**, 219–236.

MIGEON, C., PINEAU, G. & TEXIER, A. 2003 Three-dimensionality development inside standard parallelepipedic lid-driven cavities at $Re = 1000$. *J. Fluids Struct.* **17**, 717–738.

MIGEON, C., TEXIER, A. & PINEAU, G. 2000 Effects of lid-driven cavity shape on the flow establishment phase. *J. Fluids Struct.* **14**, 469–488.

PRALITS, J. O., BRANDT, L. & GIANNETTI, F. 2010 Instability and sensitivity of the flow around a rotating circular cylinder. *J. Fluid Mech.* **650**, 513–536.

ROCKWELL, D. & KNISELY, C. 1980 Observations of the three-dimensional nature of unstable flow past a cavity. *Phys. Fluids* **23**, 425–431.

ROCKWELL, D. & NAUDASCHER, E. 1978 Review – self-sustaining oscillations of flow past cavities. *Trans. ASME: J. Fluids Engng* **100**, 152–165.

ROSSITER, J. E. 1964 Wind-tunnel experiments on the flow over rectangular cavities at subsonic and transonic speeds. *Tech. Rep.* 3438, http://naca.central.cranfield.ac.uk/reports/arc/rm/3438.pdf.

ROWLEY, C. W., COLONIUS, T. & BASU, A. J. 2002 On self-sustained oscillations in two-dimensional compressible flow over rectangular cavities. *J. Fluid Mech.* **455**, 315–346.

SHATROV, V., MUTSCHKE, G. & GERBETH, G. 2003 Three-dimensional linear stability analysis of lid-driven MHD cavity flow. *Phys. Fluids* **15**, 2141–2151.

SIPP, D. 2012 Open-loop control of cavity oscillations with harmonic forcings. *J. Fluid Mech.* **708**, 439–468.

SIPP, D. & JACQUIN, L. 2000 Three-dimensional centrifugal-type instabilities of two-dimensional flows in rotating systems. *Phys. Fluids* **12**, 1740–1748.

SIPP, D., LAUGA, E. & JACQUIN, L. 1999 Vortices in rotating systems: centrifugal, elliptic and hyperbolic type instabilities. *Phys. Fluids* **11**, 3716–3728.

SIPP, D. & LEBEDEV, A. 2007 Global stability of base and mean flows: a general approach and its applications to cylinder and open cavity flows. *J. Fluid Mech.* **593**, 333–358.

THEOFILIS, V. 2000 Globally unstable basic flows in open cavities. *AIAA Paper* 00-1965.

DE VICENTE, J., BASLEY, J., MESEGUER-GARRIDO, F., SORIA, J. & THEOFILIS, V. 2014 Three-dimensional instabilities over a rectangular open cavity: from linear stability analysis to experimentation. *J. Fluid Mech.* **748**, 189–220.

DE VICENTE, J., RODRIGUEZ, D., THEOFILIS, V. & VALERO, E. 2010 Stability analysis in spanwise-periodic double-sided lid-driven cavity flows with complex cross-sectional profiles. *Comput. Fluids* **43**, 143–153.

YAMOUNI, S., SIPP, D. & JACQUIN, L. 2013 Interaction between feedback aeroacoustic and acoustic resonance mechanisms in a cavity flow: a global stability analysis. *J. Fluid Mech.* **717**, 134–165.

ZHANG, K. & NAGUIB, A. M. 2006 Dispersion relation and mode selectivity in low-Mach-number cavity flows. *AIAA Paper* 2006-3229.

ZHANG, K. & NAGUIB, A. M. 2008 Effect of cavity width on the unsteady pressure in a low-Mach-number cavity. *AIAA J.* **46**, 1878–1880.

ZHANG, K. & NAGUIB, A. M. 2011 Effect of finite cavity width on flow oscillation in a low-Mach-number cavity flow. *Exp. Fluids* **51**, 1209–1229.

Paper 4

European Journal of Mechanics B/Fluids 50 (2015) 1–8

Contents lists available at ScienceDirect

European Journal of Mechanics B/Fluids

journal homepage: www.elsevier.com/locate/ejmflu

Multiple-scale approximation of instabilities in unsteady boundary layers

Vincenzo Citro *, Paolo Luchini

DIIN, Universitá degli Studi di Salerno, Via Giovanni Paolo II, 84084 Fisciano (SA), Italy

ARTICLE INFO

Article history:
Received 27 December 2013
Received in revised form
10 October 2014
Accepted 27 October 2014
Available online 4 November 2014

Keywords:
Unsteady boundary layer
Ray theory
Eikonal equation

ABSTRACT

A general procedure is developed to study the stability of unsteady boundary layers using complex-ray theory. The propagation of small disturbances is described by a high-frequency (optical) approximation similar to the one adopted for wave propagation in nonuniform media. The ray trajectories, formally defined as the characteristic lines of the eikonal equation, are described by a system of first-order differential equations. These lines are complex valued and provide the main contribution to the propagation of the wave (its Green's function). As an application, we present the analysis of the flow past on an oscillating airfoil. The propagation of a harmonic disturbance inside the boundary layer is considered and some numerical transition-prediction results are discussed.

1. Introduction

Ever since Ludwig Prandtl introduced the notion of boundary layer, the study of the stability of boundary-layer flows has been of primary importance. In the analysis of steady two-dimensional boundary layers several approaches have been proposed in order to analyze the propagation of small disturbances [1]. Initially the analysis focused on parallel flows, neglecting the growth of the boundary layer thickness [2]. Subsequently, many efforts were made to improve the approximation by considering non-parallel effects (see e.g. Gaster [3]). In this context, Saric and Nayfeh [4] successfully took into account variations of the mean flow and of the disturbance amplitude along the streamwise direction. They considered the stability of the Falkner–Skan and Blasius flow and, in this last case, they found agreement between their neutral stability curve and the available experimental data.

The spatial and temporal evolution of wave packets inside three-dimensional boundary layers aroused a large interest in the following decades. The flow past swept wings is a classical example in aerodynamics. As a consequence of the three-dimensionality, the spanwise wavenumber of the disturbance is generally not constant. The onset of linear instability, in the case of swept wings, was investigated by Cebeci and Stewartson [5] and Herbert and Bertolotti [6] among others. De Matteis et al. [7] formulated the stability problem on swept wings by means of the theory of complex rays in dispersive and anisotropic media.

This theory is employed in many fields of physics, such as radio-wave propagation and attenuation in the ionosphere [8,9], diffraction of Gaussian beams [10] and excitation of surface waves [11]. In the context of the linearized Navier–Stokes equations, it was used for the first time by Itoh [12]. He applied the *kinematic wave theory* of Whitham [13], obtaining a homogeneous problem that was solved by the method of characteristics. The problem of boundary-layer receptivity to a mixing of different disturbances [14,15], furthermore, was solved by Zuccher [16] using ray theory. More recently this theory was employed by Gréa [17] to study the occurrence of caustics in boundary layers.

Here, we focus our attention on the stability of *unsteady* two-dimensional boundary layers. The study of the linear stability of this kind of flows is of interest in many industrial applications such as helicopter rotors or wind turbines, and is related to a variety of physiological processes like blood flow through arteries.

A classical example of unsteady shear-layer flows is the Stokes layer, i.e. a shear layer generated by imposed harmonic oscillations of an infinite flat plate. Because the base flow is periodic in time, Floquet theory was initially used to study the linear stability of this problem [18]. Unfortunately, this attempt produced a considerable discrepancy with experiments [19]. Vittori and Verzicco [20] showed that, for practical disturbance amplitudes, Floquet theory is not able to predict the instability of Stokes layers because, owing to the large growth that occurs during a part of the cycle, the instability directly attains the non-linear stage, thus making the linear Floquet theory inapplicable. Therefore, in such kind of flows, the only alternative to direct numerical simulation (DNS), up to now, is to use a quasi-steady approach.

* Corresponding author.
E-mail address: vcitro@unisa.it (V. Citro).

http://dx.doi.org/10.1016/j.euromechflu.2014.10.004
0997-7546/

The aims of the present work are (i) to provide a general procedure, based on complex-ray theory, that describes the propagation of disturbance wave trains in a *generic* (periodic or even non periodic) unsteady, three-dimensional boundary layer, and (ii) to provide an application to a two-dimensional time-periodic flow (arising in oscillating airfoil problems) that, in addition, allows us to estimate the error introduced using a quasi-steady approach in the stability analysis.

The present paper is structured in the following way. Firstly, we present the problem formulation in the case of a generic unsteady boundary-layer flow. The equations for the infinitesimally small perturbations are obtained and a multiple-scale analysis is performed. Subsequently, the dispersion relation of the leading-order problem is introduced and the ray equations are derived. The problem of analytical continuation, and a possible alternative, is also discussed in detail. As an application, we perform the stability analysis of the boundary layer past an oscillating Kármán–Trefftz airfoil and show some transition-prediction results.

2. Problem formulation

We investigate the stability characteristics of a generic unsteady, three-dimensional boundary layer flow. The coordinate system has the x axis in the streamwise direction, the y axis normal to the wall and the z axis orthogonal to the first two. The motion of a viscous fluid that has constant density ρ and constant kinematic viscosity ν is governed by the incompressible Navier–Stokes equations written in non-dimensional form, as

$$U_x + V_y + W_z = 0, \tag{1a}$$

$$U_t + UU_x + VU_y + WU_z + P_x = \frac{1}{\mathrm{Re}}(U_{xx} + U_{yy} + U_{zz}) \tag{1b}$$

$$V_t + UV_x + VV_y + WV_z + P_y = \frac{1}{\mathrm{Re}}(V_{xx} + V_{yy} + V_{zz}) \tag{1c}$$

$$W_t + UW_x + VW_y + WW_z + P_z = \frac{1}{\mathrm{Re}}(W_{xx} + W_{yy} + W_{zz}) \tag{1d}$$

where $\boldsymbol{U}(\boldsymbol{x}, t)$ is the velocity field, with components U, V, W and $P(\boldsymbol{x}, t)$ is the reduced pressure. The Reynolds number $\mathrm{Re} = L_{ref}U_{ref}/\nu$ is based on the, yet unspecified, reference length L_{ref} and velocity U_{ref}.

2.1. Linear stability analysis

The onset of instability is studied within the framework of linear theory. We consider three-dimensional infinitesimal disturbances superposed to a two-dimensional unsteady base flow and decompose the total velocity $\boldsymbol{U}$ and pressure P fields as

$$\boldsymbol{U}(x, y, z, t) = [u^b, v^b, 0](x, y, t) + [u', v', w'](x, y, z, t), \tag{2a}$$

$$P(x, y, z, t) = p^b(x, y, t) + p'(x, y, z, t), \tag{2b}$$

where superscript b denotes a base-flow quantity and the prime denotes a disturbance quantity. Introducing this decomposition into (1), we obtain two problems describing the base flow and the evolution of the unsteady perturbation. In what follows, we shall only retain first-order terms in the disturbance quantities. The perturbed field is then described by the following set of linearized unsteady Navier–Stokes equations (LNSE)

$$u'_x + v'_y + w'_z = 0, \tag{3a}$$

$$u'_t + u^b u'_x + v^b u'_y + u' u^b_x + v' u^b_y + w' u^b_z + p'_x = \frac{1}{\mathrm{Re}}(u'_{xx} + u'_{yy} + u'_{zz}) \tag{3b}$$

$$v'_t + u^b v'_x + v^b v'_y + u' v^b_x + v' v^b_y + w' v^b_z + p'_y = \frac{1}{\mathrm{Re}}(v'_{xx} + v'_{yy} + v'_{zz}) \tag{3c}$$

$$w'_t + u^b w'_x + v^b w'_y + p'_z = \frac{1}{\mathrm{Re}}(w'_{xx} + w'_{yy} + w'_{zz}). \tag{3d}$$

The base flow $\boldsymbol{u}^b, p^b$ is supposed to be known without any approximation.

If the flow is parallel, L_{ref} is the vertical characteristic length scale and the system (3) has an exact exponential solution with a finite characteristic wavelength of the perturbation ℓ_{pert} in the streamwise direction which may, in general, not coincide with L_{ref}. We assume the flow to be quasi-parallel, i.e. the velocity to vary slowly in x over a characteristic length scale ℓ_{bf} much larger than either L_{ref} or the perturbation length scale ℓ_{pert}. We assume, furthermore, that the characteristic length scale of the base flow in the direction z is also ℓ_{bf}, and that the characteristic time scale is ℓ_{bf}/U_{ref}.

Thus, we introduce the small parameter $\epsilon = L_{ref}/\ell_{bf}$ and consider the base flow as a function of (X, y, Z, T) where

$$X = \epsilon x, \qquad Z = \epsilon z, \qquad T = \epsilon t. \tag{4}$$

As a direct consequence of the continuity equation (1a), the base-flow component v^b is of order ϵ and can be written as $v^b = \epsilon V^b(X, y, Z, T)$.

We do not make any additional assumption on the motivation why the base flow has different scales in the streamwise and wall-normal direction; thus, ϵ and the Reynolds number Re are independent parameters.

Even when the base flow is unsteady a multiple-scale approximation can be used to study the evolution of the instability just as Gaster [3] and others did in the past for the corresponding steady problem. The multiple-scale approach originates from the high frequency (optical) approximation of linear dispersive waves. According to this method, the perturbation field $\boldsymbol{q}'$ is expressed in the form of the Wentzel–Kramers–Brillouin (WKB) [21] asymptotic expansion:

$$\boldsymbol{q}'(X, y, Z, T) = e^{i\frac{\Theta(X,Z,T)}{\epsilon}} \sum_{k=0}^{\infty} \hat{\boldsymbol{q}}_k(X, y, Z, T)\epsilon^k \tag{5}$$

where $\boldsymbol{q}' = [u', v', w', p']$, $\hat{\boldsymbol{q}}_k = [\hat{u}_k, \hat{v}_k, \hat{w}_k, \hat{p}_k]$ and Θ is named the eikonal function; its spatial and temporal derivatives respectively represent the local wavenumber components and the frequency of the perturbation. The following notation is used for such quantities

$$\alpha = -\frac{\partial\Theta}{\partial X}, \qquad \beta = -\frac{\partial\Theta}{\partial Z}, \qquad \omega = \frac{\partial\Theta}{\partial T}. \tag{6}$$

Substituting the above expansion (5) into the perturbation equations (3), taking into account the relation (4) and grouping terms multiplied by the same power of ϵ, a hierarchy of equations is obtained. The leading-order approximation is governed by the following differential problem, formally identical to the one corresponding to the parallel-flow case but for non-constant α, β and ω

$$-i\alpha\hat{u}_0 + \hat{v}_{0y} - i\beta\hat{w}_0 = 0, \tag{7a}$$

$$i\omega\hat{u}_0 - i\alpha u^b\hat{u}_0 + u^b_y\hat{v}_0 - i\alpha\hat{p}_0 - \frac{1}{\mathrm{Re}}(\hat{u}_{0yy} - \alpha^2\hat{u}_0 - \beta^2\hat{u}_0) = 0, \tag{7b}$$

$$i\omega\hat{v}_0 - i\alpha u^b\hat{v}_0 + \hat{p}_{0y} - \frac{1}{\mathrm{Re}}(\hat{v}_{0yy} - \alpha^2\hat{v}_0 - \beta^2\hat{v}_0) = 0, \tag{7c}$$

$$i\omega\hat{w}_0 - i\alpha u^b\hat{w}_0 - i\beta\hat{p}_0 - \frac{1}{\mathrm{Re}}(\hat{w}_{0yy} - \alpha^2\hat{w}_0 - \beta^2\hat{w}_0) = 0, \tag{7d}$$

$$\hat{u}_0 = \hat{v}_0 = \hat{w}_0 = 0 \quad \text{as } y \to \infty, \tag{7e}$$

$$\hat{u}_0 = \hat{v}_0 = \hat{w}_0 = 0 \quad \text{at } y = 0. \tag{7f}$$

Higher order equations can be derived with a procedure similar to the case of the steady flow with no additional difficulties. The linear system (7) admits a non-trivial solution if and only if a compatibility condition is satisfied; this relation between $(X, Z, T, \alpha, \beta, \omega)$ is called the *dispersion relation*.

3. The dispersion relation

The concept of dispersion relation appears in many different fields of physics, such as quantum mechanics or optics. In fluid dynamics there are many problems leading to a dispersion relation, for example in the study of gravity waves. Dispersion is a word borrowed from optics, where it represents the physical phenomenon of the separation of different colors due to the dependence of the speed of light in a medium on the wavelength. This relation allows us to describe the dispersion process, providing a quantitative relation between the angular frequency ω of a wave and its wave vector $\boldsymbol{k}$. The information about the propagation of a given wave is contained in the appropriate dispersion relation, which also allows some important parameters to be obtained, such as the phase velocity or the group velocity.

In the case under investigation, the eigenproblem (7) admits non-trivial solutions only for suitable values of wave vector and the frequency. When problem (7) is discretized in y direction, the dispersion relation identifying these values is obtained by equating to zero the determinant of the system:

$$\mathcal{D}\left(X, Z, T, \alpha, \beta, \omega\right) = 0; \tag{8}$$

thus, $\mathcal{D}$ represents the discretized dispersion relation whatever numerical method is used for the discretization. The dispersion relation of the differential problem can be considered as the limit of this determinant according to Fredholm's formulation for integral equations.

4. The ray equations

Inserting the definition of the local frequency and local wavenumber (6) in the dispersion relation leads to a first-order partial differential equation for the complex eikonal function Θ:

$$\mathcal{D}\left(X, Z, T, -\frac{\partial\Theta}{\partial X}, -\frac{\partial\Theta}{\partial Z}, \frac{\partial\Theta}{\partial T}\right) = 0. \tag{9}$$

This equation is the analogue of the Hamilton–Jacobi equation of analytical mechanics [22] and once the values of the eikonal function are assigned on a non-characteristic strip, then a unique solution of the Cauchy problem exists [23].

Following Whitham [13, Ch. 5], we solve the eikonal equation by the method of characteristics. The resulting characteristic equations read:

$$\frac{dX}{d\sigma} = -\frac{\partial\mathcal{D}}{\partial\alpha}, \qquad \frac{dZ}{d\sigma} = -\frac{\partial\mathcal{D}}{\partial\beta}, \qquad \frac{dT}{d\sigma} = \frac{\partial\mathcal{D}}{\partial\omega}, \tag{10a}$$

$$\frac{d\alpha}{d\sigma} = \frac{\partial\mathcal{D}}{\partial X}, \qquad \frac{d\beta}{d\sigma} = \frac{\partial\mathcal{D}}{\partial Z}, \qquad \frac{d\omega}{d\sigma} = -\frac{\partial\mathcal{D}}{\partial T}, \tag{10b}$$

$$\frac{d\Theta}{d\sigma} = \frac{\partial\mathcal{D}}{\partial\alpha}\alpha + \frac{\partial\mathcal{D}}{\partial\beta}\beta + \frac{\partial\mathcal{D}}{\partial\omega}\omega. \tag{11}$$

The differential equations (10) are called *ray equations*, i.e. the characteristic lines of the eikonal equation. Eq. (11), on the other hand, is directly derived from the definition of Θ; it will be used to compute the value of the eikonal function along the ray.

The solution of this system of differential equations is a curve in the six-dimensional space $(X, Z, T, \alpha, \beta, \omega)$ represented as a function of the parameter σ. In order to have a unique solution of (10), it is necessary to provide the values of $\left(X_0, Z_0, T_0, \left.\frac{\partial\Theta}{\partial X}\right|_0, \left.\frac{\partial\Theta}{\partial Z}\right|_0, \left.\frac{\partial\Theta}{\partial T}\right|_0\right)$ in a point [24].

There is an analogy between the equations of Hamiltonian mechanics and the characteristic equations (10). The trajectory of a material point, in mechanics, can be selected either by an initial position and momentum $(\mathbf{X_0}, \mathbf{p})$ or by an initial and final position $(\mathbf{X_0}, \mathbf{X_1})$ [25]. The choice to assign the initial conditions $(\mathbf{X_0}, \mathbf{p})$ lead to a solution of an initial value problem (IVP), while, the use of two different points to specify the spatial path leads to a boundary value problem (BVP). Similarly, we can select a ray both by its initial location and wave vector $(X_0, Z_0, T_0, \alpha_0, \beta_0, \omega_0)$ or by its initial and final positions $(X_0, Z_0, T_0, X_1, Z_1, T_1)$.

The choice of the parameter σ affects the expression of $\mathcal{D}$; as a particular case, the form of the dispersion relation can be chosen so that the independent variable σ is one of X, Z or T. We note that these choices require $\mathcal{D}$ to be an invertible function. For a physical problem this is always true when the parameter σ is time. In general, when we choose x as σ (for example in the stationary flow over an airfoil or a flat plate), it is not guaranteed that $\mathcal{D}$ is invertible, but it can easily verified a posteriori.

The procedure presented in this section is also known in literature as Monge's method [26].

5. The choice of the independent variable

The solution of system (10) is generally complex-valued and an analytical continuation of the base flow is required. When the base flow depends only on one among X, Z, T, for example in the case of a steady two-dimensional flow, we can choose this coordinate as independent variable. This choice is important because it can be kept real avoiding the need to calculate the base flow for complex values. In this situation the solution of the ray equations reduces to the calculation of the phase integral. In the classical example of the stability of the steady base flow, this integral is the one used in the classical e^N method:

$$N(X_0, X_1) = \int_{X_0}^{X_1} \Im(\alpha) dX. \tag{12}$$

As another example, when the flow depends on y and T only (as in the case of the Stokes layer [27–29]) the solution of the ray equations reduces to the integral:

$$\Theta = \int_{T_0}^{T_1} \omega dt.$$

A discussion of the accuracy of this approximation applied to the Stokes layer can be found in [30].

In a generic flow, when the base flow depends on more than one coordinate, no specific choice of the independent variable reduces the solution of the problem to an integral. Whereas time as the independent variable would seem the most natural choice, using X in this role allows us to approach the steady solution (12) with continuity.

We consider a mean flow which is homogeneous in the spanwise direction; the eikonal equation can be written as follows:

$$\frac{\partial\Theta}{\partial X} = \mathcal{F}\left(X, Z, T, \frac{\partial\Theta}{\partial T}\right) \tag{13}$$

and the ray equations (10) as

$$\frac{dT}{dX} = \frac{\partial\mathcal{F}}{\partial\omega}, \tag{14a}$$

$$\frac{d\omega}{dX} = -\frac{\partial\mathcal{F}}{\partial T}. \tag{14b}$$

$$\Theta(X_0, T_0; X_1, T_1) = \int_{(X_0,T_0)}^{(X_1,T_1)} (-\alpha\, dX + \omega\, dT) = -\int_{X_0}^{X_1} \left(\alpha - \omega\frac{dT}{dX}\right) dX. \quad (15)$$

System (14) gives the trajectory of a ray in the five-dimensional space $(X, \Re(T), \Im(T), \Re(\omega), \Im(\omega))$, where $\Im(\cdot)$ and $\Re(\cdot)$ represent the imaginary and real part operator. After getting the solution of (14), then, we can compute the values of eikonal function from (15).

6. The real-path approximation as an alternative to analytical continuation

The solution of the ray equations (10), as mentioned in the previous section, implies an analytical continuation of the base flow. The determination of a ray between two given points $X_0, X_1 \in \mathbb{R}$ is a boundary-value problem once the initial and final times are specified. These values are usually assumed to be real, but in all intermediate points both frequency ω and time T are generally complex. Complex rays have two computational inconveniences: (i) every X_1 that we consider requires a new boundary value problem, i.e. each path is different in the complex plane; (ii) the calculation requires the base flow to be known for complex values of time.

When the base flow has been obtained from a system of differential equations, its analytical continuation can be obtained by solving these equations again for complex values of the independent variable. On the other hand, when the system of PDE is not available, or the base flow is empirical data, a Taylor expansion can be used but such procedure is usually ill-conditioned.

This difficulty can be avoided at the cost of an additional approximation by moving the whole path from complex time to real time. This approximation is analogous to using the stationary-phase rather than the saddle-point approximation of an integral.

Thus, we consider a variation of the ray path of the form $T \to T + \delta T$ and $\omega \to \omega + \delta\omega$ where $\delta T(X_0) = \delta T(X_1) = 0$. The first variation of Eq. (15) can be written as

$$\delta\Theta = \int_{X_0}^{X_1} \left[-\frac{\partial\alpha}{\partial\omega}\delta\omega - \frac{\partial\alpha}{\partial T}\delta T + \delta\omega\frac{dT}{dX} + \omega\delta\left(\frac{dT}{dX}\right)\right] dX. \quad (16)$$

Integrating by parts the last term we obtain

$$\begin{aligned}\delta\Theta &= \int_{X_0}^{X_1} \left[-\frac{\partial\alpha}{\partial\omega}\delta\omega - \frac{\partial\alpha}{\partial T}\delta T + \delta\omega\frac{dT}{dX} - \delta T\frac{d\omega}{dX}\right] dX \\ &\quad + [\omega\delta T]_{X_0}^{X_1} \\ &= \int_{X_0}^{X_1} \left[-\delta\omega\left(\frac{\partial\alpha}{\partial\omega} - \frac{dT}{dX}\right) - \delta T\left(\frac{\partial\alpha}{\partial T} + \frac{d\omega}{dX}\right)\right] dX \\ &\quad + [\omega\delta T]_{X_0}^{X_1}. \end{aligned} \quad (17)$$

In this way, we can conclude that the first variation is zero since the terms in the round brackets are Eqs. (14), which vanish by assumption, and the last term is zero because at the bounds of the integral the variation of time is zero. In optics, this result is known as Fermat's principle. This physical principle states that the optical path of the ray that passes through two given points is an extremum.

This property allows us to replace the exact solution of Eq. (10) by an approximate ray with only a second order error in the eikonal Θ. In particular we can replace the complex ray, as shown in Fig. 1, by its projection on the plane $(X, \Re(T))$. This replacement corresponds to taking $\delta T = -i\Im(T)$ in Eq. (17). Since $\Im(T(X_0)) = \Im(T(X_1)) = 0$ Fermat's principle applies to this variation.

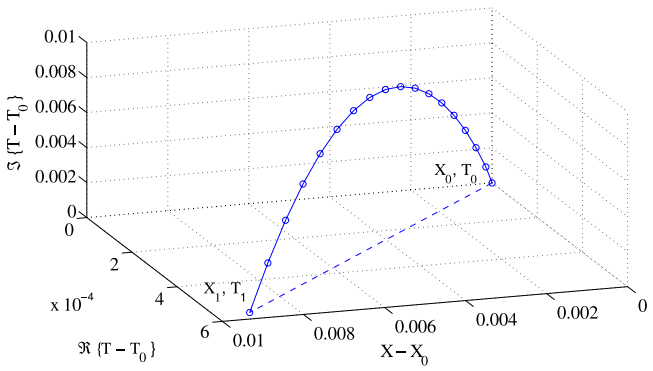

Fig. 1. Ray path in the complex plane for the oscillating airfoil problem discussed in Section 8. The complex trajectory is denoted by a solid line (−); the associated real-path by dashed line (−−). Parameter settings: Re $= 1 \cdot 10^6$, $\gamma_A = 0.1$, $\omega_0 = 500$, $\gamma_0 = 0.1$ and $\tilde{k} = 0.63$.

This procedure gives the following system of modified ray equations

$$\frac{dT}{dX} = \Re\left(\frac{\partial\mathcal{F}}{\partial\omega}\right), \quad (18a)$$

$$\frac{d\omega}{dX} = -\frac{\partial\mathcal{F}}{\partial T}. \quad (18b)$$

A numerical verification of the error we make using the real-path approximation is also reported in the Appendix.

7. The special case of a harmonic initial disturbance

Eq. (3) governing the evolution of the small perturbations is linear; its general solution can be expressed as a linear combination:

$$\boldsymbol{q}' = \sum_m A^{(m)} e^{i\Theta^{(m)}/\epsilon} \sum_{k=0}^{\infty} \hat{\boldsymbol{q}}_k^{(m)}\ \epsilon^k \quad (19)$$

where $\Theta^{(m)}$ and $A^{(m)}$ are respectively the eikonal function and the amplitude of the mth mode.

When, as usually happens in boundary layers, one eigenmode is much more unstable than the others, we can just retain the term of the summation (19) related to this eigenvalue alone. Considering then the leading-order term of the WKB expansion (5) (in what follows we shall neglect the apex "(0)" related to the zeroth order), we can write the final amplitude in a generic point (X, T) as

$$A(X, T) = A(X_0, T_0) e^{i\Theta(X_0,T_0,X,T)/\epsilon} \quad (20)$$

where Θ is the eikonal of the ray passing through the given pair of initial and final points (as explained in Section 4). Since there is a continuum of rays that have the same final point, the total amplitude A_{tot} can be written as

$$A_{tot}(X, T) = \int A(X_0, T_0) e^{i\Theta(X_0,T_0,X,T)/\epsilon} dX_0 dT_0. \quad (21)$$

Thus, we are able to calculate the influence of an initial condition on the final value of the phase in a generic point. Eq. (21) represents an approximation of Green's integral for the mode considered; $e^{i\Theta}$ represents an approximation of the impulse response to an initial condition.

If the initial condition in space is a harmonic disturbance $A_0 = e^{i\omega_0 t_0/\epsilon}$:

$$\begin{aligned} A_{tot}(X, T) &= \int e^{i\omega_0 T_0/\epsilon} e^{i\Theta(X_0,T_0,X,T)/\epsilon} dX_0 dT_0 \\ &= \int e^{i(\omega_0 T_0 + \Theta(X_0,T_0,X,T))/\epsilon} dX_0 dT_0. \end{aligned} \quad (22)$$

Integral (22) can be approximated by the method of stationary phase (see *e.g.* Bender and Orszag [21]), which is a consistent approximation since we are in the limit of small ϵ.

The point (X_0, T_0) where the phase is stationary is

$$\frac{\partial}{\partial T_0}\left[\omega_0 T_0 + \Theta(X, T, X_0, T_0)\right] = 0. \tag{23}$$

Thus, the exponent of Green's integral, calculated in this point (X_0, T_0), can be expressed as

$$\chi(X_0, \omega_0, X, T) = \Theta(X_0, T_0, X, T) + \omega_0 T_0. \tag{24}$$

The change of variables (24) is a Legendre transformation. Just as $\omega_0 = -\frac{\partial \Theta}{\partial T_0}$ (because of (23)) it can be proved that $T_0 = \frac{\partial \chi}{\partial \omega_0}$. This procedure is the same that is used in quantum mechanics to relate the classical quantum theory with the semi-classical quantum theory, and in optics, where it represents the link between the point eikonal and angle eikonal (see *e.g.* Gitin [31]).

8. An example: transition prediction on oscillating airfoils

We consider, as an example, the application of the present theory to the flow arising beside an oscillating airfoil invested by a uniform stream.

The system of Eqs. (1a), (1d) is made dimensionless with the velocity magnitude of the incoming uniform stream U^*_{ref}, the chord of the airfoil c and the reference pressure ρU^{*2}_{ref}. Thus, the Reynolds number can be expressed as

$$\mathrm{Re} = \frac{c\, U^*_{ref}}{\nu}. \tag{25}$$

The oscillating periodic motion of the airfoil is governed by the unsteady pitching law

$$\gamma(t) = \gamma_0 + \gamma_A \sin(\tilde{k} T), \tag{26}$$

where γ is the angle of attack, γ_0 is the mean angle of attack, γ_A is the variation amplitude of the pitching angle and $\tilde{k}$ is the reduced frequency. This dimensionless parameter [32] is defined as $\tilde{k} = \Omega c / U^*_{ref}$, where Ω is the angular frequency of oscillation.

In this section, we present numerical results on a Kármán–Trefftz profile characterized by a trailing-edge angle of 10° and a complex plane singularity [33] located in $-1.24 + \mathbf{i}0.1$.

8.1. Transition prediction in unsteady boundary layers

Instability of laminar flows and transition to turbulence in boundary layer problems are important issues of fluid dynamics. We recall, for example, that the drag due to turbulent boundary layers over the surface of aircraft accounts for a large portion of the total drag. There are several methods proposed to detect transition location [34] but the most used is undoubtedly the e^N method [35] that is based on the amplification of linear instability waves. The main idea, which is the basis of this method, is that the transition occurs when the wave amplitude $\mathcal{A}$ is e^N times the wave amplitude at the neutral point. The value of N depends on the level of turbulence and is typically chosen equal to 9. The classical application of the e^N method to a steady two-dimensional boundary layer starts by calculating

$$\ln\left(\frac{\mathcal{A}}{\mathcal{A}_0}\right) = N(X_0, X_1) = -\Im(\Theta(X_0, X_1)) = \int_{X_0}^{X_1} \Im(\alpha) dX \tag{27}$$

where X_0 is the first point where $\Im(\alpha)$ vanishes. The obtained value of N is a function of frequency. The worst case, then, is detected by the identification of the optimal disturbance frequency, i.e. the frequency that minimizes the position at which N reaches the empirically determined target value $\tilde{N}$.

In order to apply this method to unsteady boundary layer flows, we have to consider an initially harmonic disturbance as shown in the previous section. The N corresponding to this case, then, can be computed, using (24), as

$$N(X_0, \omega_0, X_1, T_1) = -\Im(\chi) = \int_{X_0}^{X_1} \Im\left(\alpha - \omega \frac{dT}{dX}\right) dX - \Im(\omega_0 T_0). \tag{28}$$

According to Section 7, we are computing the value of N starting from the condition (X_0, ω_0) marching in the X direction till the final position (X_1, T_1); the initial time T_0, then, can be determined as $\partial\chi/\partial\omega_0$. In (28), unlike the steady case, the final frequency ω is different from the initial frequency ω_0. We have to note that there is also a difference between an initial time, at which the real part of the streamwise wavenumber vanishes (i.e. on the lower branch of neutral curve), and a final time where the transition process to turbulence occurs. Furthermore, we can easily show that the relation (28) is consistent in the limit of steady base flow.

In this case we have a constant frequency $\omega = \omega_0$ since $\mathcal{F}$ is independent of T

$$\frac{d\omega}{dX} = -\frac{\partial \mathcal{F}}{\partial T} = 0. \tag{29}$$

Thus, we can rewrite the expression of the N-factor as follows

$$N(X_0, \omega_0, X_1, T_1) = \int_{X_0}^{X_1} \Im(\alpha) dX - \Im[\omega_0(T_1 - T_0)] - \Im(\omega_0 T_0) = \int_{X_0}^{X_1} \Im(\alpha) dX - \Im(\omega_0 T_0). \tag{30}$$

This relation, for real ω_0 and T_0, becomes the previously given definition (27).

8.2. Computation of the base flow

We note that the multiple-scale approximation described in the previous section is independent of the use of an exact or approximate base flow, in particular insofar as a comparison with a quasi-steady approach is concerned, as will be the subject of Section 8.4. From the viewpoint of the practical application the consequences of approximating the base flow are not trivial and discussed in [36]. However, since the solution of linearized equations is independent of the calculation of the base flow, for the purpose of this example we use a base flow obtained from unsteady boundary layer equations.

The outer, inviscid velocity field around the Kármán–Trefftz profile described at the beginning of this section is obtained from conformal mapping theory, with unsteadiness appearing parametrically trough the attack angle defined in (26). The analytically calculated inviscid velocity at the wall represents the outer boundary condition for the boundary layer solver.

The numerical method used to solve the boundary-layer equations is similar to the classical one presented in [37]. The equations are discretized by a second-order-accurate finite-difference scheme on a nonuniform grid in space. The time advancement was performed through an implicit scheme. The resulting nonlinear system of algebraic equations, along with no-slip boundary conditions at the wall and the imposed free-stream conditions, is solved by an iterative Newton–Raphson procedure.

8.3. Numerical methods for stability problem

Several numerical techniques are available to solve the eigenproblem (7) and the differential system (14) efficiently. Here, we investigate the stability of unsteady boundary layers using a finite

difference formulation. Eqs. (7) are discretized by second-order central differences over a staggered grid. The velocity components u_j and v_j are located in the grid points y_j, while the pressure p_j in the midpoint between y_j and y_{j+1}. The system of algebraic equations together with their boundary conditions are recast in the following form

$$\mathsf{L}(\alpha, \beta, \omega, \mathrm{Re}) \cdot \xi = \mathbf{0}, \tag{31}$$

where $\xi \subset \mathbb{C}^n$ is the right (direct) eigenvector and L is a diagonal banded matrix. The computational domain extends in wall normal direction from 0 to y_∞. We use the standard zero-velocity conditions at the solid wall and the asymptotic condition of inviscid outer behavior at the upper boundary y_∞ as in Luchini and Bottaro [38]. The conditions associated to wall and asymptotic behavior are inserted, respectively, in the first and in the last rows of the matrix L. The eigenvalue problem, then, is solved by the classical inverse-iteration algorithm [39].

The partial derivatives of $\mathcal{F}$ in Eqs. (14), that provide the trajectory of the ray and the evolution of the frequency along the path, are discretized by a second-order backward finite difference formula in the marching direction. Each discretization has been subjected to step size convergence tests, not shown here for the sake of brevity, and the computed eigenvalues in the steady case are found in agreement with those obtained in Giannetti and Luchini [40].

The numerical procedure, therefore, consists in the computation of characteristic lines (the rays) using Eqs. (14) where the formal expression of $\mathcal{F}$ in (13) is represented by the numerical solution of the eigenvalue problem (31). The computation of N-factor according to (28), then, starts at the neutral point. This point is defined as the streamwise location where the real part of the leading eigenvalue of (31) vanishes. The marching algorithm ends when the value of N reaches a given target value $\tilde{N}$. In the computations discussed in Section 8.4, $\tilde{N}$ is equal to 9. The optimal frequency is then identified using a Newton method in order to find the frequency that minimizes the transition position.

8.4. Numerical results

We focus our attention on the determination of the transition location and its displacement during the oscillation period in unsteady boundary layers. The parameters in the unsteady pitching law (26) have been chosen as $\gamma_A = 0.1$, $\gamma_0 = 0.1$ and $\tilde{k} = 0.63$, which fall in the range reckoned of engineering interest by Leishman [41]. The evolution of the N factor of (28) against the curvilinear abscissa X is plotted in Fig. 2 for several frequencies. We recall that the frequency of the disturbance varies along the ray trajectory because of the time-dependence of the base flow; here, the rays are labeled with the initial frequency. All curves have a monotonic behavior, just as in the corresponding steady case, and the process of disturbance amplification takes about 10% of the chord length for the considered values of the frequency. For each X after the neutral point, there is a maximum N attained for a certain value of the initial frequency ω_0. The transition position $X_{tr.}$ is defined by the e^N method as the minimum streamwise position where the value of N is equal to the target value $\tilde{N}$. In Fig. 2 for $\tilde{N} = 9$, the optimal frequency is $\omega_{opt.} \approx 600$ and the transition occurs at $X_{tr.} \approx 1.15$.

Fig. 3(a) shows the transition position $X_{tr.}$ as a function of the final time for the Reynolds number $\mathrm{Re} = 2 \cdot 10^7$. The curve showing the most amplified initial frequency as a function of final time is plotted in Fig. 3(b). We note that the maximum value of the transition position is reached when the angle of attack is about equal to its maximum value. In this condition the most amplified frequency is $\omega_{opt.} \approx 500$.

Up to the present procedure, the transition position could be calculated using a quasi-steady approach, i.e. neglecting the time dependence of the mean flow. We compare the results predicted by this quasi-steady approach with those provided from the present theory. This analysis allows us to show the effect of unsteadiness on the evolution of the linear instability waves and provide a quantitative estimation of error made using a quasi-steady approach. Fig. 4 contains the amplification factor N against the dimensionless curvilinear abscissa X for several reduced frequencies. The parameter $\tilde{k}$ has been chosen in the range $[0, 1.89]$ in order to show the effect of strong unsteadiness but, usually, only the range $[0, 0.6]$ is interesting for helicopter applications. In this range, as shown in Fig. 4, the difference between the transition location calculated in the steady case and the one characterized by $\tilde{k} = 0.63$ is of the order of 1%. Therefore, the error on the transition position computed using the quasi-steady approach is negligible in helicopter aerodynamics.

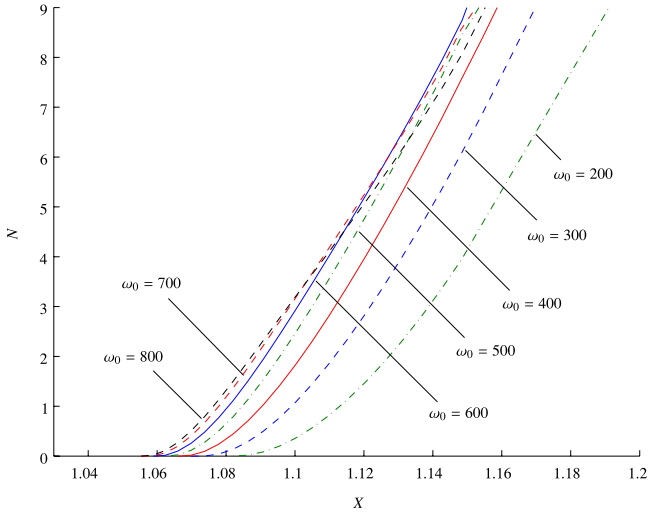

Fig. 2. N as a function of the curvilinear abscissa X at $T = 0$. Here, we chose the origin of the spatial coordinate X at the trailing edge of the airfoil and normalized it using the length of the chord section. The abscissa increases in clockwise direction starting from the origin. Parameter settings: $\mathrm{Re} = 1 \cdot 10^6$, $\gamma_A = 0.1$, $\gamma_0 = 0.1$ and $\tilde{k} = 0.63$.

This result can be explained if we remember that the ratio between the airfoil chord and the circumference described by the helicopter blade is typically small. The variation of the base flow caused by its time dependence during the time the blade moves forward by a length equal to its chord is small with respect to the variation caused by its spatial dependence. The success of the quasi-steady approach, thus, can be ascribed to the scale separation between the period of oscillation (time to travel through one circumference) and the traversal time of the base flow through one chord.

9. Conclusions

In this paper we have developed a procedure to study the linear stability of an unsteady boundary layer. The presented method can be applied to a *generic* unsteady flow different from the other existing methods that can be applied to periodic flows depending on T and y (but not on X and Z) like, for example, the first [38] or the second [29] Stokes problem. This procedure is based on a high-frequency (optical) approximation, where we suppose that the base flow typically evolves on a characteristic streamwise length scale much larger than the wavelength of the perturbation.

We introduce the dispersion relation related to the leading-order problem and, as in the Hamiltonian mechanics or in optics, we solve the eikonal equation by the method of characteristics. Since the dispersion relation is complex-valued, the characteristic paths involve analytical continuation of all dependent variables

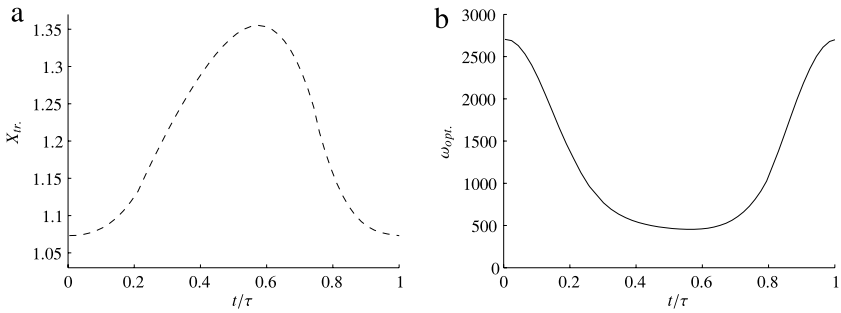

Fig. 3. (a) Transition position as a function of final time (transition detected when the target value $\tilde{N} = 9$); (b) Most amplified frequency as a function of final time. Here, we depict the results arising in a single period τ of periodic airfoil oscillations. Parameter settings: Re $= 2 \cdot 10^7$. The pitching law is characterized by $\gamma_A = 0.1$, $\gamma_0 = 0.1$ and $\tilde{k} = 0.63$.

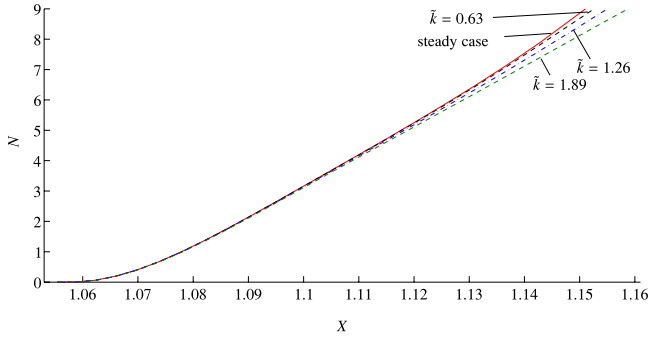

Fig. 4. Effect of reduced frequency $\tilde{k}$ on the amplification factor N. Parameters: Re $= 2 \cdot 10^6$, $\omega = 700$. The curvilinear abscissa is chosen similarly to Fig. 2.

for complex values. Then, we show how to consider an initial harmonic disturbance and deal with the possibility to express the disturbance amplitude, at a given final location, as integral of continuum of rays that have the same final point.

We consider, as an example application of the present theory, the flow past an oscillating Kármán–Trefftz airfoil. A method that allows us to determine the transition location in the unsteady case is presented. We note that, unlike the steady case, the *final* frequency ω of the ray is different from the frequency ω_0 of the *initial* harmonic disturbance. We show the transition position predicted and its displacement during the oscillation period.

The present procedure is not limited to oscillating-airfoil problems; quantitative stability calculations for other classical or industrial applications can be performed. This procedure can also be applied for problems of flow control or transition delay. In fact, the present ray method is well suited to obtain the downstream response to any kind of initial source of disturbances. It is possible, for example, to devise a strategy of wall forcing, *steady* or *unsteady* distribution of wall blowing/suction. We explicitly recall that this theory is usable also for steady or unsteady 3D boundary layer flows, where the mean flow depends on the spanwise coordinate. Furthermore, the present procedure, based on the multiple scale approximation, requires a lower computational burden than the full solution of the Linearized Navier–Stokes equations.

Before the present analysis, it was possible to estimate the transition position using a quasi-steady approach but without the possibility to quantify the error. In helicopter applications, we obtain the remarkable result that quasi-steady calculations provide acceptable results.

The proposed theory includes, as special cases, both the e^N method for stationary flows and the approximations, used in the past, for the Stokes layer problem [30].

Appendix. Numerical accuracy of the real-path approximation

In this appendix we compare the real-path approximation with the analytical continuation obtained by solving the base-flow boundary-layer equations for complex values. All it takes to solve these equations for complex values of the independent variable is to declare a few variables complex and to specify a suitable integration path.

Table A.1
Comparison between the transition position computed by analytical continuation (*a.c.*) of the base flow and by the real-path approximation (*r.p.*). Here, X_0 is the neutral point and $X_{t.r.}$ is the transition position.

ω_0	$X_{tr.}^{r.p.} - X_0$	$X_{tr.}^{a.c.} - X_0$	Relative error %
500	0.09112	0.09120	0.087%
700	0.09583	0.09592	0.093%

The comparison was carried out for the specific ray leading to $\tilde{N} = 9$ among those considered in the oscillating airfoil problem. Parameters are, as in Section 8.4: Re $= 1 \cdot 10^6$, $\gamma_A = 0.1$, $\gamma_0 = 0.1$ and $\tilde{k} = 0.63$.

We performed this comparison for a few values of the frequency ω_0; relative error of all cases was found to be of the same order of magnitude. As an example, in Table A.1, we report the results obtained for two different frequencies $\omega_0 = 500$ and $\omega_0 = 700$.

Real-path approximation, involving an error of the order of 0.1%, is computationally about a hundred times faster than the exact procedure based on analytical continuation.

References

[1] T. Tani, Boundary-layer transition, Annu. Rev. Fluid Mech. 1 (1969) 169–196.
[2] I. Tani, History of boundary layer theory, Annu. Rev. Fluid Mech. 9 (1977) 87–111.
[3] M. Gaster, On the effects of boundary-layer growth on flow stability, J. Fluid Mech. 66 (1974) 465–480.
[4] W.S. Saric, A.H. Nayfeh, Nonparallel stability of boundary-layer flows, Phys. Fluids 18 (1975) 945.
[5] T. Cebeci, K. Stewartson, On stability and transition in three-dimensional flows, AIAA J. 18 (1980) 398–405.
[6] T. Herbert, F.P. Bertolotti, Stability analysis of nonparallel boundary layers, Bull. Amer. Phys. Soc. 32 (1987) 2079.
[7] P. De Matteis, R. Donelli, P. Luchini, Application of the ray-tracing theory to the stability analysis of three-dimensional incompressible boundary layers, in: XIII AIDAA Conference, Rome, 1995.
[8] K.G. Budden, P.D. Terry, Radio ray tracing in complex space, Proc. R. Soc. Lond. Ser. A 321 (1970) 275–301.
[9] R.M. Jones, Ray theory for lossy media, Radio Sci. 5 (1970) 793–801.
[10] J.B. Keller, W. Streifer, Complex rays with an application to Gaussian beams, J. Opt. Soc. Amer. 61 (1962) 40–43.
[11] J.B. Keller, W. Streifer, Surface wave excitation and propagation, J. Appl. Phys. 31 (1960) 1039–1046.
[12] N. Itoh, Linear stability theory for wave-packet disturbances in parallel and nearly parallel flows, in: R. Eppler, H. Fasel (Eds.), Proceedings IUTAM Symposium on Laminar-Turbulent Transition, Springer, 1980.
[13] G.B. Whitham, Linear and Nonlinear Waves, Wiley, 1974.
[14] M. Choudhari, C.L. Street, A finite Reynolds-number approach for the prediction of boundary-layer receptivity in localized regions, Phys. Fluids 4 (1992) 2495–2514.
[15] J.D. Crouch, Localized receptivity of boundary layers, Phys. Fluids 4 (1992) 1408–1414.
[16] S. Zuccher, Localized receptivity of boundary layers (Ph.D. thesis), 2002.

[17] B.J. Gréa, Application de la théorie des rayons complexes á l'analyse et au contrôle des instabilités de couche limite (Ph.D. thesis), IMFT, 2005.
[18] P. Hall, The linear stability of flat Stokes layers, Proc. R. Soc. Lond. Ser. A 359 (1978) 151–166.
[19] P. Merkli, H. Thomann, Transition to turbulence in oscillating pipe flow, J. Fluid Mech. 68 (1975) 567–576.
[20] G. Vittori, R. Verzicco, Direct simulation of transition in an oscillatory boundary layer, J. Fluid Mech. 371 (1998) 207–232.
[21] C.M. Bender, S.A. Orszag, Advanced Mathematical Methods for Scientists and Engineers, third international ed., Springer, New York, 1987.
[22] H. Goldstein, Classical Mechanics, Addison-Wesley P.C., 1957.
[23] V. Smirnov, Course on Higher Mathematics. Vol. 4, Nauka, Moscow, 1974.
[24] O. Bühler, Waves and Mean Flows, Cambridge University Press, 2009.
[25] R. Talman, Geometric Mechanics: Toward a Unification of Classical Physics, Wiley, 2007.
[26] W.F. Ames, Nonlinear Partial Differential Equations in Engineering, Vol. 1, Elsevier, 1967.
[27] P.J. Blennerhasset, A.P. Bassom, The linear stability of flat Stokes layers, J. Fluid Mech. 464 (2002) 393–410.
[28] P.J. Blennerhasset, A.P. Bassom, A note on the linear stability of a two-dimensional Stokes layer, Quart. J. Mech. Appl. Math. 60 (2007) 391–396.
[29] P.J. Blennerhasset, A.P. Bassom, On the linear stability of Stokes layers, Phil. Trans. R. Soc. A 366 (2008) 2685–2697.
[30] J. Luo, X. Wu, On the linear instability of a finite Stokes layer: istantaneous versus Floquet modes, J. Fluid Mech. 22 (2010) 054106.
[31] A.V. Gitin, The Legendre transformations in Hamiltonian optics, J. Eur. Opt. Soc. 5 (2010) 10022.
[32] W. Birnbaum, Das ebene problem des schlagenden flügels, ZAMM Z. Angew. Math. Mech. 4 (1924) 277–292.
[33] L.M. Milne-Thomson, Theoretical Aerodynamics, Dover, New York, 1958.
[34] W.S. Saric, H.L. Reed, E.B. White, Stability and transition of three-dimensional boundary layers, Annu. Rev. Fluid Mech. 35 (2003) 413–440.
[35] A.M.O. Smith, N. Gamberoni, Transition, pressure gradient and stability theory, Douglas Aircraft Report ES-26388, 1956.
[36] T. Cebeci, M. Platzer, H. Chen, K. Chang, J. Shao, Analysis of Low-Speed Unsteady Airfoil Flows, Springer, 2005.
[37] J.H. Phillips, R.C. Ackerberg, A numerical method for integrating the unsteady boundary-layer equations when there are regions of backflow, J. Fluid Mech. 58 (1973) 561–579.
[38] P. Luchini, A. Bottaro, Linear stability and receptivity analyses of the Stokes layer produced by an impulsively started plate, Phys. Fluids 13 (2001) 1668–1678.
[39] W.H. Press, S.A. Teukolsky, W.T. Vetterling, B.P. Flannery, Numerical Recipes in C: the Art of Scientific Computing, second ed., Cambridge Univ. Press, New York, 1992.
[40] F. Giannetti, P. Luchini, Leading-edge receptivity by adjoint methods, J. Fluid Mech. 547 (2006) 21–53.
[41] J.G. Leishman, Principles of Helicopter Aerodynamics, Cambridge University Press, 2006.

Paper

5

PHYSICS OF FLUIDS **27**, 084110 (2015)

Global stability and sensitivity analysis of boundary-layer flows past a hemispherical roughness element

V. Citro,[1,a)] F. Giannetti,[1] P. Luchini,[1] and F. Auteri[2]
[1]*DIIN, Universitá degli Studi di Salerno, Via Giovanni Paolo II, 132, Salerno 84084, Italy*
[2]*Dipartimento di Scienze e Tecnologie Aerospaziali, Politecnico di Milano, via La Masa 34, Milano 20156, Italy*

(Received 2 November 2014; accepted 31 July 2015; published online 26 August 2015)

We study the full three-dimensional instability mechanism past a hemispherical roughness element immersed in a laminar Blasius boundary layer. The inherent three-dimensional flow pattern beyond the Hopf bifurcation is characterized by coherent vortical structures usually called hairpin vortices. Direct numerical simulation results are used to analyze the formation and the shedding of hairpin vortices inside the shear layer. The first bifurcation is investigated by global-stability tools. We show the spatial structure of the linear direct and adjoint global eigenmodes of the linearized Navier-Stokes equations and use the structural-sensitivity field to locate the region where the instability mechanism acts. The core of this instability is found to be symmetric and spatially localized in the region immediately downstream of the roughness element. The effect of the variation of the ratio between the obstacle height k and the boundary layer thickness δ_k^* is also considered. The resulting bifurcation scenario is found to agree well with previous experimental investigations. A limit regime for $k/\delta_k^* < 1.5$ is attained where the critical Reynolds number is almost constant, $Re_k \approx 580$. This result indicates that, in these conditions, the only important parameter identifying the bifurcation is the unperturbed (i.e., without the roughness element) velocity slope at the wall. [http://dx.doi.org/10.1063/1.4928533]

I. INTRODUCTION

Processes of transition to turbulence over rough surfaces are often encountered in an engineering context. For example, pipes and ducts cannot often be considered as hydraulically smooth, especially at high Reynolds numbers. A practical example in which these phenomena assume considerable importance is the flow past ice formations on aircraft surfaces that can lead to a deterioration of handling characteristics and produce noise.

The transition process on surfaces with large roughness protrusion height appears to be characterized by physical mechanisms that are different from those acting for lower roughness protrusion height and have not been clarified yet. The presence of small roughness elements at the wall produces small flow disturbances which linearly amplify while being convected downstream, eventually attaining the amplitude necessary to cause transition at a relatively large distance from the roughness elements that gave rise to them. Such disturbances are of two general types: Tollmien-Schlichting waves, well visible in experiments characterized by a two-dimensional roughness distribution,[1] or longitudinal vortices inducing a transient growth of streamwise streaks of alternating high- and low-momentum fluid, which may grow enough to cause transition before having the possibility to decay.[2,3] Surfaces with a discrete or continue distribution of roughness may be used to enhance heat transfer or mixing, or alternatively, to stabilize systems (even in the nonlinear regime, see e.g., Ref. 4) and can indeed be used for delay transition.[5]

a)Electronic mail: vcitro@unisa.it

The receptivity mechanisms[6,7] described above, however, only apply if the roughness amplitude is sufficiently small.[3,8] On the other hand, when the protrusion height is large enough, transition suddenly appears downstream of an individual roughness element. The mechanism involved in this process is not yet understood. In an effort to shed light on the transition mechanism associated with large-amplitude surface roughness, several experiments have been carried out in the past.[9,10] The results obtained have shown that if the Reynolds number based on the roughness height exceeds a critical value, then transition occurs immediately past the roughness element; conversely, if the critical value is not exceeded, the receptivity mechanisms described above are dominant and transition takes place farther downstream. These experimental data produced empirical correlations based on the roughness-based Reynolds number as far back as in the 1950s.[11] These criterions are still used in practice to predict transition in the wake of isolated three-dimensional roughness elements. Although transition correlations are useful from a practical viewpoint, they are neither able to reveal the detailed mechanism of transition nor do they assist in designing transition control strategies besides simply placing design limits on acceptable roughness levels.

Experimental data[12] and numerical simulations[13] have shown that the topology of the flow around an isolated three-dimensional roughness element in a boundary layer consists of a steady horseshoe vortex[14] that wraps around its upstream side and trails two steady counter-rotating leg vortices downstream. At sufficiently high values of the Reynolds number, unsteady hairpin vortices originate periodically from the separated region just aft of the roughness element. The observation of vortex shedding in the wake of moderate-to-large-height elements supports the idea that transition beyond the critical Reynolds number is related to a global instability of the wake flow past an isolated hemispherical roughness element.

The mechanism of transition caused by an isolated obstacle at low speeds has been first investigated by Tani *et al.*,[15] Acarlar and Smith,[16] Mason and Morton,[17] and Klebanoff *et al.*[18] Tani *et al.*[15] showed that the transition location moved closer to the roughness element when the Reynolds number Re_k exceeded a critical value. Acarlar and Smith[16] characterized the topological features of the base flow fields and highlighted that the production of hairpin vortices can be associated to the concentration of vorticity into the low-pressure recirculation zone past the obstacle. Mason and Morton[17] performed an experimental campaign on several roughness elements. They showed that the formation of the counter-rotating streamwise vortices occurred in the centre plane. Klebanoff *et al.*[18] proposed, in addition, a two-region model for the evolutionary change toward a fully developed turbulent boundary layer. This model was characterized by an inner region where the interaction between the steady and the hairpin vortices generates the turbulence and by an outer zone where the turbulent vortex rings are generated by the deformation of hairpin structures. Ergin and White[10] discussed the interaction between the unsteady disturbances and the steady-flow relaxation that stabilizes these disturbances.

The problem of transition past a roughness element is relevant also at high speeds where there is the influence of free-stream temperature, Mach number, and the thermal field at the wall. Saric *et al.*[19] suggested to take into account the three-dimensional cross-flow instability as a possible mechanism for the hypersonic boundary layer transition; Reshotko and Tumin,[20] instead, discussed the importance of non-modal growth. Schneider[21] resumed in a detailed survey, the advanced transition-estimation methods, based on simulation of the physical mechanisms, like the parabolized stability equations (PSEs), the e^N method, and direct numerical simulations (DNSs).

The linear stability theory has been widely used to characterize the transition in the wake flow past an isolated roughness element. Malik[22] discussed the numerical solution of the global and local eigenvalue problems for temporal and spatial stability analyses of linear stability equations for compressible boundary layers. Reshotko[23] showed that the transient growth can be a possible mechanism of transition to turbulence. He found that the flow presents a modal bifurcation for low-amplitude disturbances, mode interactions, and a final fully nonlinear breakdown to turbulence. Differently, when there are disturbances of large amplitude, he observed a nonlinear breakdown that is not related to any modal mechanism. Groskopf[24] investigated the stability of a box-shaped roughness element using the biGlobal theory. They highlighted a convective instability related to a couple of counter-rotating streamwise eddies. Recently, De Tullio *et al.*[25] performed a detailed stability analysis for the flow past an isolated roughness element over an isothermal wall with adiabatic boundary conditions. They used direct numerical simulations, spatial BiGlobal and three-dimensional parabolized (PSE-3D)

stability analyses. They concluded that the base flow modifications introduced by the presence of a wall-mounted obstacle can lead to significant changes in the stability features of the flow.

In recent years, the increase of computational power allowed the use of accurate numerical simulations (DNS) and heavy fully three-dimensional stability computations. Zhou *et al.*[26] carried out several DNS to investigate the transitional boundary-layer flow induced by a roughness element with the same shape considered here. Loiseau *et al.*[27] investigated the global stability of a periodic array of a cylindrical roughness element. They discussed the symmetric (varicose) and antisymmetric (sinuous) eigenmodes of instability produced by different roughness elements characterized by several aspect ratios.

The aim of the present work is to investigate the topological changes exerted by the inherent global eigenmode in large protrusion height roughness obstacles. Using the tools of linear stability analysis[28,29] and DNS, we perform a parametric study to show how the global instability depends on the inlet velocity profile. In Sec. II, the geometry, numerical methods, and code validation are presented, while results of direct numerical simulations and global stability analysis are reported in Sec. III A. Sec. III B provides conclusions based on our parametric study and, finally, a summary and discussion is presented in Sec. IV.

II. PROBLEM FORMULATION

A. Flow configuration and governing equations

We focus on the linear stability and sensitivity of viscous flows over a flat plate with a single hemispherical roughness element. The geometrical configuration and the details of the computational domain $\mathcal{P} = [-L_x^{in}, L_x^{out}] \times [-L_y, L_y] \times [0, L_z]$ are shown in Figure 1.

To ease comparisons with experimental investigations made by Klebanoff *et al.*,[18] we adopted a similar geometrical configuration. The unit-diameter hemispherical obstacle is symmetrically placed with respect to the y-axis, its center is located in $\boldsymbol{r_c} = (0, 0, 0.1R)$ and a small cylinder of height $h_c = 0.1R$ is used to connect the hemisphere to the flat plate (R is the hemisphere radius). The choice to place a small cylinder is related to the additional thickness present in Kelabanoff *et al.*[18] due to glue interposed between the hemisphere and the wall.

The fluid motion is governed by the unsteady Navier-Stokes equations for viscous, incompressible flow,

$$\nabla \cdot \boldsymbol{u} = 0, \tag{1a}$$

$$\frac{\partial \boldsymbol{u}}{\partial t} + \boldsymbol{u} \cdot \nabla \boldsymbol{u} = -\nabla P + \frac{1}{Re} \nabla^2 \boldsymbol{u}, \tag{1b}$$

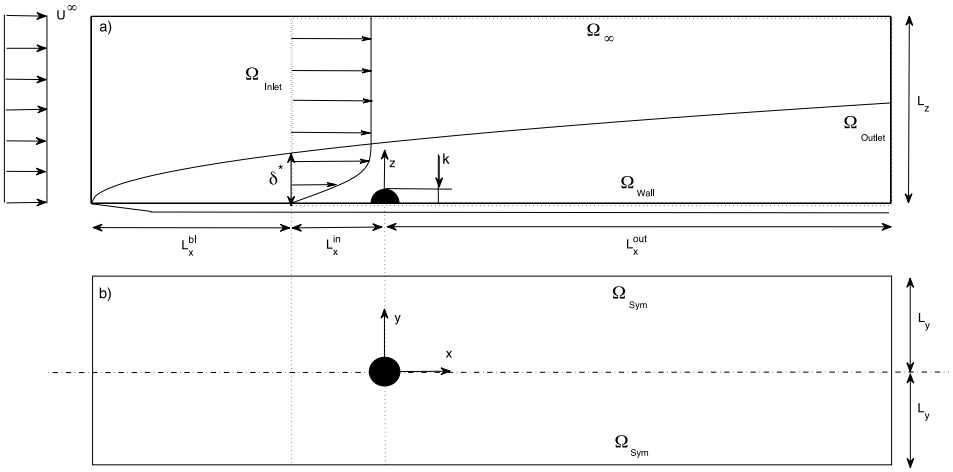

FIG. 1. Flow configuration, frame of reference, and computational domain $\mathcal{P}$ (not in scale) are depicted using (a) side view and (b) top view. The region $\mathcal{P}$, enclosed by a dotted line, extends from $x = -L_x^{in}$ to $x = L_x^{out}$ in the streamwise direction, from $z = 0$ to $z = L_z$ in the wall-normal direction, and it is symmetric in y-direction ($-L_y \le y \le L_y$). For a complete and detailed list of the geometrical cases and grids, see Sec. II D.

where $P \in \mathbb{R}$ is the reduced pressure scalar field and $\boldsymbol{u} \in \mathbb{R}^3$ is the velocity vector with components $\boldsymbol{u} = (u, v, w)$.

Equations (1) are made dimensionless using the total height k of the roughness element as the characteristic length scale and the velocity U_k of the incoming uniform stream that would exist in the boundary layer at the height k without roughness.[30] The Reynolds number is thus defined as $Re_k = U_k k/\nu$, with ν the fluid kinematic viscosity.

B. Numerical approach for DNS

We use the spectral element method (SEM) implemented in *NEK5000* to solve governing equations (1). We chose SEM because its spectral nature ensures fast spatial convergence while, at the same time, preserves the geometric flexibility of the finite element methods. Here, we provide a brief description of the underlying flow solver, the numerical methods, and the implementation are described in detail in Refs. 31 and 32.

The unknown vector (u, v, w, P) is spatially discretized onto $P_N - P_{N-2}$ spectral elements using Lagrange orthogonal polynomials in the Gauss-Lobatto-Legendre (GLL) nodes. For the temporal discretization of momentum equation (1b), a semi-implicit splitting scheme has been used that allows high-order temporal accuracy. The time advancement is divided in 3 independent subproblems : convective, viscous, and pressure problem. These last two elliptic subproblems are solved efficiently by using the overlapping Schwarz method.[32]

In order to solve the system of differential equations (1), we impose no-slip boundary conditions at the roughness surface and at the flat plate (Ω_{wall}), Neumann outflow conditions ($\mathbf{n} \cdot (\nu \nabla \mathbf{u} - p\mathbf{I}) = 0$) at the outlet ($\Omega_{outlet}$) and a fully developed Blasius profile, characterized by a boundary layer thickness δ^*_{in}, at the inlet (Ω_{inlet}). Finally, we adopt outlet boundary conditions at the upper side of the computational domain (Ω_∞) and symmetry boundary conditions at the lateral boundaries (Ω_{sym}). The convergence and the validation of the present numerical approach will be addressed in Sec. II D.

In subcritical conditions, the steady base flow solution, on which the stability analysis is performed, can be retrieved by simply integrating time dependent Navier-Stokes equations (1) over a long time interval. On the other hand, if the Reynolds number exceeds its critical value, a simple time integration fails to converge towards the unstable flow state that is required for the stability analysis. In these cases, it is therefore necessary the use of a stabilizing numerical procedure able to compute the unstable reference state. Several approaches are discussed in the literature: in Åkervik,[33] for example, the authors managed to reach the steady state by damping the unstable frequencies using a dissipative relaxation term proportional to the high-frequency content of the velocity fluctuation field; Shroff and Keller[34] computed a projection onto the small unstable subspace using a Newton procedure. Here, we adopt a different approach that allows us to obtain the unstable, steady field by correcting the new iteration of the numerical procedure using a linear combination of previous fields. This new method works for both steady and unsteady bifurcations and it is inspired by the iterant recombination method.[35] It has been already used in Refs. 36 and 37. Appendix A contains the details of this stabilizing procedure. As example application, we show in Figure 2 the effect of this procedure on the convergence history at $Re_k = 450$. The resulting field is depicted in Figure 3.

C. Linear stability tools: Eigenproblem formulations and solution methodology

The instability onset is studied using the linear stability theory. The total flow state $(\boldsymbol{u}, P)$ is decomposed in a base flow $(\boldsymbol{U}_b, P_b)$, steady solution of the governing equations, and in an unsteady small perturbation field $(\boldsymbol{u}', P')$,

$$\boldsymbol{u}(x, y, z, t) = \boldsymbol{U}_b(x, y, z) + \boldsymbol{u}'(x, y, z, t), \quad P(x, y, z, t) = P_b(x, y, z) + P'(x, y, z, t). \tag{2}$$

Substituting (2) into (1) and linearizing with respect to $(\boldsymbol{u}', P')$, the perturbation equations

$$\nabla \cdot \boldsymbol{u}' = 0, \tag{3a}$$

$$\frac{\partial \boldsymbol{u}'}{\partial t} + \boldsymbol{U_b} \cdot \nabla \boldsymbol{u}' + \boldsymbol{u}' \cdot \nabla \boldsymbol{U_b} = -\nabla P' + \frac{1}{Re} \nabla^2 \boldsymbol{u}' \tag{3b}$$

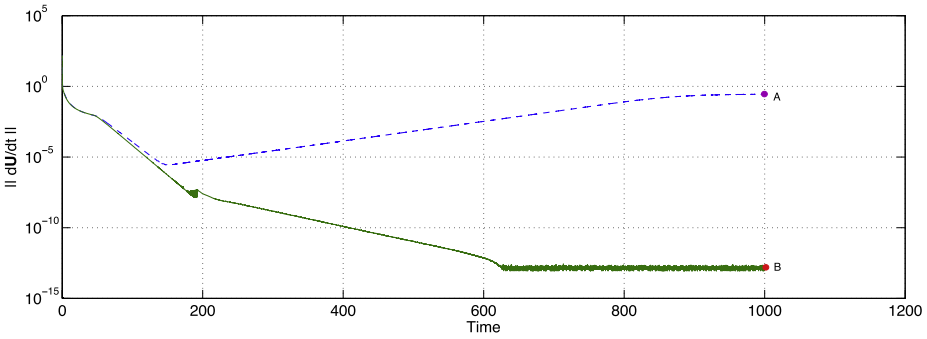

FIG. 2. Iterative stabilization procedure: *Boostconv*. The convergence history of the algorithm is depicted using a continuous line. The natural evolution of the flow is depicted using a dashed line. The final states of both computations are depicted in Figure 3(b) and Figure 4(a).

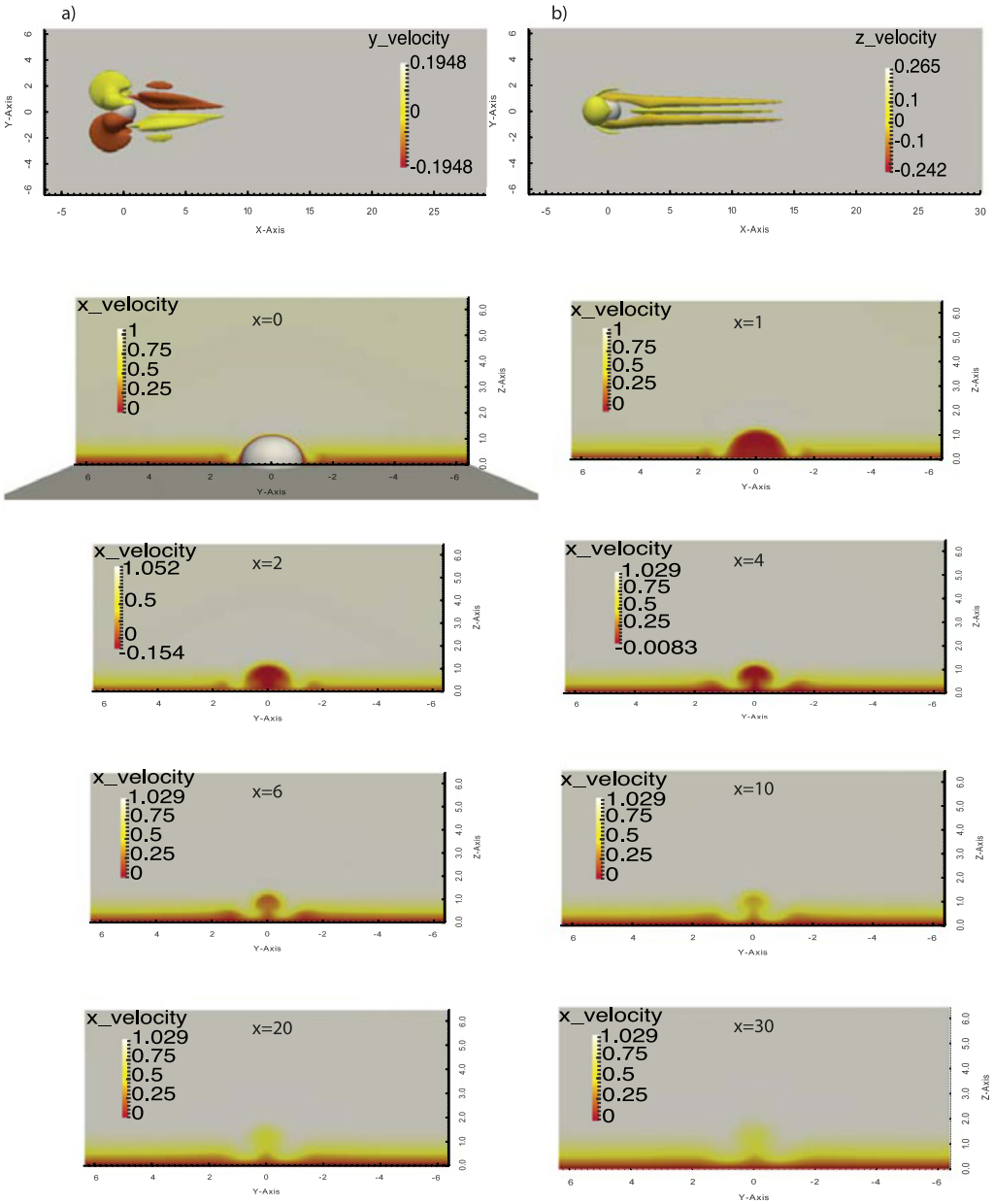

FIG. 3. Stabilized (steady) supercritical flow at $Re_k = 450$ and $k/\delta_k^* = 2.62$. Top view of contour plot of (a) y-component and (b) z-component of the base flow field. Eight slices are depicted respectively at $x = 0$, $x = +1R, 2R, 4R, 6R, 10R, 20R$ and at the outlet ($x = +30R$). In each slice we show the color map of streamwise velocity field.

are obtained. This set of equations can be recast in the following form:

$$\frac{d}{dt}\boldsymbol{q}' = \mathscr{L}\boldsymbol{q}', \tag{4}$$

where $\boldsymbol{q}' = (u', v', w', P')$ is the state vector and $\mathscr{L}$ represents the linearized Navier-Stokes operator.

In order to investigate the "core" of the instability, we consider, furthermore, the adjoint Navier-Stokes problem[28] that reads

$$-\frac{d}{dt}\boldsymbol{q}' = \mathscr{L}^{\dagger}\boldsymbol{q}'. \tag{5}$$

The eigenvalues and eigenmodes of the operators $\mathscr{L}$ and $\mathscr{L}^{\dagger}$ characterize the dynamics of the perturbation fields. The real part of the complex eigenvalue $\gamma = \sigma \pm i\omega$ represents the temporal growth rate of the disturbance, while its imaginary part is the eigenfrequency of the direct $(\hat{\boldsymbol{u}}, \hat{P})$, or adjoint $(\hat{\boldsymbol{u}}^{\dagger}, \hat{P}^{\dagger})$, global modes. All the eigenproblems involved in this paper are solved by the implicit restart Arnoldi method implemented in ParPACK[38] using the linearized DNS (direct or adjoint) time-stepper available in *NEK5000* code.

The boundary conditions associated with the direct eigenproblem are simply obtained from those used for base flow calculations, i.e., homogeneous Dirichlet conditions at the walls and inlet, outflow conditions at the outlet, and in the far field and symmetry conditions at the lateral boundaries. The conditions for the adjoint problem, instead, are chosen to eliminate the boundary terms after the application of the Lagrange identity.[39]

D. Validation and convergence analysis

The physical domain is decomposed in multi-block spectral sub-elements and the several grids are built symmetric with respect to the y-axis. In order to ensure that the spatial resolution is sufficient, several numerical convergence tests have been carried out. We compare the results obtained using four computational domains: the first one is characterized by $L_x^{in} = 7R, L_x^{out} = 30R, L_y = 10R, L_z = 8R$ (this domain will be referred to as $\mathbb{M}1$); the second, larger domain is given by $L_x^{in} = 9R, L_x^{out} = 40R, L_y = 12R, L_z = 10R$ (named $\mathbb{M}2$); the third domain ($\mathbb{M}3$) has the same size of $\mathbb{M}1$ but has a finer grid; finally, the fourth domain ($\mathbb{M}4$) is characterized by $L_x^{in} = 7R, L_x^{out} = 70R, L_y = 10R, L_z = 8R$.

The meshes $\mathbb{M}1$ and $\mathbb{M}3$ are discretized in space on a total of 8971 spectral elements having a basis of $10 \times 10 \times 10$ polynomials and $14 \times 14 \times 14$ polynomials, respectively; $\mathbb{M}2$, instead, has 16 987 elements with the same polynomial order of $\mathbb{M}1$. The longest domain $\mathbb{M}4$ has 20 933 spectral elements with a basis of $10 \times 10 \times 10$ polynomials. This choice of the polynomial basis means 1000 points per element is used for a 3D case that implies 8 971 000 points for $\mathbb{M}1$, 16 987 000 points for $\mathbb{M}2$, and 20 933 000 points for $\mathbb{M}4$. Finally, the mesh $\mathbb{M}3$ has 24 616 424 points having 13^3 functions on each element. In each case, we cluster the elements both in the wall-normal direction near the wall and along the plate near the roughness element. Table I shows the effect of the size of the computational domain on the complex eigenvalue γ and on the Strouhal number extracted from DNS at the supercritical Reynolds number $Re_k = 450$ ($k/\delta_k^* = 2.62$). We note that results are accurate almost up to three significant digits for nearly all computed Strouhal numbers using mesh $\mathbb{M}1$; the position of the upstream, downstream, and lateral boundaries has an impact on the third digit. The error made on the critical Reynolds number is order of 1%-2%. Furthermore, we compare our DNS results with Klebanoff *et al.*[18] The Strouhal number (for DNS) reported here is obtained directly from a probe located in $(x, y, z) = (5R, R, R)$, i.e., in the region past the element where the saturated nonlinear oscillations due to hairpin vortices are located.

III. RESULTS AND DISCUSSION

A. Comparison with the experimental investigation by Klebanoff *et al.*

First of all, we performed a set of 3D direct numerical simulations to compute the flow characteristics for the case $k/\delta_k^* = 2.62$ at different Reynolds numbers. We chose this value of k/δ_k^* and

TABLE I. Convergence results. (S. Direct = global stability analysis for direct eigenproblem and S. Adjoint = global stability analysis for adjoint eigenproblem.)

	Type			
	S. Direct	S. Adjoint	DNS	Klebanoff *et al.*[18]
$\mathbb{M}1$				
σ	$+8.7148 \times 10^{-2}$	$+8.7148 \times 10^{-2}$	(*unstable*)	(*unstable*)
$St = \frac{\omega k}{2\pi U_k}$	0.1659	0.1659	0.1685	≈0.16
$\mathbb{M}2$				
σ	$+8.3329 \times 10^{-2}$	$+8.3329 \times 10^{-2}$	(*unstable*)	(*unstable*)
$St = \frac{\omega k}{2\pi U_k}$	0.1653	0.1653	0.1684	≈0.16
$\mathbb{M}3$				
σ	$+8.8801 \times 10^{-2}$	$+8.8801 \times 10^{-2}$	(*unstable*)	(*unstable*)
$St = \frac{\omega k}{2\pi U_k}$	0.1661	0.1661	0.1687	≈0.16
$\mathbb{M}4$				
σ	$+7.6314 \times 10^{-2}$	$+7.6314 \times 10^{-2}$	(*unstable*)	(*unstable*)
$St = \frac{\omega k}{2\pi U_k}$	0.1658	0.1658	0.1685	≈0.16

the (hemispherical) shape of the roughness element to have a direct and easy comparison with the experimental results provided by Klebanoff *et al.*[18] The governing equations have been advanced in time until either a steady flow or a periodic flow was obtained. As the Reynolds number is increased, we observe the occurrence of a limit cycle characterized by the periodic shedding of hairpin vortices inside the boundary layer. Zhou *et al.*[26] divided these eddies in an upper portions, characterized by a legs angle greater than 45°, and a trailing region, i.e., the rest of the vortex leg. We refer to Acarlar and Smith[16] for further details about the shedding characteristics, the flow patterns, and about the structure of hairpin eddies.

The flow becomes unsteady for values of the Reynolds number around $Re_k \approx 450$. At the value of 450, the flow is already periodic and Figure 4 shows a snapshot of the computed supercritical field. Figure 5, furthermore, shows the spatial distribution of vorticity field in the symmetry plane $y = 0$. Klebanoff *et al.*[18] suggested that each hairpin structure is generated by the interaction between a concentration of spanwise vorticity in the wake region (as depicted in Figure 5) and the streamwise vortices near the roughness element. In Table I, we show the main frequencies corresponding to the shedding of these hairpin vortices obtained from the power spectrum analysis of the instantaneous

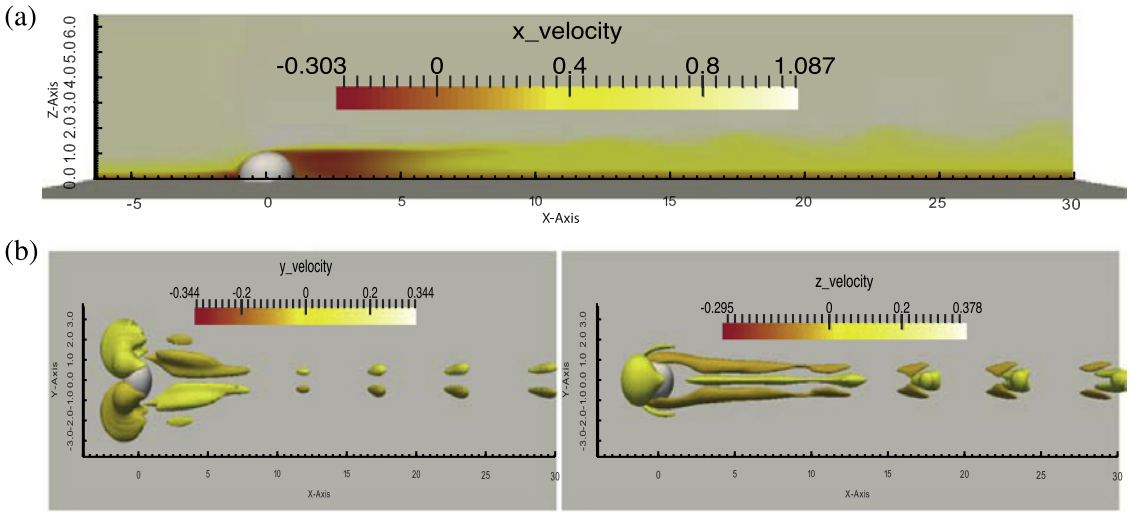

FIG. 4. Unsteady supercritical flow at $Re_k = 450$ and $k/\delta^*_k = 2.62$.

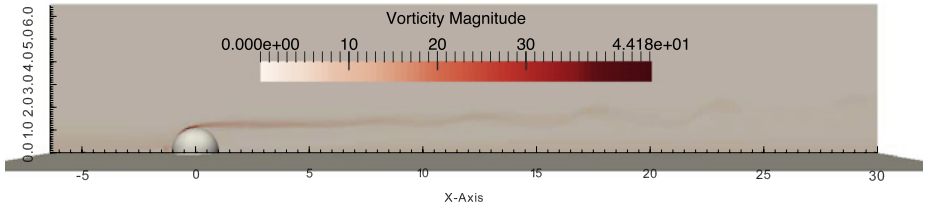

FIG. 5. Contour plot of vorticity field (y-component) in the symmetry plane $y = 0$. The flow field is the same of Figure 4.

data sampled at $(x, y, z) = (5R, R, R)$. This laminar, periodic, symmetric vortex shedding has been observed also in experiments by Acarlar and Smith,[16] and Klebanoff *et al.*[18] Such flow behavior suggests a possible link with the existence of a global instability that drives the flow to a limit cycle.

To corroborate this hypothesis, we perform a global stability analysis on top of the stabilized steady base flow at $Re_k = 450$. This was calculated using the previously mentioned stabilization procedure "*boostconv*." We note that the corresponding Reynolds number Re_{δ^*} based on the boundary layer displacement thickness δ^* is about 180, so that the undisturbed flow is locally stable with respect to Tollmien-Schlichting waves.[2] The eigenvalues computed using ParPACK are depicted in Figure 6 for several meshes. We note that the leading complex conjugate pair of eigenvalues is isolated as for the jet in cross flow[40] or the flow past a cylindrical obstacle.[27] The corresponding leading direct global mode is depicted in Figure 7. The real part of streamwise component (Figure 7) is symmetric with respect to the plane $y = 0$; a similar spatial structure was recently described by Loiseau *et al.*[27] for the varicose global instability of an array of cylindrical roughness elements with large aspect ratio. The maximum of either the streamwise, the wall-normal, or the spanwise component is found downstream of the roughness element, almost at the end of the computational domain. As for the cylinder case, the global eigenmode increases exponentially in the streamwise direction, reaches its maximum, and then slowly decays. However, even if a short domain was used for the present study, the computed eigenvalues are accurate since, as we will discuss, the instability mechanism is strongly localized behind the roughness element (see Giannetti and Luchini[39] for further details). Convergence tests performed on this configuration corroborate our statement.

The frequency of the leading eigenmode is found to agree very well with DNS data (see Table I). Moreover, the critical Reynolds number determined by the stability analysis compares well with the bifurcation threshold determined in the experimental investigation reported by Klebanoff *et al.*[18]

In addition to the direct calculations, we also computed the adjoint eigenmode (see Schmid and Henningson[2] and Luchini and Bottaro[28] for further details) of the linearized Navier-Stokes operator. As we can observe in Figure 8, the adjoint mode is spatially separated from the direct one, a feature which is due to the strong non-normality of the linearized Navier-Stokes operator. The different components of the adjoint mode reach their maximum magnitude close to the roughness element.

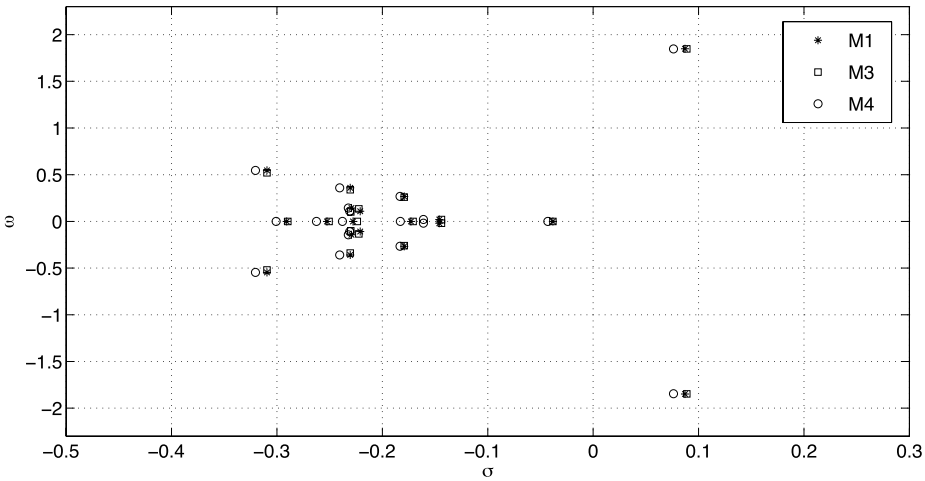

FIG. 6. Eigenvalue spectra for $Re_k = 450$, $k/\delta^*_k = 2.62$.

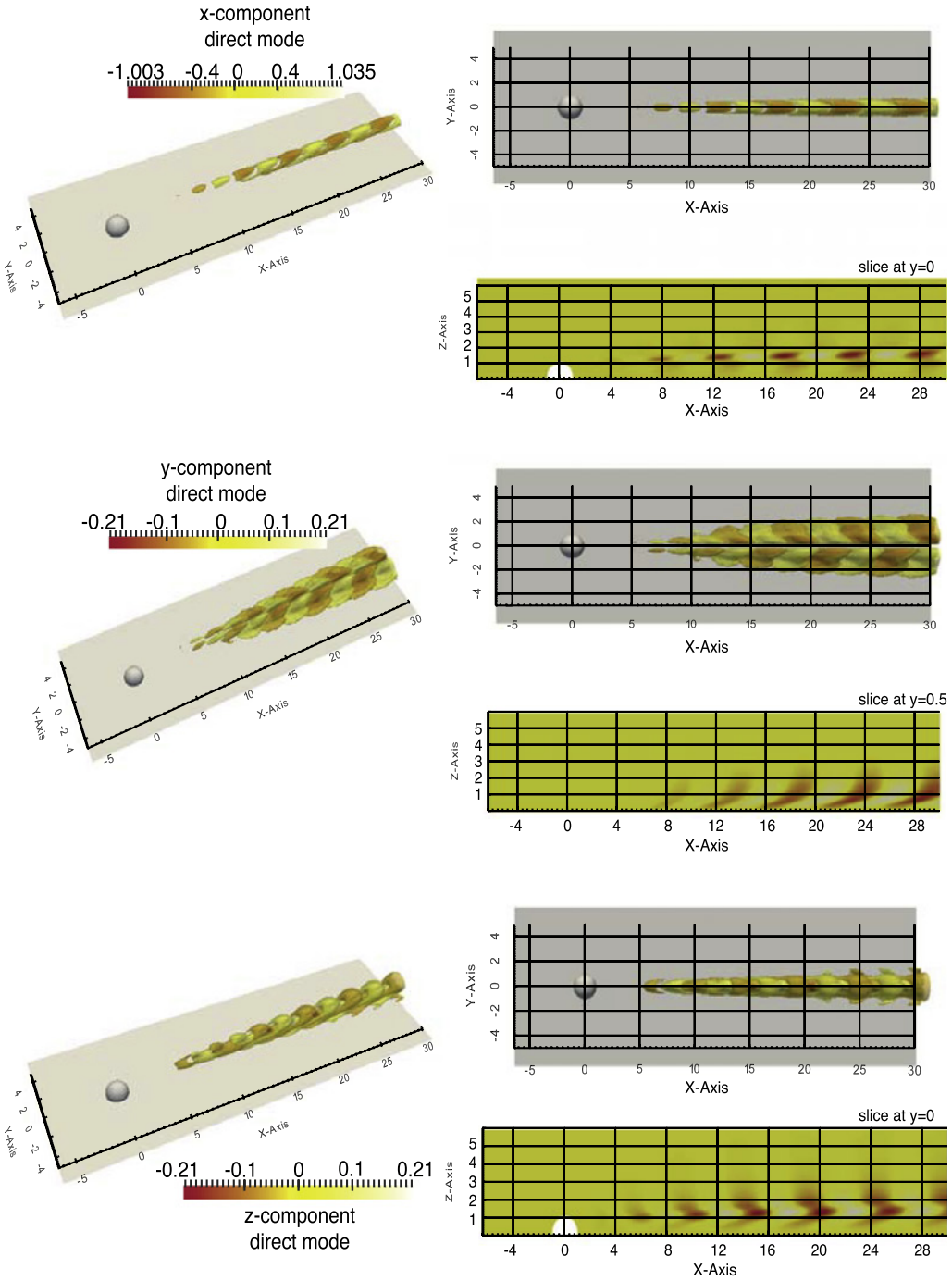

FIG. 7. Linear (direct) global leading eigenmode of the flow past the hemispherical obstacle. Here, we depict the real part of complex mode ($Re_k = 450$, $k/\delta_k^* = 2.62$).

The adjoint field gives interesting information on the receptivity of the mode to both initial conditions and to momentum forcing. Results show that the most receptive regions are those surrounding the hemisphere. In order to locate the instability mechanism, we performed a structural sensitivity analysis as explained in Ref. 39. In particular, in Figure 9, we show iso-surfaces of the spectral norm of the sensitivity tensor,

$$\mathbf{S}(x,y,z) = \frac{\hat{\mathbf{u}}^{\dagger}(x,y,z)\,\hat{\mathbf{u}}(x,y,z)}{\int_{\mathscr{D}} \hat{\mathbf{u}}^{\dagger}(x,y,z)\cdot\hat{\mathbf{u}}(x,y,z)dV}. \tag{6}$$

The structural sensitivity map is highly localized in a region just behind the roughness element, across the surface separating the outer flow from the wake region. We note that this field is

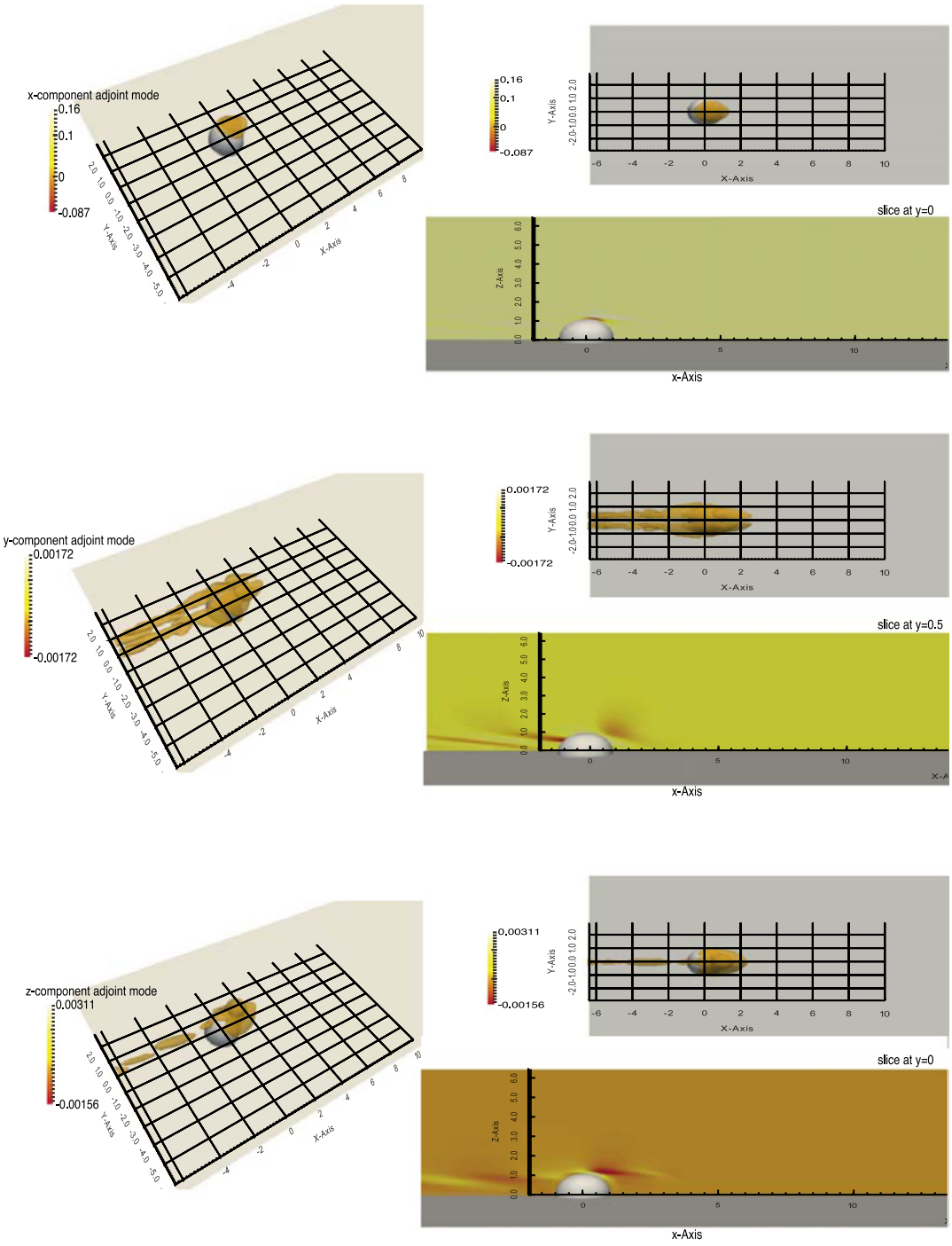

FIG. 8. Leading adjoint eigenmode for the case $Re_k = 450$, $k/\delta_k^* = 2.62$. As in Figure 7, we depict the real part of the mode.

similar to the one reported by Loiseau *et al.*[27] for the wavemaker of varicose instability. The fact that the instability mechanism ("the wavemaker") is localized in a region of strong shear suggests that the instability could be related to a feedback mechanism involving Kelvin-Helmholtz waves.

B. Parametric study

In this section, we show how the linear global instability, discussed in the previous paragraph for a fixed $k/\delta_k^*(= 2.62)$, changes as a function of this ratio. Our main objective, here, is to determine and discuss how the variation of the boundary layer thickness δ_k^* with respect to the height k of the roughness element affects the onset of the first bifurcation.

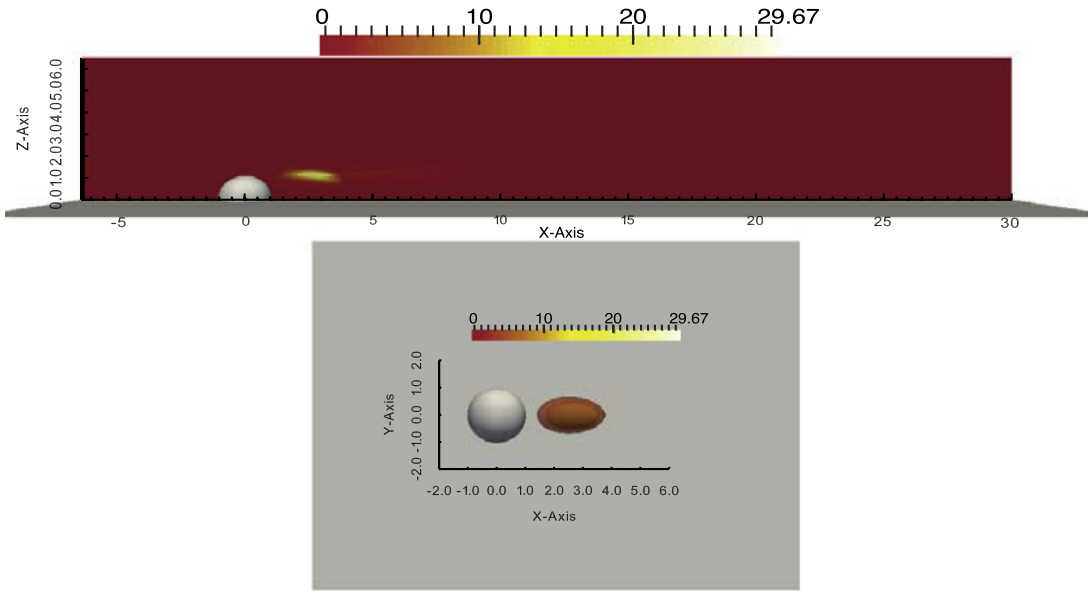

FIG. 9. Plot of structural sensitivity field for the case $k/\delta_k^* = 2.62$. (Top) We depict a slice through the wavemaker in the spanwise symmetry plane ($y = 0$).

The critical Reynolds number Re_k versus the ratio k/δ_k^* is shown in Figure 10. We performed both direct numerical simulations and global stability analyses to draw a complete picture of the dynamical system behavior. In fact, in general, it is not possible to identify a supercritical (Hopf) bifurcation without the knowledge of the nonlinear saturated state. First of all, we note that for the highest value of k/δ_k^* that has been investigated here we found perfect agreement with the experimental data provided by Klebanoff *et al.*[18] For each considered case, we start from Reynolds number Re_k = 250 to investigate the behavior of the flow. The numerical simulations, at this Reynolds number, are advanced in time starting from the Stokes solution for the hemispherical wake flow. The other simulations start from the final solution of the previously investigated Reynolds number. Appendix B reports a detailed list of the simulations carried out in the present study. We always found stable solutions, i.e., a steady state of Navier-Stokes equations, for those

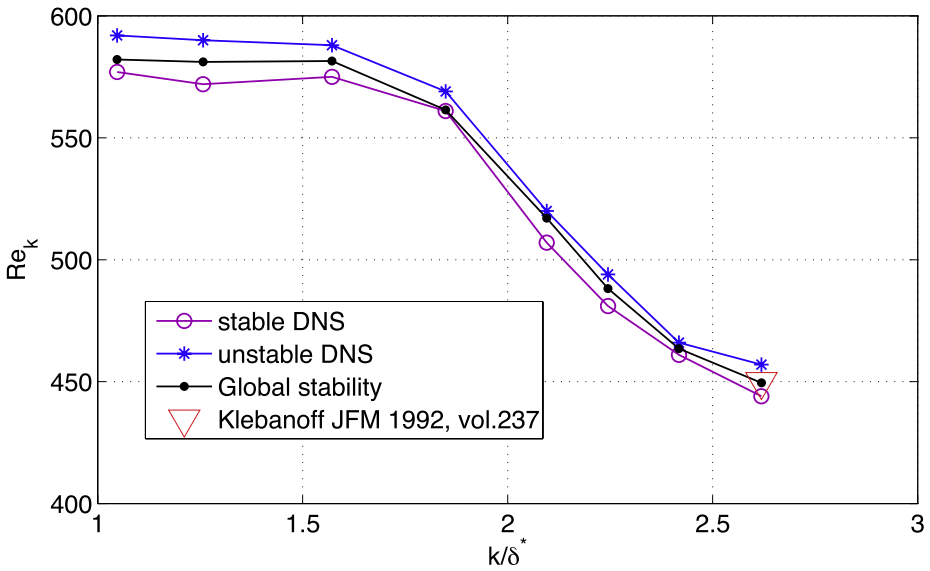

FIG. 10. Linear stability analysis results. The curve depicted using (•) identifies the neutral stability region for the hemispherical wake. Everywhere over this curve, there exist exponentially growing three-dimensional modes. Direct numerical simulations (stable (○) and unstable (∗) DNS) confirm the presence of a global instability. (△) indicates the experimental data provided by Klebanoff *et al.*[18] The critical Reynolds number for $k/\delta_k^* < 1.5$ is $Re_k \approx 580$.

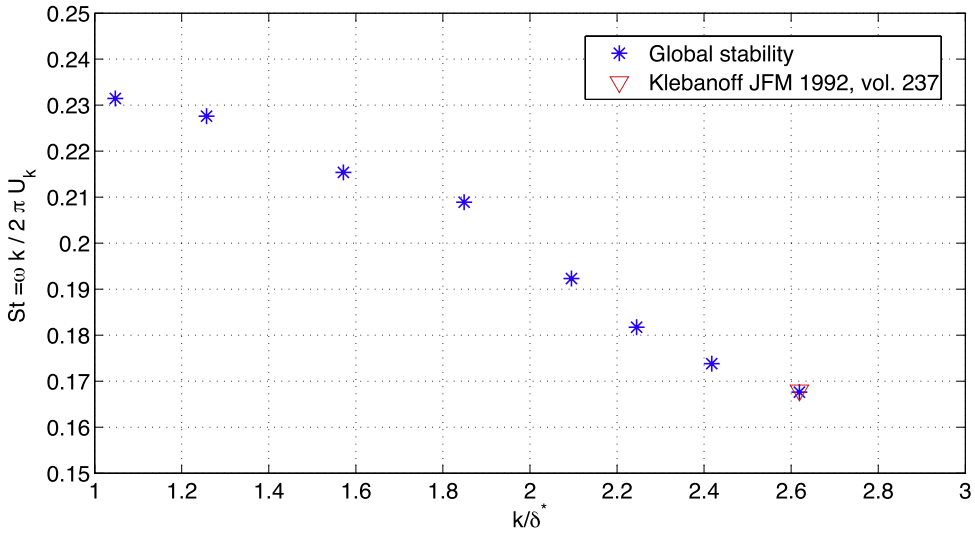

FIG. 11. Strouhal number as a function of k/δ_k^* for the flow past the hemispherical obstacle.

values of the parameters lying under the neutral curve depicted in Figure 10. In contrast, when the Reynolds number exceeds a critical value, for a fixed value of k/δ_k^*, we always found a saturated limit cycle associated to the shedding of hairpin vortices. In such cases, we recompute the unstable steady base flow using *boostconv* to perform a linear stability analysis. The neutral curve shown in Figure 10, then, is obtained by linearly interpolating the real part $\sigma(Re)$ of the leading eigenvalue of the linearized Navier-Stokes operator, i.e., we identify the critical Reynolds number by requiring that the growth rate σ, computed using the stable solution and the stabilized one, vanishes.

The critical Reynolds number on the neutral curve increases monotonically and it reaches an asymptote for $k/\delta_k^* \approx 1.5$. Thus, when the height of the roughness element k is smaller than 1.5 times the boundary layer thickness δ_k^*, an asymptotic regime is attained. This result indicates that, in these conditions, the only important parameter governing the bifurcation is the unperturbed velocity slope at the wall. The associated critical Reynolds number for this regime is $Re_k \approx 580$. This value agrees very well with critical Reynolds number $Re_k \approx 600$ reported by Tani.[41]

Figure 11 shows the dependence of the Strouhal number on the ratio k/δ_k^*. We note that the computed frequency decreases monotonically with the increase of the roughness element with respect to the boundary layer height. The Strouhal number does not reach an asymptotic value but varies linearly with k/δ_k^*. Furthermore, we also computed the adjoint and the structural sensitivity fields for each considered case. We note that the spatial structure of the direct and adjoint eigenmodes closely resemble the field presented in Figures 7 and 8. Thus, the wavemaker is always located in the region immediately past the tip of the hemisphere. For sake of brevity, we do not show here the structure of these modes. In any case, as discussed previously, we can conclude that, for each case investigated in the present work, the instability is associated to a self-sustained mechanism.

IV. CONCLUSIONS

The analysis, presented in this work, confirms the existence of a self-sustained mode in the wake of a hemispherical roughness element of large protrusion height in a Blasius boundary layer. Direct numerical simulations, stability, and sensitivity analyses were performed to better understand the stability properties of the flow. Results are in agreement with previous experimental data and show that when the Reynolds number is increased beyond a critical value, the flow undergoes an Hopf bifurcation. The self-sustained mode giving rise to the periodic shedding of hairpin vortices has been found by performing a global stability analysis. The spatial characteristics of both the direct and the adjoint modes have been analyzed and the instability mechanism localized by a structural sensitivity analysis. Results show that the instability mechanism is highly localized in the shear layer separating the outer flow region from the wake region behind the hemisphere.

We performed, in addition, a parametric study to investigate the effect of the ratio k/δ_k^* on the occurrence of the first bifurcation. We found always the same kind of instability, in agreement with the experimental findings of Klebanoff *et al.*[18] Direct numerical simulations confirm the existence of a supercritical Hopf bifurcation associated with the shedding of hairpin vortices. The variation of the leading growth rate with k/δ_k^* shows that when the boundary layer thickness is sufficiently larger than the height of the obstacle, an asymptotic linear regime is attained. In this limit, the only information that characterizes the flow behavior is the velocity gradient of the unperturbed boundary layer profile at the wall. On the contrary, we found that the Strouhal number varies almost linearly with the ratio k/δ_k^* in the investigated interval. The asymptotic value of the critical Reynolds number $Re_k = 580$ agrees very well with the existing experimental investigations, as well as other results presented in this paper.

ACKNOWLEDGMENTS

Work supported by CINECA (PRACE), by European Commission through the FP7 project "RECEPT" (Grant Agreement No. ACPO-GA-2010-265094) and by the Regione Lombardia award under the LISA initiative, for the availability of high performance computing resources and support.

APPENDIX A: STABILIZATION PROCEDURE

We briefly present the algorithm adopted for computing unstable states. Our `boostconv` procedure belongs to the class of Krylov-subspace methods to solve a linear system,

$$\mathbf{A}\mathbf{x} = \mathbf{b}. \tag{A1}$$

The main idea is to *boost* the *conv*ergence of a pre-existing classical iterative procedure, which will be written as

$$\mathbf{x}_{n+1} = \mathbf{x}_n + \mathbf{B}\mathbf{r}_n, \tag{A2}$$

where $\mathbf{r}_n = \mathbf{b} - \mathbf{A}\mathbf{x}_n$ is the residual and $\mathbf{B}$ is an approximate inverse (preconditioner) of $\mathbf{A}$. The convergence of (A2) is governed by a series of exponentially decaying/amplifying modes. The procedure will also be applicable to a non-linear system, where we expect a similar behavior when $\mathbf{x}_n$ is close enough to the exact solution $\mathbf{x}$. In the classical procedure, after a suitable number of iterations, the convergence rate is often dictated by a small number of slowly decaying (or the divergence by a small number of amplifying) modes. The present algorithm is conceived to modify the part of the spectrum composed of these modes mostly on the assumption that the remaining part of the spectrum is sufficiently damped by the original iterative procedure.

We focus our attention on an improvement of the existing iterative procedure of the form

$$\mathbf{x}_{n+1} = \mathbf{x}_n + \mathbf{B}\boldsymbol{\xi}_n(\mathbf{r}_n), \tag{A3}$$

where the modified forcing $\boldsymbol{\xi}_n$ is a suitable function of the residual $\mathbf{r}_n$ which goes to zero when and only when $\mathbf{r}_n$ does. Equation (A3) can be implemented through a black-box subroutine that modifies the residual and feeds it back to the pre-existing iterative procedure. As a consequence of (A3), the equation that governs the evolution of the residual $\mathbf{r}_n$ becomes

$$\begin{aligned} \mathbf{r}_{n+1} &= \mathbf{r}_n - \mathbf{A}\mathbf{B}\boldsymbol{\xi}_n, \quad \text{i.e.,} \\ \mathbf{r}_n - \mathbf{r}_{n+1} &= \mathbf{A}\mathbf{B}\boldsymbol{\xi}_n. \end{aligned} \tag{A4}$$

The key idea is to build a subspace of vectors on which the action of $\mathbf{AB}$ is known by storing $\boldsymbol{\xi}_n$ and the difference $\mathbf{r}_n - \mathbf{r}_{n+1}$ before each iteration. We can then, for the purpose of calculating $\boldsymbol{\xi}_{n+1}$, approximately solve (A1) by a least-square approximation over this subspace. Adding the residual of this solution back into $\boldsymbol{\xi}_{n+1}$ restores the original feedback on non-represented modes. This stabilizing procedure can be encapsulated in a black-box subroutine where the only input is the original residual $\mathbf{r}_n$ and the output is the modified residual $\boldsymbol{\xi}_n$.

APPENDIX B: THREE-DIMENSIONAL NUMERICAL SIMULATIONS

Table II lists the simulation parameters and the stability characteristics for each run.

TABLE II. Parameters and stability of the different three-dimensional (3D) numerical simulations.

k/δ_k^*	Steady state	Limit cycle	Critical Re_k
2.62	250, 300, 340, 360, 380, 400, 420, 440, 444	450, 457, 460	450
2.42	250, 350, 450, 460	467, 475, 500	463
2.24	250, 350, 450, 475, 481	492, 500	487
2.09	250, 350, 450, 500, 507	520, 550	517
1.85	250, 350, 450, 550, 561	569, 575, 600	562
1.57	250, 350, 450, 550, 575	588, 600	581
1.26	250, 350, 450, 550, 572	590	582
1.04	250, 350, 450, 550, 577	591, 600	582

[1] W. D. Saric, H. L. Reed, and E. J. Kerschen, "Boundary-layer receptivity to freestream disturbances," Annu. Rev. Fluid Mech. **34**, 291–319 (2002).
[2] P. J. Schmid and D. S. Henningson, *Stability and Transition in Shear Flows* (Springer, 2001).
[3] S. Cherubini, M. D. Tullio, P. D. Palma, and G. Pascazio, "Transient growth in the flow past a three-dimensional smooth roughness element," J. Fluid Mech. **724**, 642–670 (2013).
[4] J. H. M. Fransson, A. Talamelli, L. Brandt, and C. Cossu, "Delaying transition to turbulence by a passive mechanism," Phys. Rev. Lett. **96**, 064501 (2006).
[5] J. H. M. Fransson, L. Brandt, A. Talamelli, and C. Cossu, "Experimental and theoretical investigation of the non-modal growth of steady streaks in a flat plate boundary layer," Phys. Fluids **16**, 3627 (2004).
[6] F. P. Bertolotti, "Receptivity of three-dimensional boundary-layers to localized wall roughness and suction," Phys. Fluids **12**, 1799 (2000).
[7] L. Schrader, L. Brandt, and D. S. Henningson, "Receptivity mechanisms in three-dimensional boundary-layer flows," J. Fluid Mech. **618**, 209–241 (2009).
[8] L.-U. Schrader, S. Amin, and L. Brandt, "Transition to turbulence in the boundary layer over a smooth and rough swept plate exposed to free-stream turbulence," J. Fluid Mech. **646**, 297–325 (2010).
[9] S. D. Downs, E. B. White, and N. A. Denissen, "Transient growth and transition induced by random distributed roughness," AIAA J. **46**, 451–462 (2008).
[10] F. G. Ergin and E. B. White, "Unsteady and transitional flows behind roughness elements," AIAA J. **44**, 2504–2514 (2006).
[11] D. C. Reda, "Review and synthesis of roughness-dominated transition correlations for reentry applications," J. Spacecr. Rockets **39**, 161–167 (2002).
[12] A. Denissen and E. B. White, "Rougness-induced bypass transition, revisited," AIAA J. **46**, 1874–1877 (2008).
[13] D. P. Rizzetta and M. R. Visbal, "Direct numerical simulations of flow past an array of distributed roughness elements," AIAA J. **45**, 1967–1976 (2007).
[14] C. J. Baker, "The laminar horseshoe vortex," J. Fluid Mech. **95**, 347–367 (1979).
[15] I. Tani, H. Komoda, Y. Komatsu, and M. Iuchi, "Boundary-layer transition by isolated roughness," In Report No. 375, Aeronautical Research Institute, University of Tokyo, 1962.
[16] M. S. Acarlar and C. R. Smith, "A study of hairpin vortices in a laminar boundary layer. Part 1. Hairpin vortices generated by a hemisphere protuberance," J. Fluid Mech. **175**, 1–41 (1987).
[17] P. J. Mason and B. R. Morton, "Trailing vortices in the wakes of surface-mounted obstacles," J. Fluid Mech. **175**, 247–293 (1987).
[18] P. S. Klebanoff, W. G. Cleveland, and K. D. Tidstrom, "On the evolution of a turbulent boundary layer induced by a three-dimensional roughness element," J. Fluid Mech. **237**, 101–187 (1992).
[19] W. S. Saric, H. L. Reed, and E. B. White, "Stability and transition of three-dimensional boundary layers," Annu. Rev. Fluid Mech. **35**, 413–440 (2003).
[20] E. Reshotko and A. Tumin, "Role of transient growth in roughness-induced transition," AIAA J. **42**, 766–770 (2004).
[21] S. P. Schneider, "Effects of roughness on hypersonic boundary-layer transition," J. Spacecr. Rockets **45**, 193–209 (2008).
[22] M. R. Malik, "Numerical methods for hypersonic boundary layer stability," J. Comput. Phys. **86**, 376–413 (1990).
[23] E. Reshotko, "Transient growth: A factor in bypass transition," Phys. Fluids **13**, 1067 (2006).
[24] G. Groskopf, M. J. Kloker, and O. Marxen, "Bi-global secondary stability theory for high-speed boundary layer flows," in *Proceedings of the Summer Program* (Center for Turbulence Research, Stanford University, 2008).
[25] N. De Tullio, P. Paredes, N. D. Sandham, and V. Theofilis, "Laminar-turbulent transition induced by a discrete roughness element in a supersonic boundary layer," J. Fluid Mech. **735**, 613–646 (2013).
[26] Z. Zhou, Z. Wang, and J. Fan, "Direct numerical simulation of the transitional boundary-layer flow induced by an isolated hemispherical roughness element," Comput. Methods Appl. Mech. Eng. **199**, 1573–1582 (2010).
[27] J.-C. Loiseau, J.-C. Robinet, S. Cherubini, and E. Leriche, "Investigation of the roughness-induced transition: Global stability analyses and direct numerical simulations," J. Fluid Mech. **760**, 175–211 (2014).
[28] P. Luchini and A. Bottaro, "Adjoint equations in stability analysis," Annu. Rev. Fluid Mech. **46**, 493–517 (2014).
[29] V. Theofilis, "Global linear instability," Annu. Rev. Fluid Mech. **43**, 319–352 (2011).
[30] I. Tani, H. Komoda, Y. Komatsu, and M. Iuchi, "Boundary-layer transition by isolated roughness," Aeronautical Research Institute, Internal Report 375, pp. 129–143, 1962.
[31] A. T. Patera, "A spectral element method for fluid dynamics - laminar flow in a channel expansion," J. Comput. Mech. Phys. **54**, 468–488 (1984).

[32] P. F. Fischer, "An overlapping schwarz method for spectral element solution of the incompressible Navier-Stokes equations," J. Comput. Phys **133**, 84–101 (1997).
[33] E. Åkervik, L. Brandt, D. S. Henningson, J. Hoepffner, O. Marxen, and P. Schlatter, "Steady solutions of the Navier-Stokes equations by selective frequency damping," Phys. Fluids **18**, 068102 (2006).
[34] G. M. Shroff and H. B. Keller, "Stabilization of unstable procedures: The recursive projection method," SIAM J. Num. Anal. **30**, 1099–1120 (1993).
[35] U. Trottenberg, C. Oosterlee, and A. Schüller, *Multigrid* (Academic Press, 2001).
[36] M. Carini, F. Giannetti, and F. Auteri, "On the origin of the flip-flop instability of two side-by-side cylinder wakes," J. Fluid Mech. **742**, 552–576 (2014).
[37] M. Carini, F. Giannetti, and F. Auteri, "First instability and structural sensitivity of the flow past two side-by-side cylinders," J. Fluid Mech. **749**, 627–648 (2014).
[38] R. B. Lehoucq, D. C. Sorensen, and C. Yang, *Arpack Users' Guide* (Society for Industrial and Applied Mathematics, Philadelphia, 1998).
[39] F. Giannetti and P. Luchini, "Structural sensitivity of the first instability of the cylinder wake," J. Fluid Mech. **581**, 167–197 (2007).
[40] A. Peplinski, P. Schlatter, and D. S. Henningson, "Global stability and optimal perturbation for a jet in cross-flow," Eur. J. Mech., B: Fluid **49**, 438–447 (2015).
[41] I. Tani, "Boundary-layer transition," Annu. Rev. Fluid Mech. **1**, 169–196 (1969).

Paper

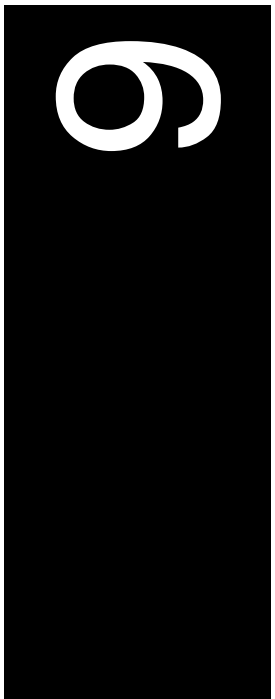

IOP Publishing | The Japan Society of Fluid Mechanics Fluid *Dynamics* Research
Fluid Dyn. Res. **47** (2014) 015503 (14pp) doi:10.1088/0169-5983/47/1/015503

Three-dimensional stability, receptivity and sensitivity of non-Newtonian flows inside open cavities

Vincenzo Citro[1], Flavio Giannetti[1] and Jan O Pralits[2]

[1] DIIN, University of Salerno, Via Ponte don Melillo, 84084 Fisciano (SA), Italy
[2] DICCA, University of Genoa, Via Montallegro 1, 16145 Genoa (GE), Italy

E-mail: vcitro@unisa.it

Received 17 October 2013, revised 1 September 2014
Accepted for publication 14 September 2014
Published 22 October 2014

Communicated by K Suga

Abstract

We investigate the stability properties of flows over an open square cavity for fluids with shear-dependent viscosity. Analysis is carried out in context of the linear theory using a normal-mode decomposition. The incompressible Cauchy equations, with a Carreau viscosity model, are discretized with a finite-element method. The characteristics of direct and adjoint eigenmodes are analyzed and discussed in order to understand the receptivity features of the flow. Furthermore, we identify the regions of the flow that are more sensitive to spatially localized feedback by building a spatial map obtained from the product between the direct and adjoint eigenfunctions. Analysis shows that the first global linear instability of the steady flow is a steady or unsteady three-dimensionl bifurcation depending on the value of the power-law index n. The instability mechanism is always located inside the cavity and the linear stability results suggest a strong connection with the classical lid-driven cavity problem.

(Some figures may appear in colour only in the online journal)

1. Introduction

Our notion about the dynamics of many flow configurations are often based on familiar Newtonian fluids such as water and air. The non-Newtonian fluid mechanics, however, can be a very important and useful field because such kinds of flows are often encountered in nature and many industrial applications, where the observed flow can be markedly different from that of its Newtonian counterpart. In this paper we focus our attention on the class of non-Newtonian fluids characterized by an instantaneous mutual relation between the rate of shear and the shear stress. In other words, such fluids have no memory of their past history.

1.1. Shear-thinning and shear-thickening fluids: the Carreau viscosity model

The shear-thinning phenomena are perhaps the most widely encountered type of time-independent non-Newtonian behavior in engineering practice. They are characterized by an apparent viscosity which gradually decreases as the shear rate increases. On the contrary, the shear-thickening fluids present an apparent viscosity that increases with the increasing of the shear rate and hence the characteristic name *dilatant flows*.

In the last century many mathematical equations and models of varying complexity and forms have been reported in the literature; some of these are straightforward attempts to fit the experimental data, while others have a theoretical basis in statistical mechanics (see e.g. Carreau *et al* (1997)). In this work we have chosen to use the Carreau viscosity model, that is based on a molecular theory (Lodge's theory) since it allows to satisfactorily describe the complex behaviors of such fluids. Moreover, it has been widely used to model non-Newtonian fluids (including for example hemodynamic studies, see Hsu *et al* (2009)), and thereby offers the possibility to validate our numerical code.

1.2. Open-cavity instabilities

The open cavity flow is a problem of great interest in many engineering applications such as military aircraft, sunroofs in automobiles or the gap between train wagons. Historically it has been given great attention since it represents a prototype problem in which there is a finite region of separated flow. Rossiter (1964) was the first to give a significant contribution to explain the unsteadiness of flows over rectangular cavities, identifying an acoustic feedback mechanism for cavities of several aspect ratios L/D (i.e. length to depth) and flow regimes. The presence of this Rossiter mode, in turn, generates self-sustained oscillations of velocity, pressure, and, in some cases, density, which may induce strong vibrations in the substrate over which the fluid is flowing. The latter may give rise to structural fatigue or acoustic noise. Many experimental and numerical studies have shown that this resonance is based on a feedback mechanism, whereby small disturbances in the shear layer are amplified by the Kelvin–Helmholtz instability (see e.g. Rowley *et al* (2002)).

However, when significant interactions between the shear layer and the flow within the cavity exist, the flow may be found in a completely different state from that of the cavity resonance that can be described with the aid of the Rossiter model (or any of its improved versions). The resultant mode appears to be a global instability whose frequency of oscillation is independent of the Mach number. Recently, Brés and Colonius (2008) have performed several 3D simulations that have proved, for the first time, the existence of 3D instabilities situated inside the cavity. They showed also that these 3D instabilities are related to centrifugal instabilities previously reported in flows over backward-facing steps, lid-driven cavity flows and Couette flows.

In the field of inelastic non-Newtonian fluids, there are only a few studies aimed at detecting the instability mechanism in the configuration under investigation. One relevant numerical and experimental investigation was reported by Cochrane *et al* (1981). They studied the behavior of the non-Newtonian (PAC) flow and the Newtonian flow (syrup-water mixture) past a square open cavity.

1.3. Goal of present work

The aim of the present work is to study the effects of shear-dependent viscosity on the instability features in incompressible open cavity flows. The goal is to provide a better description of the instability mechanism of 3D perturbations and to show that the instability is

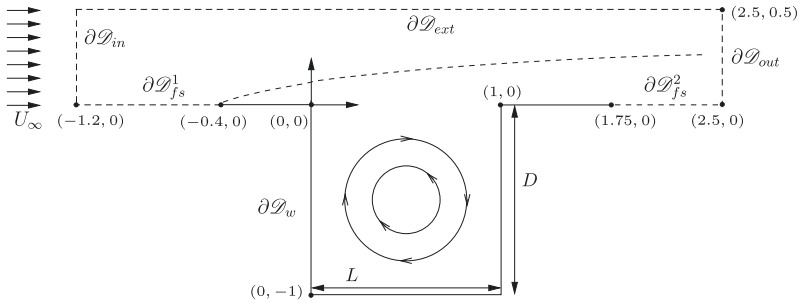

Figure 1. Flow configuration, frame of reference and the computational domain $\mathscr{D}$. The figure also shows a sketched schematic visualization of the base flow structure.

strictly correlated with the one arising in the lid-driven cavity flow. First of all, we perform an accurate analysis of the occurrence of the first instability using the linear stability theory; the critical Reynolds number Re_{cr} and the corresponding spanwise wavenumber, here denoted as the optimal spanwise wavenumber β_{opt}, are computed for different non-Newtonian fluids (i.e. for every couple of parameters n, λ of the Carreau model). After the identification of the first instability, we analyze the adjoint field in order to describe the receptivity behavior.

Furthermore, we determine the instability core by performing a structural sensitivity analysis, as discussed by Chomaz (2005), Giannetti and Luchini (2007) and Marquet *et al* (2008). The spatial map of the structural sensitivity gives a better understanding of the instability mechanism. In the present work, since the flow is globally unstable, we do not consider the sensitivity to transient disturbance growth as considered by Brandt *et al* (2011). Finally, we want to remark that the current sensitivity analysis is not directly applicable when it concerns passive control devices with the scope of controlling instability. In order to do so one must extend the current analysis the include variations of the basic flow. Examples of this can be found in Pralits *et al* (2010) and Pralits *et al* (2013).

2. Theoretical framework

We investigate the stability characteristics of non-Newtonian fluids in the case of a two-dimensionl (2D) flow arising over a square open cavity due to a uniform stream. The geometry, frame of reference and notation are shown in figure 1. A Cartesian system is located on the left edge of the cavity with the x-axis pointing in the flow direction. The fluid motion, then, can be described by the unsteady incompressible Cauchy equations,

$$\nabla \cdot \boldsymbol{u} = 0, \tag{1}$$

$$\frac{\partial \boldsymbol{u}}{\partial t} + (\boldsymbol{u} \cdot \nabla)\boldsymbol{u} = -\nabla P + \frac{1}{Re}\nabla \boldsymbol{T}, \tag{2}$$

where $\boldsymbol{u}$ is the velocity vector with components $\boldsymbol{u} = (u, v)$ and P is the reduced pressure. This system is closed when we supply a constitutive relation between the stress tensor $\boldsymbol{T}$ and the rate-of-strain tensor $\boldsymbol{D} = \frac{1}{2}\left[\nabla \boldsymbol{u} + (\nabla \boldsymbol{u})^T\right]$. In this paper we focus on fluids whose $\boldsymbol{T}$ depends linearly on $\boldsymbol{D}$ through the relation $\boldsymbol{T} = 2\mu(S)\boldsymbol{D}$, where $S = (2\boldsymbol{D}\colon \boldsymbol{D})^{1/2}$. While for a Newtonian fluid the dynamic viscosity μ does not depend on the shear rate S, for a non-Newtonian fluid this dependence cannot be ignored and the functional form of $\mu = \mu(S)$ changes with the particular fluid considered. We adopt a Carreau model that is characterized

by the following viscosity law (Bird *et al* (1987), chapter 4)

$$\frac{\mu - \hat{\mu}_\infty}{\hat{\mu}_0 - \hat{\mu}_\infty} = \left[1 + (\lambda S)^2\right]^{\frac{n-1}{2}}, \tag{3}$$

where $\hat{\mu}_\infty$ and $\hat{\mu}_0$ are the viscosities at infinite and zero shear rates (the ratio $\hat{\mu}_\infty/\hat{\mu}_0$ is set to 10^{-3}), the parameter n is the power index and λ is the relaxation time.

Equations (1) and (2) are made dimensionless using the cavity depth D as the characteristic length scale, the velocity of the incoming uniform stream U_∞ as the reference velocity and $\hat{\mu}_0$ as the reference dynamic viscosity. Thus, the Reynolds number can be expressed as $Re = \rho U_\infty D/\hat{\mu}_0$. Finally, the system of differential equations (1) and (2) is closed with the following boundary conditions: $\boldsymbol{u} = 1 \cdot \boldsymbol{e}_x$ at the inlet $\partial\mathscr{D}_{in}$, the outflow boundary condition (i.e. $P = 0$, $\partial_x u = 0$) at the outlet $\partial\mathscr{D}_{out}$, no-slip conditions $\boldsymbol{u} = \boldsymbol{0}$ on the solid walls $\partial\mathscr{D}_w$ (represented with a solid line in figure 1), free-slip condition with zero tangential stress (i.e. $\partial_y u = 0$ and $v = 0$) on the upper limit of the computational domain $\partial\mathscr{D}_{ext}$ and on the remaining boundary $\partial\mathscr{D}_{fs}$. Similar conditions are used, for the same reference geometrical configuration, by Sipp and Lebedev (2007) and Barbagallo *et al* (2009).

2.1. Global stability analysis

The instability onset is studied within the framework of the linear stability theory with a classical normal-mode analysis. The stability analysis relies on the existence of a steady solution about which infinitesimal unsteady perturbations are superimposed. The velocity and pressure fields are decomposed into a 2D base flow $\boldsymbol{Q_b}(x, y) = (\boldsymbol{u}_b, P_b)^T = (u_b, v_b, 0, P_b)^T$ and a three-dimensional (3D) disturbance flow, denoted by $\boldsymbol{q}'(x, y, z, t) = (\boldsymbol{u}', P')^T = (u', v', w', P')^T$ of small amplitude ϵ. Introducing this decomposition into (1) and linearizing, we obtain two problems describing the spatial structure of the base flow and the evolution of the unsteady perturbation field. In particular, the base flow is governed by the steady version of (1), whereas the perturbed field is described by the following set of linearized unsteady Carreau equations (uCE)

$$\frac{\partial \boldsymbol{u}'}{\partial t} + \boldsymbol{C}\left\{\boldsymbol{u}_b, Re\right\}\boldsymbol{u}' = -\nabla P', \tag{4}$$

$$\nabla \cdot \boldsymbol{u}' = 0, \tag{5}$$

where the linearized operator $\boldsymbol{C}$ can be written as

$$\boldsymbol{C}\left\{\boldsymbol{u}_b, Re\right\}\boldsymbol{u}' = \boldsymbol{u}_b \cdot \nabla \boldsymbol{u}' + \boldsymbol{u}' \cdot \nabla \boldsymbol{u}_b$$

$$-\frac{1}{Re}\nabla \cdot \left[\mu_b\left(\nabla \boldsymbol{u}' + (\nabla \boldsymbol{u}')^T\right) + \mu'\left(\nabla \boldsymbol{u}_b + \left(\nabla \boldsymbol{u}_b\right)^T\right)\right].$$

In the previous definition we have introduced μ_b and μ' that represent the base flow viscosity and the perturbation viscosity, respectively (see e.g. Lashgari *et al* (2012)).

As the base flow is homogeneous in the spanwise direction, a general perturbation can be decomposed into Fourier modes with spanwise wavenumber β. The 3D perturbations may be expressed as

$$\boldsymbol{q}'(x, y, z, t) = \frac{1}{2}\left\{\left(\hat{\boldsymbol{q}}\right)^T(x, y)\ exp\left[i\beta z + \gamma t\right] + c.c.\right\}, \tag{6}$$

where $\gamma = \sigma + i\omega$ is the angular frequency, $c.c.$ stands for the complex conjugate of the preceding expression and $\hat{\boldsymbol{q}} = (\hat{u}, \hat{v}, \hat{w}, \hat{P})$. Complex conjugation is required in (6) since $\boldsymbol{q}'$ is

real. The angular frequency γ is a complex number: its real part σ represents the temporal growth rate and its imaginary part ω the frequency of the perturbation. The physical meaning of σ is in agreement with the classical definition of stability: for $\sigma > 0$, the base flow is unstable whereas for $\sigma < 0$ it is stable. Introducing the ansatz (6) in (4- 5) that govern the evolution of the perturbation, we obtain a generalized eigenvalue problem that is expressed by means of the following formal relation

$$\mathscr{A}\hat{\mathbf{q}} + \gamma\mathscr{B}\hat{\mathbf{q}} = 0, \tag{7}$$

in which $\mathscr{A}$ is the complex linearized evolution operator. The boundary conditions associated with (7) are derived from those used for the base flow calculation, as in Sipp and Lebedev (2007). Finally, we underline that the two complex eigenpairs $(\sigma + i\omega; \hat{\mathbf{q}})$ and $(\sigma - i\omega; \hat{\mathbf{q}}^*)$ associated with a particular base flow $\boldsymbol{Q_b}$ are simultaneously a solution of the eigenproblem together with the boundary conditions. Thus, the eigenvalues are complex conjugates and the generic spectra in the (σ, ω) plane is symmetric with respect to the real axis.

2.2. Structural sensitivity and the adjoint field

In this section we introduce, in a concise manner, the analysis regarding structural sensitivity. The idea of this analysis is the concept of 'wavemaker' that was introduced by Giannetti and Luchini (2007) and Hill (1992) to identify the location of the core of a global instability (see e.g. Pralits *et al* (2010)). Recently, Luchini and Bottaro (2014) reviewed the use of adjoint equations in hydrodynamic stability analysis. They discussed in detail the adjoint-based sensitivity analysis (Appendix A, Section 9) that is able to map the structural sensitivity of a global oscillator. We refer to this paper for further details.

In Lashgari *et al* (2012) it is shown, using a perturbation analysis, that for each considered global mode $(\sigma + i\omega; \hat{u}, \hat{v}, \hat{w}, \hat{p})$, by adding a forcing term in the form of a (2×2) coupling matrix $\delta\boldsymbol{M}_0$, the following eigenvalue drift is obtained

$$\delta\gamma = \boldsymbol{S}\colon \delta\boldsymbol{M}_0 = \sum_{ij} S_{ij}\delta M_{0ij}, \tag{8}$$

where we have introduced the sensitivity tensor

$$\boldsymbol{S}(x_0, y_0) = \frac{\hat{\boldsymbol{f}}^+(x_0, y_0)\hat{\boldsymbol{u}}(x_0, y_0)}{\int_{\mathscr{D}} \hat{\boldsymbol{f}}^+ \cdot \hat{\boldsymbol{u}} dS}. \tag{9}$$

The adjoint field $\hat{\boldsymbol{f}}^+$ is obtained using the Lagrange identity (as in Giannetti and Luchini (2007)); thus, the vector field $\hat{\boldsymbol{g}}^+(x, y) = (\hat{\boldsymbol{f}}^+, \hat{m}^+)$ satisfies the following problem:

$$-\gamma\hat{\boldsymbol{f}}^+ + \boldsymbol{C}^+\left\{\boldsymbol{u}_b, Re\right\}\hat{\boldsymbol{f}}^+ + \nabla\hat{m}^+ = 0, \tag{10}$$

$$\nabla \cdot \hat{\boldsymbol{f}}^+ = 0. \tag{11}$$

in which the operator $\boldsymbol{C}^+$ is defined as

$$\boldsymbol{C}^+\left\{\boldsymbol{u}_b, Re\right\}\hat{\boldsymbol{f}}^+ = \boldsymbol{u}_b \cdot \nabla\hat{\boldsymbol{f}}^+ - \boldsymbol{u}^+ \cdot \nabla\boldsymbol{u}_b$$

$$+\frac{1}{Re}\left[\mu_b\left(\nabla\hat{\boldsymbol{f}}^+ + \left(\nabla\hat{\boldsymbol{f}}^+\right)^T\right) + \left(\nabla\boldsymbol{u}_b + \left(\nabla\boldsymbol{u}_b\right)^T\right) \cdot \nabla\hat{\boldsymbol{f}}^+\boldsymbol{V}(\boldsymbol{u}_b)\right]$$

where the viscosity fluctuation operator $\boldsymbol{V}$ can be expressed in tensorial notation (see e.g. Lashgari *et al* (2012))

Table 1. Comparison of the results obtained by the present code with those obtained by Sipp and Lebedev (2007) with the meshes $\boldsymbol{\mathcal{D}1}$ and $\boldsymbol{\mathcal{D}2}$. The eigenfrequency ω and growth rate σ have been calculated for the first 2D unstable eigenmode at $Re = 4140$. We report also the number of degrees of freedom ($n_{d.o.f.}$) and the number of triangles (n_t) for each unstructured Mesh.

Mesh	σ	ω	$n_{d.o.f.}$	n_t
$\boldsymbol{\mathcal{M}1}$	0.0007590	7.4931	998668	221045
$\boldsymbol{\mathcal{M}2}$	0.0008344	7.4937	1416630	313791
$\boldsymbol{\mathcal{M}3}$	0.0009122	7.4943	2601757	576887
$\boldsymbol{\mathcal{D}1}$	0.0007401	7.4930	880495	194771
$\boldsymbol{\mathcal{D}2}$	0.0008961	7.4942	1888003	418330

$$V_i(\boldsymbol{u_b}) = 2\left[\frac{\partial\mu}{\partial S_{i1}}(\boldsymbol{u_b})\frac{\partial}{\partial x} + \frac{\partial\mu}{\partial S_{i2}}(\boldsymbol{u_b})\frac{\partial}{\partial y} + \frac{\partial\mu}{\partial S_{i3}}(\boldsymbol{u_b})\frac{\partial}{\partial z}\right]. \tag{12}$$

The boundary conditions associated with the adjoint problem are derived from those used for the direct eigenproblem. Different norms of the tensor $\boldsymbol{S}$ can be used to build a spatial map of the sensitivity. The spectral norm is chosen here to study the worst possible case.

3. Numerical method and validation

3.1. Base flow calculation

The numerical computations of base flow have been performed using a finite element code. In particular, we first derive the associated variational formulation of the Cauchy system (1) and then use the FreeFem ++ (http://www.freefem.org) software to obtain a spatial discretization onto classical $P2 - P1$ Taylor-Hood elements. The resultant nonlinear system of algebraic equations, along with their boundary conditions, is solved with a Newton-Raphson procedure: starting from an initial guess $w_b^{(0)}$, at each step the linear system

$$CE\left(Re,\, W_b^{(n)}\right) \cdot w_b^{(n)} = -rhs^{(n)} \tag{13}$$

is inverted using the MUMPS-MUltifrontal Massively Parallel sparse direct Solver (Amestoy *et al* (2006, 2010)) and the base flow is then updated as

$$W_b^{(n+1)} = W_b^{(n)} + w_b^{(n)}. \tag{14}$$

The initial guess is chosen as the solution of the Stokes equations and the process is carried out until the L^2-norm of the residual of the governing equations becomes smaller than 10^{-12}. Three different meshes: $\boldsymbol{\mathcal{M}1}$, $\boldsymbol{\mathcal{M}2}$ and $\boldsymbol{\mathcal{M}3}$, have been generated (see table 1) with the Bidimensional Anisotropic Mesh Generator (BAMG) that is present in the Freefem ++ software.

3.2. Eigenvalue solver

Once the base flow is determined, the system (7) is used to perform stability analysis. After spatial discretization, equation (7) along with the boundary conditions are recast in the following standard form

$$\left[A\left(Re,\, W_b\right) + \gamma B\right] \cdot w = \mathbf{0}, \tag{15}$$

where w is the right (or direct) eigenvector. The large number of degrees of freedoms prohibits direct matrix methods and suggests the use of iterative techniques. This means, for example, that methods based on the QR decomposition are not appropriate for solving these large scale problems. Thus, we have chosen to adopt an efficient matrix-free iterative method based on the Arnoldi algorithm (see e.g. Arnoldi (1951)). We use the state-of-the-art ARPACK code of Lehoucq *et al* (1998), which implements the Arnoldi method with implicit restarts to limit memory requirements and to compress the information of the desired eigenvectors into a small subspace. The solutions of the linear systems (15) are determined by the use of the same sparse solver (MUMPS) used for the base flow calculations. The adjoint modes are computed as left eigenvectors of the discrete systems derived from the discretization of the linearized equations and the sensitivity function is then computed by the product of the direct and the adjoint fields. In this paper the right (direct) and left (adjoint) eigenvectors are normalized by requiring

$$\max_{x,y\in\mathscr{D}}\left\{\left|\hat{u}\left(x,\, y\right)\right|\right\} = 1, \quad \int_{\mathscr{D}} \hat{\boldsymbol{f}}^{+} \cdot \hat{\boldsymbol{u}}\, dS = 1. \tag{16}$$

3.3. Code validation

In order to perform an accurate validation of the present code (Freefem ++ code) we compare our results with three different test cases. First of all, we validate the stability analysis against the results reported by Sipp and Lebedev (2007). These authors investigate the stability of a Newtonian fluid in the present reference geometrical configuration and report as first instability a 2D eigenmode that becomes unstable at $Re = 4140$. Table 1 compares our results obtained with different meshes ($\mathcal{M}\mathbf{1}$, $\mathcal{M}\mathbf{2}$, $\mathcal{M}\mathbf{3}$) and the results obtained in Sipp and Lebedev (2007). In these particular representative runs, 50 eigenvalues were obtained, with an initial Krylov basis set of dimension 150, and the convergence criterion present in the Arnoldi iterations is based on a tolerance of 10^{-12}. The accuracy of the converged eigenpairs was then independently checked by evaluating the residual $max_i|(A_{i,j} + \gamma B_{i,j})w_j|$, and this quantity was always less than 10^{-9} for the reported results. More importantly, for the leading few eigenpairs, this residual was generally less than 10^{-12}.

We then validated the base-flow velocity profiles (not shown here for sake of brevity) relative to the non-Newtonian channel flow with Nouar *et al* (2007), and an excellent agreement was found. Finally, we compared the stability results for the classical lid-driven cavity problem with those obtained by Haque *et al* (2012). Figure 3 shows the perfect agreement in the computation of the critical Reynolds number for several non-Newtonian flows. In the present work we used the Mesh $\mathcal{M}\mathbf{2}$ to perform all computations.

4. Results

First of all, we show the effect of the shear-dependent viscosity on the spatial distribution of the base flow in figure 2. The shear layer that develops above the cavity presents a characteristic wall-normal length scale that increases as the power index n increases . In figure 4 there are displayed several profiles of velocities $u_b(y)$ and $v_b(x)$ inside the cavity for the Newtonian critical Reynolds number $Re = 1370$. In order to determine the influence of the time constant λ on the structure of the base flow, we have chosen to take the parameter n

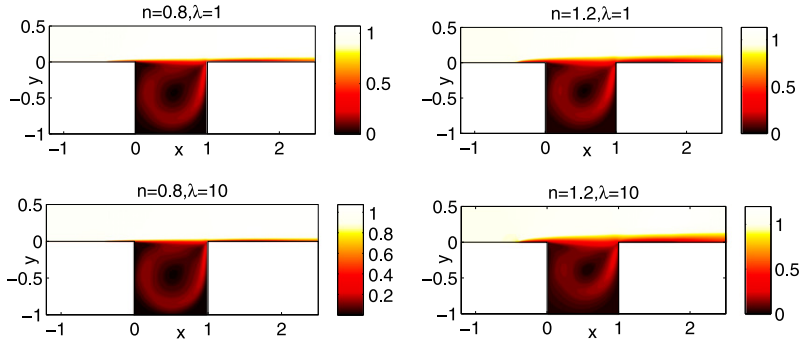

Figure 2. Spatial distribution of the base flow for several values of the parameters λ and n at constant Reynolds number $Re = 1370$. The distribution is displayed through contour plots of the velocity field modulus.

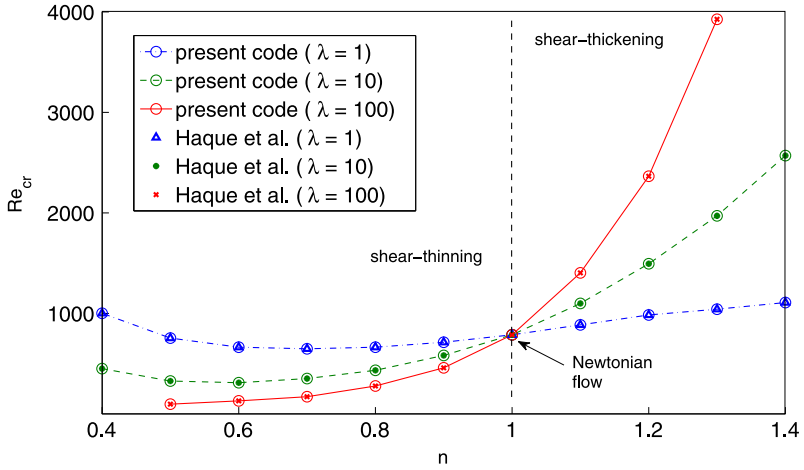

Figure 3. Determination of the critical Reynolds number Re_{cr} for several non-Newtonian lid-driven cavity flows. Comparison of the present stability results with Haque *et al* (2012).

constant and equal to 0.8. The spatial distribution of the profiles suggests that the viscosity parameter λ does not change significantly with the base flow structure inside the cavity.

The dependence of the eigenvalues on the Reynolds number and spanwise wavenumber β is presented in figure 5. In figure 5(a) we show the growth rate (real part σ) of the leading eigenvalues (i.e. the least stable) as a function of the power index n. Compared to the Newtonian fluid, shear-thickening is increasingly stable as the value of n is increased, while this monotonic behaviour is not true for the case of shear-thinning fluids. Figure 5(b) shows the optimal spanwise wavenumber β_{opt} (the value of β corresponding to the neutral curve) as a function of the parameter n. All the curves present a discontinuity in $n \simeq 1.25$ and, consequently, the wavelengths $\hat{\Lambda} = 2\pi/\beta_{opt}$ associated with the corresponding global modes increase from $\hat{\Lambda}_s = \mathcal{O}(0.4)$ (steady modes) to $\hat{\Lambda}_u = \mathcal{O}(1.5)$ (unsteady modes). We have investigated wavenumbers larger than those shown in figure 5b) and find no evidence of other

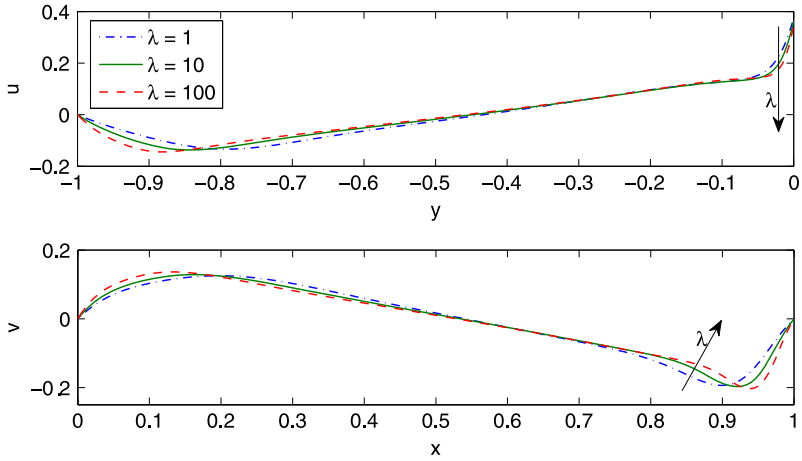

Figure 4. Velocity profiles inside the square cavity: (top) streamwise velocity component u_b at $(x, -0.5)$, (bottom) cross-stream component v_b at $(0.5, y)$. The Reynolds number is $Re = 1370$ and $n = 0.8$

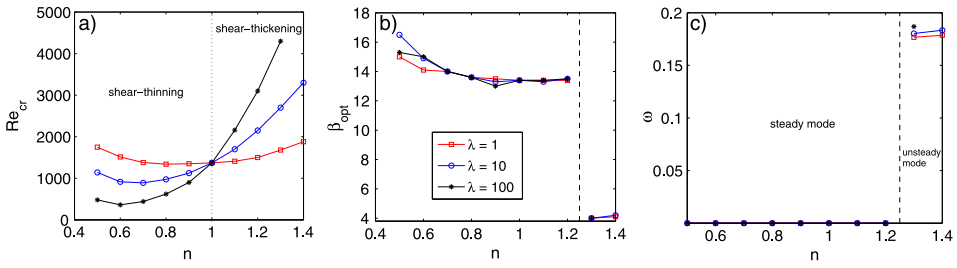

Figure 5. (a) Critical Reynolds numbers as a function of the power index n, (b) corresponding spanwise wavenumbers β (denoted optimal wavenumber) and (c) eigenfrequencies ω.

eigenvalues that would give rise to instabilities for the Reynolds numbers considered. Figure 5(c) shows the associated frequencies of the global modes. Thus, we note that the first absolute linear instability of the steady base flow is a steady or unsteady 3D bifurcation depending on the value of the power-law index n. We note that this behavior is qualitatively the same as in the case of the lid driven cavity flow (see Haque *et al* (2012)).

The data in figure 5 has been further analyzed in order to investigate if a universal scaling exists for the neutral curve. For this purpose we introduced the averaged Reynolds number, as defined in Haque *et al* (2012) based on the mean viscosity ($Re_{avg.} = \frac{1}{Area}\int Re\ (x, y)dxdy$), and plotted the neutral curve as a function of n and λ. The results are presented in figure 6. Indeed it is found that this scaling gives neutral curves that are rather independent of the values of n and λ, when compared to the case of Newtonian fluids ($n = 1$).

So far only the optimal spanwise wavenumber has been shown for a given Reynolds number. In figure 7 we present the growth rate as a function of the spanwise wavenumber for three values of the power index n and the Reynolds number chosen such that at least one

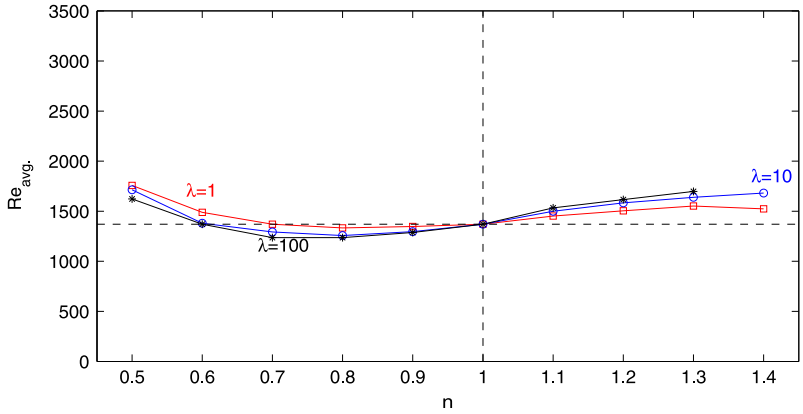

Figure 6. Rescaled neutral curve: the data in figure 5 has been rescaled using the definition of the averaged Reynolds number as found in Haque *et al* (2012).

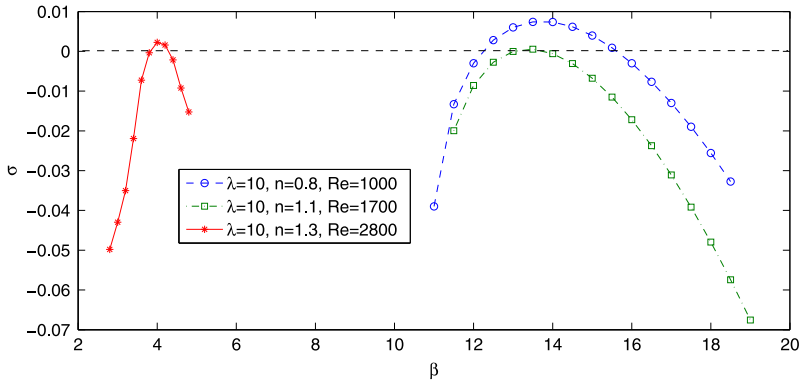

Figure 7. The growth rate σ as a function of the spanwise wavenumber β for different values of the power index n and Reynolds numbers. The value of $\lambda = 10$.

solution is unstable. In all cases $\lambda = 10$. A clear difference in the value of β for the unstable solutions is found passing from $n = 1.1$ to $n = 1.3$.

We now turn to the analysis of the linear modes that destabilize the 2D base flow. Since we want to analyze the features of both steady and unsteady modes, we select as representative cases the flows characterized by $\lambda = 10$, $n = 0.8$ (steady case) and $\lambda = 10$, $n = 1.3$ (unsteady case). Figure 8 shows the structure of the two leading eigenmodes at the respective critical Reynolds numbers and corresponding optimal spanwise wavelengths. The streamwise velocity (figure 8(a)), wall-normal velocity (figure 8(b)) and spanwise velocity (figure 8(c)) contours clearly show that the steady bifurcating mode is localized in the region inside the cavity.

In order to characterize the physical mechanism that underlies the instability, we show in figure 9 a fictitious 3D field obtained as $\boldsymbol{Q_b} + \epsilon \boldsymbol{q}'$. Since the 3D global mode weakly affects the flow outside the cavity, we represent the spatial structure of the field by three streamlines inside the cavity (plotted with solid lines in figure 9). The spatial distribution of the boundary layer developing over the cavity is also visualized by an iso-surface of streamwise velocity

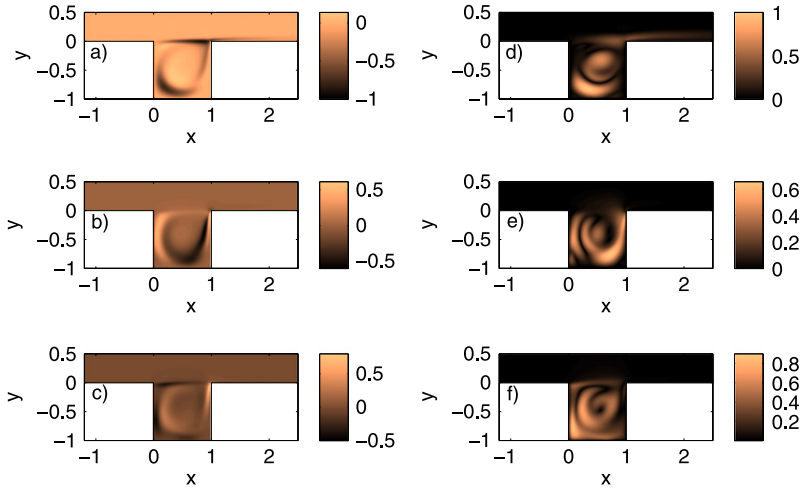

Figure 8. (a–c) Contour plots of the streamwise (a) $\hat{u}(x, y)$, wall-normal (b) $\hat{v}(x, y)$ and spanwise (c) $\hat{w}(x, y)$ direct eigenfunction of the steady mode: $Re_{cr} = 970$, $\beta_{opt} = 13.6$, $\lambda = 10$ and $n = 0.8$. (d–f) Visualization of the structure of direct eigenfunction of the non-stationary mode by contours of modulus of streamwise (d) $|\hat{u}(x, y)|$, wall-normal (e) $|\hat{v}(x, y)|$ and spanwise (f) $|\hat{w}(x, y)|$ component: $Re_{cr} = 2700$, $\beta_{opt} = 4$, $\lambda = 10$ and $n = 1.3$.

and the streamwise structure of the flow is depicted by three slices. Thus, the secondary flow generated by this instability can be described as flat rolls lying inside the cavity similar to those reported by the 3D linear instability of the lid-driven cavity flow (see Albensoeder *et al* (2001)). Figure 9 is made by taking the optimal Fourier wavelength as the transverse length. The first unsteady mode, instead, is displayed in figure 8(e–g) by the modulus of the three components $\hat{u}$, $\hat{v}$ and $\hat{w}$. The dynamics associated with this mode are a periodic oscillation concentrated in the region inside the cavity. The secondary flow generated in this case has a more complicated spatial structure with several 'rolls' but again localized within the cavity. The exact size and shape of the cavity vortex depends weakly on the global flow properties, so, the 3D instabilities, driven by this local part of the flow field, always present similar features. The receptivity behavior of the steady and unsteady mode is then investigate by an adjoint analysis. In figure 10 is reported the spatial structure of the adjoint field using the contours of the modulus of the adjoint velocity. For the stationary mode (figure 10(a)) the receptivity to a momentum forcing is strong both near the right wall of the cavity and very close to the left edge. The unsteady mode (figure 10(b)) presents the same receptive behavior with a slight difference in the distribution of the maximum of the field. We have to note that the region of high receptivity located on the left corner is the main difference with the lid-driven cavity case.

Finally, following Chomaz (2005) and Giannetti and Luchini (2007), we have examined the sensitivity of the leading eigenvalue to structural perturbations of the linear evolution operator in order to determine the region of the flow where feedback processes at the origin of a self-sustained instability are active. In figure 11 we show the structural sensitivity map for both the unsteady and steady mode. In physical terms, this overlap region identifies where local feedback will have a large impact on the leading eigenvalue. The sensitivity associated with the steady mode (figure 11(a)) and with the unsteady mode (figure 11(b)) again have a

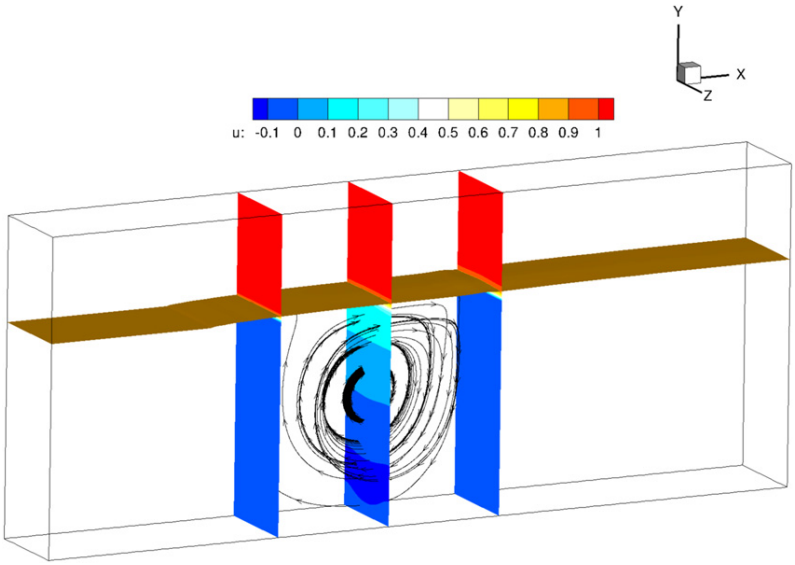

Figure 9. Perspective view of the secondary flow generated by the steady bifurcating mode ($Re_{cr} = 970$, $\beta_{opt} = 13.6$, $\lambda = 10$ and $n = 0.8$). The total field is obtained as $\boldsymbol{Q}_b + \epsilon \boldsymbol{q}'$ where the small amplitude ϵ of the perturbation field is set to $\epsilon = 0.05$. Threeslices are placed respectively at $x = 0$, in the middle of the cavity ($x = 0.5$) and at $x = 1$. The structure of the shear layer developing above the cavity is visualized by an iso-surface of the streamwise component of total velocity U (iso-surface value = 0.9). The spatial distribution of the total field is displayed within the cavity with three streamlines.

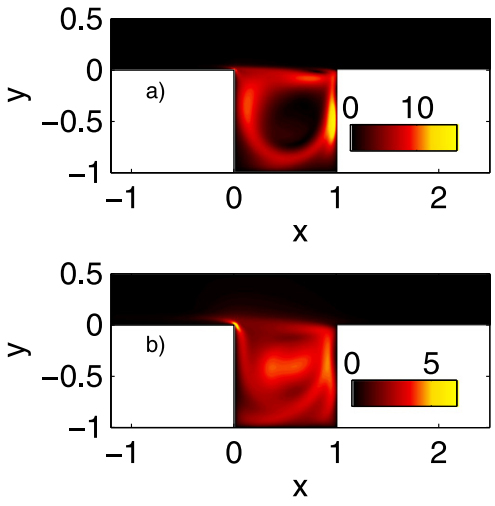

Figure 10. Contour plots of the modulus of the adjoint field for the (a) steady mode ($Re_{cr} = 970$, $\beta_{opt} = 13.6$, $\lambda = 10$ and $n = 0.8$) and (b) unsteady mode ($Re_{cr} = 2700$, $\beta_{opt} = 4$, $\lambda = 10$ and $n = 1.3$).

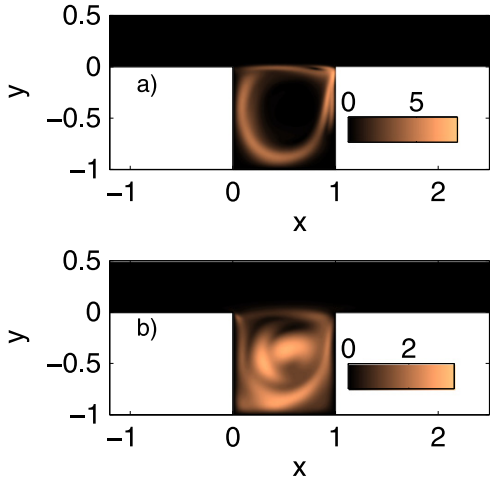

Figure 11. Visualization of the structural sensitivity for the (a) steady mode ($Re_{cr} = 970$, $\beta_{opt} = 13.6$, $\lambda = 10$ and $n = 0.8$) and (b) unsteady mode ($Re_{cr} = 2700$, $\beta_{opt} = 4$, $\lambda = 10$ and $n = 1.3$).

similar structure concentrated only inside the cavity. Thus, any local feedback applied outside this region only slightly modifies the leading eigenvalue, indicating that these regions do not play a significant role in the process giving rise to global instability. For the present flow configuration, we may conclude that the cavity vortex is the wavemaker region of the 3D instability for both modes.

5. Conclusions

In this paper we have presented the linear dynamics of a 2D flow arising in open cavity configurations for the case of non-Newtonian fluids given by the Carreau viscosity model. A global stability analysis has been performed in order to map the neutral stability curves as a function of the Reynolds number, and the model parameters n and λ. We have found that the primary bifurcation is always 3D but can have both steady or non-stationary behavior, depending on the value of the power index n. In particular, a single value of $n \approx 1.25$ separates the steady and unsteady bifurcations.

A detailed analysis of the structure of both leading global modes suggest that the instability is localized within the cavity. Furthermore, we have computed the adjoint global modes associated with the respective direct mode in order to show the receptive behavior of the base flow. An analysis of the adjoint spatial structure allowed us to localize two regions of strong receptivity to momentum forcing. The direct and adjoint modes are all concentrated inside the cavity in the same region. Thus, the overlap field is again localized within the cavity. We have further shown that if the Reynolds number is based on the average viscosity (as in Haque *et al* (2012)), a more or less universal value of the critical Reynolds number is found, independent of both n and λ. Finally, we conclude that the results summarized above suggest the same instability mechanism of the lid-driven cavity flow.

References

Albensoeder S, Kuhlmann H C and Rath H J 2001 3D centrifugal-flow instabilities in the lid-driven-cavity problem *Phys. Fluids* **13** 121–35

Amestoy P R, Duff I S, Koster J and L'Excellent J-Y 2010 A fully asynchronous multifrontal solver using distributed dynamic scheduling *SIAM Journal on Matrix Analysis and Applications* **23** 15–41

Amestoy P R, Guermouche A, L'Excellent J-Y and Pralet S 2006 Hybrid scheduling for the parallel solution of linear systems *Parallel Computing* **32** 136–56

Arnoldi W E 1951 The principle of minimized iteration in the solution of the matrix eigenproblem *Quart. Appl. Math.* **9** 17–29

Barbagallo A, Sipp D and Schmid P J 2009 Closed-loop control of an open cavity flow using reduced-order models *J. Fluid Mech.* **641** 1–50

Bird R B, Curtiss C F, Armstrong R C and Hassager O 1987 *Dynamics of Polymeric Liquids* vol 1, 2nd edn (New York: Wiley-Interscience)

Brandt L, Sipp D, Pralits J O and Marquet O 2011 Effect of base-flow variation on non-modal stability *J. Fluid Mech.* **687** 503–28

Brés G A and Colonius T 2008 3D instabilities in compressible flow over open cavities *J. Fluid Mech.* **599** 309–39

Carreau P J, Dekee D and Chhabra R P 1997 *Rheology of polymeric systems* (Munich: Hanser)

Chomaz J M 2005 Global instabilities in spatially developing flows: non-normality and nonlinearity *Annu. Rev. Fluid Mech.* **37** 357–92

Cochrane T, Walters K and Webster M F 1981 On Newtonian and non-Newtonian flow in complex geometries, Phil. Trans *Soc. Lond.* A **301** 161–81

Giannetti F and Luchini P 2007 Structural sensitivity of the first instability of the cylinder wake *J. Fluid Mech.* **581** 167–97

Haque S, Lashgari I, Giannetti F and Brandt L 2012 Stability of fluids with shear-dependent viscosity in the lid-driven cavity *J. Non-Newtonian Fluid Mech.* **173-174** 49–61

Hill D C A 1992 theoretical approach for analysing the restabilization of wakes *NASA Technical Memorandum* (Moffett, CA) 103858

Hsu C-H, Vu H-H and Kang Y-H 2009 The Rheology of Blood Flow in a Branched Arterial System with 3D Model: A Numerical Study *Journal of Mechanics* **25** 21–24

Lashgari I, Pralits J O, Giannetti F and Brandt L 2012 First instability of the flow of shear-thinning and shear-thickening fluids past a circular cylinder *J. Fluid Mech.* **701** 201–27

Lehoucq R B, Sorensen D C and Yang C 1998 *ARPACK User's. Guide: Solution of Large Scale Eigenvalue Problems With Implicityly Restarted Arnoldi Methods* (SIAM)

Luchini P and Bottaro A 2014 Adjoint Equations in Stability Analysis *Annu. Rev. of Fluid Mech.* **46** 493–517

Marquet O, Sipp D and Jacquin L 2008 Sensitivity analysis and passive control of cylinder flow *J. Fluid Mech.* **615** 221–52

Nouar C, Bottaro A and Brancher J P 2007 Delaying transition to turbulence in channel flow: revisiting the stability of shear-thinning fluids *J. Fluid Mech.* **592** 177–94

Pralits J O, Brandt L and Giannetti F 2010 Instability and sensitivity of the flow around a rotating circular cylinder *J. Fluid Mech.* **650** 513–36

Pralits J O, Giannetti F and Brandt L 2013 Three-dimensional instability of the flow around a rotating circular cylinder *J. Fluid Mech.* **730** 5–18

Rossiter J E 1964 Wind-tunnel experiments on the flow over rectangular cavities at subsonic and transonic speeds *Tech. Rep.* 3438 ARC

Rowley C W, Colonius T and Basu A J 2002 On self-sustained oscillations in 2D compressible flow over rectangular cavities *J. Fluid Mech.* **455** 315–46

Sipp D and Lebedev A 2007 Global stability of base and mean flows: a general approach and its applications to cylinder and open cavity flows *J. Fluid Mech.* **593** 333–58

Paper 7

Linear stability and weakly nonlinear analysis of the flow past rotating spheres

V. Citro[1] †, J.Tchoufag[2], D. Fabre[2], F.Giannetti[1], P. Luchini[1]

[1]DIIN, Universitá degli Studi di Salerno, Via Giovanni Paolo II, 84084 Fisciano (SA), Italy

[2]Université de Toulouse; INPT, UPS; IMFT (Institut de Mécanique des Fluides de Toulouse); Allée Camille Soula, F-31400 Toulouse, France

(Received 14th December 2015)

We study the flow past a sphere rotating in the traverse direction with respect to the incoming uniform flow, and particularly consider the stability features of the wake as a function of the Reynolds number Re and the sphere dimensionless rotation rate Ω. Direct numerical simulations and three-dimensional global stability analyses are performed in the range $150 \leqslant Re \leqslant 300$ and $0 \leqslant \Omega \leqslant 1.2$. We first describe the base flow, computed as the steady solution of the Navier-Stokes equation, with special attention to the structure of the recirculating region and on the lift force exerted on the sphere. The stability analysis of this base flow shows the existence of two different unstable modes, which occur in different regions of the Re/Ω parameter plane. Mode I, which exists for weak rotations ($\Omega < 0.4$), is similar to the unsteady mode existing for a non-rotating sphere. Mode II, which exists for larger rotations ($\Omega > 0.7$) is characterized by a larger frequency. Both modes preserve the planar symmetry of the base flow. We detail the structure of these eigenmodes, as well as their structural sensitivity thanks to adjoint methods. Considering small rotations, we then compare the numerical results to those obtained using weakly nonlinear approaches. We show that the steady bifurcation occurring for $Re > Re^{SS} = 212$ for a non-rotating sphere is changed into an imperfect bifurcation, unveiling the existence of two other base-flow solutions which are always unstable.

Key words: Bifurcation, Wakes, Global stability, Weakly nonlinear analysis

1. Introduction

Regions of separated flow past bluff bodies are a common feature of realistic configurations existing in many natural phenomena or in industrial applications. The complex three-dimensional flow past a sphere is one of the basic flow configurations which has received a great deal of attention from fluid dynamicists and has acted as a benchmark for a wide range of more complicated practical situations.

The case of a fixed sphere has been largely investigated in the past both numerically and experimentally. Natarajan & Acrivos (1993) examined the linear instability of the steady, axisymmetric base flow to three-dimensional modal perturbations. They reported the occurrence of a supercritical bifurcation, at a critical Reynolds number of $Re^{SS} \approx 210$, characterized by unitary azimuthal wavenumber. The resulting branch with a steady asymmetric wake structure, as observed also in the experimental investigation of Magarvey & Bishop (1965) and Nakamura (1976), is stable up to a Reynolds

† Email address for correspondence: vcitro@unisa.it

number of $Re^{VS} = 277.5$ (Natarajan & Acrivos 1993). Johnson & Patel (1999), subsequently, performed a comprehensive experimental and numerical study founding good agreement with the previous data. Tomboulides & Orszag (2000) performed accurate three-dimensional numerical simulations, based on a code with a spectral discretization, confirming the occurrence of the two bifurcations and the planar symmetry of the single-frequency periodic vortex shedding. Recently, Fabre *et al.* (2008) analyzed the nature of the bifurcation and identified it as a pitchfork of revolution bifurcation with $O(2)$ symmetry, following the nomenclature of Golubitsky & Stewart (2012). Namely, because of azimuthal symmetry, this bifurcation gives rise to a continuous family of asymmetric solutions with symmetry planes taking all possible orientations, instead of only two solutions as an ordinary pitchfork bifurcation. Eventually, Meliga *et al.* (2009*b*) solved direct and adjoint eigenproblems to study the receptivity and the structural sensitivity for the first bifurcation at the critical Reynolds number of $Re^{SS} = 212.6$. They found that the core of the instability (wavemaker) is located in the recirculation bubble past the sphere.

The flow past a sphere rotating around a transverse axis has received less attention. Kurose & Komori (1999) studied the drag and lift forces for $1 \leqslant Re \leqslant 500$ by means of direct numerical simulations. Niazmand & Renksizbukut (2003) also analyzed the spatial structure of the flow using DNS in presence of both rotation and surface blowing. They reported that the rotation can lead to the onset of vortex shedding at a lower Reynolds number compared to the non-rotating case. Giacobello *et al.* (2009) and Kim (2009) investigated wake transitions past the transversely rotating sphere at three different Reynolds number $Re = 100, 250, 300$. At $Re = 300$, they observed two different kind of coherent vortical structures and suggested the existence of two different unsteady mechanisms because the wakes showed a distinctly different topology and a different process of vortex shedding. This situation displays some similarity with the case of a rotating 2D cylinder, where strong rotation also leads to the onset of a new shedding mode which is distinct from the classical one existing in the absence of rotation (Pralits *et al.* 2010). Recently, Poon *et al.* (2014) simulated this flow for higher Reynolds number ($500 \leqslant Re \leqslant 1000$) revealing a new secondary regime called 'shear-layer' stable foci. They discussed also in detail the force coefficients and the Strouhal number as a function of the dimensionless rotation rate Ω. Note that the cases of a sphere rotating around an axis oriented obliquely with respect to the flow (Poon *et al.* 2010), or aligned with the flow (Pier 2013) have also been examined, yielding different but rich behaviors.

The first objective of the present paper is to reconsider and clarify the stability properties of the wake past a rotating sphere using a global stability approach. Such approaches are known to be the right tool to map the thresholds corresponding to the onset of unsteadiness, and combined to adjoint-based structural sensitivity approaches, they also provide useful hints to identify the instability mechanisms responsible for unsteadiness (Luchini & Bottaro 2014). However, performing a global stability of a 3D open flow remains costly in terms of memory requirements and computational time, and has thus became possible only very recently (Bagheri *et al.* 2009*b*; Tammisola *et al.* 2014; Citro *et al.* 2015). The case of a sphere thus constitutes a challenging benchmark for such methods, and the rotating case allows to quantify the added value of a 3D global approach towards previous studies which all assumed the flow to be close to the axisymmetric state (Natarajan & Acrivos 1993; Meliga *et al.* 2009*b*). The second objective of this paper is to clarify the nature of the transition occurring in the vicinity of the Re^{SS} threshold in the case of weak rotation, using both weakly nonlinear approaches valid in this range and results of the global approach.

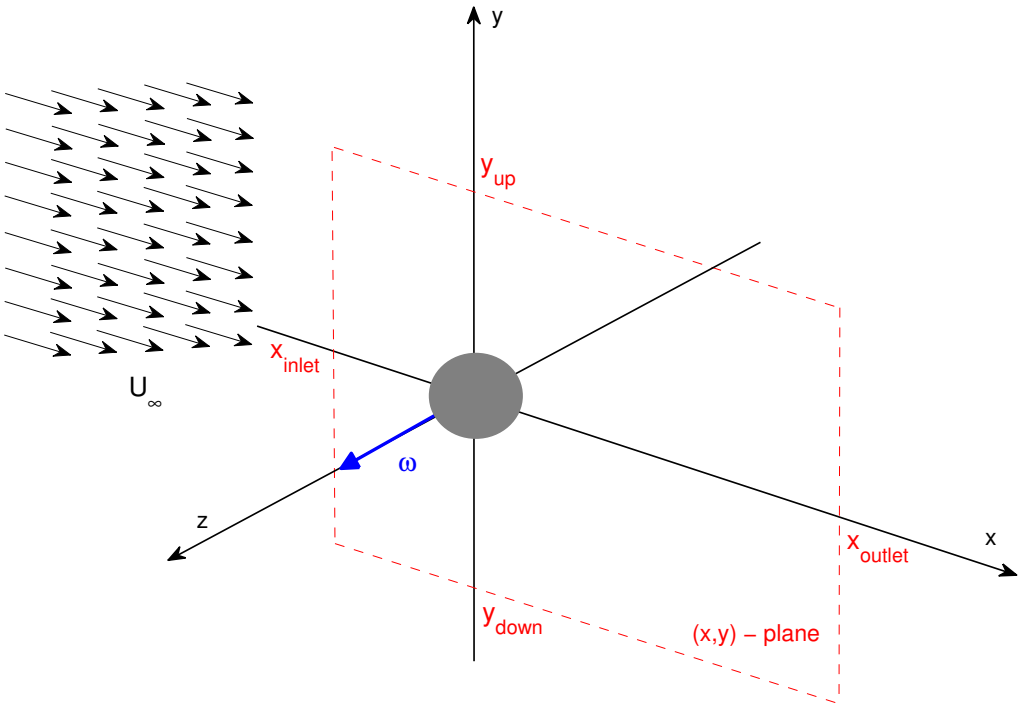

FIGURE 1. Perspective view of the computational domain and the frame of reference. This configuration is characterized by a uniform incoming flow U_∞ and by the sphere angular velocity ω that is directed along the $z-$axis. The computational domain (dashed lines) extends from x_{inlet} to x_{outlet}, from y_{down} to y_{up} and it is symmetric in the spanwise direction with a width of $z_{lat.}$.

2. Problem formulation

We consider the case of a transversely rotating sphere invested by a parallel uniform stream of velocity U_∞. The spatial and temporal domains are respectively $\mathscr{D} \subset \mathbb{R}^3$ and $t \subset [0, \tau]$. Figure 1 shows the coordinate system and the geometry adopted for the present work. The Cartesian system passes through the centre of the sphere, the x-axis has been chosen parallel to the incoming uniform velocity and the rotation rate vector $\boldsymbol{\omega}$ is aligned to the z-axis. The flow is described by the usual time-dependent Navier-Stokes equations:

$$\nabla \cdot \boldsymbol{u} = 0, \tag{2.1a}$$

$$\frac{\partial \boldsymbol{u}}{\partial t} + \boldsymbol{u} \cdot \nabla \boldsymbol{u} = -\nabla P + \nu \nabla^2 \boldsymbol{u}, \tag{2.1b}$$

where $P \in \mathbb{R}$ is the reduced pressure scalar field and $\boldsymbol{u} \in \mathbb{R}^3$ is the velocity vector with components $\boldsymbol{u} = (u, v, w)$.

This system of differential equations is completed by boundary conditions at the surface of the sphere $\partial\mathscr{D}_{sph}$ and matching condition at infinity, namely:

$$\boldsymbol{u}|_{\boldsymbol{r}=\boldsymbol{R}_{sphere}} = \boldsymbol{\omega} \times \boldsymbol{r} = \omega \hat{\boldsymbol{e}}_{\boldsymbol{3}} \times \boldsymbol{r}, \qquad \text{on } \partial\mathscr{D}_{sph}; \tag{2.2a}$$

$$\boldsymbol{u} \to \boldsymbol{U}_\infty = U_\infty \hat{\boldsymbol{e}}_{\boldsymbol{1}}, \qquad \text{as } |\mathbf{r}| \to \infty \tag{2.2b}$$

In practice, the latter condition is applied at the inlet surface $\partial\mathscr{D}_{in}$ and on the lateral sides $\partial\mathscr{D}_{lat}$ of the computational domain, while a no-traction condition is applied at the

outlet surface, namely

$$\mathbf{n} \cdot (Re^{-1}\nabla \mathbf{u} - p\mathbf{I})|_{x=x_{outlet}} = 0, \quad \text{on } \partial\mathscr{D}_{out}. \tag{2.3}$$

The hydrodynamic loads can be obtained by integrating the stress tensor over the sphere surface. In particular, the aeordynamic lift coefficient reads:

$$C_L = \frac{2}{\rho U_\infty^2 \bar{A}} \quad \text{with } \mathcal{L} = \int_{\mathscr{D}_{sph}} [-p\boldsymbol{n}_y + \mu(\nabla \boldsymbol{u} + \nabla \boldsymbol{u}^T) \cdot \boldsymbol{n}_y] dS, \tag{2.4}$$

where D and $\bar{A} = \pi D^2/4$ are the diameter and the cross-sectional area of the sphere, respectively, and $\boldsymbol{n}$ is the normal vector to the surface of the sphere, with Cartesian components n_x, n_y and n_z.

The dynamics, governed by the incompressible Navier-Stokes equations (2.1), depends on the Reynolds number $Re = U_\infty D/\nu$ and dimensionless rotation rate $\Omega = \omega D/2U_\infty$. The pressure is non-dimensionalized with respect to dynamic pressure ρU_∞^2 and the time with respect to the characteristic time scale U/D.

3. Linear stability and sensitivity

Let us focus on the linear stability problem for the flow past a rotating sphere. The starting point for the global hydrodynamical stability analysis is the assumption that the total flow field $[\boldsymbol{u}, P]$ only displays small-amplitude deviations $[\boldsymbol{u}', P']$ with respect to an equilibrium state, i.e. a fixed point, called the base flow $[\boldsymbol{U}^b, P^b]$. Namely:

$$\boldsymbol{u}(x,y,z,t) = \boldsymbol{U}^b(x,y,z) + \epsilon \boldsymbol{u}'(x,y,z,t) + O(\epsilon^2) \tag{3.1a}$$
$$P(x,y,z,t) = P^b(x,y,z) + \epsilon P'(x,y,z,t) + O(\epsilon^2) \tag{3.1b}$$

where $\epsilon << 1$. The long-term stability features of the flow are then investigated using the decomposition into the classical normal mode form

$$\boldsymbol{u}'(x,y,z,t) = \hat{\boldsymbol{u}}(x,y,z)e^{\sigma t + i\lambda t}, \tag{3.2a}$$
$$P'(x,y,z,t) = \hat{P}(x,y,z)e^{\sigma t + i\lambda t}. \tag{3.2b}$$

i.e. the perturbation is characterized by the complex spatial fields $[\hat{\boldsymbol{u}}, \hat{P}](x,y,z)$ and by the inherent growth rate σ and frequency λ. By introducing (3.1) and (3.2) into the Navier-Stokes systems (2.1) and neglecting high-order terms, we obtain two different problems: (i) the base flow problem, that is governed by the time-independent version of (2.1) with boundary condition (2.2); (ii) the global stability problem that reads:

$$\nabla \cdot \hat{\boldsymbol{u}} = 0, \tag{3.3a}$$
$$(\sigma + \mathbf{i}\lambda)\hat{\boldsymbol{u}} + \boldsymbol{U_b} \cdot \nabla \hat{\boldsymbol{u}} + \hat{\boldsymbol{u}} \cdot \nabla \boldsymbol{U_b} = -\nabla \hat{P} + \frac{1}{Re}\nabla^2 \hat{\boldsymbol{u}} \tag{3.3b}$$

This system (3.3), along with the following boundary conditions

$$\hat{\boldsymbol{u}}|_{\boldsymbol{r}} = \mathbf{0}, \quad \text{(on the sphere surface } \partial\mathscr{D}_{sph}); \tag{3.4a}$$
$$\hat{\boldsymbol{u}} = \mathbf{0}, \quad \text{(on the lateral sides } \partial\mathscr{D}_{lat} \text{ and at the inlet surface } \partial\mathscr{D}_{in}). \tag{3.4b}$$
$$\mathbf{n} \cdot (Re^{-1}\nabla \hat{\mathbf{u}} - \hat{p}\mathbf{I})|_{x=x_{outlet}} = 0, \quad \text{(on the outlet surface } \partial\mathscr{D}_{out}); \tag{3.4c}$$

lead to a generalized eigenvalue problem; when the growth rate $\sigma < 0$, the flow is linearly stable while when $\sigma > 0$ the perturbation grows exponentially in time.

In order to locate the core of the instability and to describe the features of the inherent

flow, we rely on the concept of *wavemaker* used in stability analysis (Giannetti & Luchini 2007). Following the recent review by Luchini & Bottaro (2014), we use a linear adjoint-based approach to determine this region. The resulting sensitivity tensor is given by:

$$\mathbf{S}(x,y,z) = \frac{\hat{\mathbf{u}}^{\dagger}(x,y,z)\ \hat{\mathbf{u}}(x,y,z)}{\int_{\mathscr{D}} \hat{\mathbf{u}}^{\dagger}(x,y,z)\cdot\hat{\mathbf{u}}(x,y,z)dV}, \tag{3.5}$$

where the adjoint fields $(\hat{u}^{\dagger},\hat{p}^{\dagger})$ are obtained using the generalized Lagrange identity (Ince 1926):

$$\nabla\cdot\hat{\boldsymbol{u}}^{\dagger} = 0, \tag{3.6a}$$

$$-(\sigma+\mathbf{i}\lambda)\hat{\boldsymbol{u}}^{\dagger} + \boldsymbol{U_b}\cdot\nabla\hat{\boldsymbol{u}}^{\dagger} - \nabla\boldsymbol{U_b}\cdot\hat{\boldsymbol{u}}^{\dagger} = -\nabla\hat{p}^{\dagger} - \frac{1}{Re}\nabla^2\hat{\boldsymbol{u}}^{\dagger}. \tag{3.6b}$$

Here, we use the spectral norm to build the spatial sensitivity maps.

4. Numerical methods

The results presented in this work are carried out using two different codes: (i) the spectral-finite-element software (SEM) *NeK5000* (Tufo & Fischer 1999) and (ii) a combined finite-difference second-order immersed-boundary multigrid code. We use this code to compute all results presented in section 6; the other results are computed by using *NeK5000*.

In *NeK5000*, the velocity vector field and the pressure scalar field are discretized onto $P_N - P_{N-2}$ spectral elements using Lagrange orthogonal polynomials in the Gauss-Lobatto-Legendre (GLL) nodes. The temporal discretization for the momentum equation is achieved by using a semi-implicit splitting scheme. The resulting algorithm solves the convective, the viscous and the pressure problems. An overlapping Schwarz method is adopted to solve the latter two elliptic problems. We have opted for a polynomial order of 10 for both the the base flow computation and its stability analysis. Our computational domain extends from $x_{inlet} = -12D$ to $x_{outlet} = 35D$, from $y_{down} = -12D$ to $y_{up} = 12D$ and it is symmetric in the spanwise direction with a width of $z_{lat} = 12D$.

The finite-difference code is based on a classical second-order conservative discretization of the Navier-Stokes equations on a staggered non-uniform Cartesian mesh. In order to achieve high accuracy and save computational time, a grid clustering near the sphere is used. The boundary conditions on the sphere are imposed through a second-order accurate immersed-boundary scheme, in which the stencil of the finite-difference operators near the body is modified using appropriate interpolation-extrapolation procedure. The interpolation was performed using the point closest to the body surface (which can be either an internal or an external point) and the following point on the exterior of the sphere. The interpolation is performed either in the streamwise or transverse direction according to which one is closest to the local normal. The discretized three-dimensional problem is then solved by using an in-house linear multigrid solver coupled to a Newton global linearization (Trottenberg *et al.* 2001). In order to obtain good convergence in the presence of highly stretched grids, a Collective Line Gauss-Seidel (CLGS) smoother was used. Such relaxation procedure considers a row (column) of computational cells as a main block of a Gauss-Seidel-type iteration, which leads to a banded six-diagonal system of linear equations to be solved at each sub-iteration of the multigrid algorithm. This procedure is the line version of the more classical block Vanka smoother (Vanka 1986) and has been used with a classical V cycle (Trottenberg *et al.* 2001). In our version, the matrix entries are calculated by a local linearization of the governing equations. More details on the characteristics of this kind of smoothers can be found in Feldman & Gelfgat

(2009). The discretization of the convective terms can be problematic since the classical second-order centered discretization is not h-elliptic and can lead to a severe degradation and failure of the iterative procedure. In our code, the convective terms are discretized with a standard first-order upwind discretization while the second order precision is recovered through a standard deferred-correction procedure based on classical centered discretization implemented at the smoother level. The Immersed-boundary technique with a second order interpolation is applied only on the finest level while, for simplicity, at courser levels, a stair-step geometry is considered. Such procedure does not alter the overall convergence speed of the multigrid algorithm and considerably simplify the coding and the computational time. Textbook multigrid efficiency (Trottenberg *et al.* 2001) is achieved far from the bifurcation thresholds. As for all the iterative procedures close to the transitions, a severe degradation of the performances is obtained. This is due to the existence of a limited number of eigenvalues of the iteration matrix moving and crossing the imaginary line: in this situation the whole iterative procedure diverges. In order to avoid this problem, we used a stabilizing procedure able to significantly accelerate the convergence of our multigrid.

The codes have been tested both against each other, producing identical results for the onset of the steady bifurcation occurring at $Re^{SS} = 212$. We checked also that the results are weakly affected by increasing the resolution of the discretizations.

4.1. *Computation of base flows near the bifurcations*

The 3D steady base flow solution can be obtained by simply integrating the time dependent Navier-Stokes equations (2.1) over a long time interval when the flow is in subcritical conditions, i.e. before the occurrence of a bifurcation. However, if the Reynolds number exceeds the instability threshold, we cannot use a simple time integration to compute the unstable steady base flow that is required for the global stability analysis. It is, therefore, necessary to use a stabilizing numerical procedure able to retrieve the unstable reference state. In the case of low-dimensional systems on one hand, there exist several continuation and bifurcation packages like AUTO (Doedel 1986) or CONTENT (Kuznetsov & Levitin 1996) based on direct solvers for the linear algebraic systems and eigenvalue problems involved in the computations. On the other hand, since the discretization of a full three-dimensional problem often leads to a very large discrete system, the extension to high-dimensional problems is not straightforward.

Note that computation of the steady solution using a Newton algorithm, which is the most commonly used method in global stability studies of 2D flow, is not suitable here, as it necessitates a matrix inversion which would require too much memory and time in a 3D case. An alternative, however, would be to adopt a Krylov-subspace method like the classical GMRES (Saad 2003). Other approaches can be found in the literature. In Åkervik *et al.* (2006), for instance, the authors managed to reach the steady state by damping the unstable frequencies using a dissipative relaxation term proportional to the high-frequency content of the velocity fluctuation field. Shroff & Keller (1993), instead, were able to compute unstable states by using a projection onto the small unstable subspace coupled with a Newton procedure.

In the present work, we adopt a novel efficient algorithm, inspired by the Krylov-subspace methods, to compute unstable steady states of the inherent dynamical system. This method, like GMRES, is based on the minimization of the residual norm at each integration step. It allows us to obtain the unstable, steady field by correcting the new iteration of the numerical procedure using a linear combination of previous fields. The key steps of this procedure can be found in the appendix A of Citro *et al.* (2015). However, we tested our algorithm to compute the flow past a circular cylinder. In this case, the

maximum difference between the base flow computed using our algorithm and the classical Newton-Raphson method is less than 10^{-10}. Such procedure has been implemented both in *NeK5000* and in the multigrid code.

4.2. *Global stability approach in the 3D case*

The linearized incompressible Navier-Stokes equations govern the dynamics of infinitesimal perturbations that evolve on the fixed point (the base flow) $\boldsymbol{U}^b$. As mentioned before, we compute both direct and adjoint eigenpairs; we refer to (Luchini & Bottaro 2014) for further details. Unfortunately, in three-dimensional numerical simulation of fluid flows, it is not possible to apply a matrix method to compute the eigenpairs because the size of the resulting matrix prohibits its explicit construction. Thus, the only available alternative is to adopt a matrix-free procedure based on time-steppers (Bagheri *et al.* 2009*a*). This procedure uses a Krylov subspace method built using snapshots taken from the evolution of the perturbation flow field. In the present work, we solved the eigenproblems by using the Implicit Restart Arnoldi Method implemented in ParPACK. The evolution of the perturbation field is computed by using the linearized DNS (direct or adjoint) time-stepper available in the *NeK5000* code.

The boundary conditions associated with the direct eigenproblem are given by equations (3.4). The conditions for the adjoint problem, instead, are chosen to eliminate the boundary terms after the application of the Lagrange identity (Giannetti & Luchini 2007).

5. Results

5.1. *Base flow*

Figure 2 displays the typical shape of the base flow through contour of the pressure field and streamlines in the lateral $(x-y)$ mid-plane $(z=0)$. Let us first review the case without rotation ($\Omega = 0$). For $Re < Re^{SS} = 212$ (figure 2(a)), the base flow remains axisymmetric, and the structure is the same in every transverse plane. This flow state consists of a toroidal recirculation region with closed streamlines. In topologic terms, the flow along the sphere is characterized by two detachment points in the symmetry plane, plus a central reattachment point, while the flow in the wake is characterized by two stable foci and one saddle point.

Above this threshold, intrinsic wake dynamics leads to a spontaneous symmetry breaking, the resulting state displaying only a planar symmetry with respect to an arbitrary transverse plane (which is taken here as the $(x-y)$ plane for consistency with the results in the rotating case). When observed in this symmetry plane, the recirculation region is asymmetric, one of the vortical structures becoming stronger than the other one. (see figure 2(b) for $Re = 275$). One can also note that the streamlines in the symmetry plane are no longer closed, but are spiraling towards a converging focus in the upper half and outwards from a diverging focus in the lower half. As described in detail by Johnson & Patel (1999), this feature indicates a three-dimensional flow along the toroidal structure, with streamlines diverging in the third direction from the upper focus and converging towards the lower one. Note also that the central reattachment point is shifted upwards, while the location two detachment points is weakly modified. Finally, the isocontours indicate that pressure is larger near the upper part of the sphere surface, which results in a negative lift.

In presence of rotation, the axisymmetry of the flow is always broken and replaced by a planar symmetry with respect to the transverse plane $(x-y)$ perpendicular to the rotation (z) axis. Figure 2(c) displays the base flow for a weak rotation ($\Omega = 0.01$),

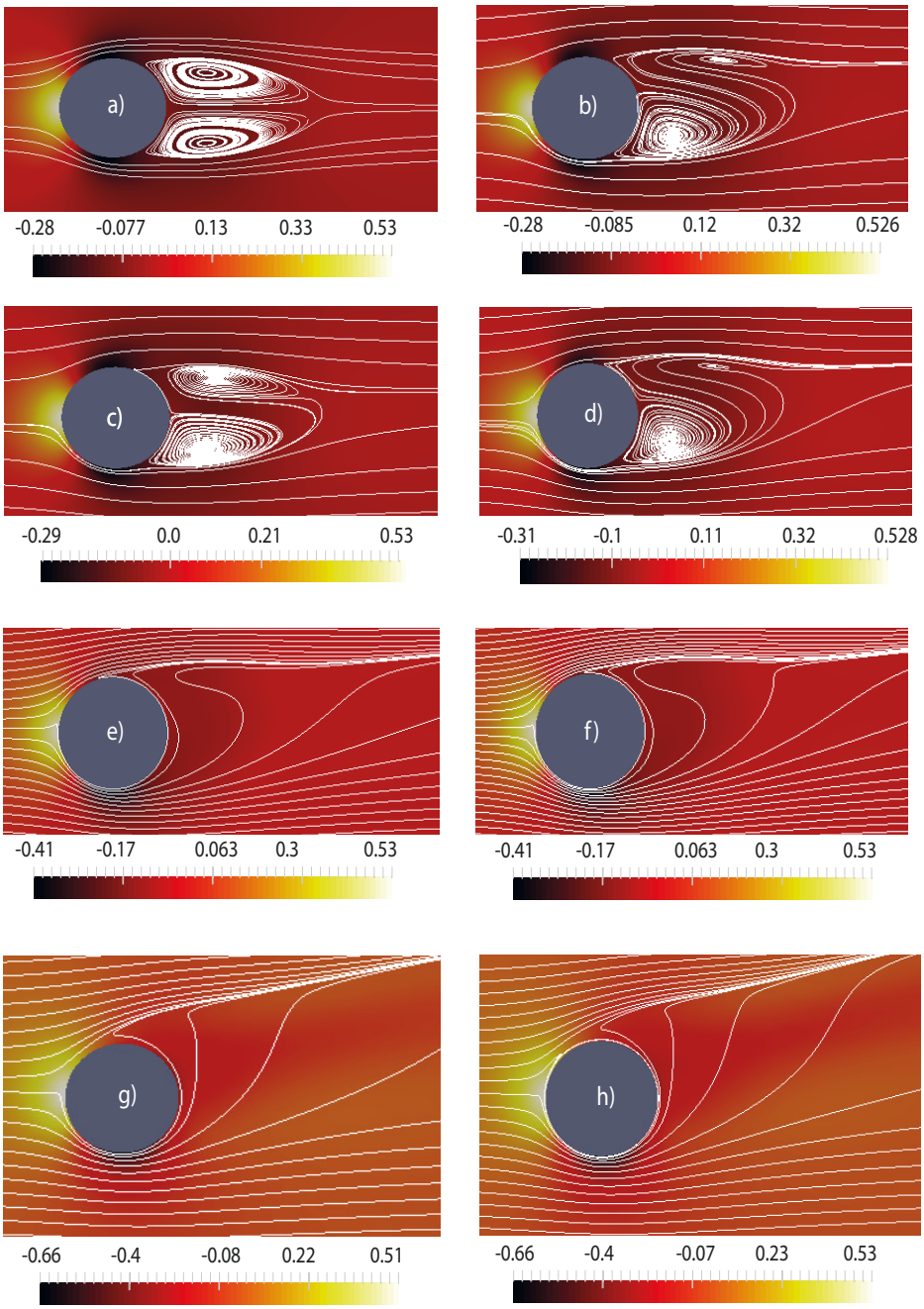

FIGURE 2. Flow past a sphere immersed in a uniform stream: contour plot of the pressure fields for several flow conditions. The white lines represent the streamlines of the flow. The fixed sphere case ($\Omega = 0.0$) is depicted using two cases: a) axysimmetric state at $Re = 200$ and b) asymmetric flow at $Re = 275$ (onset of mode I without rotation). Furthermore, we select four cases to show the spatial structure of the flow for mode I: c) $\Omega = 0.01$, $Re = 200$, d) $\Omega = 0.01$, $Re = 270$, e) $\Omega = 0.2$, $Re = 200$, f) $\Omega = 0.2$, $Re = 240$; and mode II: g) $\Omega = 0.9$, $Re = 200$, h) $\Omega = 0.9$, $Re = 270$.

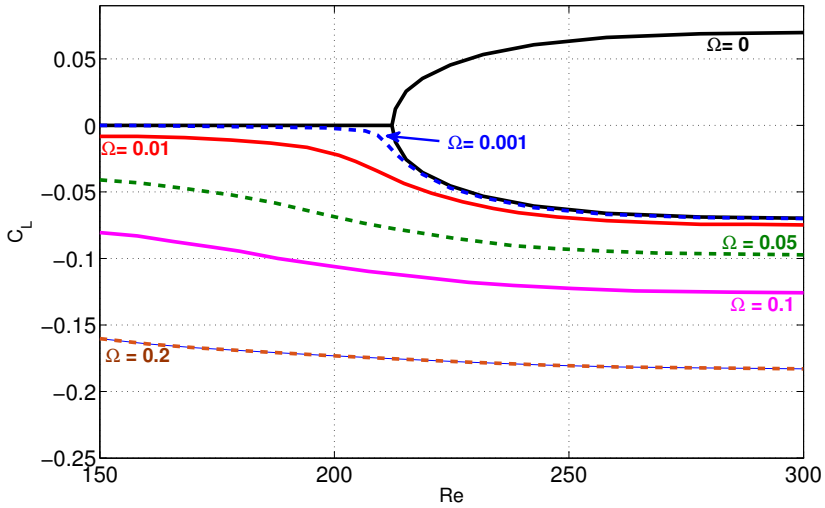

FIGURE 3. Base-flow lift C_L as function of the Reynolds number Re for various values of Ω.

and low Reynolds number $Re = 200$. Compared with the non-rotating case, one can observe that the location of the detachment point is shifted downstream in the lower half and upstream in the upper half. As a consequence, the recirculation region becomes asymmetric, the lower structure becoming stronger than the upper one. Overall, the resulting wake is very similar to the one resulting from the bifurcation at Re^{SS} in the non-rotating case, with non closed streamlines indicating divergence/convergence of the flow in the perpendicular direction. The effect of rotation on the pressure is also to decrease the pressure on the lower side of the sphere and to increase it on the upper side. This is in accordance with the classical explanation of the Magnus effect, and results in a net negative lift force. Figure 2(d) displays the base flow for the same weak rotation rate ($\Omega = 0.01$) and higher Reynolds number $Re = 270$. In this case the recirculation region becomes strongly asymmetric. We can interpret this as a superposition of the two previous effects: the Magnus effect due to rotation and the intrinsic wake mechanism responsible for the symmetry breaking in absence of rotation reinforcing each other.

As the rotation rate is further increased, the regions with spiraling streamlines in the upper and lower parts of the wake disappear, as already found by Giacobello *et al.* (2009). This is exemplified by figure figure 2(e) which displays the base flow for a moderate rotation ($\Omega = 0.2$), and Reynolds number $Re = 200$. Note that the topology of the flow becomes different and simpler compared with the previous case. Considering the flow along the sphere, there is now a single detachment point located on the upper half of the sphere instead of a pair of detachment points and a central reattachment point. Considering the flow in the wake, the two foci and the saddle point have also vanished. Consequently, the recirculation becomes fully open. As can be seen in figure 2(f) $Re = 240$, increasing the Reynolds number does not modify much the structure of the flow. In both these plots we still observe that the pressure is decreased on the lower side of the sphere and increased on the upper side. Again in accordance with the classical explanation of the Magnus effect, this results in a net negative lift force. Note that although the plots only depict the flow in the symmetry plane, the streamlines give indication about the three-dimensionality of the flow. Namely, in the vicinity of the upper detachment point, the tightening of the streamlines indicates divergence in

the perpendicular direction, while in the lower part of the wake the spreading of the streamlines indicates convergence in the perpendicular direction.

Figures 2($g-h$) display the case of a larger rotation rate $\Omega = 0.9$, respectively with $Re = 200$ and $Re = 270$. Compared with the previous cases, we can note that the open recirculation region originating from the detachment point on the upper half of the sphere becomes more open and more intense.

Figure 3 details the lift force exerted upon the sphere as function of Reynolds number, for several values of the rotation rate. Without rotation ($\Omega = 0$), one recovers the picture already described, namely zero lift below $Re^{SS} = 212$ and a bifurcation towards a non-zero lift situation above this value. For $\Omega > 0$, the lift is always negative and smaller than in the non-rotating case. This is consistent with the fact that intrinsic wake dynamics and Magnus effect reinforce each other to build the lift force, as explained previously.

Finally, in this figure, the curves corresponding to the lowest values of Ω approach the curves of the non-rotating case, except in the vicinity of Re^{SS} where a continuous transition is observed. This feature is linked to the fact that the pitchfork bifurcation existing in absence of rotation actually becomes an *imperfect bifurcation* in the case of slow rotation. Accordingly, in the vicinity of the threshold, one expects to encounter other equilibrium solutions lying on a separate branch disconnected from the one considered here. Such solutions were actually effectively found, but they turn out to be always unstable. Hence, we preferred not to document these additional solutions in the present section. The imperfect bifurcation for small rotation will be reconsidered in detail in section 6.

5.2. *Global stability*

We now detail the results of the global linear stability analysis exposed in the previous section. The main outcome of this study is depicted in figure 4(a), which displays the thresholds for linear instability in the Re/Ω parameter plane. We observe the existence of two distinct regions. The first region exists for moderate values of the rotation ($\Omega < 0.4$). This mode, called mode I in the following, is one which exist in the no-rotating case ($\Omega = 0$). As can be observed, small rotation has a destabilizing effect: the threshold Reynolds decreases from 272 in the non-rotating case to $Re_{cr}^{modeI} = 235$ for $\Omega = 0.2$. However, increasing again the rotation as the opposite effect; in the range $\Omega = [0.2, 0.4]$, the value of the critical Reynolds number becomes larger than 300. We suggest that these trends are related to the transition in the wake flow topology. In particular, when $0.0 \leqslant \Omega \leqslant 0.2$, the recirculation bubble is asymmetric and one of the recirculation regions grows; this modification to the base flow structure destabilizes the flow past rotating spheres for a mild rotation. On the other hand, when $\Omega > 0.2$ the recirculation bubble is disappeared and the flow, as a consequence, becomes more stable as the rotation rate increases.

The second region of instability occurs for larger rotations, namely $\Omega > 0.7$ in the range of Re considered. For this second mode, noted mode II, the effect of rotation is destabilizing as the threshold Reynolds decreases as Ω is further increased.

In figure 4(a), we have also displayed with symbols the DNS results of Kim (2009) and Poon *et al.* (2014) for $Re = 250$ and 300. As can be seen, these results are in excellent agreement with ours, since all their unsteady simulations fall inside the regions we found to be linearly unstable, while all their steady simulations fall in the stable one.

Figure 4(b) shows the effect of Ω on the Strouhal number associated with the eigen-frequency of the unstable global modes. We note that St displays a relatively linear dependence on Ω for mode I while it is almost constant of mode II. Thus, we can conclude that, for mode II, the rotation rate Ω weakly affects the Strouhal number that is

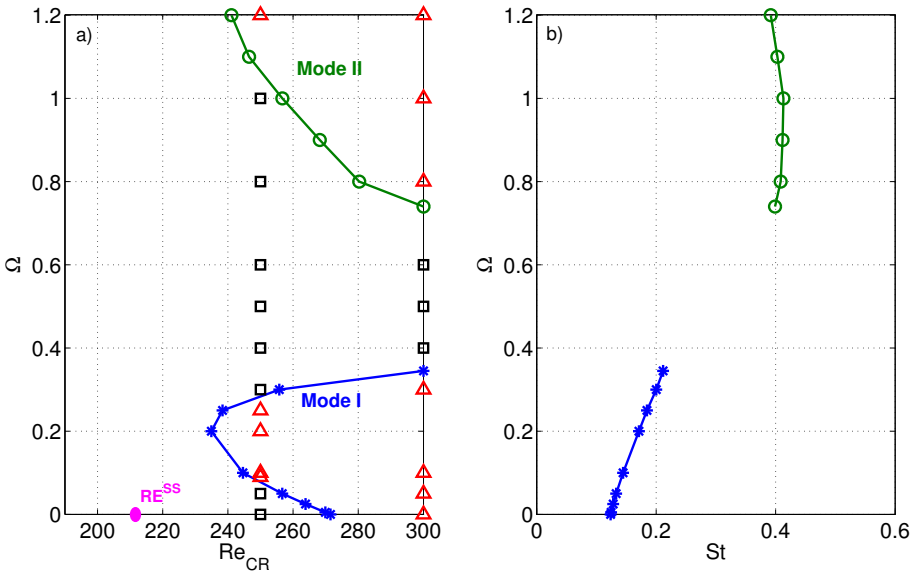

FIGURE 4. a) Neutral stability curve for the three-dimensional flow past a transversely rotating sphere: (∗) mode I ; (○) mode II. We report also DNS results provided by Kim (2009); Poon *et al.* (2014): (□) stable simulations and (△) unstable DNS (they reported the existence of a saturated limit cycle).

approximatively 0.4. Our results agree well with those reported by Kim (2009); Poon *et al.* (2014) using DNS.

Figures 5(a) and 5(b) show the spatial structure of the velocity modulus of direct mode I. This global mode is dominated by axially extended streamwise velocity disturbances located downstream of the sphere. Note that the $u-$ and $v-$component are symmetric with respect to the $(x, y)-$plane while the $w-$component is antisymmetric (figures 5(c, d, e)). This means that the unsteady mode, which emerges from this instability, respects the planar $(x - y)$ symmetry of the underlying base flow. This fact is consistent with classical results for a non-rotating sphere. Figures 5(f) and 5(g) depict the spatial distribution of the adjoint field. Note that the latter is strongly localized near the surface of the sphere, more specifically in the upper part of the sphere where the shear is largest due to opposite rotation. In order to characterize the instability mechanism, we performed also the structural sensitivity analysis. The latter region is localized in a near-wake region of the sphere, across the surface separating the outer flow from the wake region. From these observations we may infer that (i) the region responsible for this instability (wavemaker) is localized in the recirculation region behind the sphere, and (ii) the instability is mostly receptive to perturbations near the surface of the sphere.

Figure 6$(a - d)$ show the spatial distribution of the streamwise velocity component of direct and adjoint mode II. The structure of this direct global mode is again characterized by spatial oscillations downstream of the sphere. We notice that mode II presents faster spatial oscillations than mode I but presents a similar spatial shape. This means that like mode I, mode II preserves the planar symmetry of the base flow. As a result, the oscillating flow resulting from these unstable modes is not expected to display oscillations with respect to the mean-plane. Our results agree well with the DNS results provided by Kim (2009).

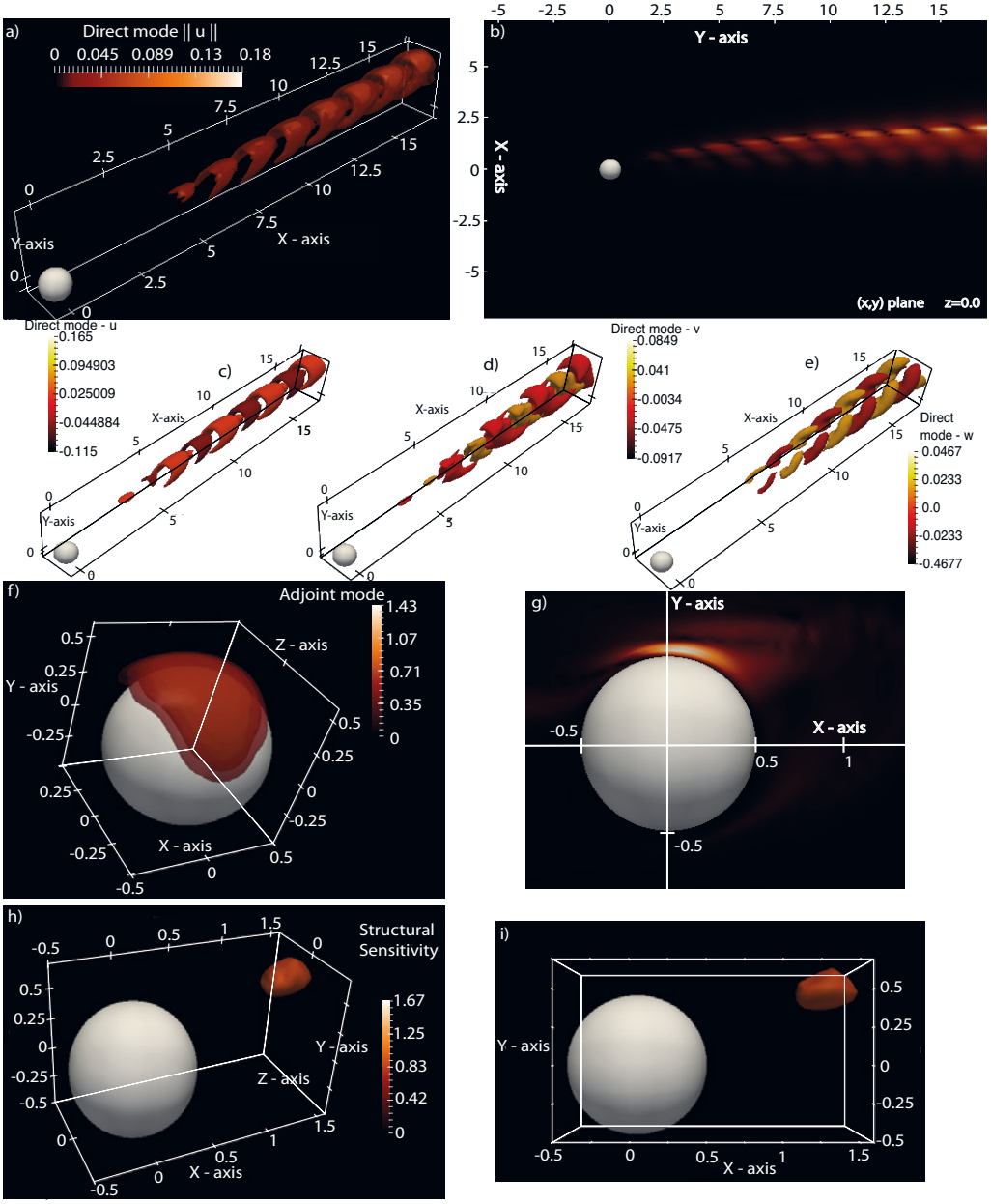

FIGURE 5. (Colour online) Contour plots of a) direct mode I, f) adjoint mode I (see fig. 4). Their structure is also depicted by using a slice at $z = 0$ in b) for the direct field and g) for the adjoint one. Furthermore, figure c), d) and e) depict respectively the $x-$, $y-$ and $z-$component of the direct mode. The structural sensitivity field is depicted in h) perspective view and i) side view. Parameter settings: $\Omega = 0.2$, $Re = 235$.

The adjoint mode is still localized near the sphere surface. On the other hand, the structural sensitivity indicates that the region responsible for instability (the wavemaker) is also localized in a region of strong shear near the sphere surface. This finding agrees well with the conclusion of Giacobello *et al.* (2009)(Section 3.3) that suggested a Kelvin-Helmholtz instability of the shear layer as the instability mechanism.

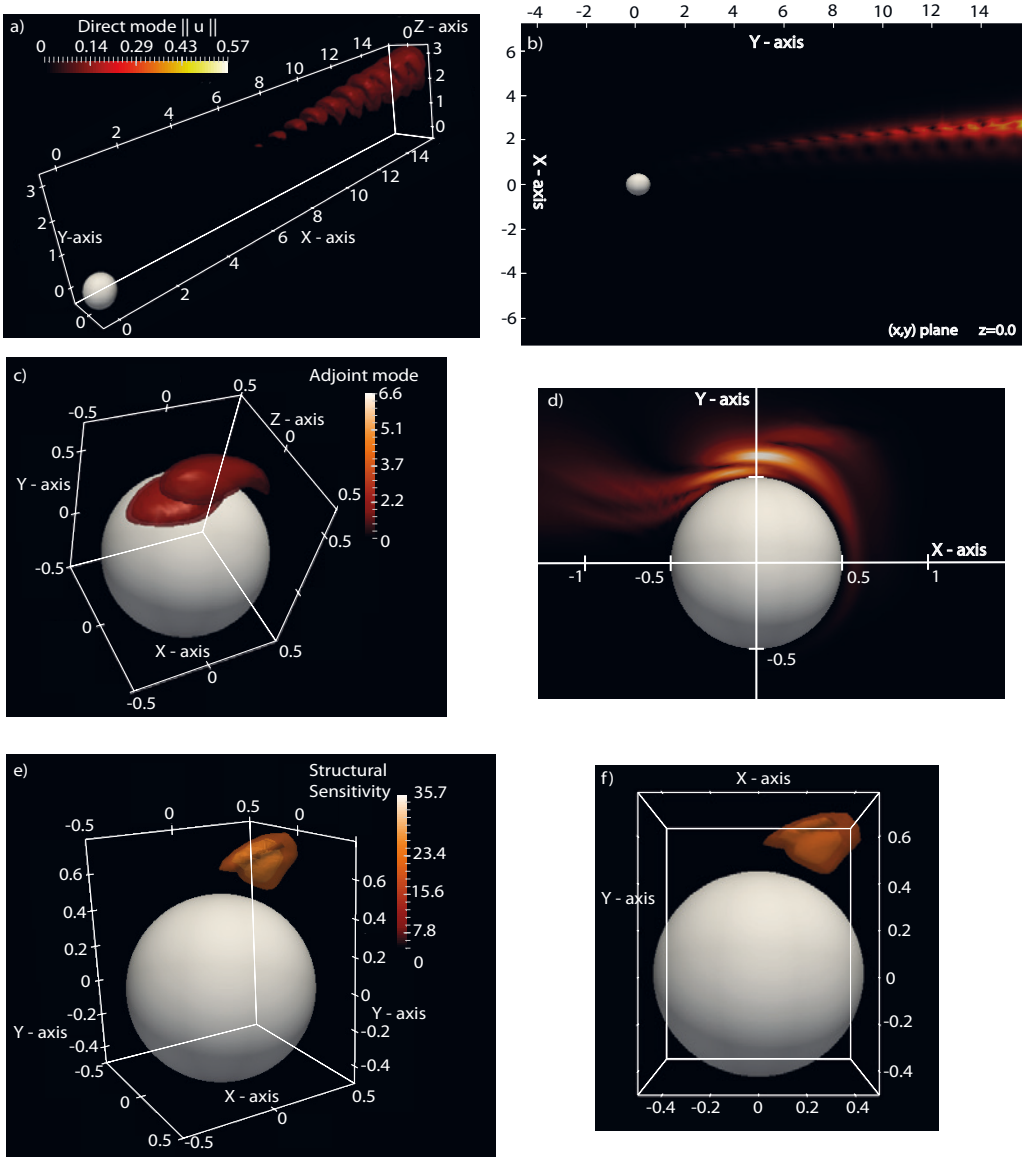

FIGURE 6. (Colour online) Contour plots of a) direct global mode II, c) adjoint mode II. We depict also the spatial structure by using a slice at $z = 0$ in b) for the direct field and d) for the adjoint one. Furthermore, figure e) shows a perspective view of the structural sensitivity field and figure f) shows its side view. Parameter settings: $\Omega = 0.9$ at $Re = 270$.

6. The case of slow rotation

As recalled in the introduction, in the non-rotating case, the flow around a sphere experiences a pitchfork bifurcation at $Re = Re^{SS} = 212$ which leads from a axisymmetric state with zero lift to a mirror-symmetric state with nonzero lift. To investigate the nature of such bifurcations, and in particular their supercritical or subcritical nature, a usual and straightforward extension of the global stability approach used in the previous section is to perform a weakly nonlinear development in terms of the distance to the threshold. This calculation was actually done in (Meliga *et al.* 2009*a*) for the case of an infinitely

thin disk, and repeated by (Tchoufag *et al.* 2011) for the disks of finite thickness. The purpose of the present section is to repeat this calculation for the case of a sphere and to extend it to include the effect of a weak rotation. We will show that the approach directly leads to an amplitude equation describing an imperfect bifurcation, in good accordance with the numerical results.

6.1. *Weakly nonlinear approach*

Following (Meliga *et al.* 2009*a*), we pose $\epsilon^2 = 1/Re^{SS} - 1/Re$ and assume this parameter to be small. The flow is thus expanded in terms of this parameter as follows :

$$\mathbf{q} = [\mathbf{u}, p] = \mathbf{q}_0 + \epsilon \mathbf{q}_1 + \epsilon^2 \mathbf{q}_2 + \epsilon^3 \mathbf{q}_3 + \cdots$$

In order to introduce the effect of rotation in the method, we also have to assume that the rotation is small. Inspection shows that the relevant scaling is to assume ω to be of order ϵ^3, so that we set

$$\omega = \epsilon^3 \omega_0$$

where ω_0 is the rescaled rotation rate of order one.

Following the standard weakly nonlinear expansion for such flows (Sipp & Lebedev 2007; Meliga *et al.* 2009*a*), we rely on a multi-time scale technique and assume $\tau = \epsilon^2 t$ where τ and t are respectively the slow and the fast time scales. Injecting this decomposition into the governing equations (2.1) along with the boundary conditions (2.2) leads to various problems to be solved for $Re = Re^{SS}$ at different orders ϵ^j, with $j = 0, 1, 2, 3, \cdots$.

- At order ϵ^0, we obtain the nonlinear problem governing $\mathbf{q}_0$, the axisymmetric base flow with no rotation.
- At order ϵ, we obtain a linear problem which can be written in a symbolic way as $\mathcal{L}\mathbf{q}_1 = 0$. Since we are at the threshold Re^{SS}, this equation has nontrivial solution with azimuthal wavenumbers ± 1 (the marginal eigenmodes). The solution at this order is thus a linear combination of the global modes at $Re = Re^{SS}$, and is taken as:

$$\mathbf{q}_1 = \hat{A}(\tau)\hat{\mathbf{q}}(r, x)e^{i\phi} + c.c \tag{6.1}$$

where $\hat{\mathbf{q}}$ is the eigenvector of azimuthal wavenumber ($m = +1$) and $\hat{A}$ is a complex amplitude that depends on the slow time scale. Note that the eigenvector $\hat{\mathbf{q}}$ can be normalized so that the real and imaginary parts of the amplitude A correspond to the y and z components of the lift (see Fabre *et al.* (2008)).
- At order ϵ^2, the solution contains base-flow viscous corrections due the departure from Re^{SS} as well as quadratic terms resulting from the self-interactions of the global mode. Using the notations of Meliga *et al.* (2009*a*), this reads:

$$\mathbf{q}_2 = \mathbf{q}_\delta + \mathbf{q}_{AA*}|A|^2 + (\mathbf{q}_{AA}A^2 e^{2i\phi} + cc.) \tag{6.2}$$

- At order ϵ^3, one obtains a linear problem which can be written in a symbolic way as follows :

$$\partial_t \mathbf{q}_3 + (\partial_\tau A\hat{\mathbf{q}}e^{i\phi} + cc.) = \mathcal{N}(\mathbf{q_2}, \mathbf{q_1}) + \mathcal{L}\mathbf{q_3} \tag{6.3}$$

where $\mathcal{N}(\mathbf{q_2}, \mathbf{q_1})$ represents the nonlinear interaction between the solutions at the two previous orders, and $\mathcal{L}$ is the same linear operator as for the problem at order one. This problem is again similar to the case of Meliga *et al.* (2009*a*), except for the fact that $\mathbf{q}_3$ has to verify the boundary condition corresponding to a steady rotation, namely:

$$\mathbf{u}_3 = \omega_0 \mathbf{z} \times \mathbf{r}.$$

The linear operator governing the system (6.3) being singular, the usual procedure to remove the secular terms consists of taking a scalar product of the forcing terms with

the adjoint of the problem. This yields a single differential equation for the amplitude A, with the form:

$$\frac{\partial A}{\partial t} = \lambda\epsilon^2 A - \mu|A|^2 A + a\omega \tag{6.4}$$

where λ, μ and a are all real. Here the coefficients λ and μ contain the effect of the forcing terms corresponding to the viscous correction ($\mathbf{q}_\delta$) and the quadratic terms constituting $\mathbf{q}_2$. These terms are computed exactly as in Meliga *et al.* (2009*a*), so their detailed expression needs not be given. On the other hand, the coefficient a comes from the non-homogeneous boundary condition.
Let $\langle \mathbf{v}_1, \mathbf{v}_2 \rangle_{\partial\mathscr{D}_{sph}} = \int_{\partial\mathscr{D}_{sph}} \mathbf{v}_1^*.\mathbf{v}_2$, i.e the hermitian scalar product between two complex vectors $\mathbf{v}_1$ and $\mathbf{v}_2$ on the surface $\partial\mathscr{D}_{sph}$. Then, the coefficient a is computed as following:

$$a = \left\langle \frac{1}{Re}\nabla\mathbf{u}^\dagger \cdot \mathbf{n}, \frac{1}{\omega_0}\hat{\mathbf{u}}_3 \right\rangle_{\partial\mathscr{D}_{sph}}$$

where $\hat{\mathbf{u}}_3 = \omega_0(\frac{x}{2}\mathbf{e}_r + \mathrm{i}\frac{x}{2}\mathbf{e}_\phi - \frac{r}{2}\mathbf{e}_3)$ (in cylindrical coordinates) because of the no-slip condition on the sphere at order ϵ^3.

The numerical values of the coefficients of equation (6.4) then read: $\lambda = 126.539$, $\mu = 94.316$, $a = -0.025$.

To study the dynamics predicted by the amplitude equation (6.4), we first look for equilibrium solutions, then consider their asymptotic trends as $\omega \to 0$, and finally investigate their stability by examining the behavior of small-amplitude perturbations with respect to them. For the latter purpose, one must ensure that the amplitude A is defined as a complex number, the real and imaginary parts contributing to the lift in the y and z directions, so that the stability with respect to both in-plane and out-of-plane perturbation has to be distinguished. The details are presented in the appendix. In summary, it is shown that the system possesses three branches of equilibrium solutions which verify the following properties:

- The first one, noted A_{01}, is real and positive, and exists for all values of ϵ^2. For very small rotation it displays the following asymptotic behaviors :

$$A_{01} \approx -\frac{a\omega}{\lambda\epsilon^2} \text{ as } \omega \to 0 \text{ with } \epsilon^2 < 0; \quad A_{01} \approx \sqrt{\frac{\lambda\epsilon^2}{\mu}} \text{ as } \omega \to 0 \text{ with } \epsilon^2 > 0.$$

This solution is stable to both in-plane and out-of-plane perturbations.

- The second branch, noted A_{02}, is real and negative and emerges from a saddle-node for $\epsilon^2 > 3 \cdot 2^{-2/3} a^{2/3}\mu^{2/3}\omega^{2/3}/\lambda$. For very small rotations it displays the following asymptotic behavior:

$$A_{02} \approx -\frac{a\omega}{\lambda\epsilon^2} \text{ as } \omega \to 0 \text{ with } \epsilon^2 > 0.$$

This second branch is unstable to both in-plane and out-of-plane perturbations.

- The third, noted A_{03}, originates from the same saddle node as the previous, and for very small rotations, it has the asymptotic behavior

$$A_{03} \approx\to \sqrt{\frac{\lambda\epsilon^2}{\mu}} \text{ as } \omega \to 0 \text{ with } \epsilon^2 > 0.$$

This last branch is stable with respect to in-plane perturbations but unstable with respect to out-of-plane perturbations.

Note that the fact that the three solutions are all real means that the corresponding

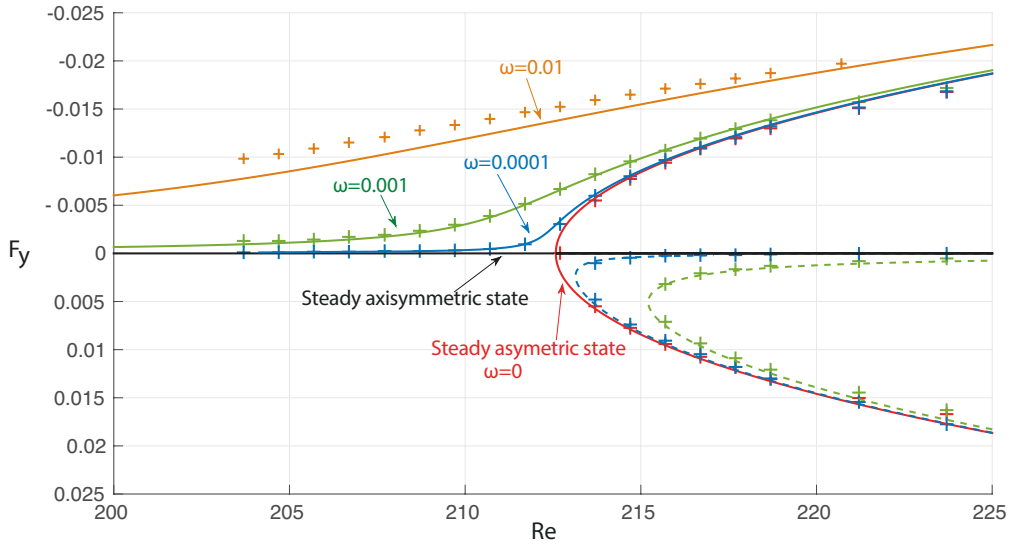

FIGURE 7. Lift force as a function of the Reynolds number for different rotation rates. Symbols correspond to DNS and lines correspond to the normal form (6.4) of the imperfect Pitchfork bifurcation. Solid (resp. dashed) lines represent stable (resp. unstable) solutions.

structures are symmetrical with respect to the transverse $(x-y)$ plane. Accordingly, these states are characterized by a constant lift in the y direction, given by their amplitude A in the original scaling.

6.2. *Comparison with 3D numerical simulations*

Recalling that owing to the normalization of the direct modes, the lift force is directly given by A, allowing one to compare, directly, the solutions of the amplitude equations to the numerical results of figure 3. The comparison is presented in figure 7, which shows that the base flow discussed in section 5.1 is in perfect agreement with the predictions of branch A_{01} of the weakly nonlinear model. In addition, the weakly nonlinear approach allows to unveil the existence of other disconnected branches of steady solutions for a rotating sphere, corresponding to branches A_{02} and A_{03}. As shown in figure 7, the global approach also allowed to confirm the existence of these states, at least for $\omega = 0.001$ and $\omega = 0.0001$. On the other hand, for larger values of the rotation rate, these branches become difficult to track. Since they are always unstable, we disregarded those branches in the stability approach described in section 5.2 and concentrated only on the primary branch A_{01}.

As expected, the discrepancies between the theory and the DNS data in figure 7 increase with the rotation rate. As the sphere spins faster, the departure from the axisymmetric base flow is greater even for Reynolds numbers far smaller than Re^{SS} and the steady global mode bifurcating from the fixed sphere configuration loses progressively its relevancy. Note also that, the weakly nonlinear expansion having been derived in the vicinity of the steady bifurcation, its comparison with DNS data is expected to be less satisfactory as the departure from criticality increases. Figure 7 confirms such behavior, for all the three solution branches and for all the rotation rate values.

7. Conclusion

We analyzed the stability of a flow past a transversely rotating sphere for various angular velocity ($0 \leqslant \Omega \leqslant 1.2$). The spectral-finite-element code *NeK5000* is used to efficiently solve the DNS and global stability problems in the primitive variables formulation. The case of slow rotation is studied by using a finite-difference second-order immersed-boundary multigrid code.

The analysis done in this work confirms the existence of two different self-sustained modes (mode I and mode II) in the wake of such rotating spheres. These unsteady modes derive from Hopf supercritical bifurcations. This result was confirmed by using Direct Numerical Simulations. The first shedding mode is dominated by axially extended streamwise velocity disturbances located past the sphere. The structural sensitivity identifies the wavemaker of these global oscillations in the near wake region. The second mode presents a frequency which is twice that of mode I but is also characterized by spatial oscillations downstream the sphere. The core of this instability is in a region of strong shear near the sphere surface. This suggests that this instability could be related to a feedback mechanism involving Kelvin-Helmoltz waves in accordance with previous experimental and numerical data (Giacobello *et al.* 2009).

A weakly nonlinear analysis was derived to investigate the asymmetric wake in presence of small rotation rates Ω. We adopted a third-order expansion using a multi-time scale technique and solved the subsequent hierarchy of equations that is obtained. We showed that this asymmetric state, prior to the vortex shedding, verifies the normal form of an imperfect Pitchfork bifurcation whose threshold is the critical Re beyond which the non-rotating sphere loses its axisymmetry. An excellent agreement between the theoretical prediction and numerical simulations is reported for all the three solution branches. We find one positive branch of solution and two negative ones as predicted by the matched asymptotic analysis of the normal form. Our results agree well with the well known Magnus effect predicting the lift produced by a rotating body in a uniform stream.

Aside from the case of a sphere rotating at an imposed rate considered in the present paper, a related and equally interesting situation is the case of a sphere free to rotate (either in free fall or held by a pivot and free to rotate around it). This case was recently considered in Fabre *et al.* (2012) using a weakly nonlinear expansion valid in the limit of small rotations. The study showed that in this situation, states with with nonzero rotation rate but with zero torque exist above a critical value of the Reynolds number $Re^{SO} = 206$ which differs from the value $Re^{SS} = 212$ corresponding to the steady bifurcation for a fixed, non-rotating sphere. However, the weakly nonlinear development of Fabre *et al.* (2012) fails in the vicinity of $Re^{SS} = 212$, so the range of existence of these zero-torque states and their stability properties remain unclear. Examining this situation through DNS and 3D stability analysis is the object of continuing studies in our research groups.

Appendix A. Stability analysis of the imperfect bifurcation solution branches

The amplitude equation (6.4) can be reduced to the following canonical form:

$$\frac{\partial X}{\partial \bar{t}} = RX - |X|^2 X + 1 \tag{A 1}$$

where we have introduced the reduced bifurcation parameter

$$R = \left(\lambda \omega^{-2/3} a^{-2/3} \mu^{-2/3}\right) \epsilon^2,$$

the reduced amplitude

$$X = \left(\omega^{-1/3} a^{-1/3} \mu^{1/3}\right) A,$$

and the rescaled time scale

$$\bar{t} = \left(\omega^{-2/3} a^{-2/3} \mu^{1/3}\right) t.$$

Let us first consider the equilibrium solutions $X = X_0$ of the amplitude equation. Such solutions correspond to the *real* roots of the cubic equation

$$RX_0 - |X_0|^2 X_0 + 1 = 0. \tag{A 2}$$

Elementary properties of cubic equations (Cardan's theorem) can be used to show that equation (A 2) has three branches of solution, and to investigate their behavior as R becomes large:

- The first one, noted X_{01}, exists for all values of R. Moreover it displays the following asymptotic behaviors : $X_{01} \to -1/R$ as $R \to -\infty$ and $X_{01} \to \sqrt{R}$ as $R \to +\infty$.
- The second, noted X_{02}, originates from a saddle point located at $[R; X] = [3 \cdot 2^{-2/3}; -2^{-1/3}]$. It exists only for $R > 3 \cdot 2^{-2/3}$ and has the asymptotic behavior $X_{02} \to -1/R$ as $R \to +\infty$.
- The last, noted X_{03}, originates from the same saddle point, has the same range of existence, and has the asymptotic behavior $X_{03} \to -\sqrt{R}$ as $R \to +\infty$.

The asymptotic behaviors presented here as $|R| \to \infty$ provide the ones for $\omega \to 0$ of the main text, which actually correspond to the distinguished limit $\omega^{2/3} \ll \epsilon^2 \ll 1$.

To investigate the stability of these states, we consider small deviations around each of these equilibrium solutions. Let us disturb the steady solution of the reduced form so that

$$X = (X_0 + x) e^{i\theta}.$$

Injecting this decomposition into equation (A 1) and linearizing in terms of $|x|$ and θ lead to

$$\frac{\partial x}{\partial t} = Rx - 3|X_0|^2 x, \tag{A 3a}$$

$$\frac{\partial \theta}{\partial t} X_0 = -\theta \tag{A 3b}$$

leading to the following eigenvalues:

$$\sigma_1 = R - 3|X_0|^2 \equiv -1/X_0 - 2|X_0|^2; \quad \sigma_2 = -\frac{1}{X_0}.$$

Note that σ_1 (resp. σ_2) represents the growth/decay rate of perturbations of the amplitude (resp. the phase).

- The first branch X_{01} is always positive, so both eigenvalues are negative. This branch is stable with respect to in-plane and out-of-plane perturbations.
- The second branch is located in the interval $-2^{2/3} < X_{02} < 0$. Hence both eigenvalues are positive: the branch is unstable with respect to both in-plane and out-of-plane perturbations.
- The third branch verifies $X_{03} < -2^{2/3}$. Hence σ_1 is negative but σ_2 is positive. This branch is stable with respect to in-plane perturbations but unstable with respect to out-of-plane perturbations.

REFERENCES

Åkervik, E., Brandt, L., Henningson, D. S., Hoepffner, J., Marxen, O. & Schlatter, P. 2006 Steady solutions of the navier-stokes equations by selective frequency damping. *Phys. Fluids* **18**, 068102.

Bagheri, S., Åkervik, E., Brandt, L. & Henningson, D. S. 2009*a* Matrix-free methods for the stability and control of boundary layers. *AIAA J.* **47** (5).

Bagheri, S., Schlatter, P., Schmid, P. J. & Henningson, D. S. 2009*b* Global stability of a jet in crossflow. *J. Fluid Mech.* **624**, 33–44.

Citro, V., Giannetti, F., Luchini, P. & Auteri, F. 2015 Global stability and sensitivity analysis of boundary-layer flows past a hemispherical roughness element. *Phys. Fluids* **27**, 084110.

Doedel, E. 1986 Auto: Software for continuation and bifurcation problems in ordinary differential equations. *Tech. Rep.*.

Fabre, D., Auguste, F. & Magnaudet, J. 2008 Bifurcations and symmetry breaking in the wake of axisymmetric bodies. *Physics of Fluids (1994-present)* **20** (5), 051702.

Fabre, D., Tchoufag, J. & Magnaudet, J. 2012 The steady oblique path of buoyancy-driven disks and spheres. *J. Fluid Mech.* **707**, 24–36.

Feldman, Y. & Gelfgat, A. Y. 2009 On pressure-velocity coupled time-integration of incompressible navier-stokes equations using direct inversion of stokes operator or accelerated multigrid technique. *Comput. Struct.* **87**, 710–720.

Giacobello, M., Ooi, A. & Balachandar, S. 2009 Wake structure of a transversely rotating sphere at moderate reynolds numbers. *J. Fluid Mech.* **621**, 103–130.

Giannetti, F. & Luchini, P. 2007 Structural sensitivity of the first instability of the cylinder wake. *J. Fluid Mech.* **581**, 167–197.

Golubitsky, M. & Stewart, I. 2012 *Singularities and groups in bifurcation theory, Vol.2*. Springer Science & Business Media.

Ince, E. L. 1926 *Ordinary Differential Equations*. Dover.

Johnson, T. A. & Patel, V. C. 1999 Flow past a sphere up to a reynolds number of 300. *J. Fluid Mech.* **378**, 19.

Kim, D. 2009 Laminar flow past a sphere rotating in the transverse direction. *J. Mech. Sci. Technol.* **23**, 578–589.

Kurose, R. & Komori, S. 1999 Drag and lift forces on a rotating sphere in a linear shear flow. *J. Fluid Mech.* **384**, 183–206.

Kuznetsov, Y. A. & Levitin, V. V. 1996 Content, a multiplatform continuation environment. *Tech. Rep.*. CWI.

Luchini, P. & Bottaro, A. 2014 Adjoint equations in stability analysis. *Annu. Rev. Fluid Mech.* **46**, 493–517.

Magarvey, R. H. & Bishop, R. L. 1965 Vortices in sphere wakes. *Can. J. Phys.* **43**, 1649.

Meliga, P., Chomaz, J. M. & Sipp, D. 2009*a* Global mode interaction and pattern selection in the wake of a disk: a weakly nonlinear expansion. *J. Fluid Mech.* **633**, 159–189.

Meliga, P., Chomaz, J.-M. & Sipp, D. 2009*b* Unsteadiness in the wake of disks and spheres: Instability, receptivity and control using direct and adjoint global stability analyses. *J. Fluid Struct.* **25**, 601–616.

Nakamura, I. 1976 Steady wake behind a sphere. *Phys. Fluids* **19**, 5.

Natarajan, R. & Acrivos, A. 1993 The instability of the steady flow past spheres and disks. *J. Fluid Mech.* **254**, 323–344.

Niazmand, H. & Renksizbukut, M. 2003 Surface effects on transient three-dimensional flows around rotating spheres at moderate reynolds numbers. *Comput. Fluids* **32**, 1405–1433.

Pier, B. 2013 Periodic and quasiperiodic vortex shedding in the wake of a rotating sphere. *J. Fluid Struct.* **41**, 43–50.

Poon, E. K. W., Ooi, A. S. H., Giacobello, M. & Cohen, R. C. Z. 2010 Laminar flow structures from a rotating sphere: effect of rotating axis angle. *Intl. J. Heat Fluid Flow* **31**, 961–972.

Poon, E. K. W., Ooi, A. S. H., Giacobello, M., Iaccarino, G. & Chung, D. 2014 Flow past a transversely rotating sphere at reynolds numbers above the laminar regime. *J. Fluid Mech.* **759**, 751–781.

Pralits, J. O., Brandt, L. & Giannetti, F. 2010 Instability and sensitivity of the flow around a rotating circular cylinder. *J. Fluid Mech.* **650**, 513–536.

Saad, Y. 2003 *Iterative methods for sparse linear systems*. Siam.

Shroff, G. M. & Keller, H. B. 1993 Stabilization of unstable procedures: the recursive projection method. *SIAM Journal on numerical analysis* **30**, 1099–1120.

Sipp, D. & Lebedev, A. 2007 Global stability of base and mean-flows: a general approach and its applications to cylinder and open cavity flows. *J. Fluid Mech.* **593**, 333–358.

Tammisola, O., Giannetti, F., Citro, V. & Juniper, M. P. 2014 Second-order perturbation of global modes and implications for spanwise wavy actuation. *J. Fluid Mech.* **755**, 314–335.

Tchoufag, J., Assemat, P., Fabre, D. & Meliga, P. 2011 Stabilité globale linéaire et faiblement non-linéaire du sillage d'objets axisymétriques. *20ème Congrès Français de Mécanique, 28 août/2 sept. 2011-25044 Besançon, France (FR)* .

Tomboulides, A. G. & Orszag, S. A. 2000 Numerical investigation of transitional and weak turbulent flow past a sphere. *J. Fluid Mech.* **416**, 45–73.

Trottenberg, U., Oosterlee, C. W. & Schüller, A. 2001 *Multigrid*. Academic Press.

Tufo, H. M. & Fischer, P. F. 1999 Terascale spectral element algorithms and implementations. In *Proceedings of the 1999 ACM/IEEE Conference on Supercomputing*. ACM.

Vanka, S. P. 1986 Block-implicit multigrid solution of navier-stokes equations in primitive variables. *J. Comput. Phys.* **65**, 138–158.

Paper

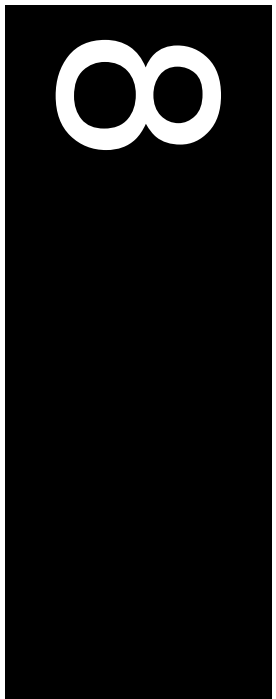

Efficient stabilization and acceleration of numerical simulation of fluid flows by residual recombination

V. Citro[a], P. Luchini[a], F. Giannetti[a], F. Auteri[b]

[a] *DIIN, Universitá degli Studi di Salerno, Via Giovanni Paolo II, 132, 84084, Italy*
[b] *Dipartimento di Scienze e Tecnologie Aerospaziali, Politecnico di Milano, via La Masa 34, 20156, Italy*

Abstract

The study of the stability of a dynamical system described by a set of partial differential equations (PDEs) requires the computation of unstable states as the control parameter exceeds its critical threshold. Unfortunately, the discretization of the governing equations, especially for fluid dynamic applications, often leads to very large discrete systems. As a consequence, matrix based methods, like for example the Newton-Raphson algorithm coupled with a direct inversion of the Jacobian matrix, lead to computational costs too large in terms of both memory and execution time.

We present here a novel iterative algorithm, inspired by Krylov-subspace methods, which is able to compute unstable steady states and/or accelerate the convergence to stable configurations. Such new algorithm is based on the minimization of the residual norm at each iteration step with a projection basis updated at each iteration rather than at periodic restarts like in the classical GMRES method. The algorithm is able to stabilize any dynamical system without negatively impacting on the computational time of the numerical procedure originally used to solve the governing equations. Moreover it can be easily inserted into a pre-existing relaxation (integration) procedure with a call to a single *black-box* subroutine.

The procedure is discussed for problems of different sizes, ranging from a small two-dimensional system to a huge three-dimensional problem involving the Navier-Stokes equations. We also show that the proposed algorithm is able to improve the convergence of an already working iterative scheme. In particular, the procedure is applied to the subcritical flow inside a lid-driven cavity. We also discuss the application of `Boostconv` to compute the steady flow past a fixed circular cylinder (2D) and the boundary-layer flow over a

hemispherical roughness element (3D) for supercritical values of the Reynolds number. We also show that `Boostconv` can be used effectively with any spatial discretization, be it a finite-difference, finite-volume, finite-element or spectral method.

Keywords: stable solution, iterative procedure, stabilization algorithm

1. Introduction

The knowledge of fixed points or periodic solutions of a dynamical system is very important for both stability analysis and the development of flow control strategies. The first step, within the framework of the stability analysis, is the computation of a reference state around which the governing equations are linearized [1]. Such state can be either a steady or a periodic solution of the nonlinear governing equations. The stability of such states usually depends on the value of a given parameter: when a critical value is reached, generally, a bifurcation occurs and the original solution becomes linearly unstable, with the system tending towards a new state. A classical example of such behaviour in fluid dynamics is the instability occurring in the wake of a circular cylinder: at low Reynolds number, i.e. for $Re < 46.7$, the flow is steady and symmetric, but for larger values of Re a global instability arises in the flow field [2] leading to the well-known von Kármán vortex street. In order to perform stability computations beyond the critical threshold we need a numerical method able to track the solution across and beyond the bifurcation point. Unfortunately, it is not possible to achieve such goal using a standard time integration of the governing equations.

For low-dimensional systems, *e.g.* models of chemical reactions, coupled oscillators or lumped element models for fluid flows [3], several continuation and bifurcation packages like AUTO [4] or CONTENT [5] are freely available on the net. They are all based on a Newton method coupled to a direct linear solver applied to an augmented algebraic system of equations. These packages have been designed also to deal with higher-codimension bifurcations and continuation of periodic orbits.

Unfortunately, the numerical treatment of PDEs often involves the solution of very large systems of algebraic equations which do not allow the use of such packages. In particular, Newton's algorithm, involving matrix inversion, cannot be used to solve large three-dimensional problems because of the extremely large memory requirements and the large computational costs (CPU

time); in these cases an alternative approach is to employ a Newton-Krylov algorithm, where a Krylov subspace method (like a GMRES or a BCGSTAB) is used to solve the linear system stemming from each Newton substep.

For large-scale systems, computations of unstable states have been performed in a limited number of studies [6], [7]. Van Noorden et al.[9] discussed the application of a continuation method with subspace iterations to compute periodic orbits of high-dimensional systems. Newton-Krylov techniques are used by Sanchez et al. [10] to obtain the fixed points of a Poincaré map. Shroff & Keller [8] proposed the Recursive Projection Method (RPM) which stabilizes an unstable iterative procedure by splitting the solution space into the direct sum of a large subspace spanned by the stable modes and a small subspace generated by the unstable ones: the algorithm uses a Newton procedure only on the small subspace while it retains the original iterative procedure on its complement. Mittelmann & Weber[12] proposed a continuation strategy coupled with a multigrid algorithm to compute solutions of nonlinear eigenvalue problems near turning points. Sanchez et al.[11] discussed the application of an incomplete lower-upper decomposition (ILU) as an effective preconditioner for the Navier-Stokes problem.

Akervik et al. [13], instead, proposed to apply a selective frequency damping method to recover the steady states of the Navier-Stokes equations. The key idea of this procedure is to damp the oscillations of the unsteady part of the solution using a temporal low-pass filter. It was successfully adopted by Bagheri et al.[14] and Ilak et al.[15] to investigate the stability of a jet in cross-flow. However, the SFD algorithm needs an estimate of the global mode frequency and it cannot be applied to compute unstable states in presence of stationary bifurcations. Moreover, all the cited techniques involve significant coding and/or changes in the original numerical algorithm.

The aim of the present work is to propose a new algorithm, inspired by Krylov-subspace methods, able to efficiently compute unstable steady states of a high-dimensional dynamical system. This method is based on the minimization of the residual norm at each integration step and can be applied as a black-box procedure in any iterative or time marching algorithm without negatively impacting the computational time of the original code.

2. Iterative solution of a discrete linear system: Krylov methods

The iterative solution of the linear system

$$\mathbf{A}\mathbf{x} = \mathbf{b} \tag{1}$$

using Krylov subspace methods has been widely studied in the last decades [16]. In the previous equation $\mathbf{A}$ is a $\mathbb{R}^{N\times N}$ matrix and $\mathbf{x}$ and $\mathbf{b}$ are $\mathbb{R}^N$ vectors representing respectively the solution and the known term of the linear system, respectively. The approximation of the solution $\mathbf{x}$ is sought such that $\mathbf{x}_j$ belongs to the shifted Krylov spaces $\mathscr{S}_j = \mathbf{x}_0 + \mathscr{K}_j(\mathbf{A}, \mathbf{r}_0)$ with

$$\mathscr{K}_j(\mathbf{A}, \mathbf{r}_0) = span\{\mathbf{r}_0, \mathbf{A}\mathbf{r}_0, ..., \mathbf{A}^{j-1}\mathbf{r}_0\}, \quad \mathbf{r}_0 = \mathbf{b} - \mathbf{A}\mathbf{x}_0, \tag{2}$$

where $\mathscr{K}_j$ is the $j-th$ Krylov subspace and $\mathbf{r}_0 \in \mathbb{R}^N$ is the residual vector with respect to the initial guess $\mathbf{x}_0$. The residual vector $\mathbf{r}_j$ lies in the Krylov residual subspace $\mathscr{R}_j$ defined as

$$\mathscr{R}_j = \mathbf{r}_0 + \mathbf{A}\mathscr{K}_j(\mathbf{A}, \mathbf{r}_0). \tag{3}$$

The main idea of this iterative procedure is that the $j-th$ approximation of the solution $\mathbf{x}_j \in \mathscr{S}_j$ is found by requiring the minimization of a functional. Thus, different Krylov methods result from different choices of this functional, on the characteristics of the matrix and on some implementation details [16]. A possible choice is to select the $\mathbf{x}_j$ approximation to minimize the 2-norm $||\cdot||_2$ of the residual,

$$\mathbf{x}_j = \min_{\mathbf{x}_j \in \mathscr{S}_j} ||\mathbf{b} - \mathbf{A}\mathbf{x}||_2. \tag{4}$$

Such method is usually referred as the *minimal residual approach* (MR) and it is largely adopted, as in the case of the popular GMRES method by Saad and Schultz [17].

The implementation of GMRES is based on the solution of the *least squares* problem (4) using an orthonormal basis of the Krylov subspace produced by the Arnoldi procedure. It is worthwhile to note that during the execution of GMRES the basis grows and, as a consequence, the storage requirements grow accordingly. In case of a large system, the number of iterations needed to achieve a sufficiently accurate solution can be excessive and the resulting Arnoldi matrix becomes unacceptably large to be stored. For this reason, usually, a restarted procedure is adopted. It consists in restarting the algorithm when the subspace dimension reaches a maximum value p. In particular, after p iterations the current new approximation $\mathbf{x}_j$ and inherent residual $\mathbf{r}_j$ are computed and GMRES is stopped. These arrays become the starting point for the new call to the algorithm. Unfortunately, the restarted algorithm usually shows a slow convergence rate [16].

Preconditioning techniques, are usually adopted for improving the performance and reliability of Krylov subspace methods. It is recognized that

preconditioning is the most critical ingredient in the development of efficient solvers for challenging problems in scientific computation [16]. As a consequence, these methods represent the real key that allows an acceptable convergence rate.

3. `BoostConv` algorithm

The main idea which inspired the proposed algorithm is similar to the one at the basis of GMRES, but in a reverse logic sequence. We start from an *existing* iterative algorithm that is modified to `Boost` the `Conv`ergence of the overall procedure.

A generic linear iteration for the solution of the linear system (1) can be expressed as

$$\mathbf{x}_{n+1} = \mathbf{x}_n + \mathbf{B}\mathbf{r}_n \tag{5}$$

where $\mathbf{r}_n = \mathbf{b} - \mathbf{A}\mathbf{x}_n$ is the residual and $\mathbf{B}$ is a matrix representing the particular iterative scheme used to solve the problem (see e.g. Ch.4 [18]). For example, the relation (5) can result from a classical Jacobi or Gauss-Seidel method or from a pseudo-temporal discretization of a dynamical system.

The convergence of procedure (5) is governed by the eigenvalues of the iteration matrix $(\mathbf{I} - \mathbf{B}\mathbf{A})$: the algorithm converges if and only if the spectral radius of the iteration matrix is less than 1. The asymptotic convergence rate is essentially governed by the slowly decaying modes. Usually, only a small part of the spectrum strongly influences the convergence rate. Even for the case of a non-linear system, the behavior will become linear when the approximate solution $\mathbf{x}_n$ is close enough to the solution $\mathbf{x}$ of the nonlinear governing equation. On the other hand, the algorithm could diverge because of a small set of unstable modes. Thus, the purpose of `BoostConv` is to modify only the part of the spectrum characterized by these slowly decaying or amplified modes, while letting the original algorithm damp the remaining (decaying) modes.

In order to obtain this stabilization, like in the GMRES algorithm, we could use the information provided by the state $\mathbf{x}_n$ and by the residual $\mathbf{r}_n$. The residual satisfies the homogeneous equation obtained by applying the operator $-\mathbf{A}$ to (5) and successively adding $\mathbf{b}$. In this way we easily obtain the following evolution equation for $\mathbf{r}_n$:

$$\mathbf{b} - \mathbf{A}\mathbf{x}_{n+1} = \mathbf{b} - \mathbf{A}\left[\mathbf{x}_n + \mathbf{B}(\mathbf{b} - \mathbf{A}\mathbf{x}_n)\right], \text{i.e.}$$

$$\mathbf{r}_{n+1} = \mathbf{r}_n - \mathbf{AB}\mathbf{r}_n. \tag{6}$$

Our key idea is to improve the existing procedure (5) by replacing the residual vector $\mathbf{r}_n$ with a modified residual $\boldsymbol{\xi}_n$ such that the improved algorithm reads as

$$\mathbf{x}_{n+1} = \mathbf{x}_n + \mathbf{B}\boldsymbol{\xi}_n(\mathbf{r}_n). \tag{7}$$

In the previous equation $\boldsymbol{\xi}_n$ is a suitable function of $\mathbf{r}_n$ and can be interpreted as the feedback term of a closed loop control algorithm or a structural perturbation to the original iteration matrix. In order to guarantee the consistence of the modified algorithm with the original iterative procedure and recover the solution of the linear system (1), it is sufficient that $\boldsymbol{\xi}_n$ goes to zero when $\mathbf{r}_n$ does. The introduction of the vector $\boldsymbol{\xi}_n$ modifies equation (6) leading to the new residual equation

$$\mathbf{r}_{n+1} = \mathbf{r}_n - \mathbf{AB}\boldsymbol{\xi}_n, \tag{8}$$

or equivalently

$$\mathbf{r}_n - \mathbf{r}_{n+1} = \mathbf{AB}\boldsymbol{\xi}_n. \tag{9}$$

We now minimize $\mathbf{r}_{n+1}$ by choosing a suitable function $\boldsymbol{\xi}_n = \boldsymbol{\xi}_n(\boldsymbol{r}_n)$. If we knew $(\mathbf{AB})^{-1}$ we could exactly annihilate $\mathbf{r}_{n+1}$ by computing $\boldsymbol{\xi}_n(\mathbf{r}_n)$ as

$$\boldsymbol{\xi}_n = (\mathbf{AB})^{-1}\mathbf{r}_n. \tag{10}$$

However, for large systems, the exact inversion of $\mathbf{AB}$ is out of reach or too expensive to be performed. We therefore approximate the solution of (10) by using a classical least-square method.

The action of the operator $\mathbf{AB}$ can be represented by storing a set of N vector pairs $(\mathbf{u}_i, \mathbf{v}_i)$, where the second member is produced by the action of $\mathbf{AB}$ on the first. Least-squares method is then adopted to approximate the solution of the algebraic linear system $\mathbf{AB}\boldsymbol{\xi}_n = \mathbf{r}_n$ as

$$\boldsymbol{\xi}_n = \sum_{i=1}^{N} c_i \mathbf{u}_i. \tag{11}$$

In our case the vectors $\mathbf{u}_i$ and $\mathbf{v_i}$ are related by

$$\mathbf{v_i} = \mathbf{AB}\mathbf{u_i} \quad \text{for } i = 1, .., N. \tag{12}$$

while the coefficients c_i are chosen to minimize $|\mathbf{r}_n - \mathbf{AB}\boldsymbol{\xi}_n|^2$. The standard least-squares procedure leads to a system of equations for the coefficients c_i of the form

$$D_{kl}\, c_l = t_k \tag{13}$$

where $t_k = \mathbf{v}_k \cdot \mathbf{r}_n$ and $D_{kl} = \mathbf{v}_k \cdot \mathbf{v}_l$ is a small $N \times N$ matrix. Matrix $\mathbf{D}$ is usually ill-conditioned and an orthogonalization procedure (QR decomposition) is usually needed to find the solution. However, when N is small, as for the cases we are considering, the solution can be simply found with a classical LU decomposition. This least-square solution is not exact and produces a residual $\boldsymbol{\rho} = \mathbf{r_n} - \mathbf{AB}\xi_\mathbf{n}$ which can be expressed in terms of $\mathbf{v_i}$ as

$$\boldsymbol{\rho} = \mathbf{r_n} - \mathbf{AB}\xi_\mathbf{n} = \mathbf{r_n} - \mathbf{AB}\left(\sum_{i=1}^{N} c_i \mathbf{u_i}\right) = \mathbf{r_n} - \sum_{i=1}^{N} c_i \mathbf{ABu_i} = \mathbf{r_n} - \sum_{i=1}^{N} c_i \mathbf{v_i}. \tag{14}$$

However, inserting the so calculated $\boldsymbol{\xi}_n$ in (7) is not yet sufficient to produce a converging algorithm because $\boldsymbol{\xi}_n$ could converge to zero even when the residual $\mathbf{r}_n$ is not identically zero, but simply orthogonal to the leading N (basis-)vectors $\mathbf{u}_i$. Remembering that the original iterative algorithm (5) simply had $\boldsymbol{\xi}_n = \mathbf{r}_n$, we restore a convergent procedure by adding the residual $\boldsymbol{\rho} = \mathbf{r}_n - \sum_i c_i \mathbf{v}_i$ to $\boldsymbol{\xi}_n$, so that the complete algorithm now reads

$$\boldsymbol{\xi}_n = \sum_i c_i \mathbf{u}_i + \mathbf{r}_n - \sum_i c_i \mathbf{v}_i \tag{15}$$

The rationale behind this procedure is to invert exactly the part of the problem represented by the dominant, slower decaying modes, while letting the original iterative algorithm to handle the remaining modes. We now go back to the issue of selecting a convenient set of vectors $\mathbf{u_i}$. In the case of `BoostConv`, both $\mathbf{u}_i$ and $\mathbf{v}_i$ can be conveniently calculated by observing that, according to (8), for each n we have

$$\mathbf{r}_n - \mathbf{r}_{n+1} = \mathbf{AB}\boldsymbol{\xi}_n. \tag{16}$$

For a given N, in a cyclic fashion, at the beginning of a new iteration, we add a new vector pair by selecting $\mathbf{u}_N = \boldsymbol{\xi}_{n-1}$ and $\mathbf{v}_N = \mathbf{r}_n - \mathbf{r}_{n-1}$. In order to keep the size of the basis constant, another pair must be discarded which typically will be the oldest. Such choice is dictated by the fact that applying the algorithm to a nonlinear system it is beneficial to use the freshest

information on the system dynamics in order to account for the change of the system Jacobian (in our case represented by the linear operator $\mathbf{A}$). We also note that in matrix D_{kl} of (13) only the row and the column involving a new pair need to be updated. Such selection procedure works when we already have N vector pairs. At the beginning of the algorithm (for $n < N$) we can still use the same procedure but continuously increasing the basis dimension from 1 to the chosen value of N. In this first stage, no vector pairs are discharged.

From a programming viewpoint, the `BoostConv` algorithm can be encapsulated in a black-box procedure where the only input is $\mathbf{r}_n$ and the only output is $\boldsymbol{\xi}_n$. If $\boldsymbol{\xi}_n$ is returned in the same vector where $\mathbf{r}_n$ was provided, the only modification necessary to boost the convergence of the pre-existing iterative algorithm (5) is a single line of code containing the call to `BoostConv`. Thus, we can do this in a very compact way because the original algorithm can be seen as a simple feedback loop as illustrated in figure 1. As a consequence, we can simply insert our algorithm in the subroutine evaluating the residual as depicted in figure 2.

4. Implementation details

As mentioned in the previous sections, a key feature of the outlined method is the possibility to code it into a black-box computer algorithm. Here, we provide some useful programming guidelines concerning the proposed procedure summarized in the Algorithm 1. The only required input at each step is the residual $\mathbf{r}_n$ at the current iteration n: using such information the procedure calculates the modified residual vector $\boldsymbol{\xi}_n$ (of the same dimension). Here, in order to compact the resulting algorithm, we define an auxiliary vector $\mathbf{w}_h = \mathbf{u}_h - \mathbf{v}_h$.

Once provided the dimension of vector basis N, the procedure can be divided in four parts: i) from line 2 to 6 of Algorithm 1, we discard the oldest pair of vectors $\mathbf{u}$ and $\mathbf{v}$ to store the new pair computed by using the data provided at the current step n; ii) from line 7 to 13, we build the least-square matrix $\mathbf{D}$ of eq. 13 and the known term $\mathbf{t}$; iii) in line 14 we solve the linear problem arising from the least-square method by using a simple LU decomposition on the small $N \times N$ system; iv) in line 15 we compute the new modified residual $\boldsymbol{\xi}_n$ according to eq. 15.

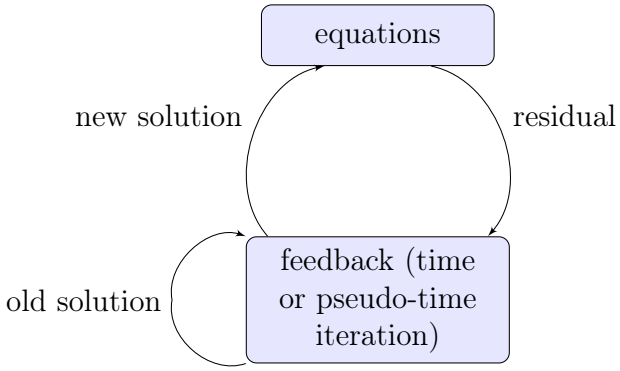

Figure 1: Original iterative procedure. Unmodified integration of governing equations.

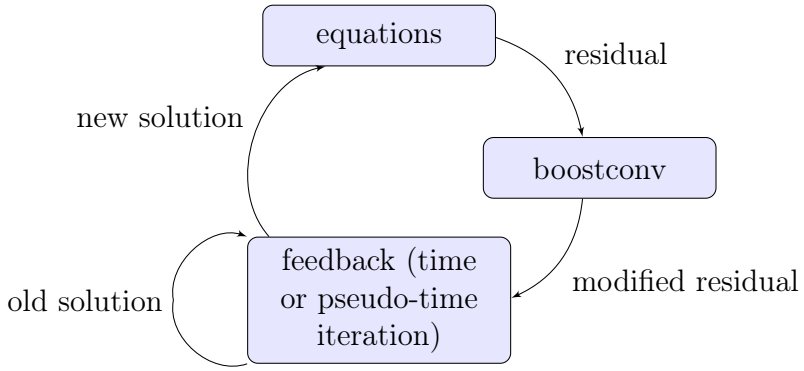

Figure 2: Modification of an existing iterative scheme: stabilized iterative procedure.

Algorithm 1 `BoostConv`

Input: $\mathbf{r}_n$(current residual); **Output:** $\boldsymbol{\xi}_n$(modified residual);
for $\{h = 1$ to $N-1\}$ **do**
    $\mathbf{v}_h = \mathbf{v}_{h+1}$; $\mathbf{w}_h = \mathbf{w}_{h+1}$; ▷ Discard the oldest vectors
    ▷ (remember that $\mathbf{w}_h = \mathbf{u}_h - \mathbf{v}_h$)
end for
$\mathbf{v}_N = \mathbf{r}_{n-1} - \mathbf{r}_n$; $\mathbf{w}_N = \boldsymbol{\xi}_{n-1} - \mathbf{v}_n$; ▷ Update the vector basis
for $\{m = 1$ to $N\}$ **do**
    $D_{N,m} = \mathbf{v}_N \cdot \mathbf{v}_m$; ▷ Update the least-square matrix (eq.13)
end for
$D_{m,N} = D_{N,m}$; ▷ Least-square matrix is symmetric
for $\{k = 1$ to $N\}$ **do**
    $t_k = \mathbf{v}_k \cdot \mathbf{r}_n$; ▷ Build known term of eq.13
end for
$\mathbf{c} = \mathbf{D}^{-1} \cdot \mathbf{t}$; ▷ Solve the least-square problem (eq.13)
$\boldsymbol{\xi}_n = \mathbf{r}_n + \sum_i c_i \mathbf{w}_i$; ▷ Compute the modified residual (eq.15)

5. Numerical Results

We now apply the procedure to a set of fluid problems in order to show its performances.

5.1. Acceleration of a stable procedure: the lid-driven cavity flow

The flow inside a lid-driven cavity has been extensively studied in the last decades and it is usually taken as a benchmark solution for CFD problems (see e.g. [19],[20]). This configuration presents a singularity at the corners where the lid moves. Recently, Auteri *et al.*[21] obtained an accurate solution of such kind of flow by using a second-order spectral projection method that allowed to localize the critical Reynolds number for the first Hopf bifurcation at $Re_{cr} \approx 8018$.

The `BostConv` algorithm is applied to compute the steady state at $Re = 500$: such configuration is stable and a classical time integration converges towards a steady state solution. Our aim is to show the effect of the present algorithm on the convergence rate of the existing iterative procedure. We use the Spectral element code *Nek5000* to accurately solve the governing equations. The results presented in this section are obtained by using a constant time step equal to $\Delta t = 0.001$ and the dimension of the `BostConv` basis is set to $N = 15$.

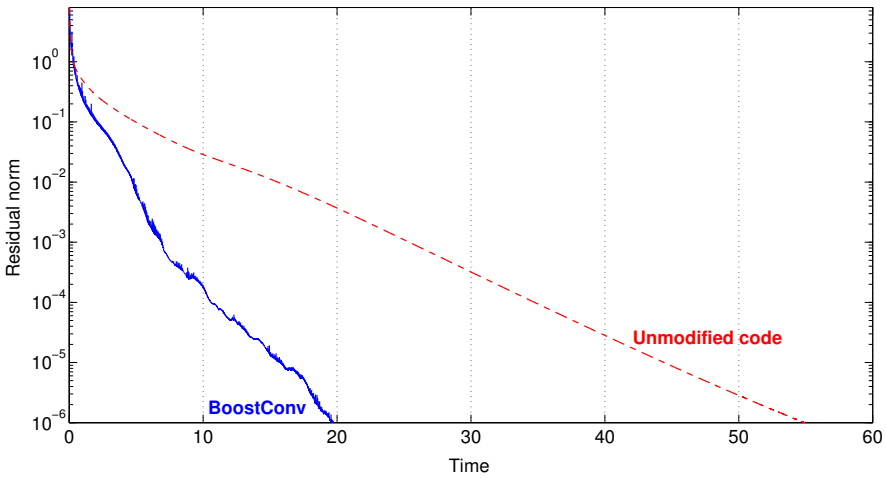

Figure 3: Two-dimensional flow inside a lid-driven cavity at $Re = 500$. In particular, we show the evolution of the residual norm as a function of the time.

Figure 3 shows the evolution of the residual as a function of time. We observe that the residual norm obtained from the unmodified time-integration procedure, depicted using a dash line, reaches the target value of 10^{-6} at $t \approx 54$. The solid line, on the other hand, represents the evolution of the residual when the call to `BostConv` is added to the original code. We note that the application of the proposed algorithm accelerates the convergence of the procedure by a factor of ≈ 2.85. Finally, we recall that the introduction of `BostConv` implies only the solution of a linear system associated to the least-square method: consequently, the computational time of each time step is increased just by $\approx 5\%$.

5.2. Two-dimensional flow past a circular cylinder

The most common example of two-dimensional flow past a bluff body is the flow past an infinitely long circular cylinder. The problem of viscous incompressible flow past this geometrical configuration has for a long time received great attention, both theoretically and numerically [22].

At low Reynolds numbers the steady flow is symmetric and is characterized by a small recirculation bubble behind the cylinder. When the Reynolds number based on the cylinder diameter D exceeds the critical value of $Re^I_{cr} = 46.7$, the flow becomes unstable and a periodic Von-Kármán vor-

tex street appears [23]. Linear stability analysis performed on the inherent base flow shows also the existence of a second unstable wake mode for $Re > Re_{cr}^{II} = 110.8$.

In the present section, we consider the flow at the (supercritical) Reynolds number of $Re = 120 > Re_{cr}^{II}$. The natural evolution of the governing equations produces a saturated limit cycle depicted in figure 4a). We inserted `BoostConv` to compute the base flow in three-different codes: 1) a time-marching finite-difference immersed boundary code [23]; 2) the spectral element (SEM) code NEK5000 [24]; 3) the finite-element code Freefem++ [25],[26]. As in the previous section, for each code, the modification of the existing time integration procedure consists in a single line of code that contains the call to our subroutine. All results presented in this section are obtained by using a time step equal to $\Delta t = 0.001$ and a `BoostConv` basis composed by 15 vectors.

Figure 5 shows the evolution of the residual norm as function of time. The blue line represents the case in which the standard time integration procedure is not modified (leading to the saturated limit cycle). For this case, we show that the algorithm is able to compute the base flow starting from two different initial conditions: 1) a uniform flow, i.e. the initial field is (u,v)=(1,0); 2) the saturated limit cycle. We note that the residual target value is obtained for both the initial conditions at $t \approx 170$. Figure 4b) shows the resulting base flow.

The velocity and pressure distributions of the computed steady flow along the vertical line $x = D$ are depicted in figure 6. We note that each code converges (when `BoostConv` is called during the time integration) perfectly to the base flow computed by using the Newton method and taken as reference solution.

5.3. High-dimensional problem: three-dimensional DNS of a boundary layer flow over a hemispherical roughness element

As discussed in the previous sections, `BoostConv` is conceived to stabilize the dynamical system without a negative impact on the computational burden of the simulation. In this section we show the application of this algorithm to a high-dimensional test case that would be infeasible with a matrix-based method. In fact, we are dealing with a case in which the three-dimensional domain is discretized with ≈ 24 million of points.

In particular, we consider the three-dimensional flow past a hemispherical roughness element immersed in a laminar Blasius boundary layer. This

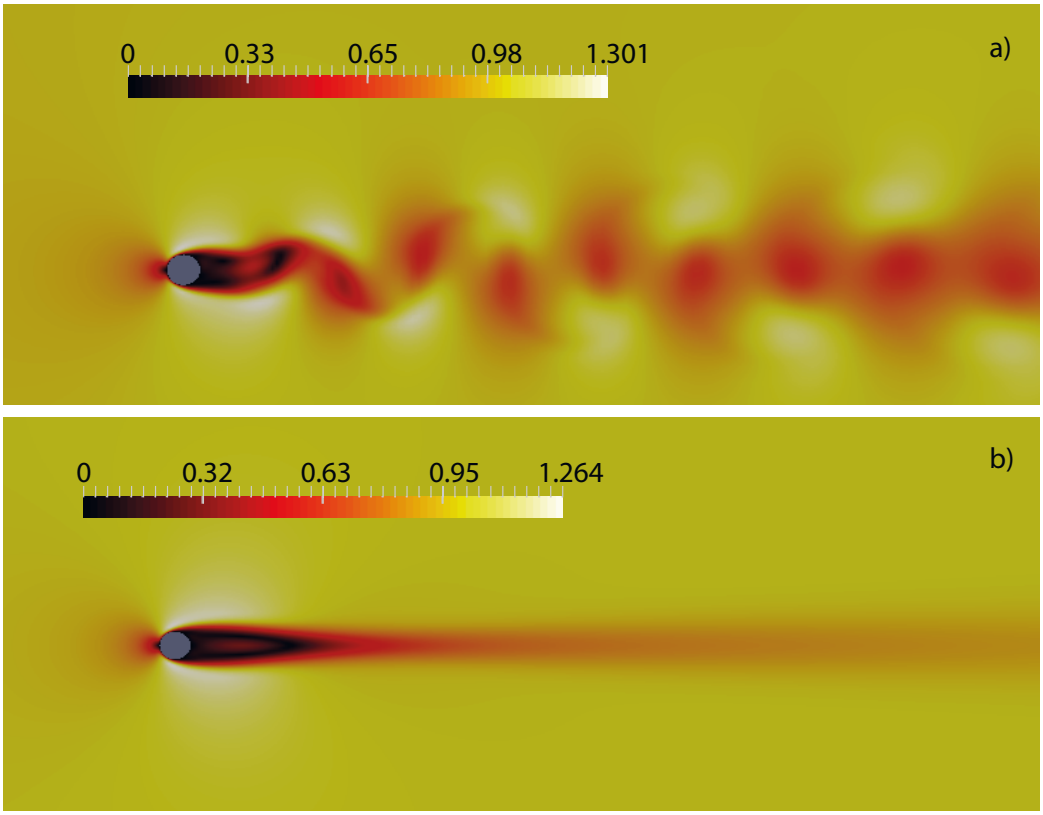

Figure 4: Two-dimensional flow past a circular cylinder at $Re = 120 > Re_{cr}^{II}$. a) Snapshot of the saturated limit cycle (unmodified integration of Navier-Stokes equations). b) Base flow: stabilized simulation using `BoostConv`. The evolution of the residual norm associated with these simulations is depicted in Figure 5.

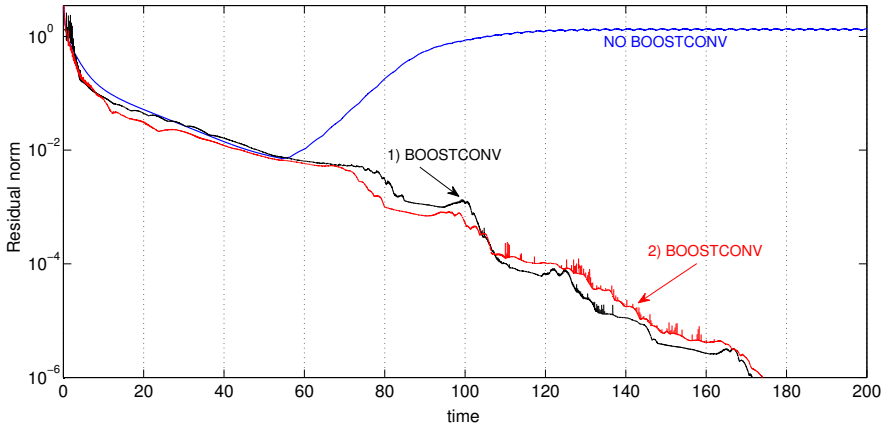

Figure 5: Stabilization of the cylinder flow by using `BoostConv` at $Re = 120$. We started from two different initial conditions: 1) saturated limit cycle and 2) uniform flow in the streamwise direction. The flow simulations are carried out by using the code *Nek5000*.

geometrical configuration is the same chosen by Klebanoff et al. [27] in their experimental investigations. As considered by Tani et al.[28] and Citro et al.[29], the Navier-Stokes equations are made dimensionless using the total height k of the roughness element as the characteristic length scale and the velocity U_k of the incoming uniform stream that would exist in the boundary layer at the height k when the roughness element is absent. The resulting Reynolds number can be written as $Re_k = U_k k/\nu$, with ν being the kinematic viscosity of the fluid. The other important parameter that influences the flow dynamics is the ratio between the displacement thickness δ_k^* of the incoming boundary layer and the height k of the hemisphere.

For this test case, we chose $k/\delta_k^* = 2.62$ and $Re_k = 450$ that are the same conditions in which Klebanoff et al. [27] documented their experimental results. As also shown by Citro et al.[29], the inherent three-dimensional flow pattern beyond the Hopf bifurcation is characterized by coherent vortical structures called *hairpin vortices* that periodically detach from the hemisphere. A contour plot of a snapshot of the resulting periodic flow is depicted in Figure 7a) by taking a mid-plane slice. In this side view of the unsteady supercritical flow, we plotted the iso-contours of the velocity magnitude. As discussed before for the cylinder case and for the case of the lid-driven cavity, we plot the evolution of the residual as a function of time for both the

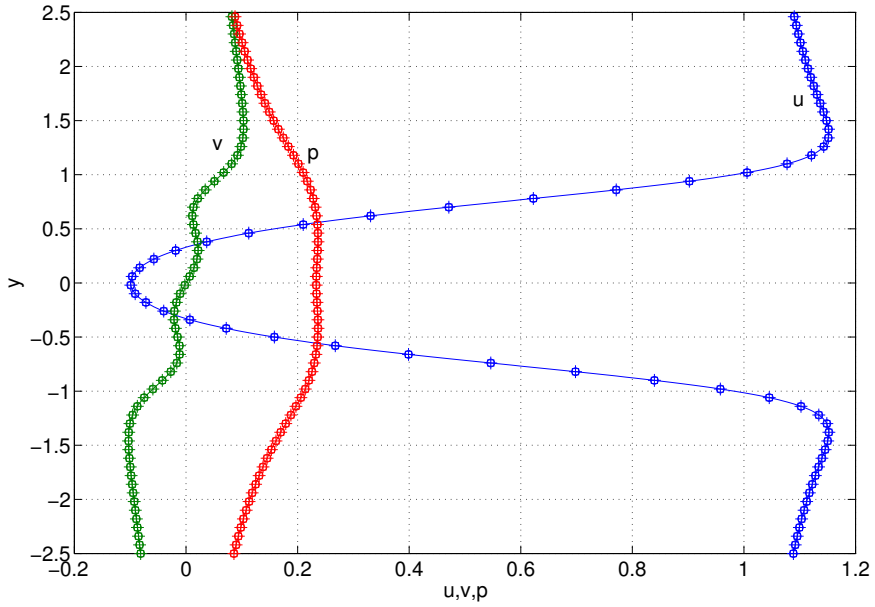

Figure 6: Velocity and pressure distributions in the wake of a circular cylinder at $x = D$ ($Re = 50$). Here, we compare the solutions obtained using (o) finite-difference immersed-boundary code, ($+$) spectral element code (NEK5000) and ($\square$) finite element (time-marching) code. The profiles depicted using solid lines ($-$) are obtained by using Newton method.

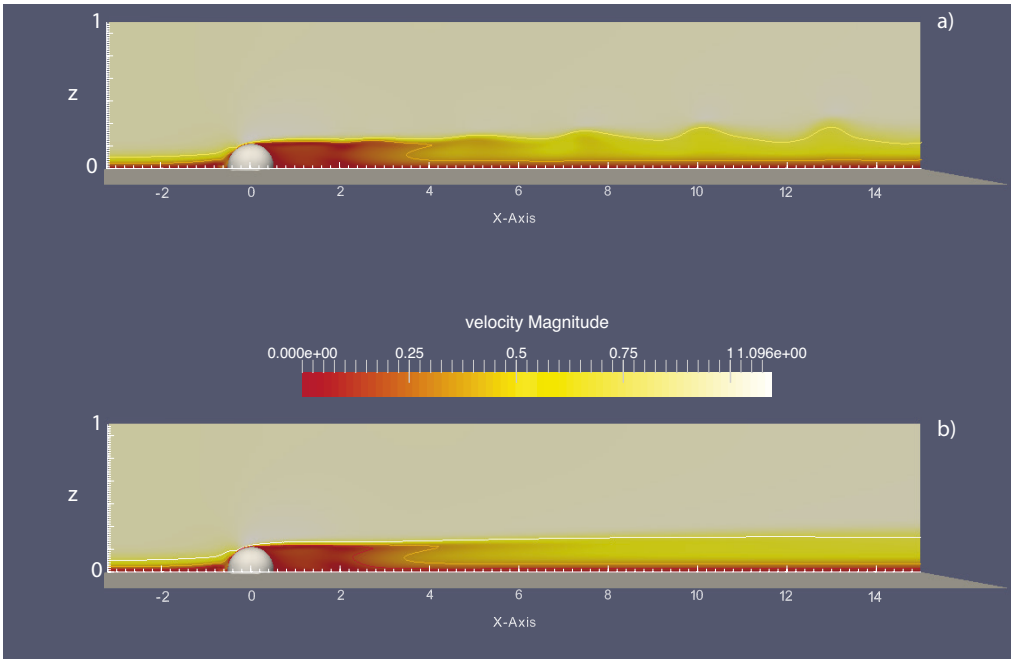

Figure 7: Three-dimensional flow past a hemispherical roughness element: contour plot of the velocity magnitude. Perspective view of a) unsteady supercritical flow (without the application of `BoostConv`) and b) stabilized flow obtained by using the `BoostConv` algorithm. Parameter settings: $Re_k = 450$ and $k/\delta_k^* = 2.62$.

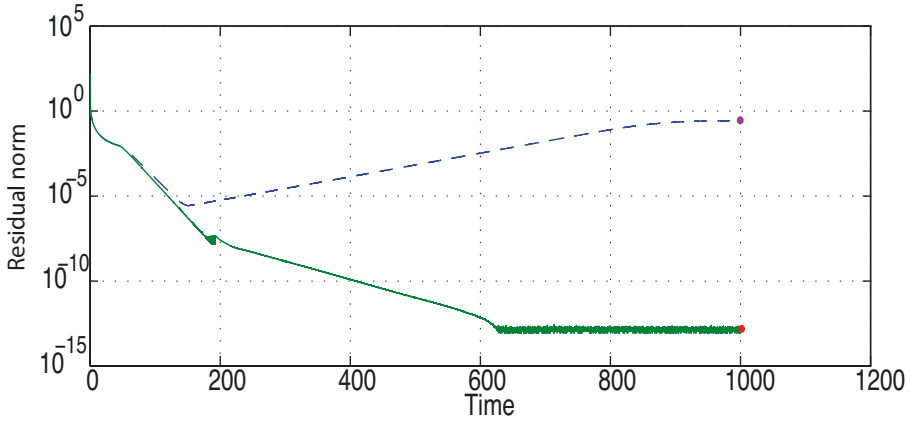

Figure 8: Flow past a hemispherical roughness element. Solid line ($-$): convergence history of `BoostConv`. Dashed line ($--$): time integration of the governing equations.

original time-stepper (dashed line) and for the modified procedure involving `BoostConv`. The convergence history is reported in figure 8. For this case, we performed a DNS using the SEM code Nek5000; the dimension of the basis used is $N = 15$ (see section 3) and the time step is $\Delta t = 0.001$. The initial field is a uniform flow as for the case of the circular cylinder. The run was performed on an IBM BG/Q Supercomputer at CINECA and we found that the stabilization procedure increased the simulation time of about 9%. The inherent base flow is shown in figure 7b).

6. Conclusions

In this paper we present a novel, efficient and easy-to-implement algorithm inspired by the Krylov-subspace projection methods, which is able to compute unstable steady states of any dynamical system. `BoostConv` is based on the least-square minimization of the residual norm at each step of an existing iterative procedure. The key idea of the proposed method is to invert only the small part of the problem represented by the dominant and slower decaying modes exactly while letting the original iterative algorithm to handle the remaining modes. As a consequence, it is very efficient because the linear system that we need to invert at each time step is small compared with the dimension of the problem. From a programming viewpoint, `BoostConv` can be encapsulated in a black-box routine where the only required input is the residual $\mathbf{r}_n$ and the only output is the modified residual $\boldsymbol{\xi}_n$. We underline that the only modification necessary to stabilize or boost the convergence of a pre-existing iterative algorithm is a single line of code containing the call to `BoostConv`.

We also report numerical results obtained with the new procedure. We start from the classical case of the two-dimensional lid-driven cavity flow. At a subcritical Reynolds number, we show that `BoostConv` is able to accelerate the convergence of the existing time integration procedure. Subsequently, we consider the two-dimensional flow past an infinitely long circular cylinder. For this case, we show, with several different codes, that `BoostConv` is able to drive the iterative procedure to the exact base flow (computed using a Newton method). We note that the initial field, being it a uniform flow or the inherent saturated limit cycle, does not affect the stabilization. A three-dimensional case is also considered to examine the application of `BoostConv` to a high-dimensional problem. In the case of the flow past a hemispherical roughness element immersed in a laminar Blasius boundary layer, we found

that the resulting modification of the time integration does not negatively affect the computational burden of the simulation. Furthermore, the proposed algorithm can be used also to stabilize unstable periodic orbits. In fact, recently, thanks to the application of this procedure, Carini et al.[30] were able to explain the flip-flop mechanism in the flow past two side-by-side circular cylinders.

Unlike Krylov methods such as GMRES, `BoostConv` is able to take into account for the change of the system Jacobian during the time evolution of the dynamical system. We underline also that the proposed algorithm can be combined with any spatial discretization method and can be used to stabilize a dynamical system even in presence of bifurcations with higher codimension.

[1] Drazin, P., Reid, W. *Hydrodynamic Stability*, Cambridge University Press, 1981

[2] Theofilis, V. *Global Linear Instability*, Annu. Rev. Fluid Mech., Vol. 43, pp. 319-352, 2011

[3] Govaerts, W.J.F. *Numerical Methods for Bifurcations of Dynamical Equilibria*, Soc. for Industr. & Appl. Math., 2000

[4] Doedel, E. *AUTO: Software for continuation and bifurcation problems in ordinary differential equations*, Report Applied Mathematics, California Institute of Technology, Pasadena, USA, 1986

[5] Kuznetsov, Y.A., Levitin, V.V. *CONTENT, a multiplatform continuation environment*, Technical report, Amsterdam, The Netherlands, 1996

[6] Lust, K., Roose, D., Spence, A., Champneys, A.R. *An adaptive Newton-Picard algorithm with subspace iteration for computing periodic solutions*, SIAM J. Sci. Comput., Vol. 19, pp. 1188-1209, 1998

[7] van Noorden, T.L., Verduyn, S.M., Bliek, A. *The efficient computation of periodic states of cyclically operated chemical processes*, IMA J. Appl. Math., Vol. 68, pp. 149-166, 2003

[8] Shroff, G.M., Keller, H.B. *Stabilization of unstable procedures: the recursive projection method*, SIAM J. Numer. anal., Vol. 30, pp. 1099-1120, 1993

[9] van Noorden, T.L., Verduyn, L., Bliek, A. *A Broyden Rank $p+1$ Update Continuation Method with Subspace Iteration*, SIAM J. Sci. Comput., Vol. 25, pp. 1921-1940, 2004

[10] Sanchez, J., Net, M., Garcia-Archilla, B., Simo, C. *Newton-Krylov continuation of periodic orbits for Navier–Stokes flows*, J. Comput. Phys., Vol. 201, pp. 13-33, 2004

[11] Sanchez, J., Marques, F., Lopez, J.M. *A continuation and Bifurcation Technique for Navier-Stokes Flows*, J. Comput. Phys., Vol. 180, pp. 78-98, 2002

[12] Mittelmann, H.D., Weber, H. *Multi-grid solution of bifurcation problems*, SIAM J. Sci. Stat. Comput., Vol. 6, 1985

[13] Akervik, E., Brandt, L., Henningson, D.S., Hoepffner, J., Marxen, O., Schlatter, P. *Steady solutions of the Navier–Stokes equations by selective frequency damping*, Phys. of Fluids, Vol. 18, pp. 068102, 2006

[14] Bagheri, S., Schlatter, P., Schmid, P.J., Henningson, D.S. *Global stability of a jet in crossflow*, J. Fluid Mech., Vol. 624, pp. 33–44, 2009

[15] Ilak, M., Schlatter, P., Bagheri, S., Henningson, D.S. *Bifurcation and stability analysis of a jet in cross-flow: onset of global instability at a low velocity ratio*, J. Fluid Mech., Vol. 696, pp. 94–121, 2012

[16] Simoncini, V., Szyld, D.B. *Recent computational developments in Krylov subspace methods for linear systems*, Numer. Linear Algebra Appl., Vol. 14, pp. 1–59, 2007

[17] Saad, Y., Schultz, M.H. *GMRES: A generalized minimal residual algorithm for solving nonsymmetric linear systems*, SIAM J. Sci. Stat. Comput., Vol. 7, pp. 856–869, 1986

[18] Saad, Y. *Iterative Methods for Sparse Linear Systems (2nd edn)*, SIAM, 2003

[19] Ghia, U., Ghia K.N., Shin, C.T. *High-Re solutions for incompressible flow using the Navier-Stokes equations and a multigrid method*, J. Comput. Phys., Vol. 48, pp. 387–411, 1982

[20] Schreiber R., Keller H.B., *Driven cavity flows by efficient numerical techniques*, J. Comput. Phys., Vol. 49, pp. 310–333, 1983

[21] Auteri F., Parolini N., Quartapelle L., *Numerical investigation on the stability of singular driven cavity flow*, J. Comput. Phys., Vol. 183, pp. 1–25, 2002

[22] Williamson, C.H.K. *Vortex Dynamics in the Cylinder Wake*, Annu. Rev. Fluid Mech., Vol. 28, pp. 477-539, 1996

[23] Giannetti, F., Luchini, P. *Structural sensitivity of the first instability of the cylinder wake*, J. Fluid Mech., Vol. 581, pp. 167–197, 2007

[24] Fischer, P.F. *An overlapping schwarz method for spectral element solution of the incompressible Navier-Stokes equations*, J. Comput. Phys., Vol. 133, pp. 84–101, 1997

[25] Hecht, F. *New development in FreeFem++*, J. Num. Math., Vol. 20, pp. 251–265, 2012

[26] Citro, V., Giannetti, F., Brandt, L., Luchini, P. *Linear three-dimensional global and asymptotic stability analysis of incompressible open cavity flow*, J. Fluid Mech., Vol. 768, pp. 113–140, 2015

[27] Klebanoff, P.S., Cleveland, W.G., Tidstrom, K.D. *On the evolution of a turbulent boundary layer induced by a three-dimensional roughness element*, J. Fluid Mech., Vol. 237, pp. 101–187, 1992

[28] Tani, I., Komoda, H., Komatsu, Y., Iuchi, M. *Boundary-Layer Transition by Isolated Roughness*, Aeronautical research institute, Internal report, Vol. 375, pp. 129–143, 1962

[29] Citro, V., Giannetti, F., Luchini, P., Auteri, F. *Global stability and sensitivity analysis of boundary-layer flows past a hemispherical roughness element*, Phys. Fluids, Vol. 27, pp. 084110, 2015

[30] Carini, M., Giannetti, F., Auteri, F. *On the origin of the flip-flop instability of two side-by-side cylinder wakes*, J. Fluid Mech., Vol. 742, pp. 552–576, 2014

Paper

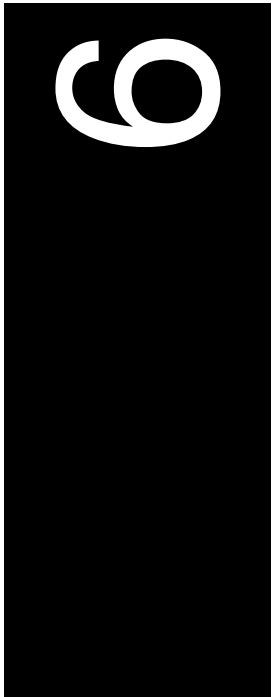

Noname manuscript No.
(will be inserted by the editor)

Error Sensitivity to Refinement: a criterion for optimal grid adaptation

Paolo Luchini · Flavio Giannnetti · Vincenzo Citro

Received: date / Accepted: date

Abstract Most indicators used for automatic grid refinement are suboptimal, in the sense that they do not really minimize the global solution error. This paper concerns with a new indicator, related to the sensitivity map of global stability problems, suitable for an optimal grid refinement that minimizes the global solution error. The new criterion is derived from the properties of the adjoint operator and provides a map of the sensitivity of the global error (or its estimate) to a local mesh refinement. Examples are presented for both a scalar partial differential equation and for the system of Navier-Stokes equations. In the last case, we also present a grid adaptation algorithm based on the new estimator and on the $FreeFem++$ software that improves the accuracy of the solution of almost two order of magnitude by redistributing the nodes of the initial computational mesh.

Keywords grid adaptation · error estimation · adjoint · sensitivity

1 Introduction

Grid refinement is a powerful tool that can be used in intensive and memory demanding applications to reduce the computational costs and at the same time retain and even improve the accuracy of the numerical problem. Reducing both errors and costs in a numerical simulation is a general and fundamental problem in computational sciences and is strictly related to uncertainty quantifications analysis. Different strategies have been proposed and adopted in the past to implement grid refinement algorithm. Here, we will study the problem by using a control theory approach where the aim is to control a numerical algorithm. The problem consists in finding an optimal grid that minimizes the error of a numerical computation. For such purpose, we first need a quantitative definition of the error we are trying to minimize: different possibilities can be used, producing different kind of grid refinement algorithms. A commonly used approach in structural mechanics and computational fluid dynamics (CFD) is to adopt the mean square quadratic

P. Luchini & F. Giannetti & V. Citro
DIIN, University of Salerno, Via Giovanni Paolo II, 84084, Fisciano (SA), Italy
E-mail: vcitro@unisa.it (Vincenzo Citro)

error: indicating by u the numerical solution and u_{ex} the exact solution, the error can be defined as

$$E_2 = \left(\int_{\Omega} |u_{ex}(\mathbf{x}) - u(\mathbf{x})|^2 dS \right)^{1/2}, \tag{1}$$

where Ω is the computational domain over which the problem is defined. Minimizing E_2 in this case means to reduce the difference between the exact and the numerical solution in a least square sense. This is of course an old topic and many different strategies have been proposed to reach the goal. Most of them are however suboptimal, i.e. they are based on indictors that do not really minimize the error (1) but they actually reduce some quantity that is related to it. Typical examples are given by the widely-adopted recovery-based approach, the goal-oriented approach and τ-criterion. The recovery-based approach is probably the most popular grid-adaptation criteria. The idea was proposed by Zienkiewicz & Zhu [1] in the context of linear elasticity. This approach is driven by the norm of the gradient error, improperly refereed as "residual"

$$\eta = \left(\int_{\Omega} |\nabla u - \nabla u_h|^2 \, d\Omega \right)^{1/2}. \tag{2}$$

In practical implementations, an estimator based on equation (2) is built by replacing the exact gradient ∇u with a reconstruction of the field obtained by a post-processing of the discrete u_h solution on grid Ω_h. Grid refinement is then performed when η on a element (or cell) is larger than a given threshold. This approach leads to an equipartition of the residual among the elements (cells) of the discretization. Generally the algorithm leads to a reduction of the error, but this does not guarantee to find the real minimum of the problem, i.e. the minimum of integral (1). A different approach which evolved in the context of finite-differences and finite-volumes is the $\tau - criterion$ [2]. For such kind of discretizations, it is common to use a refinement criteria based on some estimates of the *residual*, i.e. the quantity that is obtained when the exact solution of the problem is inserted into the discrete equations. From a practical point of view, if the exact solution is not available, we can replace it with the solution obtained on a sufficiently fine grid. In the context of multigrid, the so called (h-2h)-relative truncation error

$$\tau_h^{2h} = L_{2h} I_h^{2h} u_h - I_h^{2h} L_h u_h \tag{3}$$

is considered as a natural indicator for local grid refinement. Here, L indicates the differential operator defining the problem, I_h^{2h} is the fine-to-course interpolation operator and the subscripts $_h$ and $_{2h}$ refer respectively to fine and course grid quantities. By definition τ_h^{2h} is the quantity that has to be added to the r.h.s of the discrete problem on the coarse grid Ω_{2h} in order to obtain the accuracy of the fine grid (up to interpolation) and, in practice, represents an approximation of the difference between the truncation error on the fine and course grid. A useful local refinement criterion based on this quantity consists in comparing $h^d \tau_h^{2h}$ with a given tolerance ϵ, where d indicates the dimension of the problem: in the simplest approach the grid is then refined locally wherever the estimator is larger than ϵ. This is a good criterion especially if we know that in some regions τ_h^{2h} is large: in this case it is reasonable to assume that the grid is too course there. However, refining the grid in those regions does not necessarily minimize the integral (1).

A third approach that is widely-adopted in CFD (and is more optimization based) is the so-called goal-oriented approach. In some applications, in fact, it is useful to reduce the error of some global output (as for example drag, lift, moment, etc.), rather than the local error of the solution. This goal-oriented error can be truly minimized using an adjoint-based approach. If $J(u)$ is the quantity of interest then the aim is to control

$$|J(u) - J(u_h)|. \tag{4}$$

This leads to a minimization problem in which a forced adjoint equation has to be solved. In this way it is possible to arrive to an error-estimate of the form

$$|J(u) - J(u_h)| \approx < \rho(u_h), \omega_h(z) > \tag{5}$$

where z is the adjoint solution and $\omega_h(z)$ is a weight function describing the effect of local variations of the residual $\rho(u_h)$. Examples can be found in the work of Giles & Pierce [3] or in Becker & Rannacher [4]. Once again the procedure is suboptimal since it minimizes the goal, not the solution error (1). In this paper we will investigate a new adjoint-based approach to derive a new optimal criterion for an effective mesh refinement strategy which aims at minimizing the global solution error. Such criterion is derived by using the properties of the adjoint operators and is based on the sensitivity of the error (or its estimate) to a local mesh refinement. This sensitivity is derived from the knowledge of two numerical solutions, one calculated on a coarse and one on a fine mesh. A system of forced adjoint equations is then derived from a minimization problem in which the objective function is an estimate of the L_2 error norm. By combining the adjoint variables with the local values of the coarse-grid residual we obtain a spatial map representing the sensitivity of the error to a local refinement of the mesh. The spatial structure of these sensitivity maps highlights the regions of the flow where a local refinement of the mesh would be most effective. The error sensitivity so derived can be used as an effective indicator to implement an optimal strategy of adaptive local refinement.

2 Error Sensitivity to local grid Refinement (ESR)

The strategy we are going to describe is inspired by the structural sensitivity analysis introduced by [5] to study fluid-dynamic oscillators. In order to characterize the global instability generating the Von Kárman street, Giannetti & Luchini[5] performed an adjoint analysis to determine the sensitivity of the unstable eigenvalue to a generic structural perturbation of the linearized governing equations. In a discrete setting, given a problem of the form

$$\mathbf{A} \cdot \mathbf{u} = \lambda \mathbf{u} \tag{6}$$

it is possible to determine the effect of a generic matrix perturbation $\delta\mathbf{A}$ on the eigenvalues of the problem. This is easily obtained by multiplying (6) by the corresponding adjoint eigenvector and by using the bi-orthogonality properties between the direct (right) and adjoint (left) solutions. In this way, we are left with the following explicit expression for $\delta\lambda$

$$\delta\lambda = \frac{\mathbf{v} \cdot \delta\mathbf{A} \cdot \mathbf{u}}{\mathbf{v} \cdot \mathbf{u}}. \tag{7}$$

In the context of fluid-dynamics problems, such procedure can be applied in space rather than just to a matrix: the right and left eigenvectors are now fields, function of space, with a precise meaning. In particular the direct mode represents the perturbation of the velocity and pressure fields, while the adjoint expresses the sensitivity of the mode amplitude with respect to a forcing term in the linearized equations. By combining together the information contained in both direct and adjoint fields, it is possible to characterize the sensitivity of the eigenvalue to a structural modification of the problem consisting in a localized feedback from velocity to force. In the case of a fluid problem, such approach models the effect of a small object placed somewhere in the flow and is useful to localize in space the feedback mechanism ("the wavemaker") responsible for the instability. In practice, such localization is performed by taking the point-wise product between the direct and adjoint fields and by inspecting where such spatial map assumes largest values. A similar procedure consisting in combining information between the direct and adjoint solutions can also be used to derive an effective indicator for grid refinement strategies.
Suppose we want to numerically solve a differential problem on a domain Ω with given b.c. on $\partial\Omega$. Let's denote by $\boldsymbol{N}_h$ the algebraic operator obtained through a discretization of the continuous problem on a mesh with characteristic spacing h. If $\boldsymbol{u}_h$ is a solution of the discrete problem then

$$\boldsymbol{N}_h(\boldsymbol{u}_h) = \mathbf{0} \tag{8}$$

while the exact solution of the continuous problem $\boldsymbol{u}_{ex}$ satisfies

$$\boldsymbol{N}_h(\boldsymbol{u}_{ex}) = \boldsymbol{r}_h \tag{9}$$

where the term $\boldsymbol{r}_h$ is named "residual". We measure the error between the approximate and exact solution using (for instance) the definition (1), where the integral is replaced by its numerical approximation. In general this can be expressed as

$$E_2^2 = \sum_i w_i \left(u_{h,i} - u_{ex,i}\right)^2 \tag{10}$$

where w_i are suitable weights composing a numerical quadrature formula. We want now to determine the sensitivity of the error E_2 to a small variation in the residual $\delta\boldsymbol{r}_h$ (its *gradient* $\mathbf{v}_h$), or in other terms the gradient of E_2 with respect to $\delta\boldsymbol{r}_h$.

A small variation $\delta\boldsymbol{u}_h$ in the numerical solution $\boldsymbol{u}_h$ produces a variation in the error of the form

$$E_2 \delta E_2 = \mathbf{y}\, \delta\boldsymbol{u}_h \tag{11}$$

where $\mathbf{y}$ is the vector with components $y_i = w_i(u_{h,i} - u_{ex,i})$. By applying the adjoint analysis we now write E_2 as a linear function of the residual. In order to achieve this, we first note that a small variation in the solution produces a small change in the residual according to

$$\mathbf{A}\, \delta\mathbf{u}_h = \delta\mathbf{r}_h \tag{12}$$

where $\mathbf{A} = \frac{\partial \mathbf{N}_h}{\partial \mathbf{u}}$ is the Jacobian of the differential operator in (8). By multiplying (12) by a vector $\mathbf{v}_h$ and using the definition of the adjoint operator we can write

$$\mathbf{v}_h \cdot \mathbf{A}_h \delta\mathbf{u}_h = \delta\mathbf{u}_h \cdot \mathbf{A}_h^T \mathbf{v}_h = \mathbf{v}_h \cdot \delta\mathbf{r}_h \tag{13}$$

If we now choose the adjoint vector $\mathbf{v}_h$ such to satisfy

$$\mathbf{A}_h^{\mathrm{T}}\,\mathbf{v}_h = \mathbf{y}/E_2 \tag{14}$$

we can rewrite the variation of the error in terms of a small residual change as

$$E_2\delta E_2 = \mathbf{y}\cdot\delta\mathbf{u}_h = E_2\mathbf{v}_h\cdot\mathbf{A}_h\delta\mathbf{u}_h = E_2\mathbf{v}_h\cdot\delta\boldsymbol{r}_h. \tag{15}$$

Assume now that, asymptotically for small h, $\mathbf{r}_h \sim h^p$ for some integer exponent p (the order of the discretization). A variation in h (a grid refinement) by a factor m (say 1/2) will then induce a variation in the residual proportional (with opposite sign) to the residual itself, i.e.

$$\delta\boldsymbol{r}_h = \boldsymbol{r}_{mh} - \boldsymbol{r}_h \simeq (m^p - 1)\boldsymbol{r}_h. \tag{16}$$

This is, in fact, the rationale behind recovery-based methods: refining where the residual is largest produces the maximum reduction in the residual. We may also notice that, when the residual is related to the truncation error of a differential operator, the relationship between residual and refinement is a *local* one. Such relation is still not what we really look for: in fact our aim is to know what happens when we refine the grid, which is not the same as changing the residual. To get the complete answer to our problem we need to consider what happens to the residual when we refine the grid.

Recall now that the spatial map of the residuals give us an indication where a local refinement will mostly decrease the residual itself. On the other hand, the spatial map of the adjoint provides information on the location where a change in the residual will mostly affect the error. These two quantities can be compared with the direct and adjoint solution of the structural sensitivity analysis for fluid flow problems with self-exciting instabilities cited above. As for those cases, we can now make a step forward and combine the information provided by the two maps by taking the local product between the residual and the adjoint field. In this way we define the Error Sensitivity to Refinement (ESR)

$$s_i = E_2^{-2} v_{h,i}\, r_{h,i} \tag{17}$$

where no implicit summation is assumed. This quantity indicates where a local refinement (by a fixed factor m) will mostly affect the error E_2 and is therefore a natural indicator to really minimize (1). In general, both error and residual require a knowledge of the exact solution. Just as for all the other mesh-adaptation indicators, the latter can be estimated and replaced by a solution on a finer mesh. In particular, if both the error and the residual asymptotically decrease like h^p, we obtain the following relation

$$\mathbf{u}_{2h} - \mathbf{u}_h \simeq (1 - 2^{-p})(\mathbf{u}_{2h} - \mathbf{u}_{ex}) \simeq (2^p - 1)(\mathbf{u}_h - \mathbf{u}_{ex}) \tag{18}$$

between the error on grid h and the error of the solution with respect to a finer grid. Furthermore, considering that u_{2h} is the discrete solution on the course mesh, it is also possible to write

$$\mathbf{N}_{2h}(\mathbf{u}_h) - \underbrace{\mathbf{N}_{2h}(\mathbf{u}_{2h})}_{=0} \simeq (1-2^{-p})(\mathbf{N}_{2h}(\mathbf{u}_{ex}) - \underbrace{\mathbf{N}_{2h}(\mathbf{u}_{2h})}_{=0}) \simeq (2^p-1)\mathbf{N}_h(\mathbf{u}_e x) \tag{19}$$

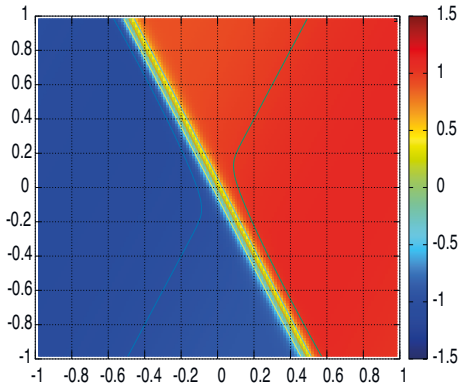

Fig. 1 Analytic solution of the Poisson problem (20).

which gives an estimate of the residual using the solution on a finer mesh. As a final remark we note that the error sensitivity $s_i = E_2^{-2} v_{h,i}\, r_{h,i}$ tends to a grid-independent limit for $h \to 0$ so that sensitivity maps obtained on different grids will be similar provided the mesh spacing h is sufficiently small. We now apply the new indicator to study two different problems: the first one consists in solving a scalar elliptic partial differential equation, while the second deals with the solution of a system of PDEs, namely the Navier-Stokes equations governing the motion of an incompressible fluid.

3 Numerical Results

3.1 Poisson equation

We start by considering the following Poisson problem on the square domain $\Omega = [-1..1] \times [-1..1]$

$$\Delta_2 u = g(x, y) \tag{20}$$

with *r.h.s.* term $g(x, y)$

$$g(x, y) = -0.5 \sin(2x - y) - \frac{10}{\epsilon^2} \operatorname{sech}\left[\frac{2x + y}{\epsilon}\right]^2 \tanh\left[\frac{2x + y}{\epsilon}\right] \tag{21}$$

and boundary conditions chosen such that

$$u(x, y) = 0.1 \sin(2 * x - y) + \tanh\left[\frac{2x + y}{\epsilon}\right] \tag{22}$$

is a solution of the problem. When the parameter ϵ in the r.h.s is small, the solution develops a steep gradient on the line $y = -2x$. It is therefore reasonable to expect that a grid refinement localized around that region is able to improve the accuracy of the computation and minimize the error. In what follows we set $\epsilon = 0.1$. A contour map of the analytic solution $u(x, y)$ is shown in figure 1. Since the exact solution for this problem is known in analytic form we can easily compute the error, the residual and the ESR on grid characterized by different mesh spacings. By inspecting the spatial ESR map we can easily check if the original expectation is correct or not. In order to perform the sensitivity analysis, the differential problem is discretized by using second-order finite differences on a

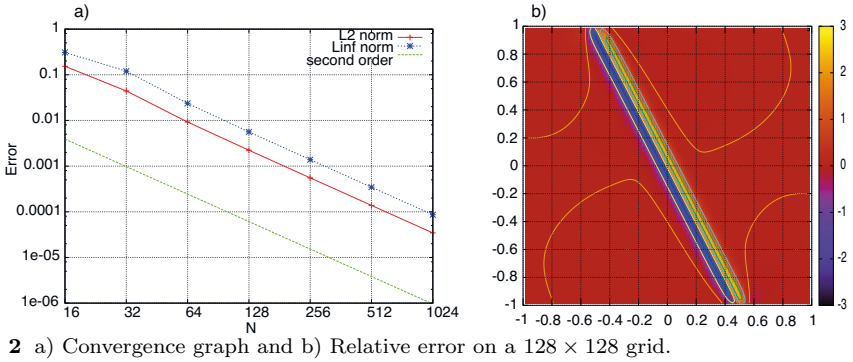

Fig. 2 a) Convergence graph and b) Relative error on a 128×128 grid.

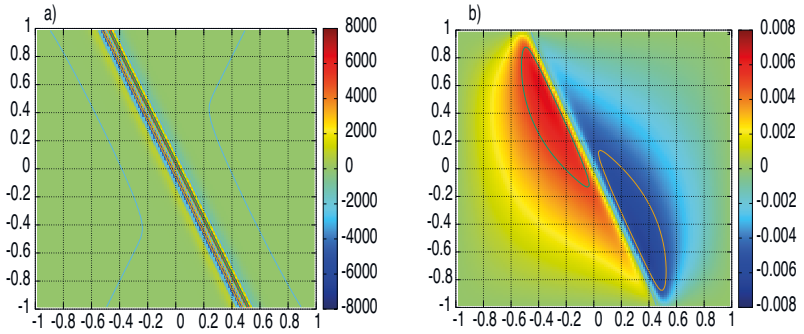

Fig. 3 a) Rescaled residual $r_h(x,y)/E_2^2$ and b) adjoint solution on a 128×128 grid.

uniform mesh with spacing $h = 2/n$. Here n represents the number of interval in the horizontal (or vertical) direction. The resulting discretization, together with the boundary conditions, produces a set of linear algebraic equations whose solution is found by a sparse LU solver (UMFPACK package). The adjoint problem is solved by using the discrete adjoint approach, i.e. by taking the adjoint (transpose) of the discretized operator. Figure 2a) shows the E_2 and the E_∞ error as a function of the number of intervals (we get a second order convergence) while Figure 2b) shows the point-wise error (the difference between the numerical and the exact solution) evaluated on a 128×128 grid. Note that, as expected, larger errors are located close to the steep variation of the solution.

Figure 3a) shows the spatial distribution of the rescaled point-wise residual on a 128×128 grid and 3b) the adjoint solution defined by (14). As expected the largest influence of a residual change on the residual itself is clearly localized across the region of strong variation, while the sensitivity of the error to a residual change (expressed by the adjoint solution) has an antisymmetric distribution with respect to $y = -2x$, reaching its extreme values in regions close to such line.

Finally, figure (4) displays the ESR map evaluated for a 128×128 (a) and 64×64 (b) grid. As expected the indicator assumes larger values around the region $y = -2x$ where the solution presents sharp gradients, indicating that in order to really minimize the error it is necessary to refine the mesh in that regions. As a final remark observe that the two maps obtained on different grids have the same scale range: apart from a different spatial resolution the figures are both quantitatively

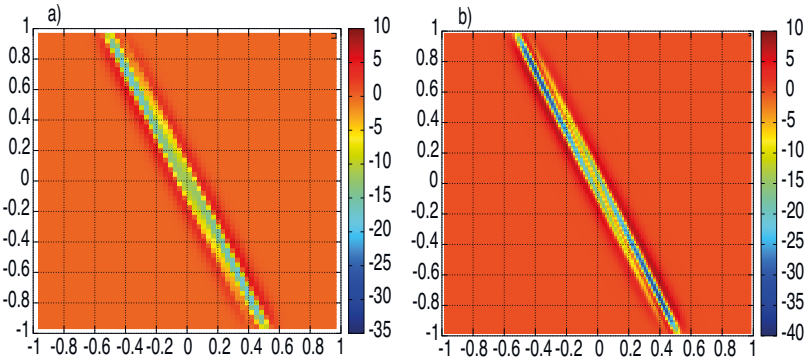

Fig. 4 ESR map on a a) 64×64 grid and b) 128×128 grid.

and qualitatively similar, proving that, as underlined in the previous section, the error sensitivity to refinement ESR tends to a grid independent quantity.

3.2 Navier-Stokes equations

The second example concerns the numerical solution of the incompressible Navier-Stokes equations. In particular we test the new indicator on Kovasznay flow, an analytical solution of the Navier-Stokes equations resembling the flow behind a grid of obstacles. The solution was originally found by [6] and is given by the following expressions

$$\lambda = Re/2 - \sqrt{\frac{Re^2}{4} + 4\pi^2} \tag{23}$$

$$u(x,y) = 1 - e^{\lambda x}\cos(2\pi y) \tag{24}$$

$$v(x,y) = \frac{\lambda}{2\pi} e^{\lambda x}\sin(2\pi y) \tag{25}$$

$$p(x,y) = p_0 - 0.5e^{2\lambda x} \tag{26}$$

$$\tag{27}$$

where $u(x,y)$ and $v(x,y)$ are respectively the horizontal and vertical velocity components, $p(x,y)$ is the pressure and Re is the flow Reynolds number. As an example figure 5 shows the streamlines of the flow at $Re = 40$ on the computational domain $[-0.5 : 1.5] \times [-1.5 : 1.5]$.

The numerical solution of the problem was obtained with two different approaches: we solved the equations both using a second-order finite difference-discretization on a staggered uniform mesh and by using a finite-element second-order discretization based on Taylor-Hood elements on a triangular mesh implemented in the software package FreeFem++ (`http://www.freefem.org`). In both cases we obtained similar results, cross-checking in this way our numerical implementations. For sake of brevity and ease of comparison with the previous scalar example, we will present here only the numerical results obtained with the finite-difference code, with the exception for the mesh adaptation test which was per-

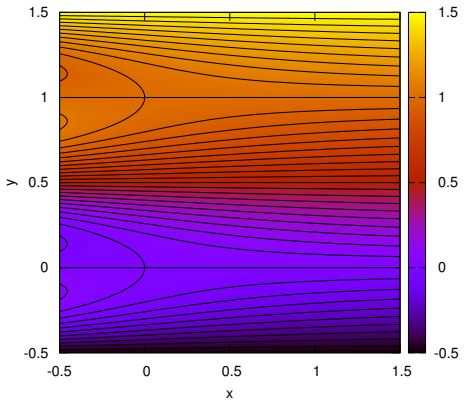

Fig. 5 Velocity magnitude and streamlines of the Kovasznay flow at $Re = 40$.

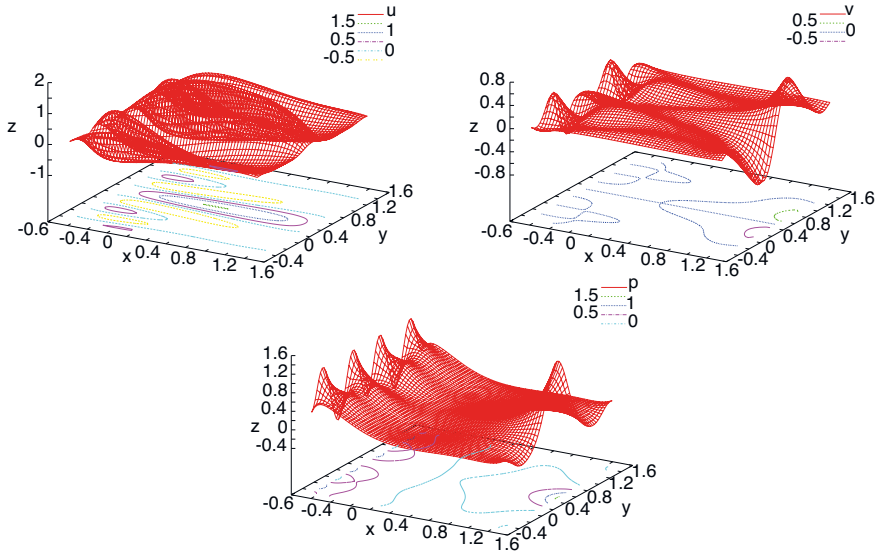

Fig. 6 Scaled error $(\boldsymbol{e}(x, y)/E_2)$ on a 64×64 grid.

formed only with the finite-element code. The adjoint equations and the sensitivity in both cases were derived using the discrete adjoint approach.

Figure 6 displays the different components of the rescaled local error $\mathbf{e}(x, y) = |\mathbf{q}_h - \mathbf{q}_{ex}|/E_2$ relative to the exact solution $\mathbf{q}_{ex} = [u_{ex}(x, y), v_{ex}(x, y), p_{ex}(x, y)]$. It is not a surprise that these quantities are larger near the flow entrance because the solution is exponentially decaying in the downstream direction. This can be noted also in figure 7 which displays the different components of the adjoint solution evaluated on a 64×64 mesh, i.e. the sensitivity of the error to a small change in the residual. Finally figure 8 shows the ESR map for each component of the solution vector, i.e. the product of the scaled residual and the adjoint for each equation of the system.

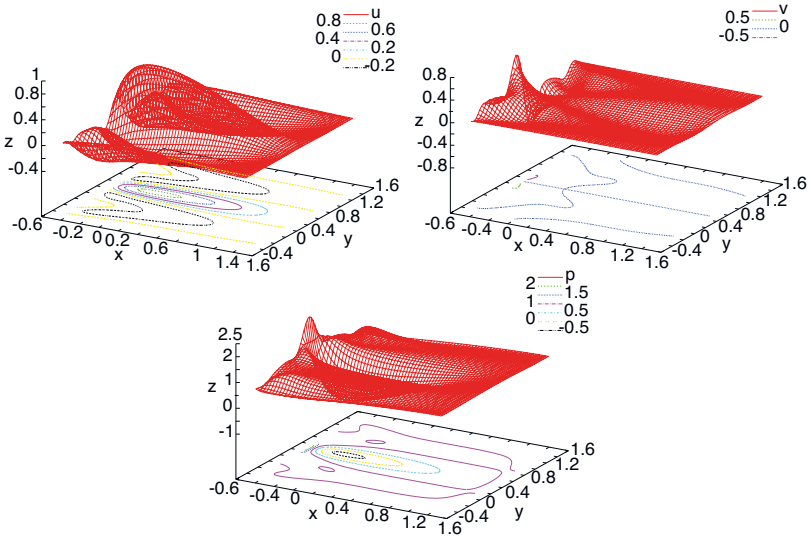

Fig. 7 Components of the adjoint solution evaluated on a 64×64 grid.

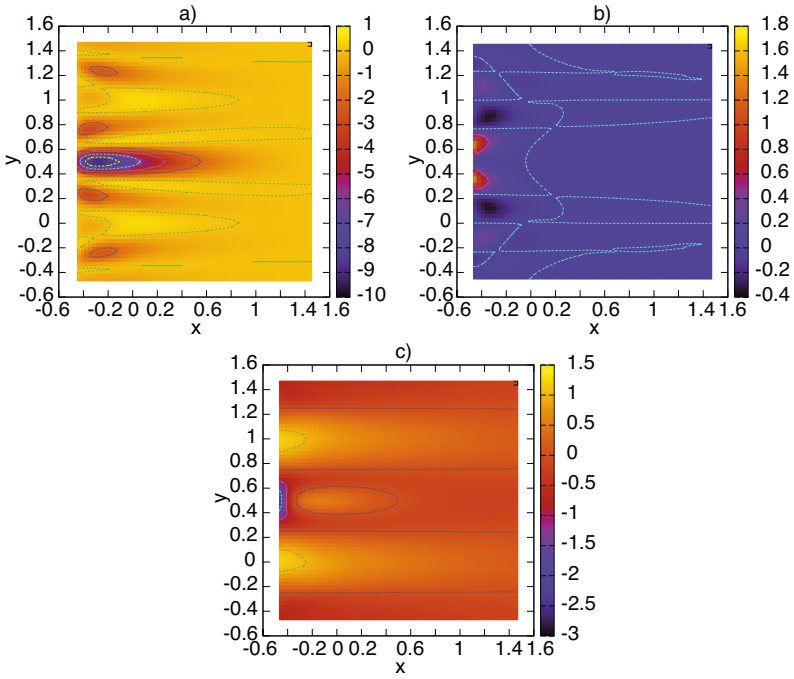

Fig. 8 ESR maps for the diffrent component of the solution vector $\mathbf{q}_h$: a) u_h, b) v_h and c) p_h.

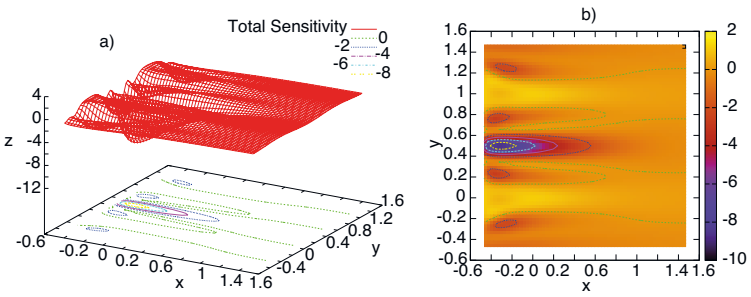

Fig. 9 Total ESR map for grid adaptation of Kovasznay flow: left) 3D perspective view and right) contour plot.

Looking at such diagrams one should wonder what is the meaning of each graph. In principle we could imagine to perform an ideal experiment and refine the grid for just one component of the solution $\mathbf{q}_h$ but not for the others. Of course this is not a clever way to proceed but from a theoretical point of view each map is able to quantify the effects associated to a grid refinement for one component only. In practice, however, we want to modify the grid contemporarily for all them. In this case the cumulative sensitivity is simply the sum of the three maps, since these represents homogenous quantities each indicating the sensitivity to a grid refinement. Figure 9 shows the total sensitivity to grid refinement: it is interesting to note that peak values are obtained in regions close to the entrance, closely matching the local characteristics of the flow which presents, in alternating fashion, accelerating and decelerating regions. According to our analysis, refining in these particular locations is most effective to reduce the global error. This, indeed, would reduce the error everywhere not just at the point of the refinement. The results presented here are obtained using the exact solution to evaluate the sensitivity. However we also tested the procedure using the error extrapolated from two grids, obtaining identical results. In order to complete the study and asses the effectiveness of the new approach we decided to implement a grid adaptation algorithm based on the new ESR indicator. For this purpose we used the FreeFem++ software and its built-in mesh-generator functions. The aim of the test is to optimize an initial grid formed by a fixed number of triangles created by the mesh generator *Bamg*[7]. For this purpose we fix the initial number of vertexes of the triangulation (and therefore we the total degrees of freedom of the discretization) and use our refinement criterion based on the ESR map to displace them. Note that we are not really refining here but we rather move points sideways in a way to refine somewhere and de-refine elsewhere. From an operative point of view we displace vertexes in a way proportional to the sensitivity map gradient.

Figure 10 shows the evolution of the error during the adaptation procedure. Three mesh snapshots are shown: the first one (left) represents the starting grid generated by the *Bamg* mesh generator, the second (centre) shows the vertex distribution after 100 iteration and the third one (right) is the final vertex distribution obtained after about 1000 iteration. The corresponding history of the E_2 is displayed in figure 10. The green boxes on the graph indicate the iteration number at which the three mesh snapshots were taken. Note that the large number of iterations used in this test is related to the necessity to avoid triangles overlapping during the re-meshing procedure implement by the *movemesh* command in $FreeFem++$. Here we did not try to optimize the step size in order to reduce the

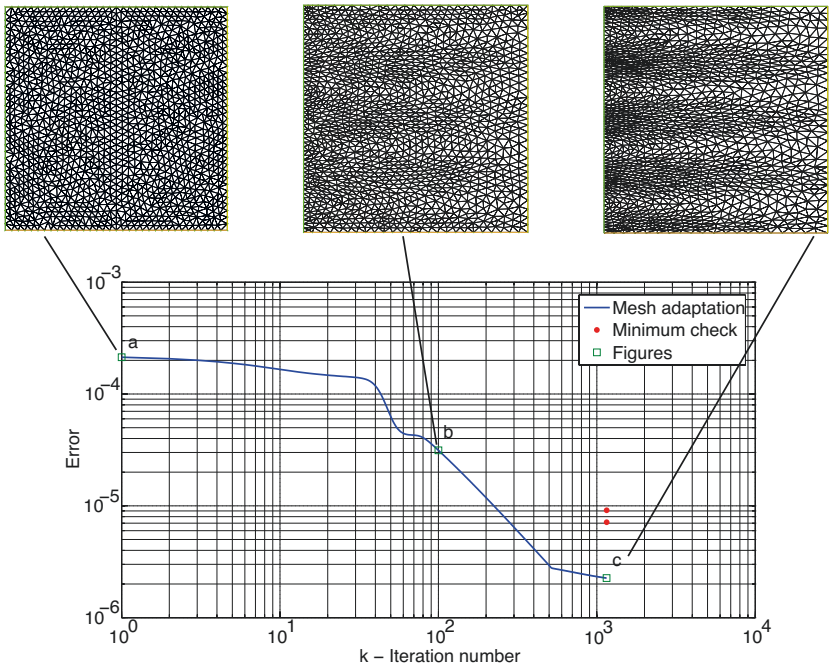

Fig. 10 Error E_2 as a function of the number of iteration of the grid adaption procedure. a), b) & c):sample grids during the adaptation procedure.

number of iterations but we were just interested in the final vertex redistribution. The procedure implemented works in an effective way, reducing the initial error of almost two order of magnitude without increasing the total number of d.o.f. but just changing the vertex density in particular regions. In order to verify if the procedure based on the new ESR indicator was effective. In order to check if the final configuration corresponds to a true minimum of the global error (1) we tried to slightly alter the grid by displacing the vertexes into opposite directions: the resulting errors related to the new grids are indicated in the graph (6) by the red points. This final test suggests that the obtained configuration is a real minimum of the integral (1).

4 Conclusions

In this paper, we have introduced a new indicator for grid adaptation and refinement which truly minimize the global error of the solution taking inspiration from the concept of structural sensitivity introduced by Giannetti & Luchini[5] in fluid problems.

Common approaches in this field are usually based on a) the adjoint solution, that allows to compute the gradient of an objective function (goal oriented approach) or b) the estimate of the residual (residual based approach or $\tau - criterion$) which leads to a suboptimal decay of the error.

Here, we propose to combine the information provided by these two approaches. The resulting ESR indicator, i.e. error sensitivity to refinement, provides a spatial map that identifies the region where a grid refinement really optimizes the

global error. We have used such approach to study both a scalar elliptic equation and system of Navier-Stokes equations. In the last case, we also implemented an iterative grid adaptation based on the ESR which improves the accuracy of the solution of almost two order of magnitude by redistributing the nodes of the initial computational mesh.

References

1. Zienkiewicz, O. C. & Zhu, J. Z. *A simple error estimator and adaptive procedure for practical engineering analysis*, Int. J. Numer. Meth. Eng. **24**, 337–357 (1987).
2. Trottenberg, U., Oosterlee, C. & Schuller, A. *Multigrid*, Academic press (2000).
3. Giles, M. B. & Pierce, N. A. *An introduction to the Adjoint Approach to Design*, Flow, Turbulence and Combustion **65**, 393–415 (2000).
4. Becker, R. & Rannacher, R. *An optimal control approach to a posteriori error estimation in finite element methods*, Acta Numerica **10**, 1–102 (2001).
5. Giannetti, F. & Luchini, P. *Structural sensitivity of the first instability of the cylinder wake*, J. of Fluid Mech. **581**, 167–197 (2007).
6. Kovasznay, L. I. G. *Laminar flow behind a two-dimensional grid*, Mathematical Proceedings of the Cambridge Philosophical Society **44**, 58–62 (1948).
7. Hecht, F. *New development in FreeFem++*, J. Numer. Math., **20**, 251–265 (2012)

Paper

10

Noname manuscript No.
(will be inserted by the editor)

The flow past a freely rotating sphere

David Fabre · Joël Tchoufag · Vincenzo Citro · Flavio Giannetti · Paolo Luchini

Received: date / Accepted: date

Abstract We consider the flow past a sphere held at a fixed position in a uniform incoming flow but free to rotate around a transverse axis. A steady pitchfork bifurcation is reported to find place at a threshold $Re^{OS} = 206$ leading to a state with zero torque but nonzero lift. Numerical simulations allow to characterize this state up to $Re \approx 270$ and confirm that it substantially differs from the steady-state solution which exists in the wake of a fixed, non-rotating sphere beyond the threshold $Re^{SS} = 212$. A weakly nonlinear analysis is carried out and is shown to successfully reproduce the results and to give substantial improvement over a previous analysis (Fabre *et al.*[10]). The connection between the present problem and that of a sphere in free fall following an oblique, steady (OS) path is also discussed.

Keywords freely moving bodies · fluid-structure interactions · weakly nonlinear expansion

1 Introduction

Free falling and rising of particles in Newtonian fluids play an important role in many industrial and natural applications, such as the settling of sediments in lakes, buoyancy-driven bodies in the atmosphere or the dynamics of catalysts in chemical reactors. The particle motion is caused by the buoyancy force that is balanced by the hydrodynamic resistance. The resulting wake dynamics can lead to completely different regimes, such as tumbling, zigzag or steady oblique paths[1]. The mechanisms leading to path destabilization are related to intrinsic wake instabilities

D. Fabre
Université de Toulouse, Institut de Mécanique des Fluides de Toulouse (IMFT) - Allée Camille Soula, 31400 Toulouse, France

J. Tchoufag
Department of Mechanical Engineering, University of California, Berkeley, CA 94720, USA

V. Citro & F. Giannetti & P. Luchini
DIIN, University of Salerno, Via Giovanni Paolo II, 84084, Fisciano (SA), Italy
E-mail: vcitro@unisa.it (Vincenzo Citro)

which induce lift and torque forces on the bodies. Yet, in general, the relation between wake instabilities around a fixed body and path instabilities around a body in free fall is not straightforward as the latter problem is fully coupled and the wake dynamics are modified by the motion of the body (as discussed for instance in Assemat et al.[6] and Auguste et al.[7]). Thus, it may be useful to consider intermediate problems in which only some degrees of freedom of the body are allowed. This is the objective of the present paper, where we will consider the flow past a sphere allowed to rotate but not to translate. In an experimental setup, this configuration may correspond, for instance, to the case of a sphere held by a thin transverse wire.

The case of a sphere is among the simplest and most generic geometries and has thus already made the object of a number of studies (see [12] for an up-to-date review). When the sphere is fixed and not rotating, the flow remains axisymmetric at low Reynolds, but bifurcates towards a steady-state (SS) solution with a planar symmetry and nonzero lift at $Re^{SS} = 212$. A subsequent Hopf bifurcation then occurs at $Re \approx 276$ leading to a periodic vortex shedding mode [5]. The case where the sphere is fixed but rotating in an imposed way was recently considered by [12]. They showed that in presence of weak rotation, the bifurcation at Re^{SS} becomes an imperfect one. They also showed that rotation has a strong effect on the secondary Hopf bifurcation. The case of a sphere in free motion also made the object of a number of studies, both experimental ([2], [4], [16]) and numerical ([3], [17]). For Reynolds numbers in the range beyond 300, up to 4 unsteady regimes were discovered, but for smaller Reynolds, all studies show that the first bifurcation is towards an oblique, steady (OS) path which bears some similarity with the steady-state (SS) existing for the fixed, non-rotating sphere. However, the connection between both states is not that straightforward, and Fabre et al.[10] showed that the OS state results from a bifurcation at a threshold $Re^{OS} = 206$ which is different from the value $Re^{SS} = 212$ for the SS state. Fabre et al. [10] also pointed out that the OS state is characterized by zero torque exerted on the sphere, so this state is also directly a valid equilibrium solution for the present problem where the sphere is free to rotate but not to translate. The study of [10] was done using an asymptotic approach which is valid under the assumption that the rotation rate is weak. However, a major drawback of this approach is that it fails in the vicinity of $Re^{SS} = 212$ and beyond, while numerical and experimental results show that the OS path still exists above this value of Re.

In the present paper, we will thus investigate the case of a sphere where rotation is allowed but not translation, which is closely related to the situation discussed above. After setting the problem in sec. 2, we will document this situation in sec. 3, through DNS results and compare with the case where both translation and rotation are blocked. We will then conduct in sec. 4 a weakly nonlinear analysis of this problem, which will confirm that a steady bifurcation occurs for the same value Re^{OS} as for the case where both rotation and translation are allowed, and overcome the difficulties encountered in the previous study of [10]. Finally, conclusions will be provided in sec. 4.

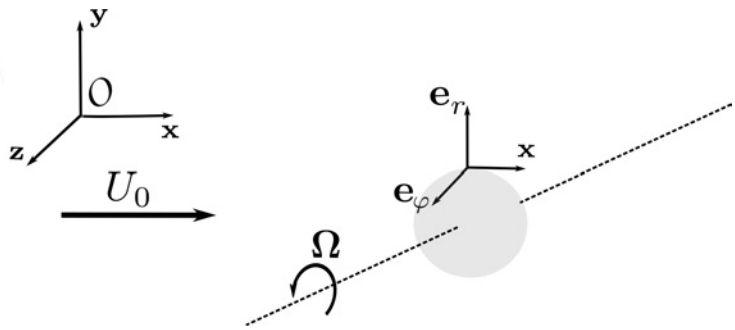

Fig. 1: Problem configuration. The sphere is free to rotate (but not to translate) around any axis.

2 Problem definition and governing equations

The situation investigated here is sketched in figure 1. A sphere of radius R and density ρ_b is placed in a flow of velocity U_0 of a fluid with density ρ_f and viscosity ν. The problem involves two dimensionless control parameters, namely the Reynolds number $Re = U_0 R/\nu_f$ and the body-to-fluid density ratio $\bar{\rho} = \rho_b/\rho_f$. We formulate the problem in a fixed system of axes (x, y, z) with the unit vector $\mathbf{x}$ aligned with the incoming velocity.

In the setup considered here, the only degree of freedom is the rotation of the sphere around its center. We note $\mathbf{\Omega}$ the angular velocity vector and decompose it over the basis as $\mathbf{\Omega} = \Omega_x\mathbf{x} + \Omega_y\mathbf{y} + \Omega_z\mathbf{z}$.

The flow field $[\mathbf{V}, P]$ and the rotation rate $\mathbf{\Omega}$ of the sphere are governed by the following equations :

$$\nabla \cdot \mathbf{V} = \mathbf{0}, \tag{1a}$$

$$\frac{\partial \mathbf{V}}{\partial t} + \mathbf{V} \cdot \nabla\mathbf{V} = -\nabla P + \frac{1}{Re}\nabla^2\mathbf{V}, \tag{1b}$$

$$\bar{\rho}\frac{\pi}{60}\frac{d\mathbf{\Omega}}{dt} = \mathbf{M}. \tag{1c}$$

These equations are coupled in two ways. First, the rotation of the sphere results in a boundary condition to be imposed for the velocity of the fluid at the surface of the sphere as $\mathbf{V} = \mathbf{\Omega} \times \mathbf{r}$. Secondly, in Eq. 1c the sphere responds to the torque $\mathbf{M}$ exerted by the fluid on it. The latter, and the associated force $\mathbf{F}$, are given by

$$\mathbf{F} = \int_{\mathscr{S}} \mathbf{T} \cdot \mathbf{n}\mathrm{dS} \equiv F_x\mathbf{x} + F_y\mathbf{y} + F_z\mathbf{z} \tag{2a}$$

$$\mathbf{M} = \int_{\mathscr{S}} \mathbf{r} \times (\mathbf{T} \cdot \mathbf{n})\mathrm{dS} \equiv M_x\mathbf{x} + M_y\mathbf{y} + M_z\mathbf{z}. \tag{2b}$$

where $\mathbf{r}$ denotes the position vector relative to the body center of inertia and $\mathbf{T} = -P\mathbf{I} + Re^{-1}(\nabla\mathbf{V} +^{\mathrm{T}} \nabla\mathbf{V})$ the stress tensor. Note that in the present case,

the coupling only involves the torque $\mathbf{M}$ while the force $\mathbf{F}$ is not coupled to the motion of the sphere, unlike in the more general case considered in [23]. Finally, this set of equations is completed by the boundary condition $\mathbf{V} = \mathbf{U_0 x}$ for $\|\mathbf{r}\| \to \infty$.

In the following we will be mostly interested in the characterization of steady-state solutions of the problem. According to 2b such states imply the torque $\mathbf{M}$ exerted by the fluid on the sphere to be zero, and the interesting, non-trivial solutions are those with nonzero rotation rate $\mathbf{\Omega}$.

3 Numerical results

We have solved numerically the set of equations 1 using a combined finite-difference second-order immersed-boundary multigrid code which is described in detail in Citro et al. [12].

The 3D steady solutions can be obtained, in subcritical conditions, by simply integrating the time-dependent equations 1 over a sufficiently long time interval. However, since in the present paper we consider also supercritical conditions, we use a stabilization algorithm to obtain directly the steady solution. The method is based on the minimization of the residual norm at each integration step. It allows us steady-state solutions even in the case where they are temporally unstable. The method is briefly described in Citro et al. [11] and was also used in Citro et al. [12] for the case where the rotation rate of the sphere is imposed. Adaptation to the freely rotating case simply adds the dynamical equation 1c to the latter problem, and adaptation of the method to this case is straightforward.

For $Re < Re^{OS} = 206$, only axisymmetric solutions with zero rotation rate and only a drag force are found. Above this threshold, depending upon initial conditions the numerical method yields either an axisymmetric solution or a set non-axisymmetric solutions with nonzero rotation rate around an axis perpendicular to the incoming flow and a nonzero lift. Because of the rotational symmetry, all orientations of axis of rotation are theoretically allowed. In the sequel we will assume a rotation rate Ω_z around the $\mathbf{z}$ axis. Accordingly the lift will be exerted along the $\mathbf{y}$ axis, and we define the lift coefficient as $C_L = 2F_y/(\pi\rho R^2)$.

Figure 2 characterizes the rotating solution through a plot of the lift coefficient as function of the Reynolds number up to $Re = 240$. The plot is characteristic of a pitchfork bifurcation occurring for $Re = 206$. In the same figure, we plot the lift coefficient in the related problem of a nonrotating sphere, with data taken from figure 3 of Citro et al. [12]. As expected in this case, the bifurcation occurs for $Re^{SS} = 212$ and the two curves notably differ up to $Re \approx 230$. For higher values of the Reynolds number, the two curves tend to approach each other, suggesting that allowing rotation has only a mild effect on the structure of the flow.

4 Asymptotic expansion of the coupled fluid-sphere system

4.1 Analysis

Using notations similar to those used in [23] of the study of objects in free fall, the solution of equations (1) may be considered as a state vector $\mathbf{Q} = \left[\mathbf{Q}^f, \mathbf{Q}^b\right]^T$, where $\mathbf{Q}^f = [\mathbf{V}(\mathbf{r}, t), P(\mathbf{r}, t)]^T$ describes the fluid local velocity and pressure and

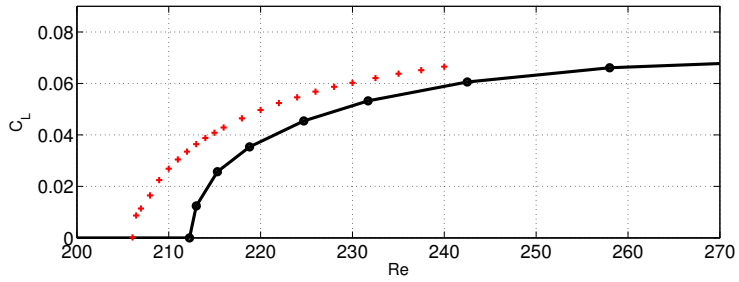

Fig. 2: Forces as function of Re for both fixed (·) and freely (+) rotating sphere.

$\mathbf{Q}^b = \mathbf{\Omega}(t)$ gathers the degrees of freedom associated with the body (here only the rotational velocity).

Thus, we investigate the vicinity of $Re_c = Re^{SO}$ by defining a small parameter $\epsilon = \sqrt{Re - Re_c}/Re_c$. To this aim, following [14] and [15], we introduce a multiscale time expansion procedure with a fast time scale t and a slow time scale $\tau = \epsilon^2 t$ so as to expand this solution in the form:

$$\mathbf{Q} = \mathbf{Q_0} + \epsilon \mathbf{Q_1}(t,\tau) + \epsilon^2 \mathbf{Q_2}(t,\tau) + \epsilon^3 \mathbf{Q_3}(t,\tau) + \cdots \tag{3}$$

Injecting these expansions in the system of governing equations (1) yields a nonlinear problem at zeroth order and a linear problem at each order ϵ^j for $j \geq 1$. The details are very similar to those given in [23], except that the component $\mathbf{Q}^b$ of the state vector contains only the rotation and that the expansion is done in terms of the Reynolds number, not the Archimedes number. We refer the reader to the supplemental material in [23] for the detailed expressions. These problems are solved for increasing j, using the finite element solver FreeFem++ [19]. The numerical details regarding mesh refinement, polynomial interpolation of velocity and pressure fields, *etc*, can be found in [22].

The base state $\mathbf{Q_0}$ corresponds to the steady, vertical fall or rise with an axisymmetric flow field, and is computed using an iterative Newton method as described in [14]. At order ϵ, $\mathbf{q_1}$ is the solution of the linear stability problem which is solved as in [22]. Taking advantage of the body axisymmetry, we express the fluid velocity and pressure fields in the body frame using cylindrical coordinates (x, r, φ) and seek this solution as a superposition of eigenmodes of the form

$$\mathbf{Q}_m = \left[\hat{\mathbf{q}}^f_m(x,r)e^{\mathrm{i}m\varphi}, \hat{\mathbf{q}}^b_m\right]^T e^{\lambda t}$$

where m is the azimuthal wavenumber and $\lambda = \lambda_r + \mathrm{i}\lambda_i$ is the complex eigenvalue. The generalized eigenproblem to be solved at this order can be recast in the matrix form:

$$\lambda \mathscr{B}\mathbf{Q}_1 + \mathscr{A}(\mathbf{Q}_0)\mathbf{Q}_1 = \mathbf{0}.$$

The solutions of this problem have to be examined for each value of the azimuthal wavenumber. The case $m = 0$ corresponds to axisymmetric modes, and

symmetry considerations show that the angular velocity component of the eigenmodes is in the axial direction, i.e. $\hat{\mathbf{q}}^b_m \equiv \hat{\omega}_0 \mathbf{x}$. It is found that all these modes are stable, and that the least damped one is a non-oscillating one ($\lambda_i = 0$) corresponding to a motion where the sphere initially spins around the axial axis and slows down due to friction. This mode also exists in the case of a freely falling disk and was analyzed in appendix C of Tchoufag et al. [22]. It this reference it was called the back-to-zero-rotation mode (BZR). Mode with $|m| \geq 2$ do not exert any torque on the sphere and hence are identical to those of the non-rotating ($\hat{\mathbf{q}}^b_m = \mathbf{0}$). Moreover these modes are also found to be always stable in the range of Reynolds considered.

Hence, the most interesting case corresponds to azimuthal wavenumbers $m = \pm 1$, and as for the fixed, nonrotating sphere, a Pitchfork bifurcation associated with a steady mode ($\lambda_r = \lambda_i = 0$) is detected for $Re = Re^{OS} = 206$. Following the assumption made by Fabre et al. [10], we consider these two modes adequate to quantitatively describe the characteristics of the nonlinear oblique motion of the sphere for $Re > Re_c$. Hence, restricting the following analysis to these modes, the general $O(\epsilon)$ solution at the threshold ($\lambda_r = 0$) may be expressed in the form

$$\mathbf{Q_1} = \hat{A}(\tau) \left[\hat{\mathbf{q}}^f_1(x,r) e^{\mathrm{i}\varphi}, \hat{\mathbf{q}}^b_1 \right]^T + c.c., \tag{4}$$

where $\hat{A}(\tau)$ is the $O(\epsilon)$ complex amplitude of the global mode and *c.c.* stands for the complex conjugate quantities, which shall be marked by a * symbol hereafter. Note that since the global mode $m = 1$ is real, its complex conjugate directly corresponds to the mode $m = -1$. Therefore, there is no need to distinguish between two amplitudes $\hat{A}^+ = A$ and $\hat{A}^- = A^*$ since the latter is completely determined once the former is.

Due to symmetry considerations (see [22]), the component of the $m = 1$ eigenmode corresponding to the rotation of the body can be written as $\hat{\mathbf{q}}^b_1 = \frac{\hat{\omega}_+}{2}(\mathbf{z} + i\mathbf{y})$, so the orientation of the rotation axis is given by the argument of $A\hat{\omega}_+$. We choose to normalize the eigenmode as $\hat{\omega}_+ = 1$, so that the norm of A directly gives the rotation rate. Moreover, a real A will correspond to rotation around the $\mathbf{z}$ axis (and lift along the $\mathbf{y}$ axis) while an imaginary A will correspond to rotation around the $\mathbf{y}$ axis (and lift along the $\mathbf{z}$ axis).

Terms of order ϵ^2 and ϵ^3 are the solution of linear inhomogeneous problems arising from the expansion of (1) at the corresponding order. Details about the mathematical structure of these problems and the numerical procedure used to solve them are given in the Supplemental Material in [23] where the weakly nonlinear analysis has been performed for the more general case of an unsteady mode. It suffices here to say that at order ϵ^2, the flow is modified by higher-order harmonics which obey the inhomogeneous linear system of equations

$$\partial_t \mathscr{B} \mathbf{Q_2} + \mathscr{A}(\mathbf{Q_0}) \mathbf{Q_2} = \mathbf{F_2}(\mathbf{Q_0}, \mathbf{Q_1}).$$

The forcing term $\mathbf{F_2}$ on the right-hand side is made of three independent terms expressing the effect of a small variation of Re on the base flow and the interaction of one mode ($\mathbf{Q_A} + c.c.$) with itself and its c.c. Using the linear superposition principle, we solve this inhomogeneous equation for each contribution to the forcing. The ϵ^2-order solution then reads $\mathbf{Q_2} = \hat{\mathbf{Q}}_{\delta_{Re}} + |A|^2 \hat{\mathbf{Q}}_{AA^*} + \left(A^2 \hat{\mathbf{Q}}_{AA} e^{2\mathrm{i}\varphi} + c.c. \right)$.

The problem at order ϵ^3 is also an inhomogeneous linear system, the forcing term $\mathbf{F_3}(\mathbf{Q_0}, \mathbf{Q_1}, \mathbf{Q_2})$ depending on lower order solutions. More specifically, $\mathbf{F_3}$ contains terms of the form $\sim e^{i\varphi}$ which are resonant because they excitate the system precisely in the direction of the unstable steady eigenmode. In order to avoid the secular responses caused by these terms, we use the Fredholm alternative and impose a compatibility condition: the resonant forcing must be orthogonal to the adjoint modes. These modes are obtained either in a continous or in a discrete form. Here, we chose the latter option, and compute the adjoint modes by solving for the eigenmodes of the hermitian of $\mathscr{A}$, the linear operator of the $O(\epsilon)$ problem. The compatibility condition then results in the following amplitude equation:

$$\frac{dA}{dt} = (Re - Re_c)\sigma A - \mu A|A|^2, \tag{5}$$

where $(Re - Re_c)\sigma$ is the exponential growth rate of $\mathbf{Q_1}$ in the linear regime, while μ is a real coefficient responsible for the nonlinear saturation. The numerical value of μ, contrary to that of σ, depends on the normalization of the unstable global mode. Solving for the steady solution of (5), the amplitude of the perturbation from the vertical fall reads

$$A = \pm\sqrt{\frac{(Re - Re_c)\sigma}{\mu}}. \tag{6}$$

Having in mind that the solution at order 1 has been normalized so that the angular velocity of the eigenmodes is 1, this equation directly yields a prediction for the rotation rate ω. It is noteworthy that the coefficients σ and μ appearing in the amplitude equation are actually independent upon the mass ratio $\bar{\rho}$. This point will be rediscussed in the conclusions.

4.2 Results and discussion

As recalled in the introduction, a previous attempt at describing the bifurcation leading to the OS state for a sphere in free fall was done in [9]. Unlike in the present approach, the analysis of [9] assumed the rotation rate ω to be small, and expanded the flow around the sphere as follow:

$$\mathbf{q} = [\mathbf{V}, P] = \mathbf{q}_0 + \omega\mathbf{q}_1 + \omega^2\mathbf{q}_2 + \omega^3\mathbf{q}_3 + \cdots \tag{7}$$

Injecting this ansatz into the incompressible Navier-Stokes equations, the analysis lead to a prediction of torque exerted on the sphere under the form:

$$M = M_\omega\omega + M_{\omega^3}\omega^3 \tag{8}$$

It was thus possible to predict the existence of solution with a non-zero rotation rate given by

$$\omega = \pm\sqrt{-\frac{M_\omega}{M_{\omega^3}}} \tag{9}$$

Note that the term M_ω becomes positive for $Re > Re^{OS}$ while the term M_ω^3 is negative in this range of Reynolds; hence Eq. 9 also predicts a supercritical bifurcation for $Re > Re^{SO}$.

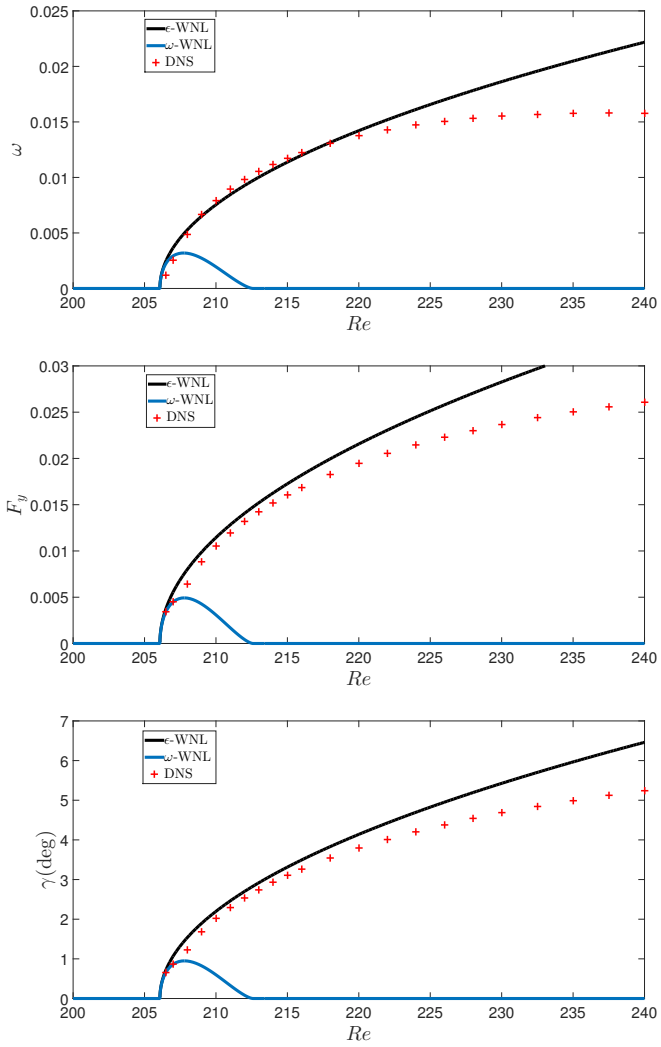

Fig. 3: Zero-Torque solutions of a sphere. Comparison between DNS (symbols), ω-asymptotic expansion (blue line), ϵ-asymptotic expansion. Top) Angular velocity. Center) Lift force as a function of the Reynolds number. Bottom) Slope angle γ, i.e. the angle between the lift force and the incoming flow.

The results to be discussed now correspond to the case of a rotation around the $\mathbf{z}$ axis, thus resulting in a lift force along $\mathbf{y}$. In figure 3(top), we compare the angular velocity ω of the SO state as predicted by the new ϵ-expansion derived in the previous paragraph (Eq. 6), as predicted by the ω-expansion of [9] (Eq. 9), and as computed numerically in section 3. We also compare in figure 3(middle) the associated lift forces corresponding to the three approaches. The comparison shows that, for both these quantities, the present ϵ-expansion reproduces much better

the numerical results than the previous ω-expansion. In particular, the failure of the ω-expansion at $Re^{SS} = 212$ is not observed anymore in the present approach.

As discussed in [10], the angle γ between the force $\mathbf{F}$ and the direction of the incoming flow $\mathbf{x}$ (given by $\tan\gamma = F_y/F_x$) directly corresponds to the slope of the path in the corresponding situation where the sphere is freely falling. This angle is plotted as function of Re in figure 3(bottom). We observe, again that the present ϵ-expansion reproduces much better the numerical results than the previous ω-expansion.

Note that Uhlmann & Dusek [17] studied the case of a sphere in free fall with density ratio $\bar{\rho} = 1.5$, and reported for $Re \simeq 243$ a steady oblique motion characterized by a slope $\gamma \simeq 5.2$ degrees and a rotation rate $\omega \simeq 0.014$. These findings thus corroborate quantitatively the results of figure 3.

5 Summary and discussion

In this paper, we investigated by using numerical simulations and a weakly nonlinear expansion the steady flow around a sphere placed at a fixed place in a uniform fluid flow and free to rotate around a transverse axis. A steady pitchfork bifurcation is reported to find place at a threshold $Re^{OS} = 206$ leading to a state with zero torque but nonzero lift. Numerical simulations allow to characterize this state up to $Re \approx 270$ and confirm that it substantially differs from the steady-state solution which exists in the wake of a fixed sphere beyond the threshold $Re^{SS} = 212$. A weakly nonlinear analysis, formally valid for $\epsilon = (Re - Re_c)/Re_c \ll 1$, is carried out and is found to reproduce accurately the results up to $Re \approx 225$, giving substantial improvement over a previous expansion conducted by [10] which was unable to predict the existence of this state beyond $Re > 212$. The connection between the present problem and that of a sphere in free fall is discussed. It is argued that the steady solution of the present problem is also an acceptable solution for the related problem of a sphere in free fall, and corresponds to the Oblique, Steady (OS) path observed in both experiments and simulations. A quantitative comparison against the data showed in Uhlmann & Dusek [17] was provided to support this.

To conclude, we shall address two interesting points which require some discussion. First, we stress again that, although the problem is characterized by two nondimensional parameters, namely Re and the density ratio $\bar{\rho} = \rho_s/\rho_f$, all results presented here are actually independent upon this latter parameter. The fact that the steady solution computed by DNS or by the time-independent solution of the amplitude equation 5 does not depend upon the mass of the sphere is actually not so surprising, since the parameter $\bar{\rho}$ is only present in the term involving the angular acceleration (left-hand-side of Eq. 1c). Hence, once the equilibrium is reached, inertia of the sphere does not enter into play any longer. It is more puzzling to note that the parameters σ and μ appearing in the amplitude equation 5 are also independent upon the mass. Therefore, in the vicinity of the threshold, not only the properties of the final state will be independent upon the mass, but also the transient dynamics experienced to reach it. This is somewhat counterintuitive, as one would expect that for a heavy sphere the transients will be longer than for a light sphere. A complementary study, considering the limit of very heavy objects

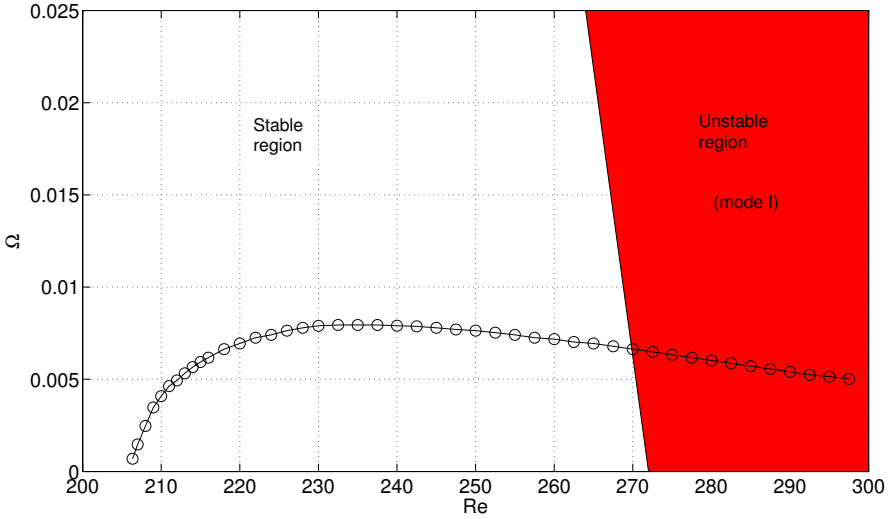

Fig. 4: (Colour online) Stability diagram in the (ω, Re) plane. The black circled line represents, for different Re, the corresponding rotation rate leading to a zero-torque flow around the sphere. The red area represents the unstable region for mode I [12].

(where a quasi-static approach is possible), is underway to explain this apparent paradox.

Secondly, the issue of secondary instability of the steady solution considered here is an open question to be addressed in future studies. In effect, the ability of the sphere to rotate (or to both rotate and translate) is expected to have an effect on the Hopf bifurcation which is known to occur in the range $Re \approx 270$. In the time-dependent states resulting from this secondary bifurcation, the angular velocity of the sphere will no longer be constant but will be given by the time-dependent solution of Eq. 1c. As a first step towards a rigorous study of this problem, we may look at the stability of the flow around a sphere rotating at exactly the angular velocity of the OS solution described above. This case actually constitutes a subset of a more general study conducted by [12], who gave a stability map in the $\omega - Re$ plane of the flow around a sphere rotating at a fixed, constant angular velocity. We plot in figure 4 a zoom of this stability map and superpose it to the curve defining the OS state described above. This figure indicates that the weak rotation of the OS state slightly enhances the instability, and that the threshold is advanced from 272 in the non rotating case to approximately 270. A more rigorous study of this problem, including the effect of the density ratio, is left for future studies.

References

1. Ern, P., Risso, F., Fabre, D. & Magnaudet, J. *Wake-induced oscillatory paths of bodies freely rising or falling in fluids*, Annu. Rev. Fluid Mech. **44**, 97–121 (2012).
2. Mordant, N. & Pinton, J.F. *Velocity measurement of a settling sphere*, Eur. Phys. J B **18**, 343–352 (2000).
3. Jenny, M., Dusek, J. & Bouchet, G. *Instabilities and transition of a sphere falling or ascending freely in a Newtonian fluid*, J. Fluid Mech. **508**, 201–239 (2004).
4. Horowitz, M. & Williamson, C. H. K. *The effect of Reynolds number on the dynamics and wakes of freely rising and falling spheres*, J. Fluid Mech. **651**, 251–294 (2010).
5. Johnson, TA and Patel, VC, *Flow past a sphere up to a Reynolds number of 300*, J. of Fluid Mech., **378**, 19–70 (1999).
6. Assemat, P., Fabre, D. & Magnaudet, J. *The onset of unsteadiness of two-dimensional bodies falling or rising freely in a viscous fluid: a linear study*, J. Fluid Mech. **690**, 173–202 (2012).
7. Auguste, F., Magnaudet, J. & Fabre, D. *Falling styles of disks*, J. Fluid Mech. **719**, 388–405 (2013).
8. Auguste, F. *Instabilités de sillage générées derrière un corps solide, fixe ou mobile dans un fluide visqueux* , PhD dissertation, University of Toulouse, 2010.
9. Fabre, D., Auguste, F. & Magnaudet, J. *Bifurcations and symmetry breakings in the wake of axisymmetric bodies*, Phys. Fluids **20**(5), 051702 (2008).
10. Fabre, D., Tchoufag, J. & Magnaudet, J. *The steady oblique path of buoyancy-driven disks and spheres*, J. Fluid Mech. **707**, 24–36 (2012).
11. Citro, V., Giannetti, F., Luchini, P. & Auteri, F. *Global stability and sensitivity analysis of boundary-layer flows past a hemispherical roughness element*, Phys. Fluids **27**, 084110 (2015).
12. Citro, V., Tchoufag, J., Fabre, D., Giannetti, F. & Luchini, P. *Linear stability and weakly nonlinear analysis of the flow past rotating spheres*, Submitted to Journal of Fluid Mechanics.
13. Natarajan, R. & Acrivos, A. *The instability of the steady flow past spheres and disks*, J. Fluid Mech. **254**, 323–344 (1993).
14. Sipp, D. & Lebedev, A. *Global stability of base and mean-flows: a general approach and its applications to cylinder and open cavity flows*, J. Fluid Mech. **593**, 333–358 (2007).
15. Meliga, P., Chomaz, J. M., & Sipp, D. *Global mode interaction and pattern selection in the wake of a disk: a weakly nonlinear expansion*, J. Fluid Mech. **633**, 159–189 (2009).
16. Obligado, M., Machicoane, N., Chouippe, A., Volk, R., Uhlmann, M. & Bourgoin, M. *Path instability on a sphere towed at constant speed*, J. Fluids Struct. **58**, 99–108 (2015).
17. Uhlmann, M. & Dusek, J. *The motion of a single heavy sphere in ambient fluid: a benchmark for interface-resolved particulate flow simulations with significant relative velocities*, Int. J. Mutl. Flow **59**, 221–243 (2014).
18. Uhlmann, M. & Doychev, T. *Sedimentation of a dilute suspension of rigid spheres at intermediate Galileo numbers: the effect of clustering upon the particle motion*, J. Fluid Mech. **752**, 310–348 (2014).
19. Hecht, F. *New development in FreeFem++*, J. Numer. Math. **20**, 251–265 (2012).
20. Assemat, P., Fabre, D., & Magnaudet, J. *The onset of unsteadiness of two-dimensional bodies falling or rising freely in a viscous fluid: a linear study.*, J. Fluid Mech. **690**, 173-202 (2012).
21. Tchoufag, J., Magnaudet, J. & Fabre, D. *Linear stability and sensitivity of the flow past a fixed oblate spheroidal bubble*, Phys. Fluids **25**, 054108 (2013).
22. Tchoufag, J., Fabre, D., & Magnaudet, J. *Global linear stability analysis of the wake and path of buoyancy-driven disks and thin cylinders*, J. Fluid Mech. **740**, 278-311 (2014).
23. Tchoufag, J., Fabre, D., & Magnaudet, J. *Weakly Nonlinear Model with Exact Coefficients for the Fluttering and Spiraling Motion of Buoyancy-Driven Bodies*, Phys. Rev. Lett. **115**, 114501 (2015).